ABSTRACT

Title of Dissertation: DESIGN AND EXPERIMENTAL CHARACTERIZATION OF METAL ADDITIVE MANUFACTURED HEAT EXCHANGERS FOR AEROSPACE APPLICATION

Fabio Battaglia,
Doctor of Philosophy, 2020

Directed By: Professor Michael Ohadi,
Mechanical Engineering

High temperature heat exchangers are key to the success of emerging high-temperature, high-efficiency solutions in energy conversion, power generation and waste heat recovery applications. When applied to the aerospace applications, the main objective is to develop heat exchangers that can realize significant performance improvement in terms of gravimetric heat exchange density (kW/kg).

In the present study, two air-to-air crossflow heat exchangers were designed, built and tested to determine their potential for high performance, pre-cooling heat exchanger for aircraft applications. A novel design based on manifold-microchannel technology was chosen as it provided localized and optimum distribution of the flow among the heat transfer surface micro channels, offering superior heat transfer performance and low pressure drops, when compared to conventional, state of the art heat exchangers for the chosen application. However, fabrication of the manifold microchannel design for high temperature with super alloys as the heat exchanger material presents serious manufacturing challenges fabrication techniques. To overcome this limit,

direct metal laser sintering (DMLS) additive manufacturing technique was selected for the fabrication of the Ni-based superalloy manifold-microchannel heat exchangers in the present study. Extensive work was performed to characterize the printing capability of different metal 3D-printers in terms of printing orientation, printing accuracy and structure density. Based on the knowledge acquired, two units were printed, with overall size of 4”x4”x4” and 4.5”x4”x3.5” and fin thickness of 0.220 mm and 0.170 mm, respectively. The printed units were the largest additively printed, superalloy-based manifold-microchannel heat exchangers found in the literature. The experimental characterization was carried at high temperature (600°C) and the model prediction of the performance was updated to characterize the behavior of the heat exchangers in this operational conditions. Based on the experimental results, a gravimetric heat duty of 9.4 kW/kg for an effectiveness (ε) of 78% was achieved, which corresponds to an improvement of more than 50% compared to the conventional designs. The characterization of the performance at high temperature was then completed by analyzing the thermo-mechanical stress generated by the simultaneous presence of temperature gradient and pressures. The current study is the first to characterize the behavior of manifold-microchannel heat exchanger under high temperature in terms of performance prediction and thermo-mechanical analysis.

DESIGN AND EXPERIMENTAL CHARACTERIZATION OF METAL ADDITIVE MANUFACTURED HEAT EXCHANGERS FOR AEROSPACE APPLICATION

By

Fabio Battaglia

Dissertation submitted to the Faculty of the Graduate School of the
University of Maryland, College Park, in partial fulfillment
of the requirements for the degree of
Doctor of Philosophy
2020

Advisory Committee:
Professor Michael Ohadi, Chair
Professor Hugh A. Bruck
Professor Christopher Cadou
Professor Marino DiMarzo
Professor Jungho Kim

Dedication

To my family and Margherita
who have helped, encouraged, and supported me always

Acknowledgements

First and foremost I would like to thank my advisor Dr. Michael Ohadi and my supervisors Dr. Amir Shooshtari, Dr. Martinus Arie, Dr. Farah Singer and Dr. Raphael Mandel for their guidance, help, encouragement, and support for my research.

I would like to express my gratitude to the U.S. Department of Energy/ARPAE division for providing financial support and guidance for my thesis project and its technical and techno-economical milestones.

Lastly, I am also grateful to my friends at Smart and Small Thermal Systems Laboratory (S2TS), for providing a constructive and peaceful environment and also their helpful tips and suggestions regarding my research.

Table of Contents

List of Tables

List of Figures

Nomenclature

A	Area [m^2]
B	ratio of difference of temperatue [-] see Eq. (60)
C_2	inertial resistance factor [1/m]
c_p	Specific heat [J/kgK]
C_{max}	Maximum heat capacity rate [W/K]
C_{min}	Minimum heat capacity rate [W/K]
COP	Coefficient of Performance [-]
C_r	Heat capacity rates ratio [-]
D_H	Hydraulic diameter [m]
EB	Energy balance [-]
F	Maldistribution [%]
f	Fanning Friction factor [-]
FR	force resistance [N]
h	Heat transfer coefficient [W/m^2K]
H	Height [m]
k	Thermal conductivity [W/mK]
k_c	Coefficient of constriction [-]
k_e	Coefficient of expansion [-]
L	Length [-]
m	fin parameter [1/m]
$\dot{m}$	Mass flow rate [kg/s]
M	Mass
MAE	Mean absolute error [%]
n	Design coefficient for safety factor [-]
N	Total number [-]
NTU	NTU [-]
Nu	Nusselt number [-]
P	Pressure [Pa]
ΔP	Pressure drop [Pa]
Q	Heat duty [W]
ΔQ	Heat duty difference between the two sides of the heat exchanger [W]
$Q/m\Delta T$	Gravimetric heat transfer density [W/kgK]
$Q/V\Delta T$	Gravimetric heat transfer density [W/ m^3K]
R	ratio of the thermal capacities of the two streams [-] see Eq. (57)
RT	Temperature ratio [-]
Re	Reynold Number [-]
s	size [m]
S	source term for the momentum equation [N/m^3]
SF	safety factor
T	Temperature [°C]
ΔT	Temperature difference [°C]
t	Thickness [m]
U	Overall heat transfer coefficient [W/m^2K]
Un	Uncertainty [-]
V	Volume [m^3]

v	Velocity [m/s]
W	Width [m]
YS	Yield strength [Pa]
x, y, z	Distance in Cartesian coordinate [m]

Greek symbols

α,β.γ	Printing orientation angles [°]
α	Permeability [m^2]
$1/\alpha$	Viscous resistance coefficient [$1/m^2$]
β	Corrective factor for interfacial area density [-]
γ	Porosity [-]
Γ	Perimeter [m]
ε	Heat exchanger effectiveness [-]
μ	Viscosity [kg/ms]
ρ	Density [kg/m^3]
η	Fin efficiency [-]
σ	Area ratio of minimum free flow area to frontal area [-]

Subscript

1	related to plane 1
2	related to plane 2
avg	average
base	base of the manifold
bc	boundary condition
cf	curve fitting
chn	channel
cold	cold side
core	referred to the heat exchanger from manifold inlet to manifold outlet without headers
dyn	dynamic pressure component
ext	extension
f	fluid
fin	fin
fin-base	at the starting point of the fin from the separator plate
flow	average flow between entrance and exit of the heat exchanger
full	referred to manifold entrance with designed height (as opposite to half)
half	referred to manifold entrance with half the designed height (as opposite to full)
hdr	header
hot	hot side
in	inlet
ideal	assuming no maldistribution (as opposite of real)
inclined	referred to inclined fins
laser	referred to the sintering si<w of the laser spot
LM	logarithmic mean
mnd	manifold
mnd-chn	manifold-channel
no-flow	direction perpendicular to the fluid flows in a cross-flow heat exchanger
out	outlet
opening	referred to the sum of the frontal area projection of the manifold channels

PC	printed circuit
ph	referred to projected area of headers to the heat exchanger
PM	porous medium
r	ratio of two terms
real	considering maldistribution (as opposite of ideal)
s	solid part
stack	elementary unit to represent a manifold-microchannel design
straight	referred to straight fins
sys	system
th	thermal
tot	average fluid flow from manifold channel inlet to manifold channel outlet
w	welding joint
wall	referred to manifold wall

Abbreviations

AM	additive manufacturing
CVD	chemical vapor deposition
DMLS	direct metal laser sintering
DOE	design of experiment
EBM	electron beam melting
ECS	environmental control system
EDM	electrical discharge machining
HIP	hot isostatic pressing
HX	heat exchanger
HTHX	high temperature heat exchanger
HVAC-R	heating, ventilation, air-conditioning and refrigeration
LCM	lithography/based ceramic manufacturing
LOM	laminated-object manufacturing
LTE	local thermal equilibrium
LTHX	low temperature heat exchanger
LTNE	local thermal non-equilibrium
M2HX	manifold-microchannel heat exchanger
MDT	micro deformation technology
MHX	microchannel heat exchanger
ODS	oxide dispersion strengthen
PCHX	printed circuit heat exchanger
PLIS	pressure laminated integrated structure
PM	porous medium
PFHX	plate-and-fin heat exchanger
PHX	plate heat exchanger
RQ	root mean square height
SLM	selective laser melting
SMM	single manifold microchannel
SPC	arithmetic mean peak curvature
SRD	developed interfacial area ratio
TUC	thermal unit cell

Chapter 1 Introduction

1.1 Motivation and Background

Heat Exchangers (HXs) are devices used to transfer heat between two fluids at different temperatures [1]. They are applied in a multitude of different fields, such as power plants, automotive, Heating, Ventilation, Air-Conditioning and Refrigeration (HVAC-R), aerospace, petrochemical, food process, *etc*. Specifically in the aerospace industry, HXs are mainly used in three systems: (1) gas turbine cycle [2], (2) Environmental Control System (ECS), and (3) thermal management of power electronics.

The HX developed in this work is intended for ECS of aircrafts. ECS is employed in aerospace vehicles such as large commercial aircraft to provide comfortable flight conditions for the passengers [3]. The ECS provides both cooling or hot air to pressurize the passenger cabin, which controls temperature, fresh air ventilation and cabin altitude (via pressurisation, by moderating the outflow valves) [4]. There are two types of design to achieve this goal: vapor cycle refrigeration system and air cycle air-conditioning. The focus will be on the latter.

For air cycle air-conditioning, the source of air used by the ECS is typically bleed air from gas turbine compressor, which is at high temperature and high pressure. The hot bleed air is then cooled to an acceptable temperature before entering the passenger cabin. This is achieved using an air-conditioning package that is composed of several units, including a number of HXs cooled by ambient ram air. The hot bleed air from the compressor is metered through a bleed air valve and then cooled by the primary HX. Then the air passes to the air cycle machine for pressure adjustment and finally into the secondary HX for temperature adjustment before entering the cabin [3]. A schematic view of the ECS, including pre-cooler, primary and secondary HXs, bleed air valve and air cycle machine is shown in Figure 1-1.

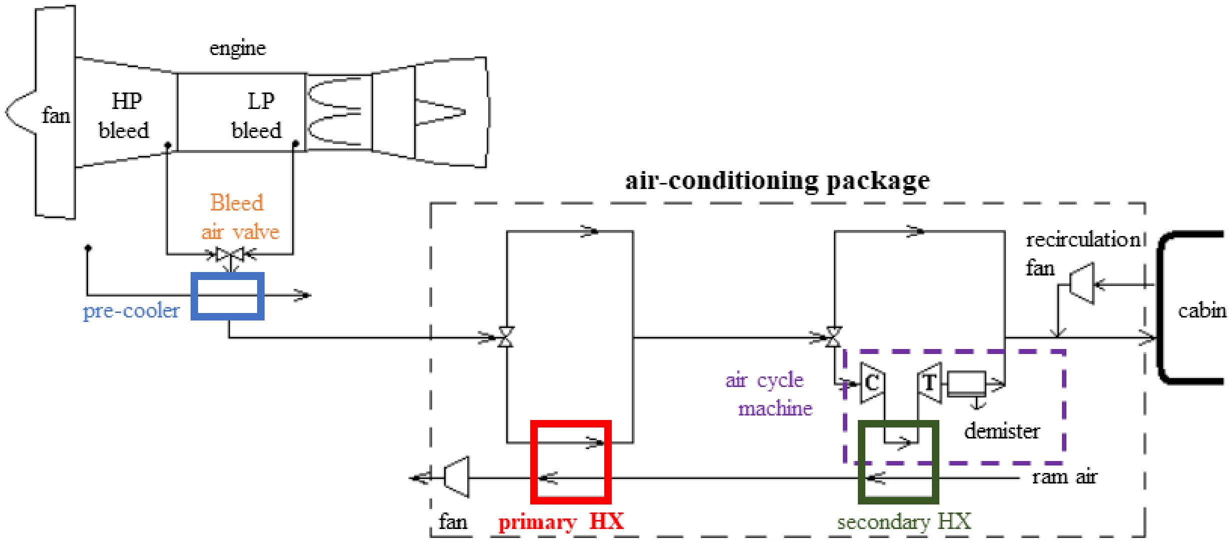

Figure 1-1: ECS schematic (adapted from [5]*)*

Due to the variety of the applications, HXs can have different shapes, sizes, materials, working media and ways of being built. In the specific case of aerospace, the choice of each of these variables is based on the following considerations [3]:

- Compactness and lightweight: compact HXs are required due to the limited space in the aircraft and the goal of reducing volume and mass, keeping high heat transfer performance. Light material and structure are preferred when possible
- High temperature and high pressure: the compressed air leaving though the bleed valve can be at a temperature as high as 1,000 K and a pressure up to 50 bar. The HX's material and the design need to be selected to withstand the thermal and mechanical stresses at the same time
- High effectiveness and minimum pressure drop: the design for aerospace HXs is particularly critical for the strict pressure drop limitations. Therefore. the HXs must me developed to optimize the tradeoff between high heat transfer coefficient and low pressure loss
- Gas-to-gas applications: the working fluid used by aerospace HXs is either ram air or bleed from the engine (compressed air or exhaust). Due to the low thermal performance of gas, heat transfer enhancement techniques for the HXs are required. They can classified as passive (no external power

required) or active (external power required). Due to durability concern, the passive enhancement techniques are preferred e.g., surface coating, fins, inserts, curved tubing.

- Reliability: HXs in aerospace often play a critical role. The failure of the HX can result in catastrophic consequences for the entire aircraft. For this reason, a detailed analysis and experimental tests are required before delivering the final product.

Typical State-of-the-Art HXs for aerospace applications are constructed using plate-and-fin technology [6]. Due to the challenges in fabrication of fins out of superalloy, the fins are usually fabricated out of stainless steel and then brazed into the separator plate that is made out of higher temperature material such as superalloy. This limit the maximum temperature of the HXs. A real life example of the Boeing 747-8 Air Conditioning Pack is shown in Figure 1-2.

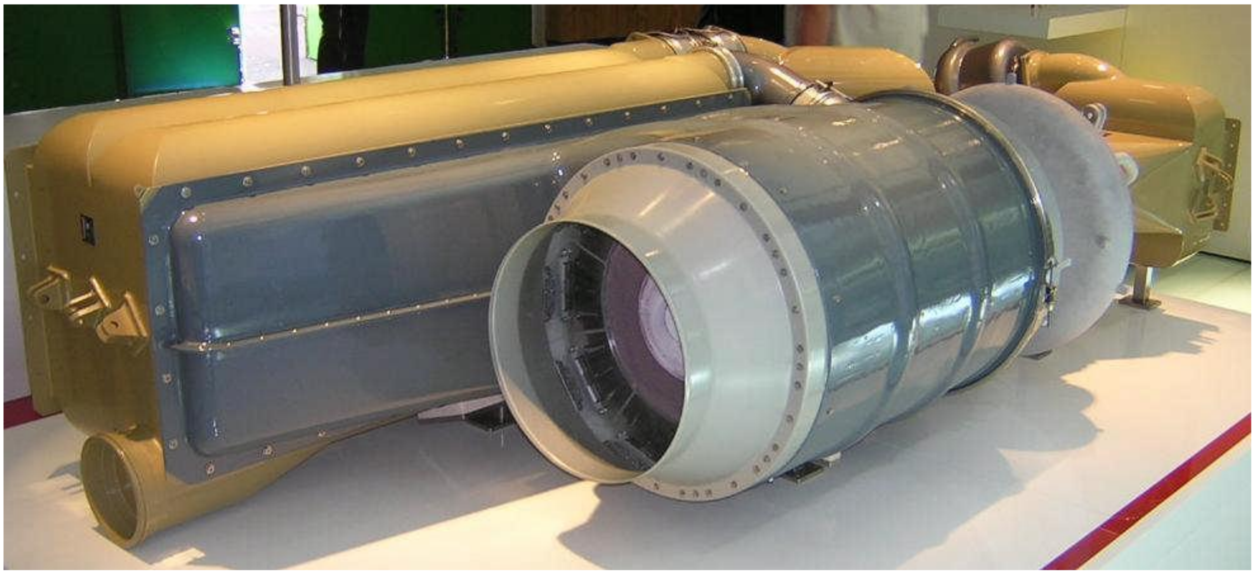

Figure 1-2: Boeing 747-8 Air Conditioning Pack [7]

As previously mentioned, the requirements for aerospace HXs are quite challenging. In order to provide a more advanced HX compared to the State-of-the-Art, it is necessary to develop at least one of the following aspects: novel heat transfer enhancement technique, new material, new design concept or new fabrication techniques. The final HX is based on the best assessment of thermal performance, pressure drop, weight, size, cost, yield and reliability.

1.2 Dissertation Objective

The main objective of this dissertation is to design, build and test a gas-to-gas HX that promises significant performance improvement over conventional HXs for the aerospace industry in terms of gravimetric heat density (kW/kg). In order to achieve this goal, it is essential to use a combination of advanced heat transfer surfaces, advanced fabrication technique and design optimization. The outcome of this process is a lightweight and compact gas-to-gas HX that can have much needed applications for aircrafts environmental control system as well as other fields where high temperature conditions are required. In order to achieve this goal it is essential to develop a model that can predict the performance of the HX when operating at high temperature (600°C) and pressure (3 bar). Moreover, the thermo-mechanical analysis performed on the HX represents an important step towards the development of HX working under high temperature and high pressure conditions.

1.3 Approach

In order to achieve the objective of the dissertation, the following steps were followed:

1. **Literature review of high temperature heat exchanger**

   First, a detailed study for designing the High Temperature Heat Exchanger (HTHX) was performed. The literature study included identifying material options, common types of HTHX and possible manufacturing techniques used in highly complex geometry and high thermo-mechanical resistance materials. The study covered different industries of application, but a more detailed analysis was done for the aerospace field.

2. **Design requirements and design optimization**

   Comparing the literate review with the requirements for the HX, manifold-microchannel technology was selected as design, due to the high performance that this technology can yield. The manufacturing technique selected to fabricate such a complex design out of Inconel was additive manufacturing. Based on a predictive model developed for manifold-microchannel HXs, the design was obtained with the target of minimizing its weight.

3. **Printers capability study and subscale unit fabrication**

   Different setting parameters were studied, such as build orientation, layer thickness and laser power intensity. The main focus of this test was to optimize those parameters to achieve the smallest fin thickness and the smallest wall thickness able to contain the pressure requirements. Once completed the printers study, the design was finalized and the subscale unit printed.

4. **Subscale unit test and characterization analysis**

   The subscale unit was tested under both low- and high- temperature conditions. The experimental heat transfer performance and pressure drops were compared with the numerical predictions. If the difference was too large, possible reasons of the deviation were considered, e.g. inaccurate predicting model, poor energy balance, printing defects. The experimental data of the unit were also used to assess the performance of the HX when compared to conventional designs.

5. **Model improvements**

   One of the possible causes of the difference between experimental data and numerical prediction could be the assumptions made in the model. The model was then examined and updated on the basis of the experimental data

1.4 Major Novel Contributions

The major innovative contributions of this work are:

- Conducted a novel design, simulation/optimization, fabrication and testing of a compact, lightweight HX for high temperature applications and demonstrated up to 22% improvement in gravimetric heat exchange density (kW/kg) when compared to the state of the art HXs for the selected aerospace application.
- For the first time, optimized printer settings to achieve resolutions beyond the settings suggested by the manufacturer. Therefore, this work demonstrated the successful outcome of pushing the limit of metal AM beyond the current State-of-the-Art

- Demonstrated potential for scalability of Ni-based supper alloy metal manifold microchannel heat exchangers by fabricating two units with overall size of 4”x4”x4” (0.094x0.0876x0.0944 m^3) and 4.5”x4”x3.5” (0.155x0.090x0.055 m^{3}”) and fin thickness of 0.220 mm and 0.170 mm, respectively. These two units represented the largest yet built volume reported for the Ni-based high power density manifold micro channel HXs.
- For the first time, developed a model for a manifold microchannel heat exchanger with fluid and solid properties dependence on temperature
- For the first time, developed a model for thermo-mechanical analysis of manifold microchannel heat exchangers for high temperature applications and with Ni-based super alloys as material of construction.

1.5 Dissertation Layout

The layout of the dissertation is as follows. First, a literature review of conventional and State-of-the-Art HTHXs is presented in Chapter 2. Design requirements and manifold-microchannel description are presented in the first part of Chapter 3. The rest of chapter 3 focuses on model prediction and optimization routine to obtain full-scale and subscale designs of the first manifold-microchannel heat exchanger. Chapter 4 presents the results from the printing coupons study and describes the role of printer parameters on printer resolution and leak-proof units. Fabrication of the first unit and preliminary analysis are also included in this chapter. Chapter 5 discusses the experimental characterization of the first HX. Comparison between experimental data at low and high temperature is presented. Comparison between model and experimental data is also addressed. Lastly, the assessment of the performance of the first HX in comparison with the conventional designs is considered. Next, the printing characterization of the in-house printer is presented in Chapter 6, along with the design and fabrication of the second HX. The experimental performance of this unit is analyzed in Chapter 7. The comparison between experimental data and numerical prediction, as well as the updated model to improve the prediction are discussed in Chapter 7 as well. Chapter 8 describes the thermo-mechanical model and results of the study. Chapter 9 presents the preliminary results of the porous medium approach in place of the U-shaped microchannels design. The conclusion of the work done and the proposed future tasks are presented in Chapter 10

Chapter 2 Literature review

2.1 Introduction

HXs are devices used to transfer heat between two streams, one at a higher temperature than the other. As mentioned by the second low of the thermodynamic, the higher the temperature at which the heat is exchanged, the higher the "value" of the heat is. For this reason, there are multiple demands for development of HTHXs (arbitrarily meaning temperatures above 650°C[8]). In the power production field, for example, supercritical CO_2 power cycles can positively benefit from improving HTHXs. Supercritical CO_2 power cycles, in fact, are externally fired cycles where the heat needs to be transferred from the source stream to the supercritical CO_2 of the power cycle. This is possible due to a HTHX, thus enhancing the HTHX capability will increase the maximum temperature of the cycle and the overall power plant efficiency as a consequence [9]. Waste heat recovery [10,11], hydrogen production [12,13] and high temperature fuel cell [14] are other areas that are using HTHX. As shown in Section 1.1, another important field for the HTHXs is the aerospace, when used as recuperators for gas turbine engine [15–17] or in the ECS. In these cases, lightness and compactness, as well as small pressure drop, are key factors that need to be taken in consideration when designing the HTHXs. In order to develop a new HTHX that can surpass the performance of the State-of-the-Art, it is necessary to perform a literature review with particular focus to the aerospace applications. Despite temperature being the main driving factor, the ability of the HXs to handle high pressure will be considered as well.

2.2 Challenges for High Temperature Heat Exchangers compared to Low Temperature Heat Exchangers

As mentioned by Sunden [18], when moving from low temperature heat exchangers (LTHXs) to HTHXs, a series of important differences need to be considered:

- The choice of the material, the design parameters and the mechanical stress analysis are governed by the thermal stresses at high temperature
- Oxidation, thermal shock and thermal stresses fluctuations during the startup, shutdown and load can be significant
- The thermal expansion can greatly affect the unit when operating at a much higher temperature than the environmental temperature
- Heat losses to the outside need to be carefully prevented
- Fouling and erosion due to suspended dirt particles worsen with the high temperatures

2.3 Material options

In order to overcome the aforementioned challenges, metals like aluminum, copper or steel are not suitable for this application.

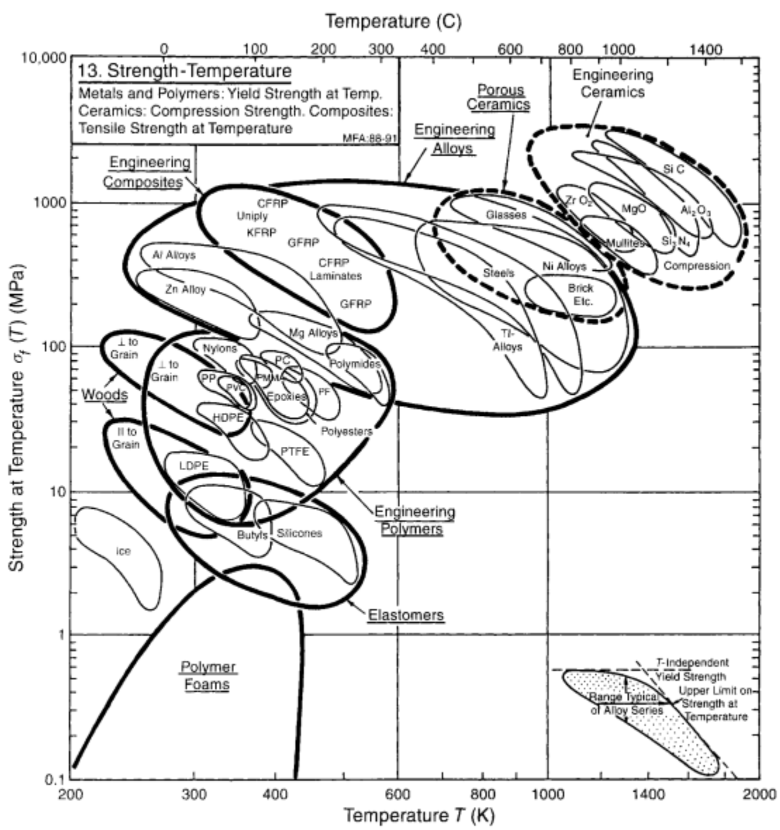

Figure 2-1: Strength plotted against temperature [19]

Considering the mechanical behavior of different materials at different temperatures, as shown in Figure 2-1, ceramic is the solution that can withstand the highest temperature. The most common ceramic used for HTHXs is Sintered Silicon Carbide (SiC) [20,21]. As shown in Figure 2-1, SiC components can operate at temperature above 1,000°C and it is also a good solution for highly corrosive environment [22]. The main drawback of ceramics is that the strength shown in Figure 2-1 refers to the compression stress only. When comparing compressive and tensile stresses for ceramics, tensile is at most 10% of the compressive strength [23]. For SiC, in particular, this value drops to 5-8% [24]. The only commercially available HTHX that can withstand high pressure is reported by HTI [25], a shell-and-tube HX with a maximum operational pressure of 13 bar. However, this design is not suitable for aerospace due to the lack of compactness. Moreover, ceramic HXs built with conventional manufacturing techniques require joints that need to withstand the service conditions. The most common solutions are tape bonding and pyrolysis of preceramic polymers; Lewinsohn [26] highlights the superior performance of tape bonding. Using more enhanced manufacturing technique becomes the only possible solution to improve the joining as well as the capability to fabricate thin features. Kee *et al.* [27], for example, used a new fabrication process called Pressure Laminated Integrated Structure (PLIS) in a ceramic counter-flow HX to enable cost-effective manufacturing. Despite the promising results, the actual conditions tested were 750°C at atmospheric pressure. Lewinsohn [28] realized a plate HX using a Laminated-Object Manufacturing (LOM) approach, but no experimental results were mentioned. Similarly, Scheithauer *et al.* [29] describe the opportunities for Lithography/based Ceramic Manufacturing (LCM), demonstrating novel designs that can increase the heat transfer area of HXs, without mentioning any test results. The most promising compact HXs found in literature [29,30] report operational condition up to 800°C and 5 bar. Despite the encouraging results (summarized in Table 2-2) and the continues effort to improve the mechanical performance of ceramic [32], the review from Sunden [18] shows that the brittle nature of ceramics is a serious obstacle in choosing this material for pressurized applications, including the aerospace.

The second most resistant materials reported in Figure 2-1 are the engineering alloys. In this case, the strength refers to yield, allowing the HXs to withstand high pressure. The most used metals for State-of-the-Art HTHXs are 300 series Stainless Steel for application up to 675°C and superalloy for temperature up to 900°C [32–34], such as Inconel, Haynes, Hastalloy, *etc*.

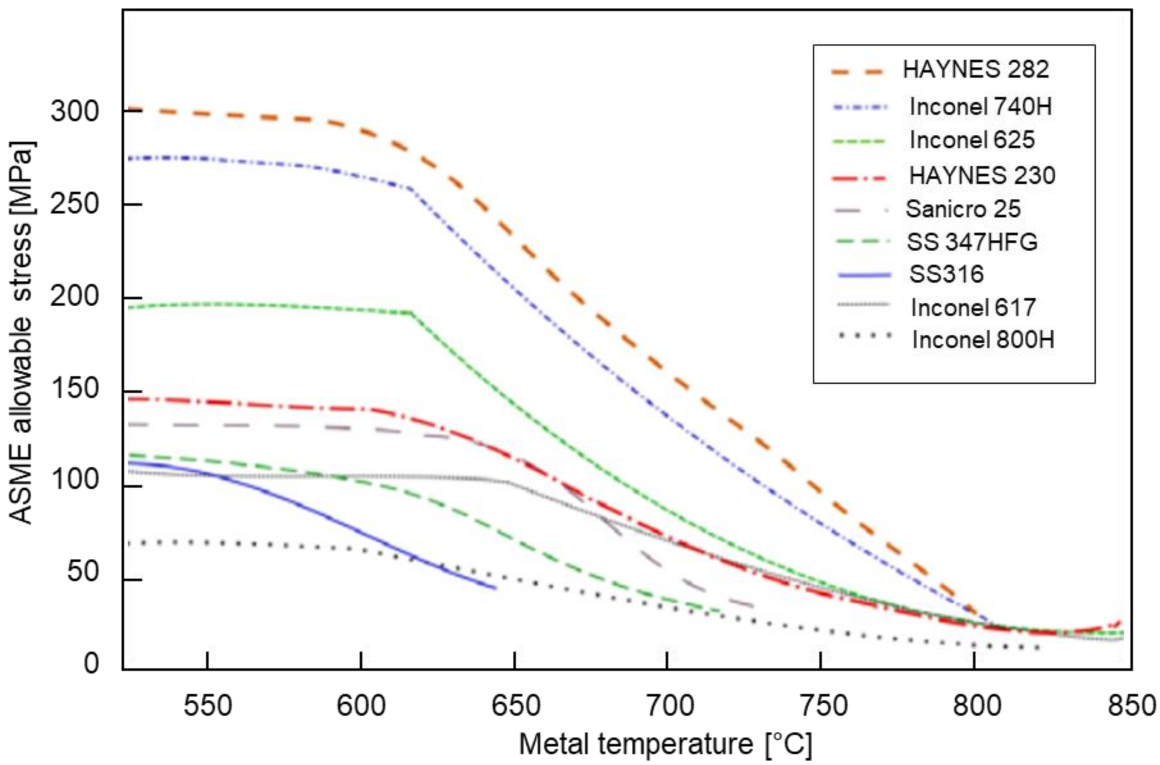

Figure 2-2: Strengths of various iron- and nickel-based alloys as a function of the temperature [36]

As shown in Figure 2-2, Haynes 282 and Inconel 740H are the most suitable metal for HTHXs when combined with high pressure, but so far they have been used to fabricate HX prototypes [37]. On the contrary, Inconel 625 is currently considered the State-of-the-Art for HTHXs [32–34].

Researches are also developing metals with even superior characteristic. For example, a family of superalloy that furtherly improve the performance is the Oxide Dispersion Strengthen (ODS) alloy. They offer exceptional high temperature strength, oxidation and corrosion resistance at high temperature exceeding 1,000°C and resistance to radiation damage [8]. They have been known for the past 50 years, but several reasons prevent this solution from being widely used. Fabrication of ODS alloying is a challenging, costly and time consuming process [38]. Spierings *et al.* [39], however, identified in Additive Manufacturing (AM) a key role to simplify the process of ODS alloy. In particular, the focus was directed to ODS modified Inconel 625 using Selective Laser Melting (SLM). Although the process is easier compared to the conventional one, neither this material is ready to be tested yet, nor have HXs made of this material been found in literature.

With more advanced materials, there is a significant increase in the cost: the prices for the material can vary from \$2-3/kg for steel to \$70/kg for Ni-based alloy [40]. An interesting alternative solution proposed by McDonald [41] is a bi-metallic components. The idea is to use superalloy in the first high temperature section of the HX and a lower grade material in the colder one for overall cost efficiency. However, research efforts are needed to better characterize the joint in terms of material selection, welding approach, fabrication method and thermo-mechanical resistance.

Another noteworthy family of materials not shown in Figure 2-1 is carbon-carbon composites. They offer the highest temperature capability (up to 3,300°C), lower density and higher thermal conductivity than metals [40,41]. However, oxidation problems start at 300-400°C and effective protection techniques are required [22]. This is the main obstacle that prevents the utilization of carbon-carbon composites in HTHXs.

2.4 High Temperature Heat Exchanger Design

After studying the possible materials, the focus is shifted to the possible designs used in HTHXs. Analyzing advantages and drawbacks of each design will help in selecting the best option for the current application.

2.4.1 Shell-and-Tube and Spiral Heat Exchangers

Among the challenges for HTHXs mentioned by Sunden [18], there is a constant reference to simplify the design. For example, it is suggested to use HXs with large feature size to limit pressure drop and the use of fins is not generally suggested due to possible fouling at high temperature. For these reasons, HXs based on those principles, such as shell-and-tube HXs [44] and spiral HXs [45] are commonly used for HTHXs. Commercially available shell-and-tube and spiral HXs are also reported in Table 2-3. Despite their simplified designs (see Figure 2-3), those types of HXs have two big drawbacks. First, they prove to be uneconomical due to the material cost and manufacturing cost of the superalloy [36]. Second, considering shell-and-tube HXs or spiral HXs, it is clear that their total volume and weight are serious obstacles in some fields. For the aerospace application, in particular, decreasing volume and/or weight is considered one of the main targets. Therefore, compact HXs are the only viable option.

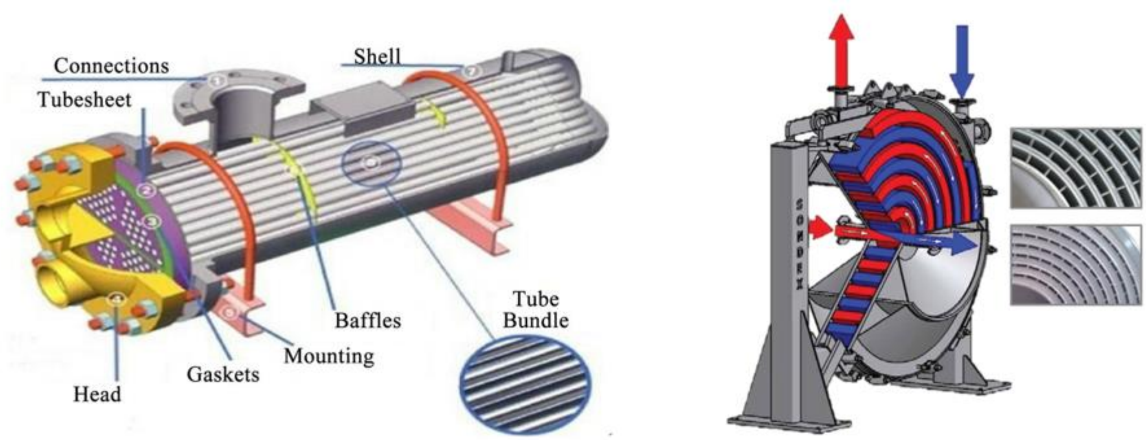

Figure 2-3: Working principle of a shell-and-tube HX [46]*(left) and a SHX* [47] *(right)*

2.4.2 Plate Heat Exchangers

The most common concept of a Plate Heat Exchanger (PHX) is the plate-and-frame HX. As shown in Figure 2-4, it consists of a series of corrugated plates supported by a rigid frame. The corrugations on adjacent plates contact or cross each other forming highly interrupted and tortuous channels. Sealing between streams is accomplished by gaskets [45].

The main weakness of this HXs is that the plate-and-frame HXs are generally restricted to low or moderate temperature and pressure applications due to the use of gaskets [45]. In order to overcome this issue, it is possible to build gasket-free PHXs, by brazing, semi-welding or fully welding the plates.

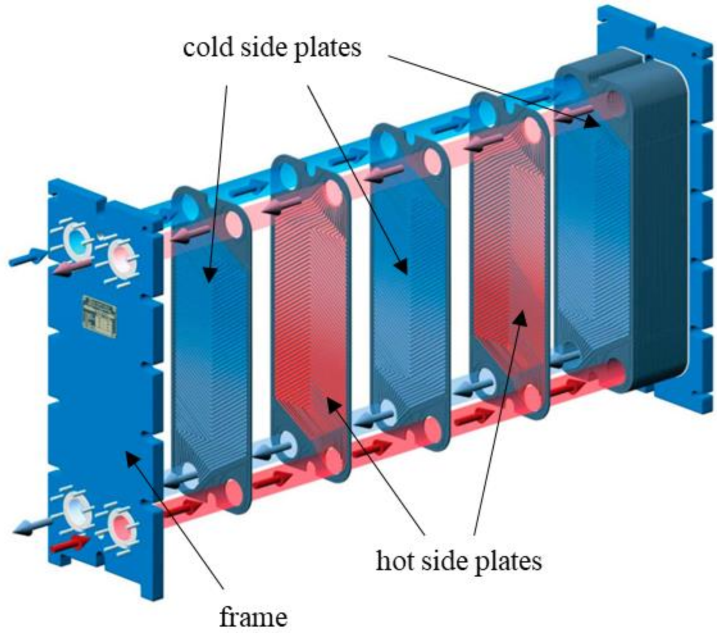

Figure 2-4: Plate-and-frame HX: working principle [48]

Apart from the plate-and-frame HXs, there are other PHXs with more complex designs. Among the commercially available ones, the most innovative are the shell-and-plate HXs and the hybrid-shell-and-tube&plate-and-frame HXs. Those designs combines the compactness of plate-and-frame HXs with the capability of shell-and-tube to withstand high temperature and pressure [49]–[54].

Table 2-4 summarizes the PHXs available in the market. Despite the encouraging operative conditions reported, in most of the cases, the maximum pressure and temperature cannot be reached simultaneously. Moreover, analyzing the field of application, none of those HXs is designed for the aerospace. It is therefore required to investigate other designs.

2.4.3 Plate-and-fin Heat Exchangers

The design of a Plate-and-Fin HX (PFHX) is based on stacking alternating layers of hot fluid fins, a separator plate and cold fluid fins. As shown in Figure 2-5, the fin passages are bounded by header bars and the last fin passages are enclosed by side plates. The components are assembled by brazing in a vacuum furnace to become a single rigid core [45].

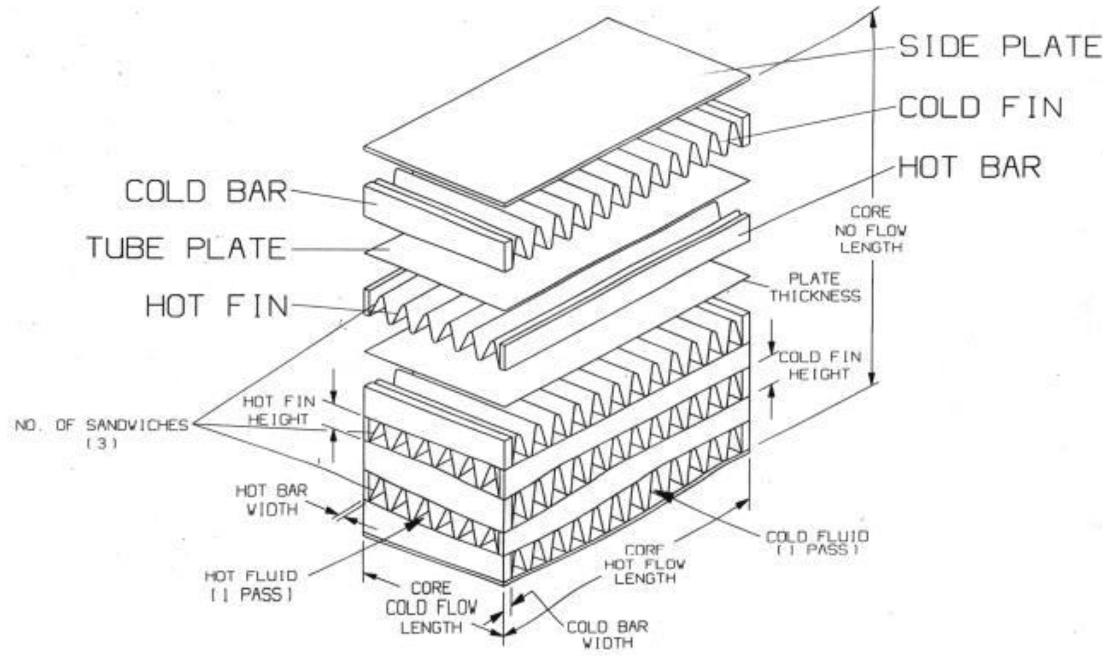

Figure 2-5: Plate-and-fin aerospace HX: assembly [55]

The most common type of fins are plain rectangular fin, triangular fin, wavy fin, offset strip fin, perforated fin, louvered fin, as summarized in Figure 2-6.

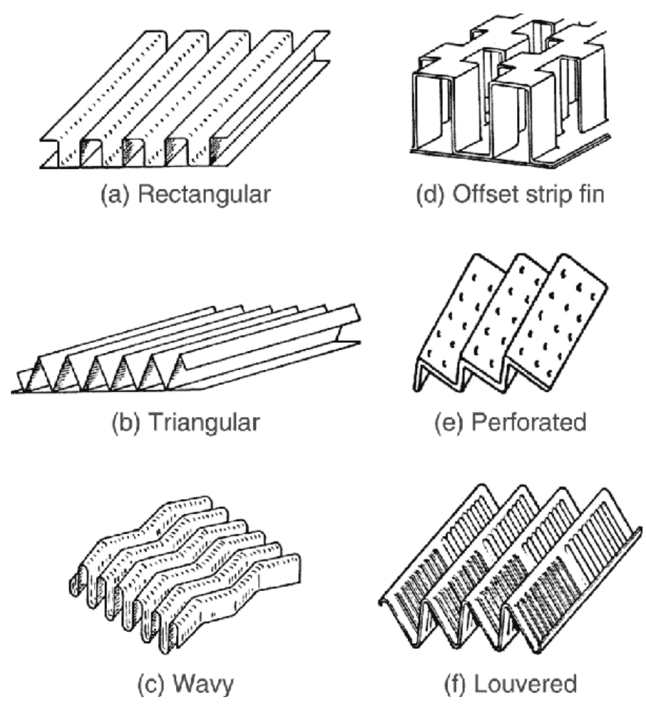

Figure 2-6: Plate-fin exchanger surface geometries [56]*: (a) plain rectangular fins; (b) plain triangular; (c) wavy; (d) offset strip; (e) perforated; (f) louvered*

Compared to plain or wavy fins, offset strips and louvered cause more breakups on the thermal boundary layer, thus enhancing the heat transfer coefficient [57]. However, this benefit also carries the inevitable increase in pressure drop per unit flow length [58]. For aerospace HXs in particular, pressure drop requirements are often more difficult to meet than the heat transfer requirements [55]. Moreover, the manufacturing cost of PFHXs is often higher than conventional HXs due to a higher level of detail required. However, the total costs can be reduced by the cost saving due to the heat transfer enhancement.

A series of conventionally manufactured PFHXs examples used in the aerospace field for high temperature and high pressure applications are reported in Table 2-5.

2.4.4 Microchannel Heat Exchangers

Microchannels Heat Exchangers (MHXs) are one of the most compact HX designs. For aerospace HXs in particular, it is used to define microchannel size simply as smaller than State-of-the-Art fin passage sizes, thus less than around 0.028 in (700 µm) in one dimension of the flow passage [55].

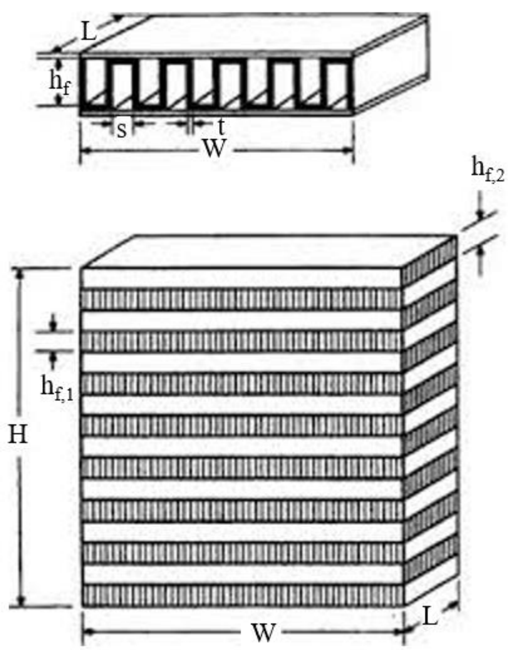

Figure 2-7: MHX design

As shown in Figure 2-7, MHXs can be considered plate-and-fin HXs with plain rectangular fins whose width of the channel *s* (with reference to Figure 2-7) is below 700 µm. Compared to most complex PFHXs (such as offset fins). MHXs do not have flow disruptor that can enhance the heat transfer. However, as the channel size is smaller the heat transfer coefficient can be bigger. The combined effect of these two factors can lead to a heat transfer coefficient that might be lower, higher or similar to PFHXs, depending on the complexity of the PFHX. However, with MHXs significantly increase the total surface area through which the heat transfer occurs. The impact of the surface improvement results in an increased overall thermal performance. However, the smaller hydraulic diameters causes an increase in pressure drop per unit length.

Only few cases were found in literature of MHXs for the aerospace application fabricated with conventional techniques (see Table 2-6). Moreover, they did not use superalloy due to the challenges of building complex structures through conventional techniques.

2.4.4.1 Manifold Microchannel Heat Exchangers

Among the MHXs, manifold microchannels HXs (M2HXs) show the most promising results, as they can increase heat transfer coefficient without significant increase in pressure drop as discussed by Cetegen [59].

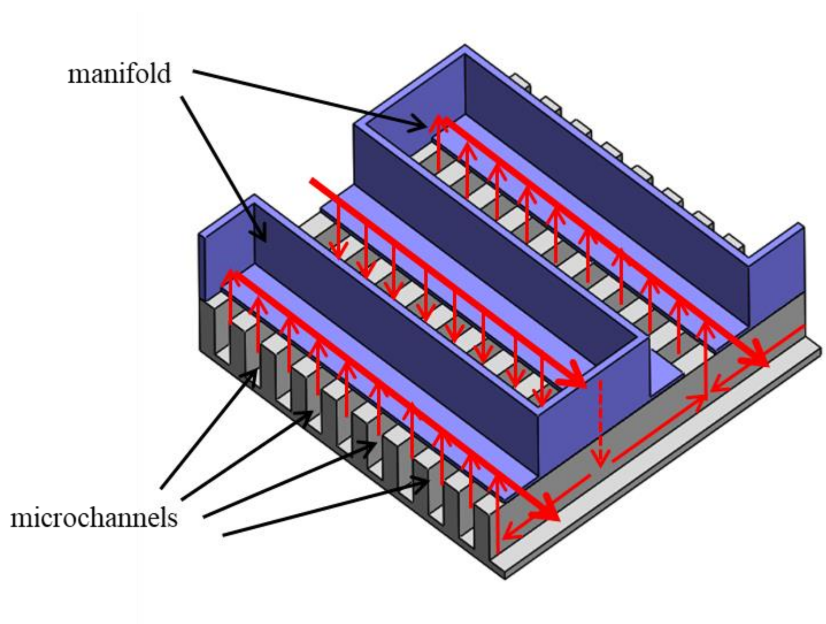

Figure 2-8: Manifold-microchannel design schematic

The schematic design of M2HX principle is shown in Figure 2-8. It is obtained by combining two components. A series of parallel fins form a microgrooved surface that constitutes the microchannels in which the working fluid can flow. The component placed on top of the microchannels is called manifold, from which the name M2HX. A manifold is usually positioned perpendicular to the microchannels, as shown in Figure 2-8. Manifolds have three tasks. First, they divide and deliver the flow into multiple microchannels. Second, they recollect the working fluid from the microchannels and deliver to the outlet. Third, they determine the flow length of the fluid in the microchannels.

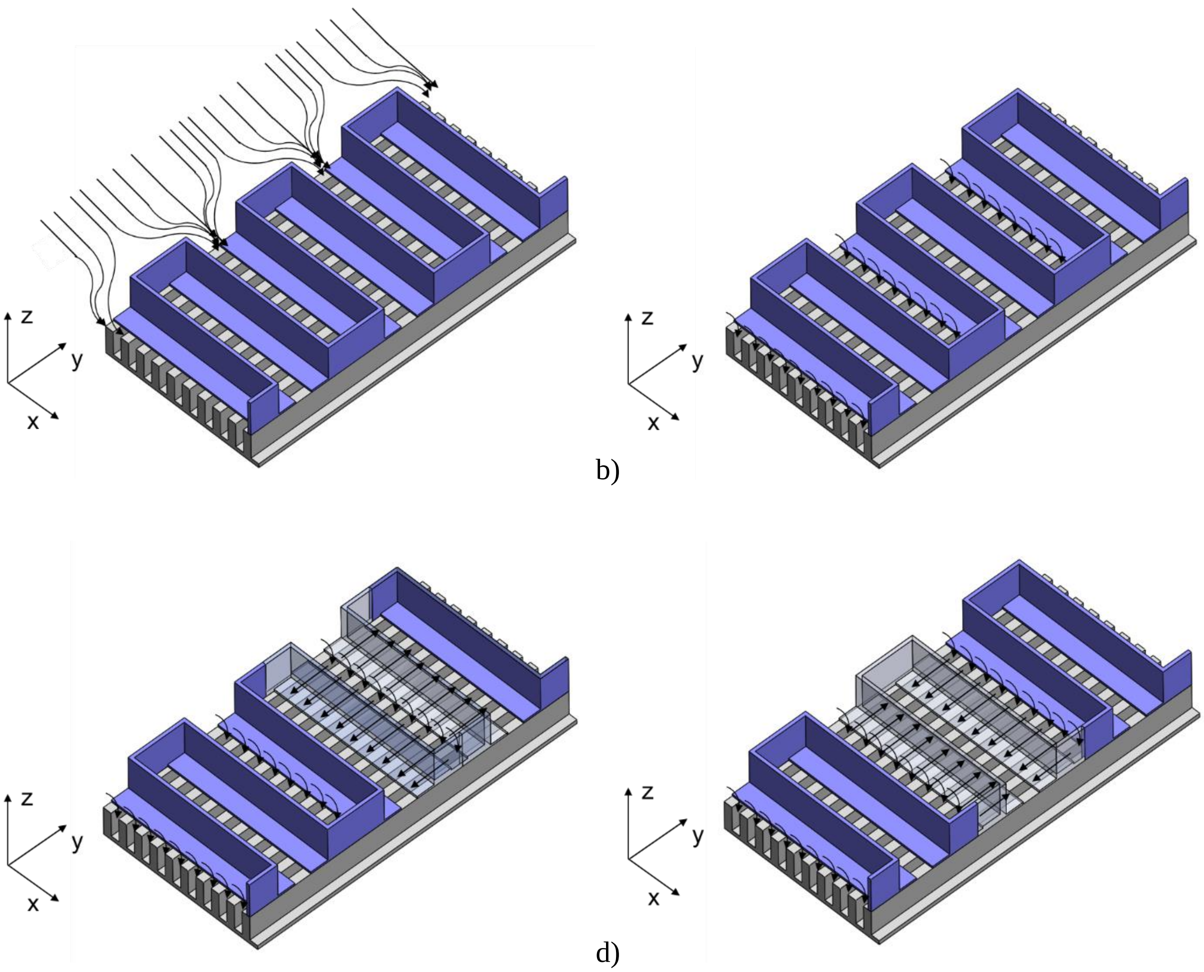

a) b) c) d)

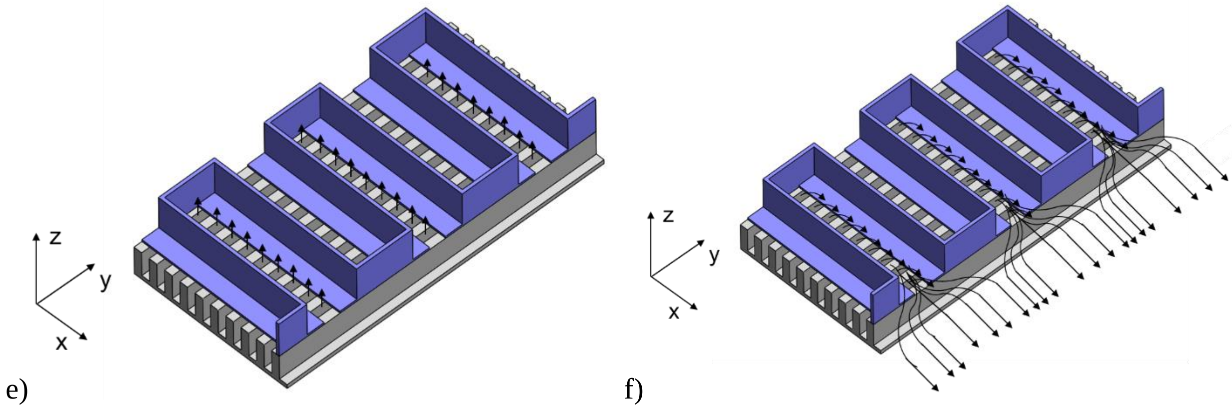

Figure 2-9: Manifold-microchannel working principle

To better understand how M2HXs work and how they are different from traditional MHXs, the flow within the device is described as follows: once the fluid enters the HX, it is split into several flows through the inlet manifold-channels (as shown in Figure 2-9 a). The fluid is then forced to turn 90° angle to enter the microchannels (from positive x-direction to negative z-direction with reference to Figure 2-9 b). After entering the microchannel area, the flow creates a stagnation point before splitting in two streams, each one turning 90° in opposite directions (in the y-direction, as shown in Figure 2-9 c). Hence, the fluid flows in the two opposite streams in the microchannel, but for only a short distance, because it collides with the counter stream coming from the neighboring inlet manifold. This is the reason why the flow length of the microchannel is given by the manifolds design, as shown in Figure 2-9 d. Once the two counter streams join, they make a third 90° turn and enter the outlet manifold sections (in the positive z-direction of Figure 2-9 e). At this point, the last 90° turn in favor of the outlet flow, allows the fluid to leave the M2HX flowing through the outlet manifold-channels (as shown in Figure 2-9 f).

Due to the short flow length on the microchannel, the flow is in the developing region, which has higher heat transfer performance compared to fully developed flow. In addition, short flow length can also reduce pressure drop, which in turn, reduces the pumping power requirement. For those reasons, M2HXs is one of the most suitable choice for aerospace application.

The main challenge in the implementation of manifold-microchannel technology is to manufacture very small-scale microchannel sizes with high aspect ratio (ratio of fin height to thickness) and high fin density using traditional manufacturing technology [60]. Fins with high aspect ratio are desirable for increasing the heat transfer area, and thinner fins can reduce the overall mass of the heat exchanger. Moreover, manifold and the microchannel sections must be manufactured separately due to the complexity of the geometry [60]. The consequent assembly process needed to create a full-scale HX can become prohibitive. Brazing or welding both components together is a challenging task by itself and it is made even harder due to necessity of using high temperature resistance materials, like superalloy.

2.5 Manufacturing Technology Alternatives

Taking as an example the conventional construction of a PFHX core, a series of manufacturing processes are required to prepare the HX components for core assembly. Using the nomenclature of Figure 2-5 as reference, the fins are usually formed to required shape. The tube plates start as rolled foil or sheet, successively coated with braze alloy on both sides and finally trimmed to required dimensions. A similar process is also required for the side plates, from rolled sheet to desired size. As to the bars, they can be rolled, extruded or cut from plate to achieve the required cross section and then trimmed to the desired length. The components are then stacked within a braze fixture and the core is heated in a vacuum furnace to the braze temperature and lastly cooled. It is clear that many operations are required for just the HX core [61].

This approach becomes uneconomical or not feasible when applied to more compact designs or when using high temperature material. Processing, machining, welding and brazing of superalloys are a challenge due to superalloys high toughness, low thermal conductivity, tendency to crack during welding or unavailability of suitable brazing materials [62]–[64]. Specialized equipment and highly trained operators are often needed for processing such materials.

For those reasons, more advanced manufacturing technologies are required to fabricate the desired HXs.

2.5.1 Photo-chemical Etching and Diffusion Bonding

2.5.1.1 Printed Circuit Heat Exchangers

In order to overcome the aforementioned issues, a possible solution is represented by Printed Circuit Heat Exchangers (PCHXs). The first PCHX concept was the result of research performed at the University of Sydney in the early 1980s and it has exclusively been commercially manufactured by Heatric Ltd. (UK) since 1985 [65]. The manufacturing technique is the same as the one used for printed circuit boards in the electronics industry. However, due to its ability to etch various metals, including titanium, nickel superalloy, and copper superalloy, and its high accuracy, the process has been also used to fabricate HXs [36].

In the first step of the manufacturing process, fine grooves are photo-chemically etched into one side of a flat metal plate forming the fluid passages. The etching process is shown in Figure 2-10.

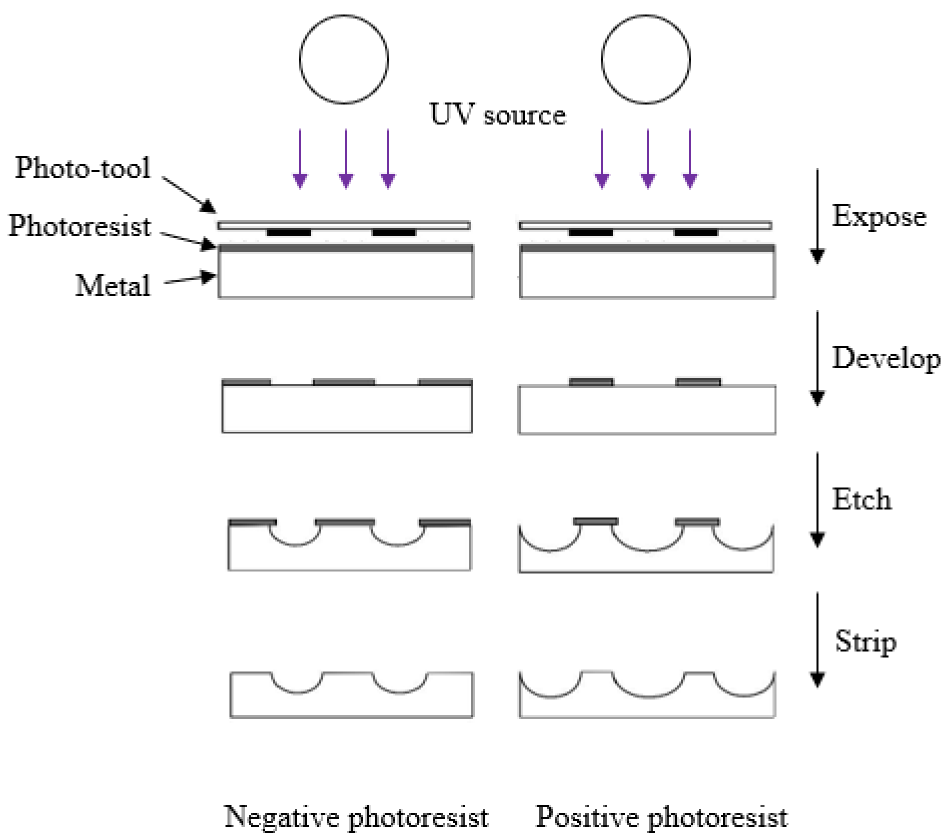

Figure 2-10: Photo-chemical etching: working principle [36]

First, a photoresist layer is deposited on the metal surface. Then, the photoresist is exposed to UV light via a photo-tool. Afterward, the exposed metal is dissolved via an etching process to form semi-circular channels. Lastly, the photoresist is removed using a solution like alkaline. If the photo-tool specifies the area that needs to be dissolved by the UV light, the process is called positive-working photoresist. If the photo-tool specifies the area that is left, the process is called negative-working photoresist [36].

The etched-out plates are then alternately joined by diffusion bonding, which is the second step, and results in compact, extremely strong, all-metal heat exchanger cores. The diffusion bonding process includes a thermal soaking period to allow grain growth, thereby essentially eliminating the interface at the joints, which in turn gives base-material strength and very high pressure containment capability throughout the entire HX [45].

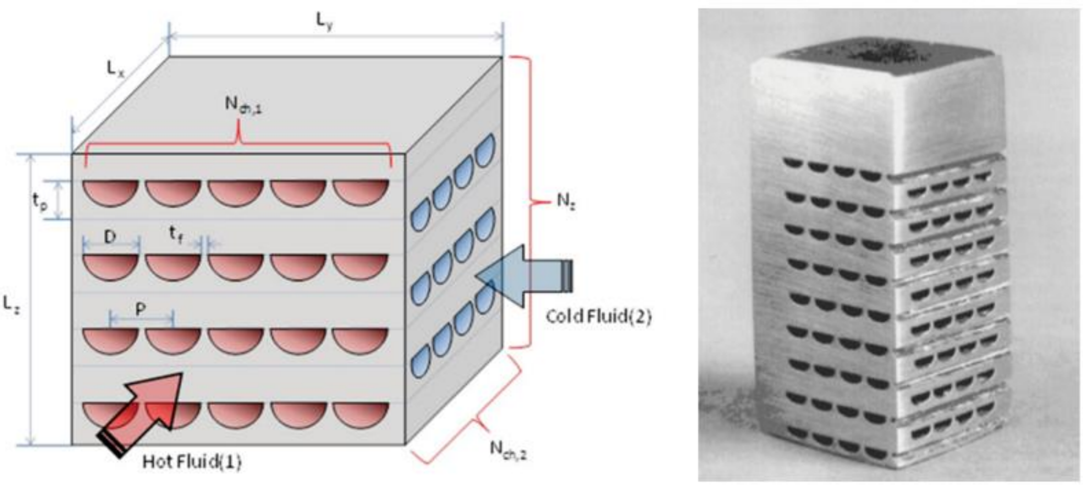

Figure 2-11: Schematic diagram of crossflow PCHX (left) [66], *PCHX sample (right)* [67] .

As shown in Figure 2-11, from the design point of view, PCHXs can be treated the same way of PFHXs with the fin of decreasing thickness towards the tip (at the plate join) [45]. The main advantages compared to the conventional manufacturing are the reduced number of steps in the building process and the elimination of brazing or welding process. Therefore the resulting PCHXs have high integrity joints, free from complex alloy metallurgy which could otherwise result in corrosion, thus minimizing the chance for leakage of one fluid stream into another [68]. Due to those qualities, they are one of the best option for HTHXs application when also high pressure resistance is required.

Examples of commercially available PCHXs and researchers' work are reported in Table 2-7.

The main limitation of PCHXs is their limed geometry flexibility. PCHXs designs are restricted to few options, as shown in Figure 2-12. Therefore, PCHXs inherit the same drawbacks as conventionally manufactured HXs: pressure drop might be a concern, being roughly inversely proportional to the channel diameter.

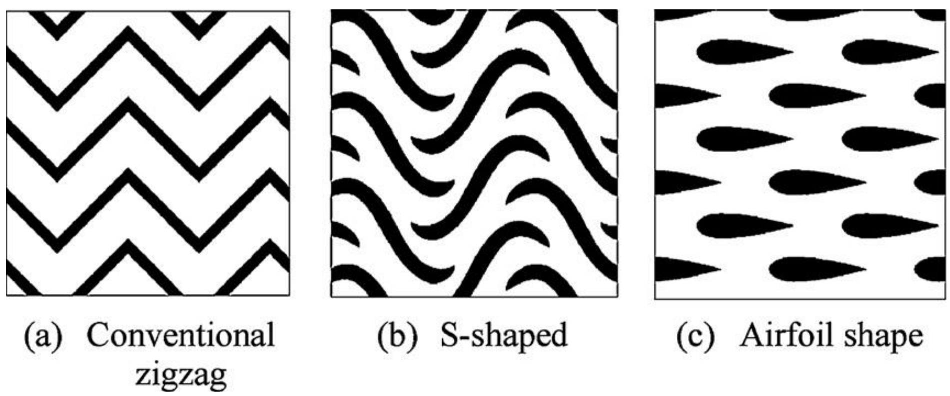

Figure 2-12: Different types of PCHX ([45]*based on Tsuzuki et al.* [69] *work).*

2.5.1.2 Marbond Heat Exchanger

Chart Marston's Marbond HX is considered one of the most innovative design based on photo-chemical etching and diffusion bonding. In contrast with the PCHX, several, thinner, slotted plates are typically stacked to form a single sub-stream, thus giving the potential for very low hydraulic diameters, depending on the width of the slots and the plate thickness [70] which significantly increases the porosity of the HX core. An example of the Marbond design in a real HX unit is shown in Figure 2-13.

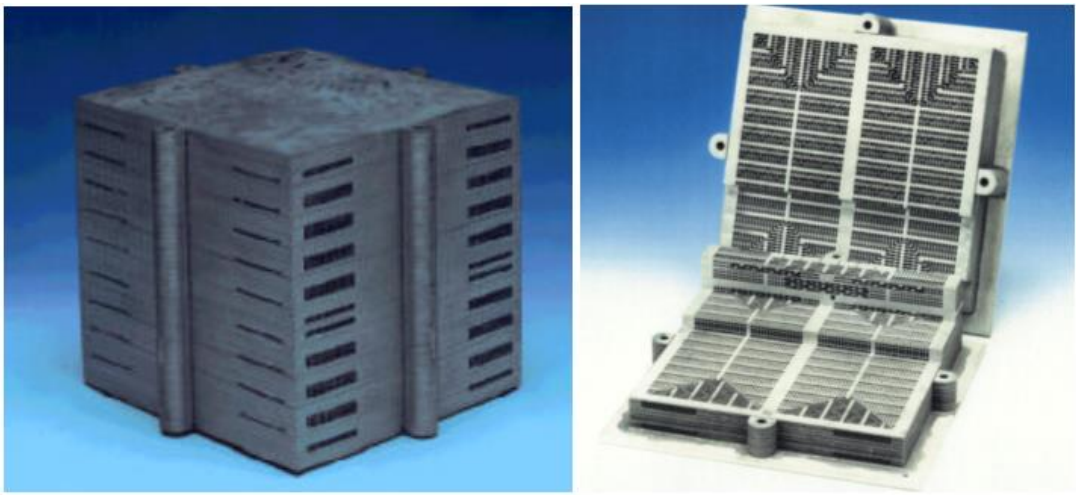

Figure 2-13: Diffusion bonded structure (left), Exploded view of Marbond (right) [68]

2.5.2 Additive Manufacturing

Additive manufacturing (AM) is an advanced fabrication technique where parts are fabricated layer by layer from a pre-programmed digital model. In the last decade, AM has seen tremendous growth thanks to a series of advantages:

- AM produces design features that are not practical with conventional techniques, allowing fabrication of complex objects which are too challenging for conventional methods. When applied to HXs, this advantage translates in the capability of building enhanced heat transfer surfaces with less pressure drop penalty and enables design features that improve thermo-mechanical structural integrity and reduce weight by tailoring wall gauges to local requirements.
- AM allows production of conformal shapes that are not currently practical, thus improving space utilization and reducing mass. In the field of aerospace, in particular, AM offers the opportunity to build HXs that conform to aircraft geometry, e.g., Engine Ducts.
- Due to its additive nature, most of the challenges met in superalloy fabrication will not be faced in AM
- AM generates less waste material compared to subtractive process

- AM allows fabrication of multiple parts into a single component, which significantly simplifies the fabrication process and reduces the lead time.
- AM allows production of the parts near the point of use

For the abovementioned reasons, AM shows big potential for HTHXs fabrication.

2.5.2.1 Additive Manufacturing Technologies

There are three major metal-based AM techniques: Selective Laser Melting (SLM), Direct Metal Laser Sintering (DMLS), and Electron Beam Melting (EBM). SLM and DMLS printers usually consist of two platforms. The first platform is a powder dispenser platform that houses the metal powder. The second platform is the build platform on which the 3D structure is built. After a layer of the 3D structure is built, the powder dispenser platform rises while the build platform lowers, so a new layer of powder can be distributed on top of the existing layer [36]. A re-coater arm is used to uniformly distribute the metal powder, as shown Figure 2-14.

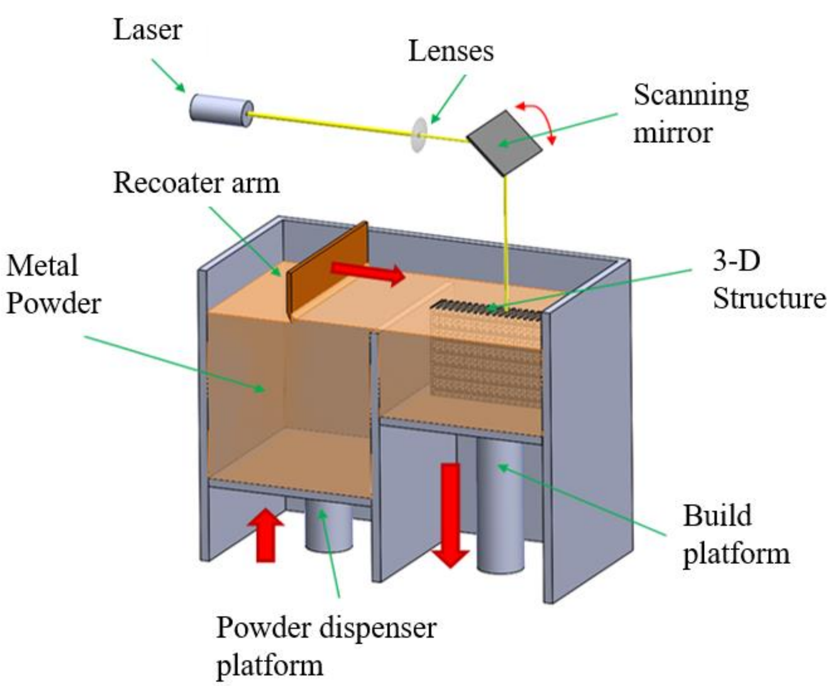

Figure 2-14: DMLS/SLM working principle [60]

The main difference between these AM technologies is the temperature of the powder bed. SLM completely melts the powder, while DMLS involves sintering rather than full melting [71]. The EBM process is similar to that of SLM. The major difference is that an electron beam is used instead of a laser to melt the powder [36]. The consequence is that EBM has higher power compared to SLM/DMLS (3kW vs 300-500W), with temperatures as high as 2,000°C [72].

Most of the work done in AM for HXs is related to research and R&D. For this reason, finding detailed information of the units printed and the actual State-of-the-Art of this technology is challenging. Jafari *et al.* [73] published a recent review of the utilization of selective laser melting technology on heat transfer devices for thermal energy conversion applications. Table 2-8 is a comprehensive summary of the available information found in literatures since AM appeared. It includes all the metal devices (HXs, heat sinks and foams) that have been created using AM, not only SLS and DMLS.

The only commercially available AM HXs found in the market are provided by Hieta [74] [75]. They cover different applications, e.g., gas turbine recuperator, waste heat recovery, air cooler for high-performance automotive applications. Thanks to the AM flexibility, the design of their HXs change to meet the different applications' requirements. The same flexibility is applied also to the materials. Nickel alloys, aluminum alloys, titanium alloys, steel alloys and copper have been used for AM HXs. Those HXs are fabricated using DMLS process using printers such as Renishaw AM250.

2.5.2.2 Post processing steps

Once the part is printed several post processing steps are required for the HXs as summarized below [76]:

- Powder Removal: AM parts build "down" in a powder-bed fusion system as new layers are added to the top, which means that parts are buried in powder when they are done. After the build has finished and the parts/build plate have cooled, the machine operator has to remove all of the powder from the build volume and sieve/filter/recycle it for later use.

- Stress Relief: the heating and cooling of the metal as the part builds layer-by-layer leads to internal stresses that must be relieved before the part is removed from the build plate. Otherwise, the part may warp or even crack. Stress-relieving the part requires an oven or furnace (preferably with environmental controls) that is big enough to fit the entire build plate. Many recommend using an oven with an inert environment to minimize oxidation on the part surface, others prefer a vacuum furnace,
- Part Removal: AM part is printed on the build plate. The most common way to cut the part from the built plate is through wire Electrical Discharge Machining (EDM). An alternative is to use a bandsaw, due to its faster speed. However, when dealing with materials such as Inconel, it becomes difficult to remove the parts from the build plate with just a bandsaw, so wire EDM is required.
- Heat Treatment: heat treatment (e.g., aging, solution annealing) improves the microstructure and mechanical properties of the parts and is necessary for nearly all metal AM parts. In many cases, this step also requires an environmentally controlled furnace with the ability to regulate the temperature and cool-down schedule. Heat treatment may affect the dimensions of the parts, so it is preferable to heat-treat parts before they are machined or any other finishing treatment is applied.
- Hot Isostatic Pressing: instead of heat treatment, many aerospace companies are starting to use hot isostatic pressing (HIP), which is frequently used in the casting industry to improve the fatigue life of cast parts. During HIP, the part is put under high pressure so it can generate better microstructure compared to regular heat treatment. However, a HIP system costs substantially more than a furnace/oven and comes with its own safety measures due to the high pressures (100 MPa or more) at which it operates.
- Machining: machining of mating interfaces, surfaces, threads and support structures might be required to ensure dimensional accuracy of the finished part. This operation can be tricky, especially for complex, organically shaped parts made with AM, thus increasing costs.

- Surface treatments: surface finishing also might be required to improve surface finish/quality, reduce surface roughness, clean internal channels or remove partially melted particles on a part. This operation should be limited to only surfaces with high tolerance requirements.

2.5.2.3 Equipment Capability

There are various manufacturers for powder bed systems available today, such as EOS, 3D Systems, Concept Laser, MTT Renishaw and Arcam. All of the above systems utilize laser-based powder bed fusion except for the Arcam system, which is electron beam-based. All of these systems use a basic configuration that includes: a powder bed coating system, mirrors and galvanometers (laser-based) or an electromagnetic coil arrangement (electron beam based) for two-dimensional scanning of the heat source on the powder layer, stages that decrease the build plate and increase the powder reservoir to accomplish each build layer, a processing chamber that provided an inert gas or vacuum environment (the vacuum is used for the electron beam-based system), and a computer controller [77]. Table 2-9 summarizes the main printers used for metal AM HXs.

2.5.2.4 Challenges

As shown in Table 2-8, several studies have been performed on AM to create solutions that can provide more enhance performance, where one of the HX parameters (heat duty, pressure drop, mass, volume) shows improvement over conventionally fabricated HXs. Despite the promising success shown in those studies, AM is not replacing conventional technique because there are still challenges that need to be overcome. The most relevant challenges for AM HXs are the following:

- building leak-proof, thin heat transfer surfaces that can match or improve State-of-the-Art values:
  - fins: 50-130 µm.
  - separator plates: 100-400 µm, depending on the material
  - tubes: 250-300 µm thick
  - porosity: fins can be porous, but other sections of the parts can not
- building self-supporting structures during the build process

- designing a path for powder removal
- improving surface finish to reduce roughness, thus minimizing pressure drop
- developing in-process sensing and monitoring
- performing stress, thermal, and CFD Analysis on non-traditional designs
- developing larger volume AM machines for larger HXs
- reducing time and cost of AM

2.5.3 Chemical Vapor Deposition

Chemical Vapor Deposition (CVD) results from the chemical reaction of gaseous precursor(s) at a heated substrate to yield a fully dense deposit [78]. When applied to refractory metals and ceramics as thin coatings on various substrate, CVD produces freestanding thick-walled structured, like the PMHX shown in section 2.5.3.1. The metal deposition follows the following reaction:

$$metal\ halide\ (g) \rightarrow metals\ (s) + byproducts\ (g)$$

A schematic visualization of the process is shown in Figure 2-15.

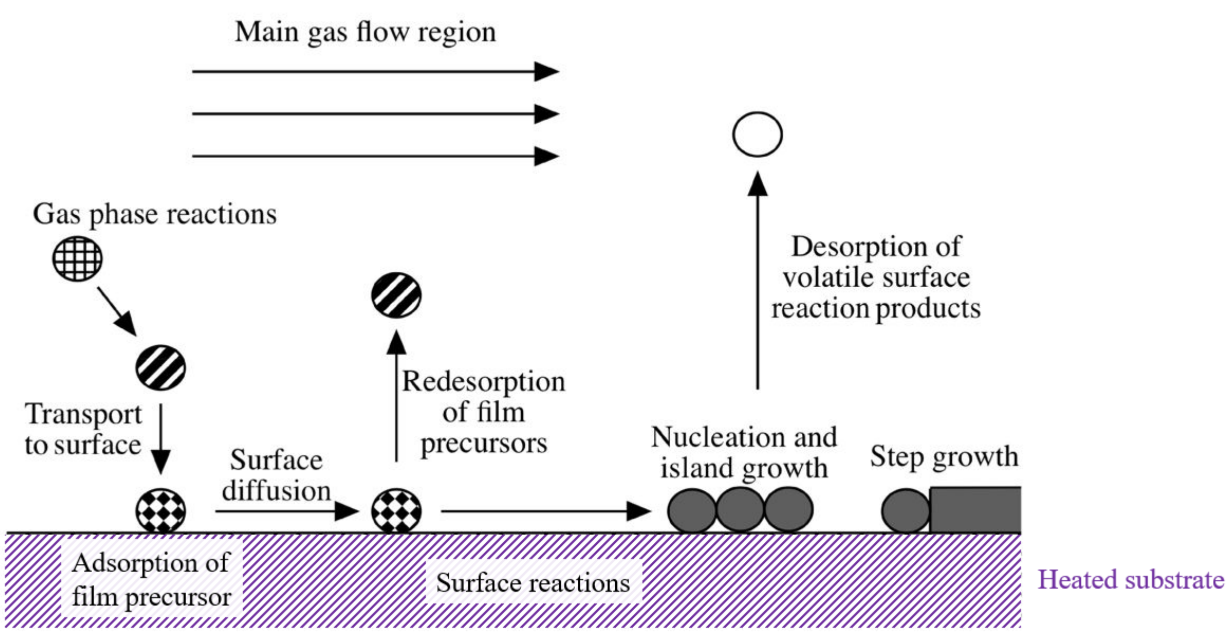

Figure 2-15: Metal CVD working principle (adapted from [79]*)*

CVD can assure several benefits over conventional manufacturing techniques [78]:

- Can be used for a wide range of ceramics and metals, including superalloys
- Can be used for coating or freestanding structures
- Fabricates net or near-net complex shapes
- Is self-cleaning: extremely high purity deposits
- Conforms homogenously to contour of substrate surface
- Has near-theoretical as-deposited density
- Has controllable thickness and morphology
- Infiltrates fiber performs and foam structures
- Coates internal passages with high length-to-diameter ratios
- Can simultaneously coat multiple components
- Coats powder

2.5.3.1 Porous Medium Heat Exchangers

Another option to enhance the rate of heat transfer is to use Porous Medium (PM). A PM is a composite medium containing interconnected voids or solid particles embedded into fluid containing medium. While the working fluid flows through the PM, it is heated or cooled by the interaction of the porous walls, thus resulting in a wide contact area. From the heat transfer point of view, the values of Nusselt number are approximately 50% higher than the values predicted for laminar flows in channels without porous materials [80]. The convective heat transfer coefficient is furtherly improved, considering that the material of the porous medium has a thermal conductivity which is higher compared to the working fluid, especially if this is a gas. Once more, the price of higher thermal performance is the high pressure drop connected [81].

PMHXs have been numerically and experimentally studied in the past, as summarized by Mahjoob *et al.* [82]. Some works also tried to use metal foam to increase the performance in the field of HTHXs. For example, Thermacore developed a porous metal HX applicable to fusion plasma-facing components in which the surface temperature reached the maximum temperature of 740 °C [83]. Ultramet, Inc. fabricated one-piece heat exchanger tubes of Chemical Vapor Deposited (CVD) tungsten (W). The new class of open cell, low density, high-temperature performance refractory foams was proposed for a variety of aerospace and industrial applications [84]. The design is illustrated in Figure 2-16.

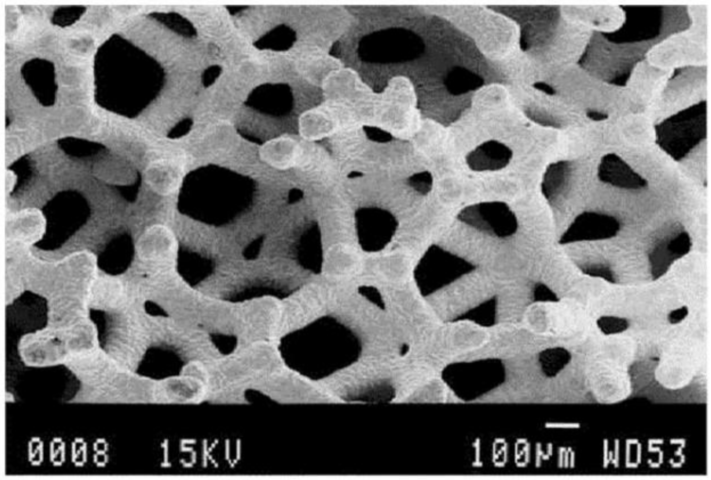

Figure 2-16: Example of Ultramet refractory foam [85]

The major disadvantages of PMHXs is their relatively high pressure drop [86] and the fact that they are not suitable for high-pressure conditions, as the maximum pressure for foam HXs is relatively low.

2.6 Comparison of selected HXs

Table 2-1 compares State-of-the-Art HTHXs. As shown in the table, ceramic HXs would be the best option if temperature was the only critical condition. However, for aerospace applications, operational pressure condition can be beyond ceramic capability. For this reason, it is necessary to select metal as the desired material. Among the available designs, the final choice is given to those that can assure high thermal performance with low pressure drop. MHXs and PCHXs are the best candidates, but their high pressure drop is the major limitation for many applications where pumping power is constrained. Novel designs are therefore the only solution left.

Table 2-1: State-of-the-Art HXs comparison

Technology	Maximum pressure [bar]	Maximum Temperature [◦C]	Compactness [m^2/m^3]
Ceramic HX [25]	13	1,300	design based
Shell and tube HX [87]	1,000	1,100	50-100
Spiral HX [45]	25	540	120-160
Fully welded PHX [88]	70	500	120-660
Shell & Plate HX [89]	200	950	≤ 300
Hybrid PHX [89]	80	900	≤ 300
PFHX [45]	120	800	800-1,500
MHX [90]	50	700	2,000-10,000
PMHX [89]	4	800	3,000-4,000
PCHX [45]	1,000	900	200-2,500
Marbond [45]	400	900	2,000-10,000

2.7 Summary

High temperature heat exchangers are key to the success of emerging high-temperature, high-efficiency solutions in energy conversion, power generation and waste heat recovery applications. The three key factors that need to be carefully chosen for high temperature heat exchangers are the material, the design, the fabrication method and most importantly life cycle duration reliability. Most common heat exchangers currently available in the market are the plate-fin, plate-and-frame and shell and tube, conventionally fabricated out of stainless steel. The ideal high temperature heat exchangers should be the result of mutually leveraging innovative design and manufacturing techniques to fabricate heat exchangers out of heat-resistant superalloy. Examples of this approach can be found in printed circuit heat exchangers, where design and fabrication technique are strongly interconnected and result in heat exchangers that can withstand high temperature and pressure resistance. Another promising opportunity can be found in additive manufacturing of superalloys for high temperature application. Due to the high flexibility in term of designing capability, it is believed that additive manufacturing could be the right solution to fabricate high temperature heat exchangers that would offer an optimum balance among heat transfer, effectiveness, pressure drop, size and weight.

Table 2-2: Ceramic HXs

Author	field	HX design	material	manufacturing technique	T up to [°C]	P up to[bar]	Working fluid
HTI [25]	gas turbine, preheater combustion air	shell-and-tube	ceramic	patented tube-to-tube sheet construction	1,300	13	air
Lewinsohn [28]	waste heat in high-temperature and corrosive environments	plate	silicon carbide, mullite, alu-mina, zirconia, and several specialty oxide compositions	Laminated-Object Manufacturing (LOM)	-	-	gas
Takeuchi *et al.* [91]	fusion reactor, High Temperature Engineering Test Reactor (HTTR) and Very-High-Temperature gas-cooled nuclear Reactors VHTR systems	plate-and-frame	SiC	-	570	-	liquid LiPb to helium
Kee *et al.* [27]	very-high-temperature gas-cooled nuclear reactors (VHTR)	plate-and-frame	CoorsTek AD-94 Alumina	Pressure Laminated Integrated Structures (PLIS)	750	ambient pressure	air
Schulte *et al.* [30] & Haunstetter *et al.* [31]	recuperator for externally fired combined cycle	plate-and-fin	SiC+EBC	sintering of green compact plates	800	5	gas

Alm *et al.* [92]	high temperature reactions, reactions with corrosive media	microchannel	alumina	stereolithography and low-pressure injection molding (LPIM)	85	8	water
Scheithauer *et al.* [29]	-	novel design	alumina and zirconia	Lithography-Based Ceramic Manufacturing (LCM)	-	-	-

Table 2-3: Commercially available metal shell-and-tube and spiral HXs

Brand - Model	**field**	**HX design**	**material**	**manufacturing technique**	**T up to [°C]**	**P up to[bar]**	**Working fluid**
Southgate Process Equipment - Standard Xchange [93]	-	shell-and-tube	316	welded	232	15.5	water, oil, corrosive fluid
Alfa Laval – Olmi [94]	petrolchemical, refineries, oil and gas, power	shell-and-tube	stainless steel, duplex and superduplex titanium, zirconium, high nickel alloy, copper alloys, and aluminum	welded	300	300	gas, liquid
Munters - Thermo-T [95]	waste heat recovery, recuperator	shell-and-tube	304L, 316L, or 309S	welded	1100	-	-
Sondex [47]	cooling and heat recovery	spiral	carbon steel	bolted or welded	350	25	demanding fluids and very high viscosities
Alfa Laval SHX [96]	petrochemical, wastewater treatment, food processing	spiral	stainless steel	Welded	400	100	fouling liquids

Table 2-4: Commercially available fully welded metal PHXs

Brand - Model	field	HX design	material	manufacturing technique	T up to [°C]	P up to[bar]	Working fluid
GEABloc [97]	chemical, petrochemical and power	plate-and-frame	304, 316, SMO 254; Alloys C22, C276, and C200; Nickel Alloys	fully-welded	288	32	liquid
Schmidt – SIGMAWIG [98]	chemical, refrigeration, reactor cooling/heating	plate-and-frame	Standard: 304, 316L On request: 904L, Nickel-alloys	fully-welded	300	35	liquid
Accessen [99]	chemical, petrochemical and power	plate-and-frame	304, 316, 316L, 904L, Titanium, Hasetlloy	fully-welded	350	35	-
Funke – FunkeBloc [100]	chemical and petrochemical	plate-and-frame	stainless steel	fully-welded	400	40	gas and oil
Alfa Laval - Compabloc [101]	petrochemical, refinery	plate-and-frame	304L, 316L, 904L; Alloys C22, C276, and B-2; Incoloy™ 825, 254 SMO, Hastelloy™ C2000	fully-welded	400	42	liquid
Nexson - GreenBoxTM [102]	heat recovery	plate-and-frame	304, 316, 904L, SMO 254; Alloys C22, C276, and C200	fully-welded	450	50	liquid
Tranter – MAXCHANGER [103]	condensers and evaporators in chiller or refrigeration systems	plate-and-frame	316	fully-welded	454	82.7	liquid
Ziemex [88]	chemical, pharmaceutical, food, petrochemicals	plate-and-frame	stainless steel, Nickel alloys, Inconel, Hastelloy, duplex, titanium	fully-welded	700	50	-

Tranter – SUPERMAX [7,8]	heating and cryogenic duties	shell-and-plate	316L	fully-welded	up to 538	up to 70	liquid, gas, steam and two-phase mixtures.
Alfa Laval – Packinox [51]	heat recovery duties	hybrid-shell-and-tube &plate	stainless steel, Inconel, Incoloy	fully-welded	650	140	gas
SPX – APV [52]	oil and gas, chemical, power	hybrid-shell-and-tube &plate	standard: 316L, SMO 254 on request: 304, 316Ti, 904L	fully-welded	up to 350	up to 40	gas
VAU [53]	chemistry, petro chemistry, food and pharmaindustry	hybrid-shell-and-tube &plate	standard: 304, 316 on request: Hastelloy, Incoloy, Titanium	fully-welded	up to 900	up to 60	liquid, gas
Kelvion – KºFlex [54]	chemical, petrochemical and power	hybrid-shell-and-tube &plate	standard: 304, 316L, 321, 316Ti. on request: Nickel-alloys	fully welded	Claimed up to 900 (300 on the brochure)	up to 100	gas, liquid and two-phase

Table 2-5: Conventionally manufactured metal PFHX for aerospace applications

Application	field	HX design	material	manufacturing technique	T up to [°C]	P up to[bar]	Working fluid
recuperator utilized in WR-21[104]	marine engine	plate-and-fin	stainless steel, Inconel, Waspaloy	brazed	575	15	air, exhaust gas
Ingersoll-Rand Energy Systems (Kesseli *et al.*) [105]	Recuperator for gas turbine	plate-and-fin	Inconel 625	welded	800 - 900	4	air, exhaust gas
MTU recuperator for EEFEA [106]	recuperated aero gas-turbine engines	profile tube heat exchanger	Inconel 625	welded	670	31	air, exhaust gas
JMHX for SKYLON [84,85]	preecooler for airbreathing rocket engines	fine tube heat exchanger	stainless steel, Nicrobraz 10	brazed	725	100	helium

Table 2-6: Conventionally manufactured metal MHXs for aerospace applications

Author	field	HX design	material	manufacturing technique	T up to [°C]	P up to[bar]	Working fluid
Strumpf *et al*. [55]	aerospace	microchannel	alluminum	welded	-	-	air+water
Nacke *et al* [109]	aerospace	microchannel	stainless steel	soldered	260	-	air+water
Williams *et al.* [61]	aerospace	microchannel		folded microchannel fins	-	-	-

Table 2-7: HXs built using Photo-chemical Etching and Diffusion Bonding

Author/Brand	field	HX design	material	manufacturing technique	T up to [°C]	P up to[bar]	Working fluid
Heatric [24–26]	HTHP applications	printed circuit	stainless steels (316L, 304L, Duplex), high nickel alloys and exotic materials such as 617	photo-chemical etching and diffison bonding	982	900	gas, liquids
Alfa Laval - PCHXs [113]	marine, oil and gas	printed circuit	316L SST (other materials available on request)	photo-chemical etching and diffison bonding	980	650	gas, liquids
Kanlayasiri *et al.* [114]		microchannel	Nickel Aluminide	photo-chemical etching and diffison bonding	-	83	air
Song [115]	supercritical CO_2 (S-CO_2) Brayton cycle	printed circuit	316L	photo-chemical etching and diffison bonding	200	216	supercritical CO_2 and water
Chen *et al.* [116] [117]Mylavarapu *et al.* [118]	very-high-temperature gas-cooled nuclear reactors (VHTR)	printed circuit	Alloy 617+ Alloy 800H	photo-chemical etching and diffison bonding	802	27	helium
Marbond HX [119]	HTHP applications	Marbond	stainless steel, titanium, higher alloy steels and Nickel	photo-chemical etching and diffison bonding	900	400	gas, liquid, two-phase

Table 2-8: Additive Manufacturing of Metallic HXs

Author	year	field	AM tech	design	material	Size [mm x mm x mm] =[mm^3]	Claims and observations
Zhang *et al.* [120]	2018	aerospace	DMLS	Manifold-microchannel on both sides	Inconel 718	66x74x27 =131,867	minimum fin thickness of 180 μm, heat duty of 2.78 kW and overall heat transfer coefficient of 1000 W/m^2K nearly 25% improvement in heat transfer density compared to conventional PFHXs
Collins *et al.* [121]	2018	electronic cooling	DMLS	permeable-membrane microchannel (PMM) heat sink	AlSi10Mg	10x10x7 =700	for the same channel width of 0.5 mm, PMM design offers 17% reduction in thermal resistance and 28% reduction in pressure drop compared to the M2 heat sink
Arie *et al.* [122]	2018	dry cooling	DMLS	air side: manifold-microchannel water side: rectangular channel	3 HXs: - SS17-4 - Ti64 - AlSi10Mg	25x44x62 = 68,200	compared to wavy fin and plain plate fin HXs, up to 30% and 40% improvement, respectively, in gravimetric heat transfer density compared to state-of-the-art dry cooling, nearly 27% improvement in gravimetric heat transfer density (COP_{air}) of 172 fin thickness of 150 μm for the air side
Collins *et al.* [123]	2018	clectronic cooling	DMLS	straight and manifold-microchannel heat sink	AlSi10Mg	15x15.5 (foot print)	manifold reduces the pressure drop by 40-90% without incurring any significant fabrication effort beyond that of the straight microchannel design 500 μm as minimum features
Romei *et al.* [124]	2017	HT spacecraft resistojet HX	SLM	recirculating flow HX	316L	16.82 x 16.82 x 26.80 = 7,582 (CT scan size)	fine structures with feature sizes below 200 μm high-resolution micro-Computed Tomography (CT) is applied as a tool for volumetric non-destructive inspection
Robinson *et al.* [125][126]	2017	electronic cooling	MICA Freeform	water cooled micro heat sink (FINJET architecture)	Valloy+ copper+ palladium	4.1x3.2x1 =13.1	30 μm as smallest feature limit water cooled heat sink with applied heat flux of 1,000 W/cm^2

Brandon *et al.* [127]	2017	hydraulic oil cooling in a commercial excavator	SLM (EOS)	plate-fin tube	AlSi10Mg	50x430x50= 11,395,000 (including headers)	capability to additively manufacture commercial-scale HXs with intricate features 500 μm as minimum features powder removal issues
Arie *et al.* [128]	2017	dry cooling	DMLS	air side: manifold-microchannel water side: rectangular channel	Ti64	150x150x32 =720,000	compared to the conventional surfaces like wavy fin, louvered fin, and plain plate fins, up to 80%, 120%, and 190% improvement in air-side heat transfer coefficients respectively fin thickness design of 0.150 mm
Saltzman *et al.* [129]	2017	aircraft oil coolers	DMLS (EOSINT M 280)	air side: fins water side: rectangular channel	AlSi10Mg	200x92.5x115 =2,127,500	air-side pressure drop for the AM HXs was double compared to conventionally built baseline HX. Heat transfer was increased by about 10% for the baseline AM and by 14% for the enhanced AM HX compared to the conventionally built baseline HX. fin thickness of 0.33 mm with AM vs 0.3 mm of the conventional manufactured one
Kasim *et al.* [130]	2017	aerospace	-	offset fins	Titanium	-	Boeing prototype examples
Gerstler and Erno [131]	2017	fuel-cooled oil cooler (FCOC)	SLM	HX including furcating unit cells [132]	4 HXs: -Aluminum - Ti 6-4 -Cobaalt Chrome - Inconel 718	-	AM design has equivalent heat transfer and pressure drop to the conventional HX while having 66% lower weight and 50% lower volume AM HX requires no braze joints thus is expected to have improved reliability compared to the conventional design.
Bacellar *et al.* [133]	2017	advanced air-liquid HXs	DMLS (ProX DMP 320)	novel fin-and- airfoil tube	Titanium grade 5	≈300,000	Optimum designs can achieve more than 50% reduction in size, material, and pressure drop compared to the baseline microchannel heat exchanger
Arie *et al.* [134]	2016	air-water Cooling	DMLS	air side: manifold-microchannel Water side: rectangular channel	Ti64	24.8x44.3x61.7 =68,200	compared to a conventional wavy fin surface and plain plate-fin surface, 15% – 50% and 95% – 110% increase in heat transfer coefficient respectively for the same pressure drop.

Gobetz *et al.* [77]	2016	aerospace	DMLS (EOS 280M)	array of cooling fins and a serpentine liquid channel;	AI-10Si:-0.5Mg		very effective and uniform cooling provided detected printing defect probably caused by improper fusion during printing
Vanapalli *et al.* [135]	2016	cryogenic	SLM	flat-panel gas-gap heat switch	Ti-6Al-4V	110x110x3.2 =38,720	demonstrated a compact flat-panel gas-gap heat switch operating at cryogenic temperature
Kirsch *et al.* [136]	2016	cooling	DMLS	wavy microchannels	Inconel 718	25.4x25.4x1.52 =980	heat transfer and pressure loss performance of AM wavy channels. channels with the longer wavelengths performed well from both a heat transfer and friction factor standpoint
Snyder *et al.* [137]	2016	gas turbine cooling	DMLS	novel geometric features of internal channels	Inconel 718	25.4x25.4x3 =1,963	45° print orientation guarantees smallest resolution deviation vertical print orientation produces smoothest AM surface roughness is much greater than traditional manufacturing techniques. different pressure drops but comparable heat transfer performance across all coupons.
Dupuis *et al.* [138][139]	2016	cooling	cold spray additive manufacturing process	pin fin arrays with different base shapes and configurations	Al6061 T6	51x51x1 =2,601	heat transfer and pressure losses of 1 mm high round base, square base and diamond base tapered pin fin arrays were assessed in both the in-lined and staggered configurations for fin densities of 8 fpi and 12 fpi
Wong *et al.* [140]	2016	electronic cooling	SLM	novel heat sink design	AlSi10Mg	50x50x5 =12,500	heat transfer performance of the aerofoil and rectangular rounded heat sinks exceeded those of the circular heat sink up to 29 and 34% respectively
Plunkett Associates [141]	2016	electronic cooling	DMLS	novel heat sink design	-	-	all models showed a significant improvement over a standard extruded heat-sink
Dede *et al.* [142]	2015	electronic cooling	additive layer manufacturing (ALM)	novel heat sink design	AlSi12	50.8x50.8x4.7 =12,130	topology optimization can create innovative heat sink designs whose COP can be up to 44% better than conventional heat sinks

Norfolk *et al.* [143]	2015		ultrasonic additive manufacturing (UAM)	microchannel heat exchanger	copper and aluminum		UAM allows complex thermal management structures with burst pressures in excess of 200 bar UAM materials have identical thermal conductivity as wrought product
Thompson *et al.* [144]	2015	electronic cooling	SLM (ProX 100)	flat-plate oscillating heat pipe (FP-OHP)	Ti–6Al–4V	50.8x38.1x15.8 =30,580	circular mini-channel (1.53 mm in diameter), channel wall consisted of partially un-melted particles, as well as amorphous melt regions thermal conductivity 400-500% higher than solid material
I3DMFG [145]	2014	electronic cooling	DMLS	novel heat sink	6061 Aluminum	-	50% and 20% enhancement (compared to milled samples) is observed for flat and finned heat sinks, respectively
Cormier *et al.* [146]	2014	electronic cooling	cold spray technology	pyramidal pin fins	Al6061 T6	51x51x2 =5,202	investigation concentrated on samples with fin densities of 12 fins per inch between 1.0 and 2.2 mm heights and samples of 1.0 mm height with fin densities varying between 12 and 24 fins per inch
Assaad *et al.* [147]	2011		pulsed gas dynamic spraying (PGDS)	novel stacked wire mesh compact HX	stainless steel 304		staggered pattern of the mesh layers results in minimal penetration of the powder particles, which is desirable as it results in lower pressure losses and higher overall heat exchanger efficiency
Hutter *et al.* [148]	2011	tubular reactors	DMLS	metal foams	high alloyed steel	-	adoption of AM in metal foams fabrication leads to 30% improvement over conventional technique
Ramirez *et al.* [149]	2011	complex, monolithic HXs	EBM (Arcam A2)	reticulated mesh and stochastic open cellular foams	copper	23x23x36 =19,044	precipitates and interconnected dislocation microstructures having average spacing of ~2μm, which provide hardness values ~75% above commercial Cu products.
Neugebauer *et al.*[150]	2011	automotive	laser beam melting	compact cooler unit	-	46x59x15 =40,710	Additive manufacturing proved to give superior properties to thecomponent compared to conventional manufacturing methods
Wong *et al.* [151]	2009	heat sink	SLM	different designs tested	aluminum 6061	50x10x100 =50,000	comparison of 5 different designs: cylindrical pin, rectangular fin, rectangular fin array with rounded corners, staggered elliptical and lattice the staggered elliptical array, which cannot be manufactured by conventional techniques,

							outperformed the other heat sinks in terms of both heat transfer performance and pressure drop
Kumar *et al.* [152]	2009	-	EBM	hexagonal periodic cellular structure	Ti-6Al-4V Al-6061	40x40x11.5 =18,400	unit cell type and size, ligament size, and cell orientation have a considerable influence on surface area, volume, density and fluid flow behavior of the lattice structure
Tsopanos *et al.* [153]	2009	-	SLM (MCP Realizer)	micro cross-flow HX with rectangular channels in both sides	316L	15x15x15 =3,375	AM provided channel range of 150-170 micron and roughness Ra of 15 micron

Table 2-9: AM printers

	ProX 200	ProX 300	M290	RenAM500M	M1 cusing	SLM 280	Q10plus	A2Xplus
Manufacturer	3D System		EOS	Renishaw	Concept laser	SLM - Solutions	Arcam	
Origin	France, with USA branch		Germany, with USA branch	UK, with USA branch	Germany, with USA branch	Germany, with USA branch	Sweden, with USA branch	
Build Area	140 x 140 x 140 mm^3	250 x 250 x 330 mm^3	250 x 250 x 325 mm^3	250 x 250 x 250 mm^3	250 x 250 x 250 mm^3	280 x 280 x 365 mm^3	200 x 200 x 180 mm^3	200 x 200 x 380 mm^3
Accuracy	0.05mm	0.05mm	Depend on the laser power	Depend on the laser power	Depend on laser power	Depend on laser power	0.05mm	0.15mm
Minimum feature size	0.1mm	0.1mm	0.1mm	0.10mm	0.15mm	0.14mm	0.4mm @ 3000W laser (Lower feature size is possible with lower laser power)	
Laser Power	300W	500W	400W	500W	400W	Single or dual laser up to 1,000W	3,000W	
Process Monitoring	None		EOSTATE Monitoring Suite (optional)	Place to mount monitoring devices available	Photodiode, camera, and video camera can be added	None	Camera-based monitoring system and Xray included. Scanning electron microscope will be added in near future	None
Material Compatibility	Stainless Steel, Cobalt Chrome, Aluminum Alloy, Maraging Steel, Nickel Alloy		Aluminium AlSi10Mg, Cobalt Chrome, Maraging Steel, Nickel Alloy, Stainless Steel, Titanium	Stainless Steel, Cobalt-Chrome, Aluminum Alloy, Titanium Alloy, Titanium, Inconel	Stainless Steel, Cobalt-chrome, Aluminum Alloy, Titanium Alloy, Titanium, Bronze	Stainless-steel, Cobalt-chrome, Aluminum Alloy, Titanium Alloy, Titanium, Tool Steel, Inconel	Titanium Alloy, Cobalt-Chrome	Titanium, Titanium Alloy, Inconel, Cobalt-Chrome
Estimated Price	$300k	$500-600k	$600-700k	$725k	$450-600k	$650k-750k	$1M	$1.2M

Source: Quote from AM companies

Chapter 3 Conceptual Design, Performance Prediction Models, Optimization, and Scaling Down Approach for the 4” x 4” x 4” Unit

3.1 Introduction

This chapter discusses the design requirements for the HTHX under development. The HTHX design is a gas-to-gas HX, cross-flow configuration based on manifold microchannel technology. The concept behind the design as well as a full geometrical description are included. The chapter also discussed about a single objective optimization process performed to find the optimal design that meets the requirements. A detailed description of the subscale unit used to validate the outcome of the optimization process is also included.

3.2 Design requirements

The design requirements were provided by an aerospace company for an aerospace turbofan pre-cooler in the ECS of an airplane. The current conventional design is based on a compact plate-and-fin HX that incorporates the microchannel technology. The detailed design specifications including overall mass (M), mass flow rates ($\dot{m}$), inlet temperatures (T_{in}), system pressures (P), and pressure drops (ΔP) on both hot and cold sides are shown in Table 3-1 and Table 3-2.

Table 3-1: Physical specifications for full-scale HX

Parameter	**Unit**	**value**
COP	-	>47.6
ε	-	>0.9
Material	-	Inconel

Table 3-2: Operation specifications for full-scale HX

Parameter		Unit	Nominal Condition
Hot side	Flow Rate	kg/s	**
	Temperature	°C	560
	System Pressure	Pa	300,000
	Pressure Drop	Pa	**
Cold side	Flow Rate	kg/s	**
	Temperature	°C	25
	System Pressure	Pa	101,325
	Pressure Drop	Pa	**

** Industry confidential data

3.3 Manifold Microchannel Technology

The working principle of the manifold microchannel technology as well as the advantages over conventional MHXs were explained in Section 2.4.4.1. As shown in Table 3-1 and Table 3-2, the requirements are based on minimizing pressure drop and mass, while maximizing heat duty or equivalently effectiveness (ε) of the HX. Therefore, M2HX is one of the best design possible to achieve these targets.

Manifold-microchannel technology was first introduced by Harpol and Eninger [154], where they estimated heat transfer coefficient in the order of 100 W/cm^{2}K and pressure drop of 100 kPa or 200 kPa. In this work dated 1991, manifold-microchannel technology was meant for electronic cooling and in particular liquid cooling. After this initial success, other studies have demonstrated the benefits in electronic cooling, extending the working principle to two-phase cooling [155]–[159]. Other works implemented manifold microchannels into other fields like solar collector heat sink [160], liquid cooling of concentrating photovoltaic cells (CPC) [161] , liquid-liquid HX for absorption cooling system [162] and dry cooling [122], [134].

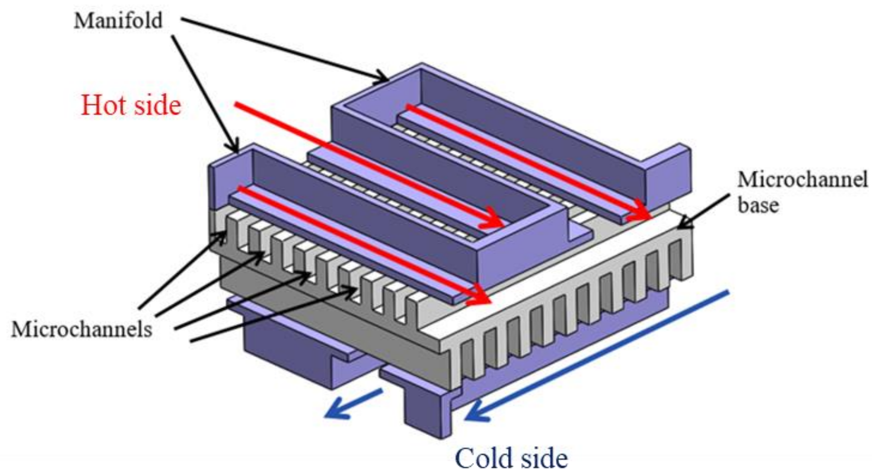

Figure 3-1: Gas-to-gas cross-flow M2HX conceptual design

Manifold-microchannel technology was implemented for the first time in a gas-to-gas application by Zhang *et al.* [120] in air-to-air HX used on aircraft. When applied in a cross-flow configuration for a gas-to-gas HX, the representative unit showed in Figure 2-8 needs to be applied to both hot and cold-side. The two sides of a stack are rotated 90° with respect to each other due to the cross-flow configuration.

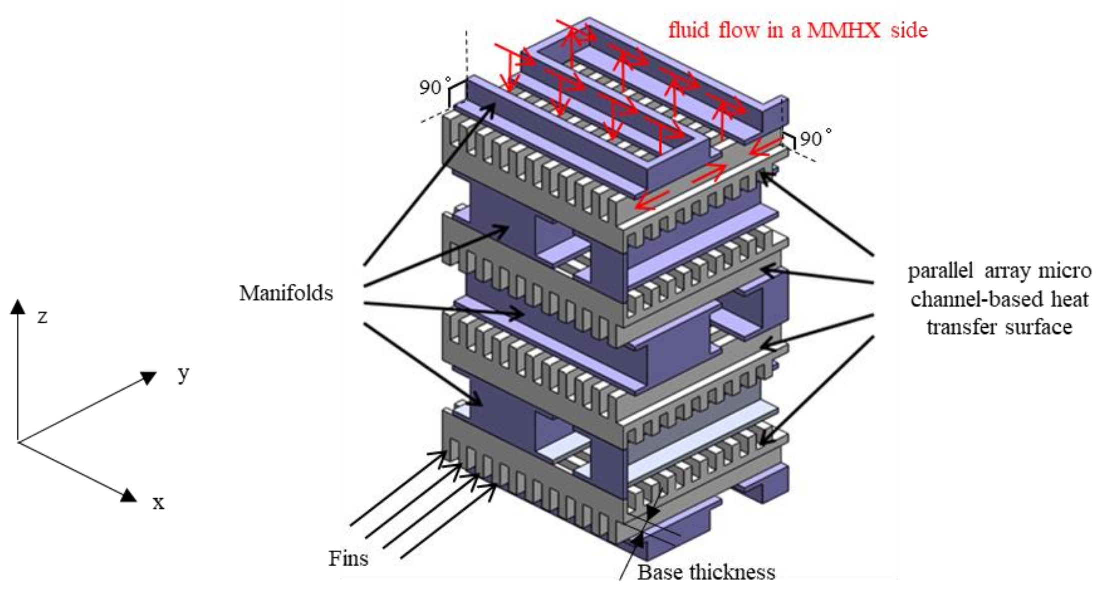

Figure 3-2: Multi-layer cross-flow M2HX conceptual design

A separator plate is used to separate the two sides, as shown in Figure 3-1. Figure 3-1 will be addressed in the rest of the dissertation as a stack unit. A full HX usually consist of multiple manifold-microchannel stacks, as shown in Figure 3-2.

3.3.1 Design Parameters

In order to fully characterize the manifold microchannel technology, it is useful to describe the design parameters shown in Figure 3-3.

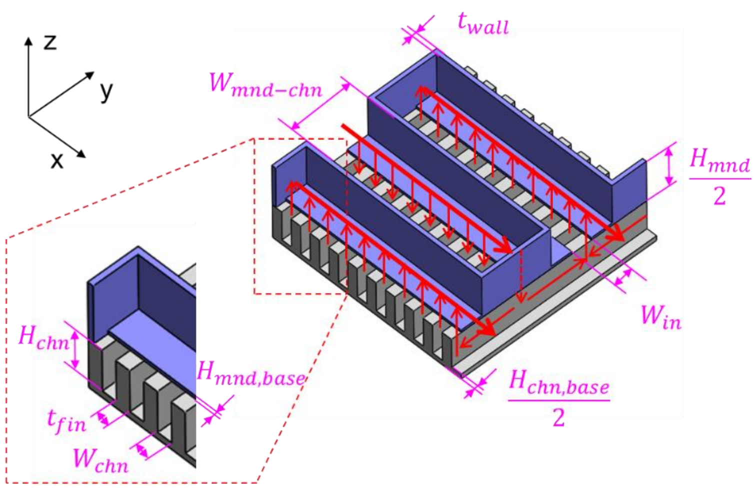

Figure 3-3: Manifold-microchannel design layout

The parameters can be divided into two categories: the ones describing the microchannels and the ones for the manifold. Starting with the formers, t_{fin} is used for the fin thickness while W_{chn} and H_{chn} are respectively width and height of the microchannels. $H_{chn,base}$ is the thickness of the separator plate and $\frac{H_{chn,base}}{2}$ is the distance between the base of the fins and the middle plane of the separator plate. Finally, N_{chn} is the number of total microchannels on one side. Moving to the manifold, t_{wall} is the thickness of the manifold wall, $W_{mnd-chn}$ is the manifold channel width and N_{mnd} is the number of manifold channels ($W_{mnd-chn} + t_{wall}$) that can fit in one side. $H_{mnd,base}$ is the thickness of the flat component of the manifold in contact with the microchannel, called manifold base. W_{in} is the width of the openings left in the manifold base to allow the fluid passage between microchannels and manifolds channels, both at inlet and outlet levels. H_{mnd} is the total height of the manifold. It is common practice to analyze manifold microchannel design as shown in Figure 3-1. This is defined as a stack, thus N_{stack} is the number of elements shown in Figure 3-1 stacked in the vertical direction in Figure 3-2, called $L_{no-flow}$. With this concept in mind, the manifold channel height shown in Figure 3-3 is only half of the total height, due to its symmetrical nature.

3.4 Model for Performance Prediction

When designing the full-scale M2HX, the large number of microchannels in the HX and the large number of cells per microchannel required to achieve mesh-independent results make a full three-dimensional simulation not feasible. Therefore, it is required to use a simplified model that provides sufficiently accurate results in a much shorter time.

3.4.1 Hybrid Method

Arie [60] developed a hybrid method capable of evaluating pressure drop and heat transfer performance in M2HXs in much shorter time than a full CFD simulation, which makes it suitable for optimization problem where hundreds of different geometries need to be evaluated. The main assumptions of this model are:

- uniform flow distribution in all microchannels
- heat transfer in manifold-channels can be neglected compared to the heat transfer in the microchannels
- Constant fluid properties and isotropic solid properties
- Constant temperature Nusselt number

The method involves using a Single Manifold-Microchannel (SMM) CFD simulation to calculate the heat transfer coefficient and the pressure drop in the microchannel (Δp_{12} with reference to Figure 3-4). The model control volume and the boundary conditions of the SMM are shown in Figure 3-4 and Figure 3-5, respectively.

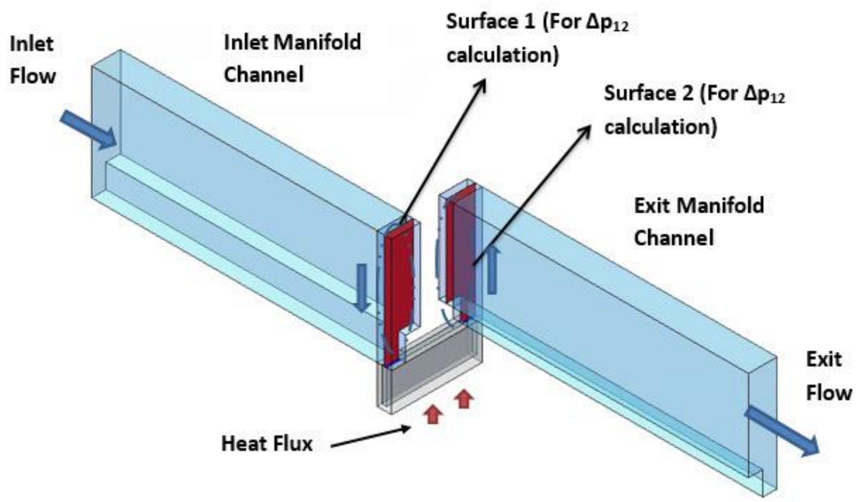

Figure 3-4: Single manifold-microchannel model control volume [60]

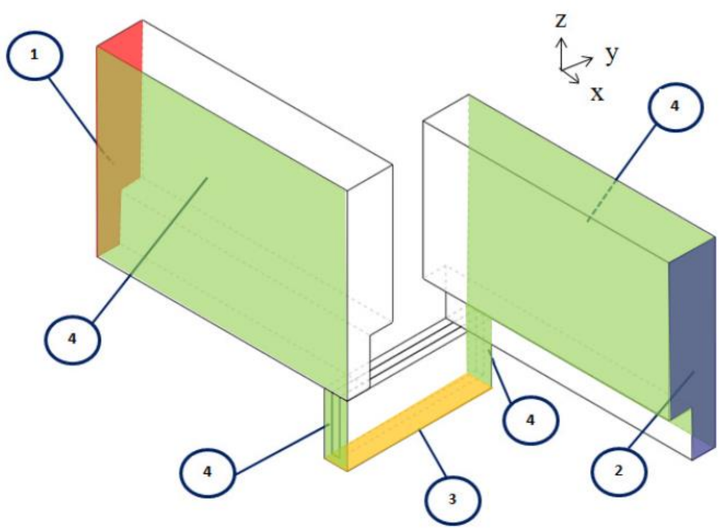

Figure 3-5: Computational domain and boundary conditions: mass flow inlet and constant temperature (1), constant pressure outlet (2), constant surface temperature (3), symmetry plane (4),and insulated wall surface for all other boundaries [60]

Due to the assumptions of uniform microchannel flow distribution and constant fluid properties, it is possible to run the CFD only once per side and only for a single microchannel at the nominal flow rate. The manifold pressure drop, on the other hand, was calculated by solving a 1-D differential equation on mass and moment balance in the manifold channel. This approach was extensively applied and validated in several other works [59][163][157][164]. The detailed description of the method can be found in Ref. [60].

3.4.2 Heat Spreading Model

Once solved the single unit, it is necessary to compute the overall capacity of the HX. Due to the short flow length typical of M2HXs, heat spreading occurs in the separator plate, causing the conventional NTU-ε method correlation for cross-flow HX effectiveness to be inaccurate. It is therefore required to use a model that it is customized for the manifold microchannel technology. The model used to predict the performance of the M2HX under analysis was developed by Mandel *et al.* [165] specifically for a double-sided, cross-flow M2HX. The unit cell and the modeled domain with the boundary conditions are shown in Figure 3-6.

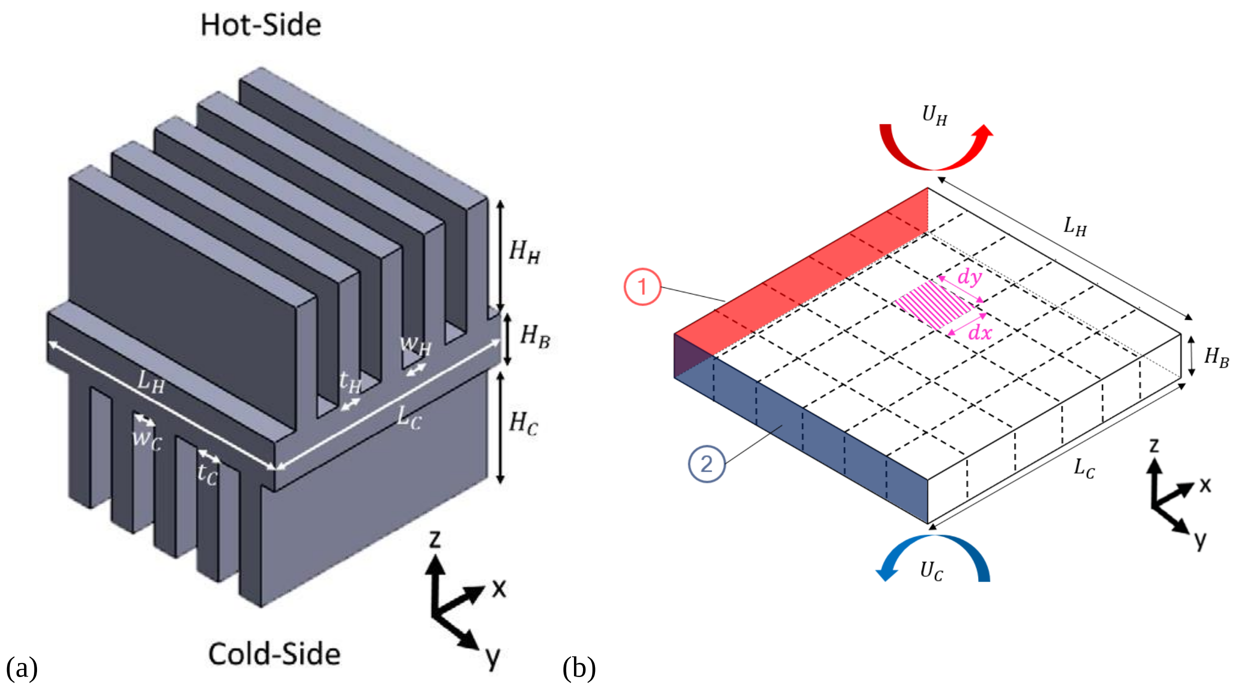

Figure 3-6: (a) Unit-cell pattern and geometric definitions [165]*, and (b) final model domain and sample mesh with boundary conditions: mass flow inlet and constant temperature for hot side (1), mass flow inlet and constant temperature for cold side (2), the effective hot- and cold-side conductances between the hot- and cold-side fluids Geometry and mesh enlarged to show details*

The effective hot- and cold-side conductances between the hot- and cold-side fluids (U_C and $U_H$of Figure 3-6b) are outputs of the SMM model. Using the simplified approach domain shown in Figure 3-6b, a custom-coded two-dimensional model was developed by solving the governing partial differential equations through a custom-solution algorithm. The detailed description can be found in Ref. [165].

For the case study analyzed by Mandel *et al.* [165], the model matches the three-dimensional CFD validation within 1.4%. The M2HX under development will be used as an experimental validation of the model described.

3.5 Single-Objective Optimization

A single-objective optimization was performed to minimize the weight of the M2HX while maintaining the design requirements mentioned in Table 3-1 and Table 3-2.

3.5.1 Problem Definition

For the optimization problem definition, the M2HX geometrical constraints are adopted from the manufacturing limits of DMLS or based on the printing results obtained in previous studies [120][122], as summarized in Table 3-3.

Table 3-3: AM optimization constraints for the first HX

Parameter	Constraint	Reason
H_{chn}	0.2-5 mm	powder removal, printability
$\frac{W_{chn}}{t_{fin}}$	1-5	powder removal, printability
W_{chn}	0.05-0.5 mm	powder removal, printability
$W_{mnd-chn}$	2-25 mm	powder removal
H_{mnd}	3.0-20mm	powder removal, printability
N_{chn}	50-1000	reasonable interval
W_{in}	1-5 mm	powder removal
t_{fin}	≥ 0.200 mm	manufacturing limit, the smaller the better
$H_{chn,base}$	≥ 0.500 mm	manufacturing limit, the smaller the better
$H_{mnd,base}$	≥ 0.150 mm	manufacturing limit, the smaller the better
t_{wall}	≥ 0.300 mm	manufacturing limit, the smaller the better

Beside the constraints already mentioned, due to manifold-microchannel design, some other geometrical relations needs to be considered:

$$L_{hot} = N_{chn,hot} * \left(W_{chn} + t_{fin}\right)_{hot} \quad (1)$$

$$L_{cold} = N_{chn,cold} * \left(W_{chn} + t_{fin}\right)_{cold} \tag{2}$$

$$L_{hot} = (W_{mnd-chn} + t_{wall})_{cold} * N_{mnd,cold} \tag{3}$$

$$L_{cold} = (W_{mnd-chn} + t_{wall})_{hot} * N_{mnd,hot} \tag{4}$$

$$N_{chn}\text{: integer} \tag{5}$$

$$N_{stack}, N_{mnd}\text{: even integer} \tag{6}$$

where L_{hot} and L_{cold} are the flow length for the hot- and cold-side of the HX respectively. N_{stack} and N_{mnd} are recommended to be an even number to guarantee more uniform flow distribution of the M2HX.

The final problem definition can be obtained by combining all the information mentioned so far in one statement only:

$$\begin{cases} \min M \\ \text{s.t.} \quad COP, \varepsilon, AR, \Delta P_{cold}, \Delta P_{hot}\ constraints\ from\ \text{Table 3-1}\ and\ \text{Table 3-2} \\ \quad\quad AM\ optimization\ constraints\ of\ \text{Table 3-3} \\ \quad\quad geometrical\ constraints\ of\ equations\ (1)-(6) \end{cases} \tag{7}$$

where:

variables hot- and cold-side: W_{chn},t_{fin},H_{chn}, W_{in}, $W_{mnd-chn}$,H_{mnd},N_{mnd},N_{chn} and H_{base},N_{stack}

parameters: $T_{in,cold}$, $T_{in,hot}$, P_{cold}, P_{hot},$\dot{m}_{cold}$,$\dot{m}_{hot}$ $from$ Table 3-2

3.5.2 Optimization Process

Approximation-assisted optimization was employed to solve the problem defined by (7). The main advantage of this method is that it can reduce computational time by using a metamodel to predict the performance of the HX.

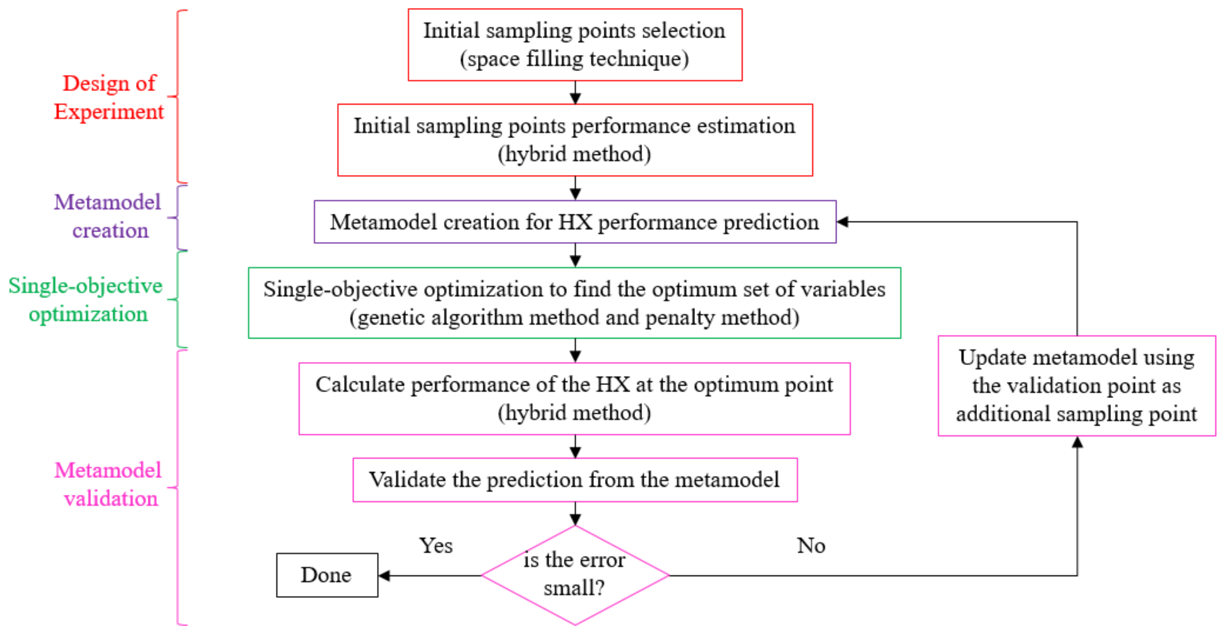

Figure 3-7: Single-objective optimization process flow-chart

The flowchart reported in Figure 3-7 shows the 4 stages in which the optimization methodology is divided.

1. Design of Experiment (DOE): initial limited sampling data of the feasible domain for the metamodel was performed using space filling method developed by Aute *et al.* [166]. For each sampling point, the objective function was directly calculated using the hybrid method and the heat spreading model described in Section 3.4.1.
2. Metamodel creation: the metamodel is as an approximation function to predict the response of the system at unobserved points over the feasible domain by using the known information at the sampling points obtained from the DOE (observed points). Dace, a Kriging-based metamodel toolbox developed by Lophaven *et al.* [167], was utilized for this purposed.
3. Single-objective optimization: the single-objective optimization was performed using genetic algorithm with penalty method to force the constraints of the problem defined by (7). The basic principle of genetic algorithm is to use concept like natural selection to eliminate inferior solutions and retain high performance solutions.

4. Metamodel validation: Since the metamodel is an approximation of the system behavior, the optimum points obtained must be validated. This validation was performed by calculating the actual performance of the optimum point using the hybrid method and the heat spreading model described in Section 3.4.1 and compare it to the one predicted using the metamodel. If the error between the predication and the actual value is small, the process concludes and the optimal point is confirmed. Otherwise, the metamodel is recreated by using the validation point as additional observed point. The process is repeated until the calculated error is below the design threshold.

3.5.3 Optimization Results

The optimal set of variables that minimizes the problem described by (7) is shown in Table 3-4.

Table 3-4: Full-scale parameters obtained from single objective optimization the first HX

Parameter		Unit	Value
Cold side	W_{chn}	mm	0.200
	t_{fin}	mm	0.200
	H_{chn}	mm	1.20
	W_{in}	mm	3.00
	$W_{mnd-chn}$	mm	7.00
	$H_{mnd,base}$	mm	0.150
	H_{mnd}	mm	14.80
	N_{mnd}	-	94
	N_{chn}	-	235
Hot side	W_{chn}	mm	0.200
	t_{fin}	mm	0.200
	H_{chn}	mm	0.900
	W_{in}	mm	2.00
	$W_{mnd-chn}$	mm	23.2
	$H_{mnd,base}$	mm	0.150
	H_{mnd}	mm	7.00
	N_{mnd}	-	4
	N_{chn}	-	1,715
$H_{chn,base}$		mm	0.500
N_{stack}		-	18

3.5.4 Full-scale M2HX Projected Performance

The HX obtained through the single-objective optimization code is the full-scale M2HX that is used for a direct comparison with the baseline HX given by the aerospace company. The results reported in Table 3-5 are obtained using the model of Section 3.4.

Table 3-5: Performance comparison between target and first full-scale M2HX

	Unit	Target	Full-scale M2HX
COP	-	>47.6	53
ε	-	>0.9	0.9
L_{cold}	mm	--	94
L_{hot}	mm	--	686
$L_{no-flow}$	mm	--	257
ΔP_{cold}	Pa	**	-1%
ΔP_{hot}	Pa	**	-27%
V	L	--	16.6
M	kg	<21.5	19.4

**Industry confidential data

The HX is designed to be fabricated out of Inconel 718, since it is the most suitable material for this applications as shown in Section 2.3. Table 3-5 shows that the end results of the optimization is a 9.7% mass reduction compared to the baseline, while matching all other performance targets called for the problem statement.

3.6 Subscale Unit Design

As shown in Table 2-9, none of the AM printers analyzed can print such a unit. It is therefore required to design a subscale that can be printed and that can validate the model developed. The overall size identified for the subscale unit is for an approximate 4” x 4” x 4” M2HX. This size would represent the biggest M2HX ever printed and among the biggest HXs realized through AM with minimum feature size of 0.200 mm.

An important feature of manifold-microchannel technology is that it mostly decouples heat transfer performance from footprint, which means that is easy for scaling up and down. The $L_{no-flow}$ length, for example, can be easily changed by changing N_{stack} without affecting pressure drop and heat transfer coefficient. For cold-side, L_{cold} is already below 4", therefore L_{cold} is not scaled down, thus both the manifold and the microchannel feature sizes on the cold side are set to be the same as full-size design. On the contrary, L_{hot} needs to be reduced to 4". To keep the same heat transfer performance, the microchannels and fins geometry as well as the flow rate per channel are set to be the same as the full-size design. For the manifold scaling, all features but manifold height (H_{mnd}) are set to be the same as full-size design. The manifold height (H_{mnd}), instead, is reduced to keep the same pressure drop in the manifold per manifold length. However, as shown in Table 3-3, 3.0 mm is the minimum manifold height, as lower than this number may cause problem for powder removal. For this reason, even though setting H_{mnd} equal to 3.0 mm results in a lower pressure drop in the manifold per manifold length compared to the full-scale, no further reduction is acceptable. The results of the scale-down procedure are reported in Table 3-6.

Table 3-6: Scale down procedure outcomes of the first HX

Parameter	Full-scale	Subscale	Deviation
N_{stack}	18	8	-55.6%
$N_{mnd,cold}$	94	12	-87.2%
$H_{mnd,cold}$	14.8 mm	14.8 mm	0%
$N_{chn,cold}$	235	235	0%
$N_{mnd,hot}$	4	4	0%
$H_{mnd,hot}$	7.0 mm	3.0 mm	-57.1%
$N_{chn,hot}$	1,715	219	-87.2%
L_{cold}	0.094 m	0.094 m	0%
L_{hot}	0.686 m	0.0876 m	-87.2%
$L_{no-flow}$	0.256 m	0.0944 m	-63.3%
M	19.4 kg	1.13 kg	-95.3%
COP	53	24.5	-54.7%
ε	0.9	0.93	+3.0%

3.6.1 M2HX Design Enhancement

It was reported by Arie [60] that straight manifold channels, as shown in Figure 3-1, may induce a large maldistribution when the number of microchannels is high (N_{chn}>45), which makes the assumption of uniform flow distribution invalid for the numerical model discussed in Section 3.4. Therefore, the manifold channels on both hot and cold sides will be designed as tapered channels, as shown in Figure 3-8, to better control the maldistribution.

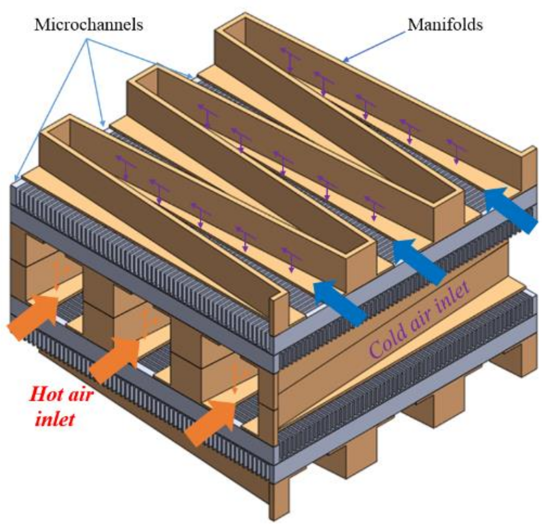

Figure 3-8: Gas-to-gas cross-flow Tapered M2HX conceptual design

As shown in Figure 3-8, the flow area in the inlet manifold-channels decreases longitudinally as more flow is fed into the microchannels. The opposite process occurs for the outlet manifold-channel, where the flow area increases as more flow leaves the microchannels.

3.6.2 4” x 4” x 4” M2HX Unit

The 4” x 4” x 4” M2HX unit based on the scale-down procedure described and the design enhancement is shown in Figure 3-9.

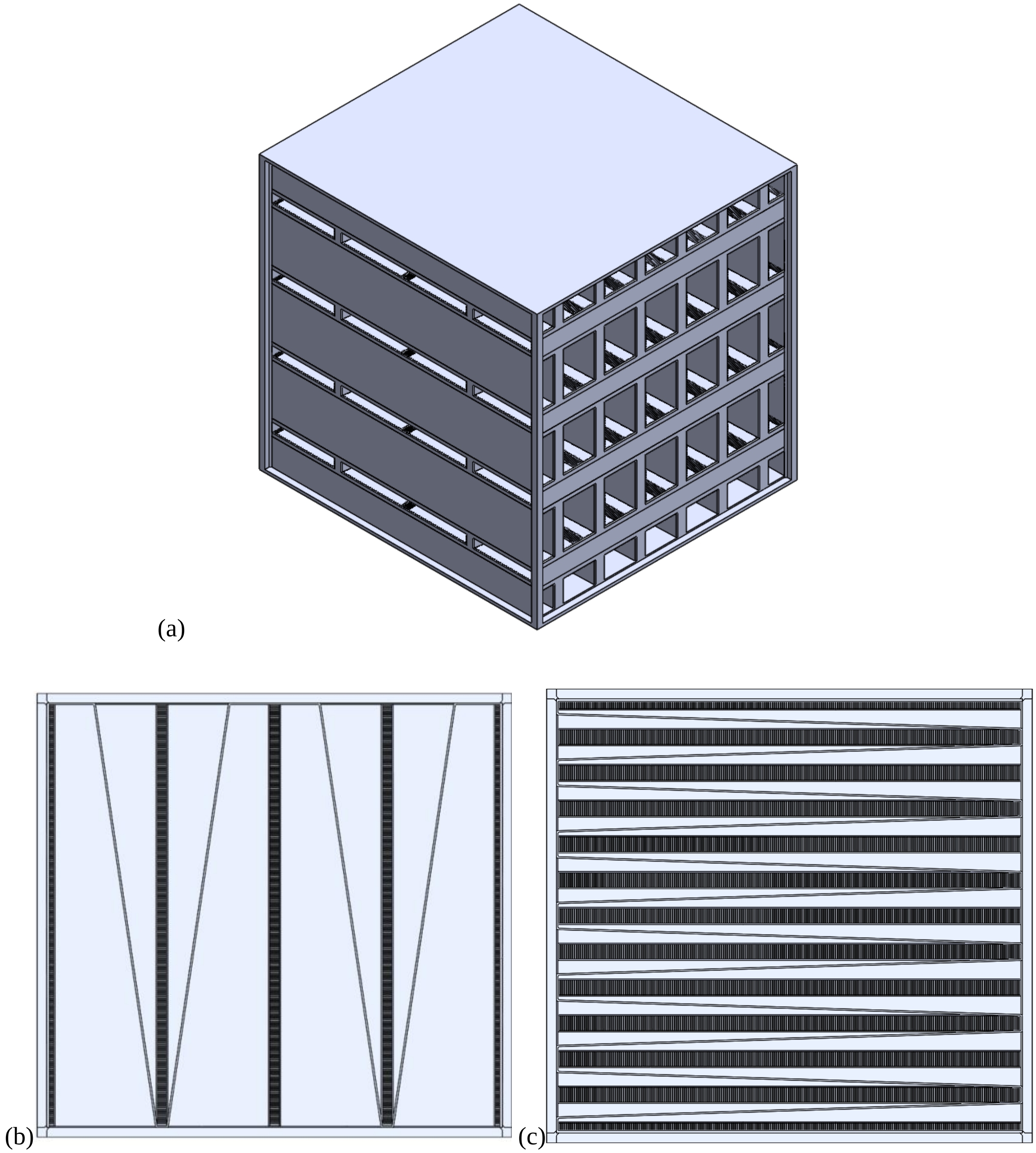

Figure 3-9: 4" x 4" x 4" M2HX unit (a) isometric view, (b) hot-side section, (c) cold side section

Figure 3-9(a) shows the isometric view of the 4" x 4" x 4" M2HX unit, while Figure 3-9(b) and Figure 3-9(c) show the cut sections of the hot- and cold-side, respectively. Those cut sections are taken at $H_{mnd}/2$ and show the manifold design of the two sides. W_{in} openings also show the number of fins and the microchannel structure.

3.7 Summary

In this chapter the design requirements for the high temperature heat exchanger were presented based on the operating and physical specification provided by an aerospace company for an aerospace turbofan pre-cooler. Manifold-microchannel technology was selected for the heat exchanger design because it has shown superior heat removal density (kW/kg) at moderate pressure drops, compared to state-of-the-art heat exchangers. A single-objective optimization (minimization of mass at given mass flow rates, pressure drops and effectiveness) for the gas-to-gas cross-flow manifold-microchannel heat exchanger was performed, leading to a mass reduction of 9.7% compared to the target. The details of the optimum design, including the performance improvement, were listed. Lastly, the optimized full-scale heat exchanger was scaled down for fabrication and experimental testing.

Chapter 4 : Test Print Coupons and Subscale 4” x 4” x 4” Unit Fabrication

4.1 Introduction

This chapter first discusses the possible alternatives for the printing orientation of the subscale unit obtained in the previous chapter. Once assessed the optimal printing orientation, test print coupons were fabricated to evaluate the printing capability of different 3D-machines. The coupon’s geometry was designed to study the outcomes of key parameters for manifold-microchannel heat exchanger: fin thickness and base plate thickness. Different printer settings were varied to study their role in the build quality. Based on the outcomes of the coupons’ study, several units of increasing volume were printed, concluding with the 4”x4”x4” subscale unit made out of Inconel 718.

4.2 Conventional Fabrication Overview

The conventional fabrication process of a M2HX involves multiple steps, since the microchannel surfaces and manifolds have to be fabricated separately. For the microchannel surface, if the flow configuration of the HX is parallel- or counter-flow, it can be fabricated through micro deformation technology (MDT). As a non-subtractive manufacturing method, MDT employs a fixed tool which mechanically and plastically deforms the work piece to form finite and repeatable channels [168]. However, if the M2HX has a cross-flow configuration as the case under analysis, either photo-chemical etching or laser micro-machining is needed for the double-side cross-flow microchannel surface’s fabrication. Photochemical etching is usually used to fabricate microchannel surfaces for PCHXs to form semi-circular channels with typical channel width of 0.50-2.00 mm [169]. Laser micro-machining is another approach to fabricate a double-side cross-flow microchannel surface. By applying a high power laser beam, energy of the laser is converted to heat which vaporizes or melts the metal material to form the microchannel structure [170]. However, laser micro-machining is a very time-consuming process as it may take up to 2 days to fabricate one 389 × 132 × 1.3 mm^3 size microchannel surface [171]. Depending on the complexity of the manifold’s geometry, CNC machining, sheet metal forming, and injection molding can be applied for the manifold's fabrication. Considering the fabrication time and cost, CNC machining is a good approach for prototyping while sheet metal forming and injection molding can be used for mass production. Since a M2HX generally consists of many layers of manifolds and microchannel surfaces, brazing, welding, or diffusion bonding are needed to assemble the parts. Due to the small size of the microchannels, improper brazing or welding between the manifold and microchannels can cause clogging in the microchannels which can reduce the heat transfer performance and increase the pressure drop significantly. If diffusion bonding is used, in order to meet the parallel and flatness requirements for the bonding surfaces, considerable effort is required to post-process the microchannel surfaces and manifolds.

To address the challenges in fabrication of M2HX through conventional methods, the use of DMLS is proposed. A M2HX with either parallel-/counter-flow or cross-flow configuration can be 3D printed as a single unit without any assembly process through the AM approach, which also reduces the fabricating lead time significantly.

4.3 M2HX's Fabrication Orientation with AM

Overhang occurs when the next layer in the printing direction is larger than the previous layer without adding a support structure during the 3D printing process.

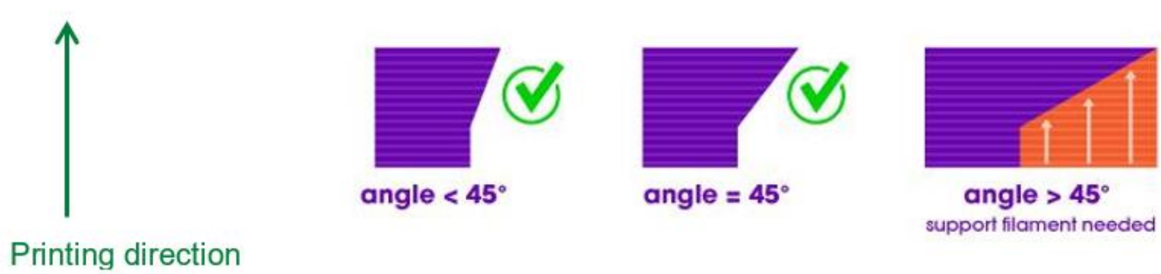

Figure 4-1: Overhang effect on printability [172]

As shown in Figure 4-1, overhang is tolerable till an angle of 45° with respect to the printing direction, while for angle above 45° a supporting structure is needed to avoid the part to fail. Overhang is therefore a big challenge for M2HX's fabrication through DMLS, which can cause a fabrication failure if not properly oriented. For a cross-flow M2HX, depending on the 3D printing orientation, the overhang issue will either occur at the manifold base and microchannel fins as shown in Figure 4-2 (a), or at the manifold walls and microchannel fins as shown in Figure 4-2 (b). Considering the complexity of M2HX's geometry, no support structure should be used on the interior of the HX during the fabrication. Therefore, the M2HX needs to be modified such that all structures can be self-supported to avoid overhang during the fabrication process.

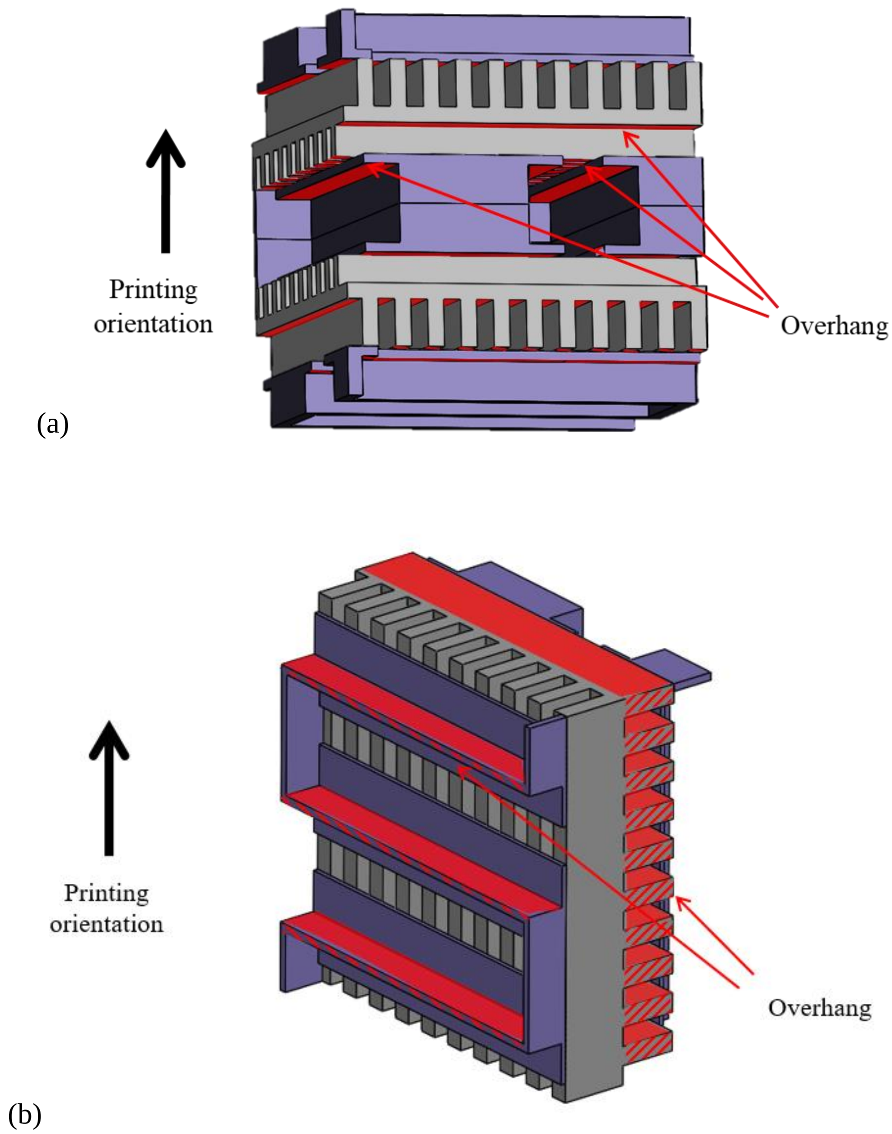

Figure 4-2: Overhang issue with cross-flow M2HX: overhangs at the manifold base and microchannel fins (a); overhangs at the manifold walls and microchannel fins (b)

In order to successfully print M2HXs using DMLS, fins' angle with respect to the build plate should not be less than 45°. Otherwise, support structure will need to be added. Since support removal from the interior structure of M2HXs is not possible, fins should be placed in more than 45° angle. A cross flow M2HX consists of fins in both the hot and cold sides, which are perpendicular to each other as shown in Figure 3-1. As studied by Zhang et al. [120], it is very challenging to print a M2HX if the printing orientation shown in Figure 4-2 (a), is chosen. Therefore, for successful fabrication of the M2HX there are two alternatives. First, using printing orientation of Figure 4-2 (b), it is possible to change the orientation of the features of the M2HX (see Figure 4-3 (a)), thus both inclined fins and inclined manifold walls have a self-supporting angle of 45°, avoiding the problem of the overhanging. Second, fabricate the entire M2HX at 45° angle with respect to the build plate (see Figure 4-3 (b)).

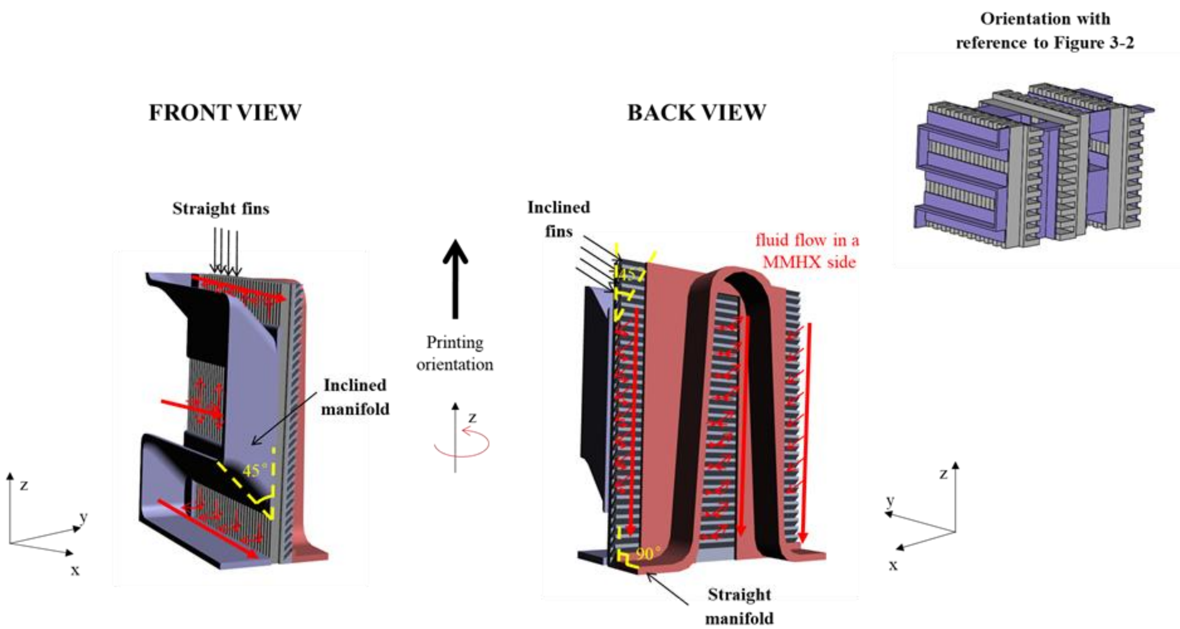

(a)

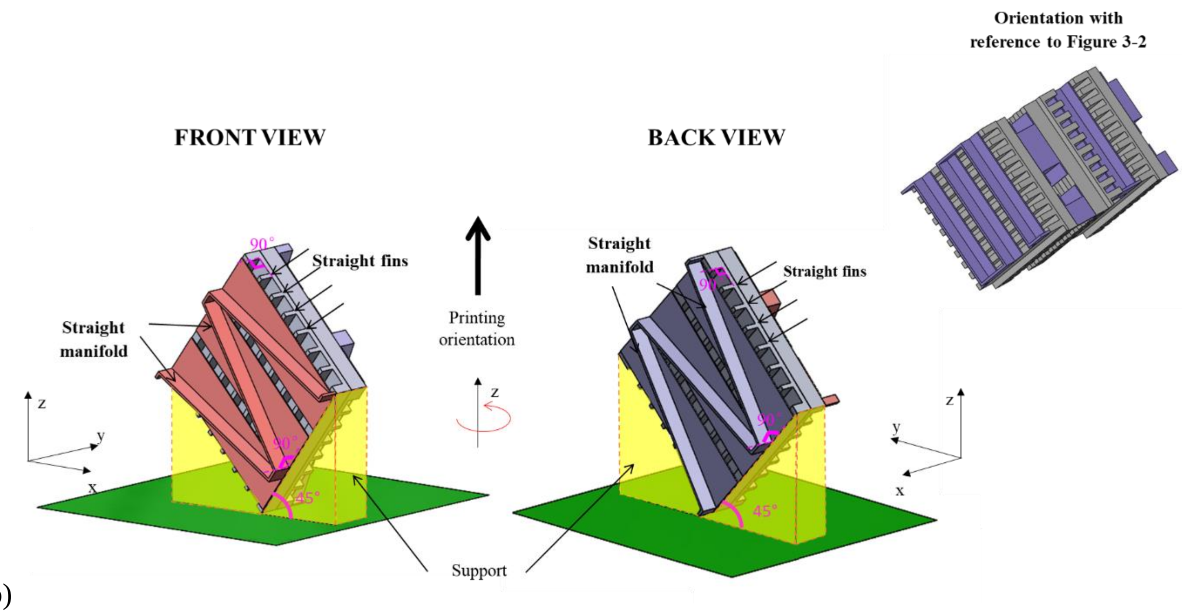

(b)

Figure 4-3: M2HX alternatives to avoid overhang. (a) Inclining fins on one side and inclining manifold on the other side (b) double view of fabrication at 45° angle with respect to the build plate

To fabricate the 3D printed M2HX, Zhang *et al.* [120] implemented inclined fins on one side and inclined manifold walls on the other side, as shown in Figure 4-3 (a). Despite the possible printability of the HX, this solution affects the flow in the HX, thus leading to the similar heat duty as the straight channel, but higher pressure drop. The detailed description of the effects of this printing orientation on performance can be found in Ref. [120]. Moreover, when selecting the configuration of Figure 4-3 (a), the fins on the two sides of the HX might have different thicknesses due to the different orientation.

Instead of modifying the structures within the HX, the entire unit can be oriented at a 45° angle with respect to the build plate, as shown in Figure 4-4 (a). In this orientation, unsupported overhang inside of the HX can be avoided by adding supporting structures outside as shown in Figure 4-4 (b)-(d).

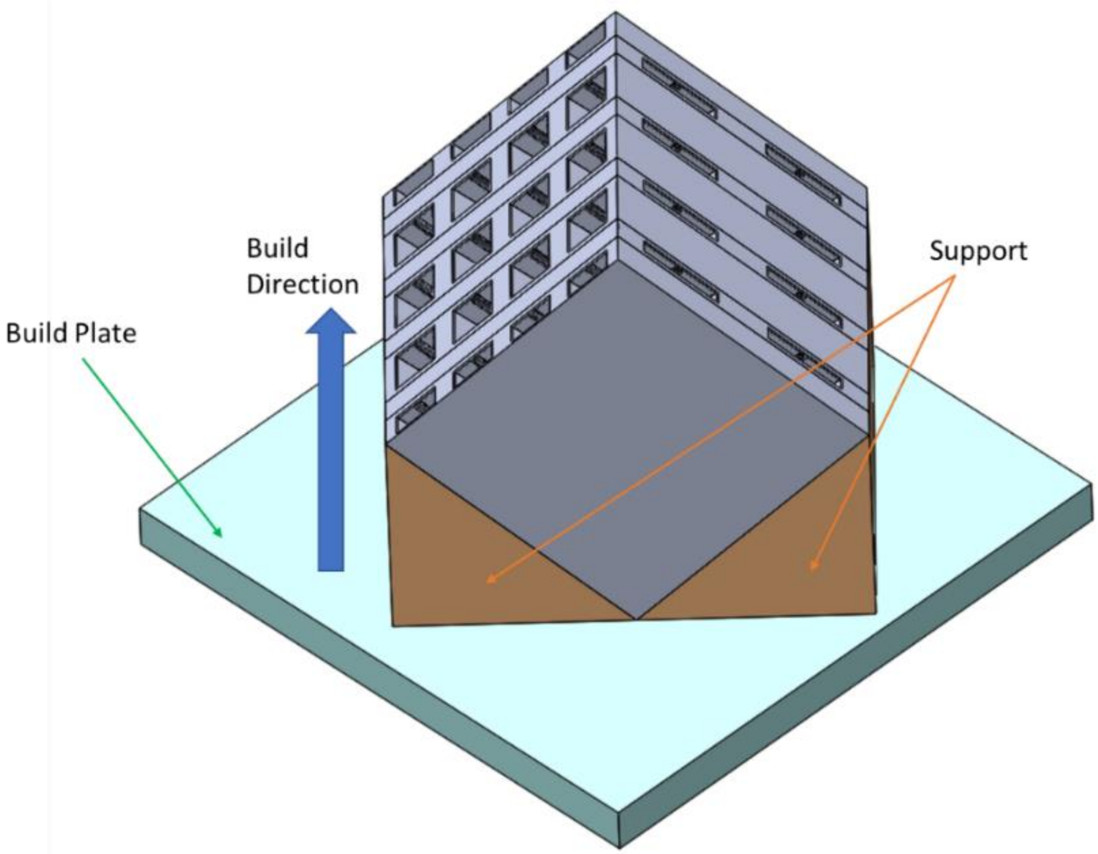

(a)

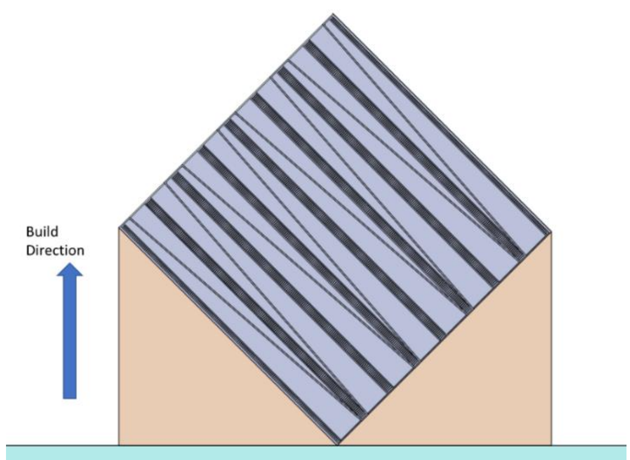

(b)

(c) 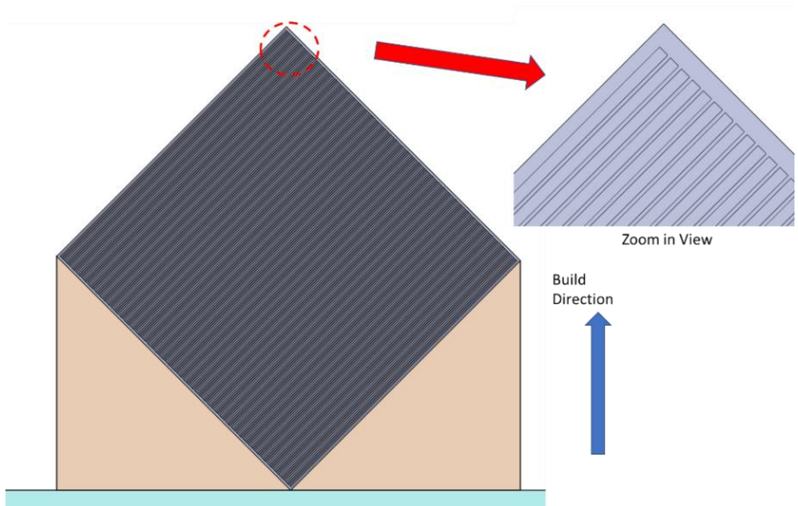

(d) 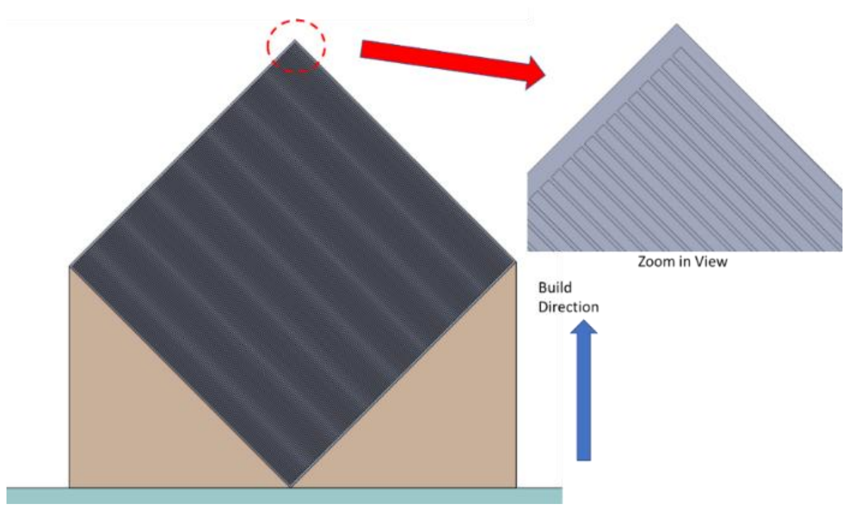

Figure 4-4: Inclined printing orientation for M2HX: (a) Complete View (b) Cross-section view of manifold (c) Cross-section view of cold side fins (d) Cross-section view of hot side fins

The first advantage of printing in this orientation is to allow for fabrication of straight fins and manifold channels. As mentioned previously, when the fluid flows in the microchannel following the ideal MMHX configuration of 90° turns, the pressure drop in the microchannels is smaller compared to the inclined fins. Moreover, the 45° inclined printing orientation allows higher fin density to be printed compared to the printing orientation and design inclination adopted in the solution of Figure 4-3 (a) To better explain this statement, Figure 4-5 provides a visualization of the printing process that occurs during the solutions of Figure 4-3 (a) and (b). The figure shows the sequences of layers that are used to create the desired designs:

a hatched area represents the portion of the layer in which the powder has been sintered, while the non-sintered one is left blank.

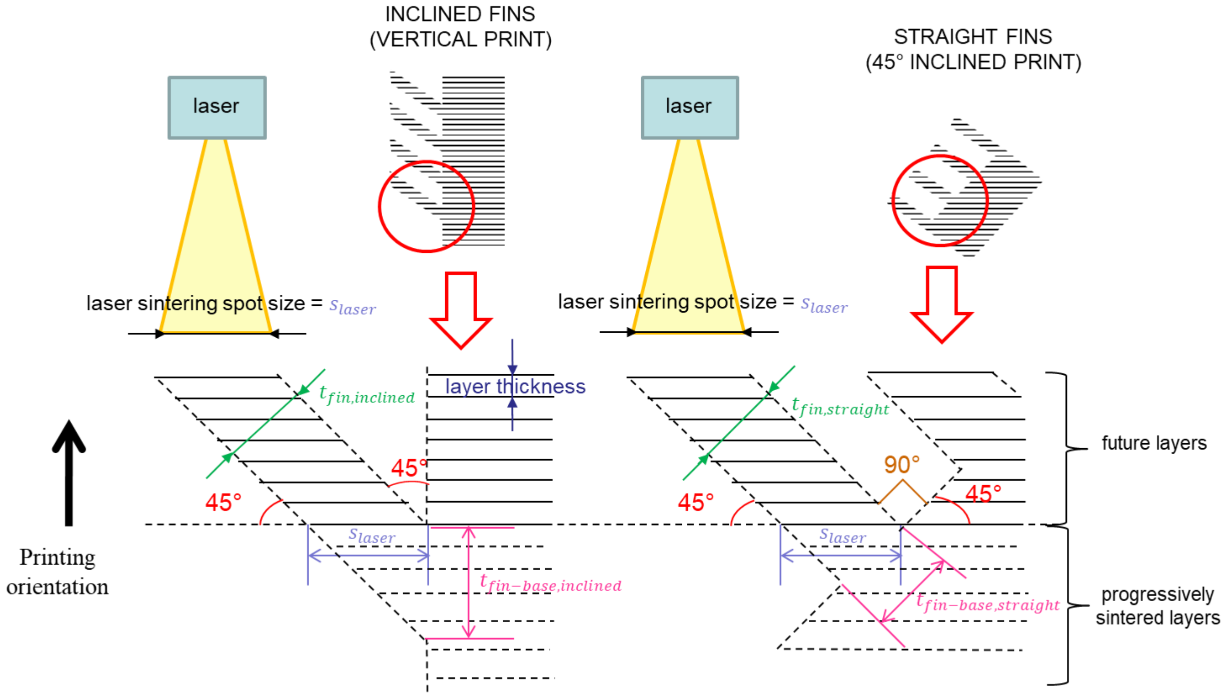

Figure 4-5: Comparison of the inclined fin size of M2HX printed using Figure 4-3 (a) solution and fin size of M2HX using Figure 4-3 (b)

Figure 4-5 shows that in both cases the fins are built with an inclination of 45° with respect to the horizontal line. To have a fair comparison, the same printer is adopted, thus leading to the same laser sintering spot size (s_{laser}) and same fin thickness (t_{fin}), as a result:

$$t_{fin,inclined} = \frac{s_{laser}}{\sqrt{2}} = t_{fin,straight} \qquad (8)$$

The difference between the two configurations in Figure 4-5 is the angle between the fin and the base. For the inclined fin solution, the thickness of the fin measured at the base ($t_{fin-base}$) can be obtained from

$$t_{fin-base,inclined} = \sqrt{2}t_{fin,inclined} \qquad (9)$$

In contrast, inclining the entire HX, the angle between the base and the fin is 90°. As a result, the straight fins are characterized by:

$$t_{fin-base,straight} = t_{fin,straight} \tag{10}$$

and combining equations (8)-(10)

$$t_{fin-base,straight} = \frac{t_{fin-base,inclined}}{\sqrt{2}} \tag{11}$$

Thus, for the same fin thickness (t_{fin}), the space occupied at the base with straight fins obtained by changing the inclination of the print to a 45° orientation ($t_{fin-base,straight}$) is 30% less than the vertical print with the inclined fins ($t_{fin-base,inclined}$). This demonstrates the possibility of printing higher fin density surfaces with the orientation shown in Figure 4-3 (b). This analysis is valid for both sides of the M2HX, thus allowing the HX to have the same fin thickness (t_{fin}) on both sides.

4.4 Fin Thickness Study

Arie [60] demonstrated that the performance of an MMHX design with a printable minimum fin thickness of 0.15 mm can significantly surpass that of most conventional designs: for example, up to nearly 60% increase in gravimetric heat transfer density (kW/kgK) is achieved when compared to a wavy fin design. In order to evaluate the capability of AM to fabricate M2HX with small fin size, multiple coupons with different fin thicknesses and channel sizes were fabricated using different 3D printer machines. These coupons were fabricated in the same orientation as the subscale M2HX (see Figure 4-4), to be representative of the final HX. The coupon consists of fins with three different sizes: 0.100 mm, 0.125 mm, and 0.150 mm. They are separated by a thick wall for convenience of measurement. Fins' spacing is set to be 0.260 mm for all cases, thus the channels' width varies between 0.110 mm, 0.135mm, and 0.160 mm for section with fin thickness of 0.150 mm, 0.125 mm, and 0.100 mm respectively. A schematic drawing of the fabricated coupon and its printing orientation are shown in Figure 4-6 (a).

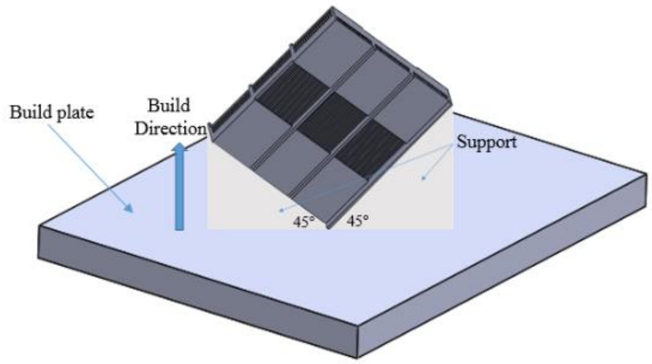

(a)

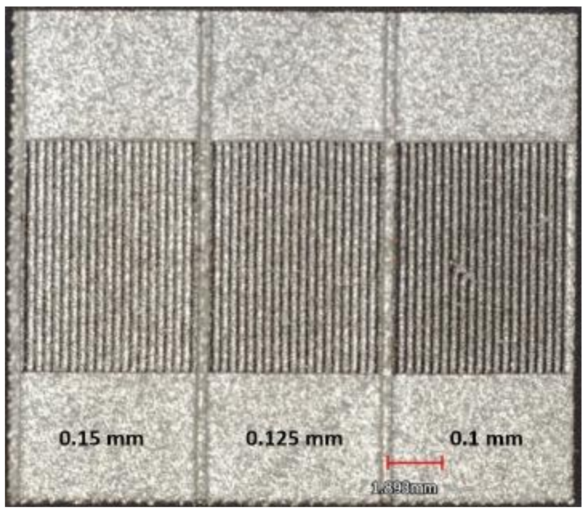

(b)

Figure 4-6: (a) Build orientation for fin thickness study coupon and (b) image of the printed coupon for fin thickness study

Multiple coupons were fabricated using a ProX DMP 200 [173], a ProX DMP 300 [174], and an EOSINT M 290 3D printer [175]. Table 4-1 lists the material used for each printer, the maximum printer build size and the layer thickness. The layer thickness is a measure of the layer height of each successive addition of material in the 3D printing process in which layers are stacked. Layer height is essentially the vertical resolution of the z-axis [176], as shown in Figure 4-5. Figure 4-7 shows the fabricated fin thickness compared to the design fin thickness used to create the CAD file for the different 3D printers.

Table 4-1: Printers details including material used, maximum build size and layer thickness

Printer Model	Material	Printer build size [inch^3]	Layer thickness [µm]	Code Name
ProX 200	Maraging Steel	5.51 x 5.51 x 4.92	30	ProX 200
ProX 300	Inconel 718	9.84 x 9.84 x 13.0	40	ProX 300 (Inc718)
ProX 300	Inconel 625	9.84 x 9.84 x 13.0	40	ProX 300 (Inc625)
EOS M290	Inconel 625	9.85 x 9.85 x 12.8	40	EOS M290 (40 µm)
EOS M290	Inconel 625	9.85 x 9.85 x 12.8	20	EOS M290 (20 µm)

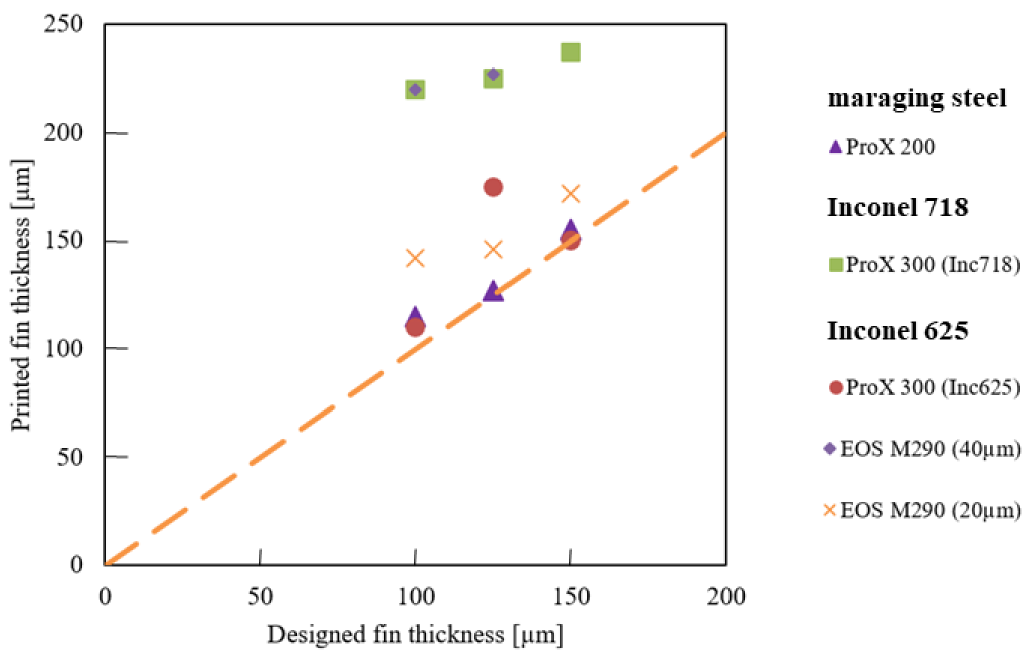

Figure 4-7: Printed fin thickness versus design fin thickness for different 3D printer machines

Figure 4-7 shows that ProX 200 machine has the closest agreement between the design fin thickness and actual fin thickness for the maraging steel. This result can be understood by checking the information reported in Table 4-1. First, the printer has a smaller build volume, meaning the distance between the laser and the build plate is smaller, compared to the other printers. This allows a higher resolution in the printing feature. Second, the layer thickness is smaller than the conventional 40 µm. Third, ProX 200 was the only in-house printer and a parameters customization was possible to enhance the feature resolution. Despite these promising results, maraging steel is not suitable for high-temperature applications which require superalloy materials. The printer was used as an initial test because it is located at the University of Maryland, College Park (MD) and it is easily accessible for the author of this work. Despite these promising results, maraging steel is not suitable for high temperature applications which require superalloy materials. Maraging steel, in fact, has a maximum service temperature of 400°C. On the other hand, given the need for a bigger printer to accommodate bigger HXs (since the build orientation negatively affects the build size requirement), other machines and different materials were tested. ProX 300 machine has been investigated in two different configurations. ProX 300 (Inc625) showed a small deviation from the fin design values for 0.100 and 0.150 mm, but a significant deviation for 0.125 mm. This lack of consistency in the printer can become an issue when printing bigger parts. On the other hand, ProX 300 (Inc718) showed a more consistent trend, but the deviation from the desired values has to be carefully taken in consideration during the design stage: knowing that the printed part will be bigger than the CAD file, the features need to be designed smaller to mitigate the deviation. A similar trend was also shown by EOS M290 (40µm).

4.4.1 Layer thickness Effect on Fin Size

As shown in Figure 4-7 when comparing EOS M290 (40µm) with EOS M290 (20µm), a significant improvement in the fin thickness can be obtained when reducing the layer thickness. Changing the layer thickness of Inconel 625 from 40 to 20 µm allows for fabrication of feature with much smaller deviation. Both powder sizes show consistency in the trend, making EOS M290 a more robust machine, which requires smaller layer thickness to get the same results in terms of fin resolution.

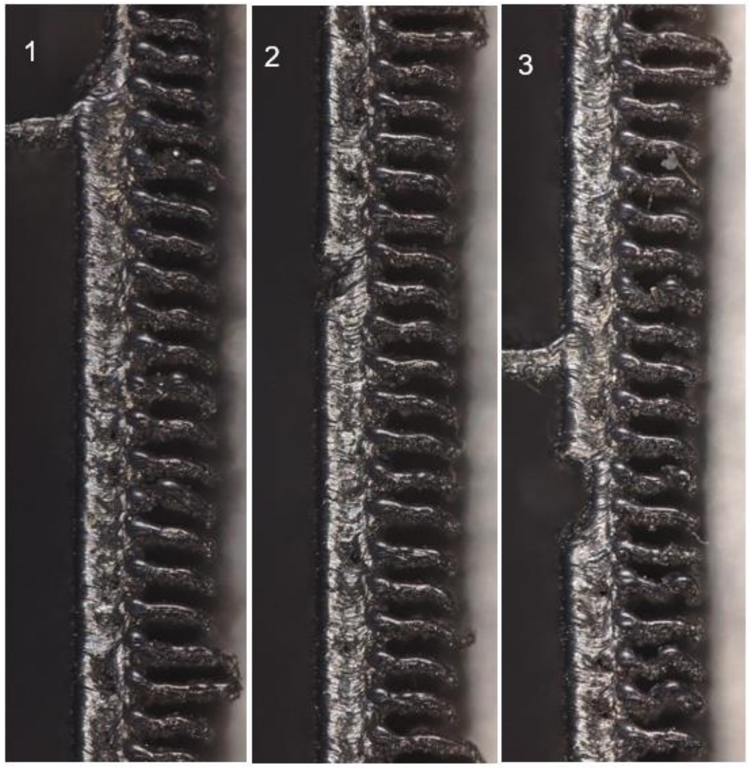

Figure 4-8: Additively manufactured microchannels using M290 (20µm) with different fin thickness: 0.100 mm (1); 0.125 mm (2); 0.150 mm (3)

As shown in Figure 4-8, three coupons were 3D printed through the EOS M290 (20µm) machine, and analyzed using Keyence 3D digital microscope at University of Maryland, AM Center. Based on the measurements reported in Figure 4-7, the difference of the actual fin thickness compared to the design value can be quantified as ~20 µm for the design values of 0.150 mm and 0.125 mm, and as ~40 µm for the design values of 0.100 mm. The deviation is 13% for the design values of 0.150 mm, 15% for 0.125 mm and 35% for 0.100 mm. The drawbacks of reducing the powder size are longer printing time (double, if halving the powder size) and higher cost, due to more expensive powder and longer printing time. Smaller powder size should therefore be selected only in those cases where fin thickness reduction and consistency are needed.

4.4.2 Laser Power Effect on Fin Size

Printing parameters can be adjusted by machine operator and can significantly affect the quality of the printed parts [177]. Laser power is a crucial factor that affects the fabrication quality of the parts, printed using DMLS. The effect of laser power on the fins' thickness was investigated through printing multiple single manifold-microchannel coupons using maraging steel for the ProX 200 at University of Maryland, College Park, as shown in Figure 4-9 (a). Six coupons were fabricated with three different fin sizes and two different laser power settings, as shown in Figure 4-9 (b).

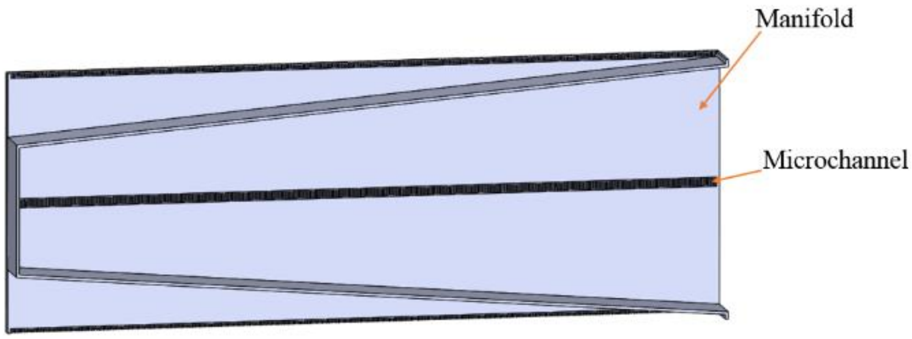

(a)

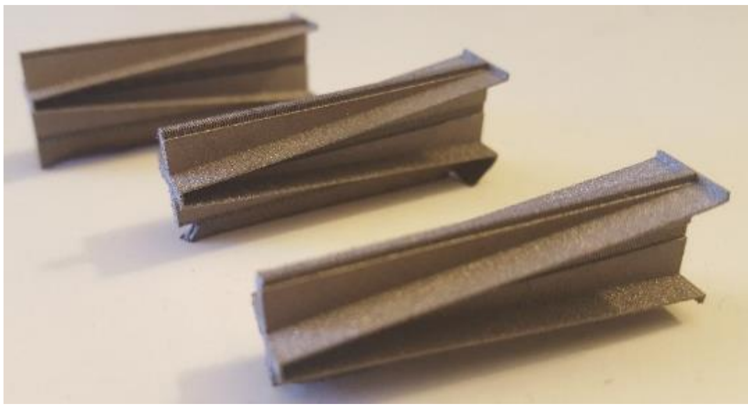

(b)

Figure 4-9: (a) CAD model of a single manifold-microchannel, and (b) Picture of single manifold-microchannel fabricated at different laser power

Table 4-2 shows design fin thickness and fabricated fin thickness which were fabricated using 300 and 225 W laser power setting in ProX 200 machine.

Table 4-2: Effect of laser power on the fin size

Design fin thickness [μm]	**Actual fin size at 300 W laser power [μm]**	**Actual fin size at 225 W laser power [μm]**
100	133	115
125	156	131
150	188	157

From Table 4-2, it can be concluded that smaller fins size can be fabricated using smaller laser power. This is due to the fact that, the higher the laser power, the larger the melting pool, and the more difficult it is to fabricate fine features. As a drawback, the porosity of the part can be higher and lead to leakage when tested under the design pressure. Figure 4-10 shows the microscopic image of the fins of 115 µm size.

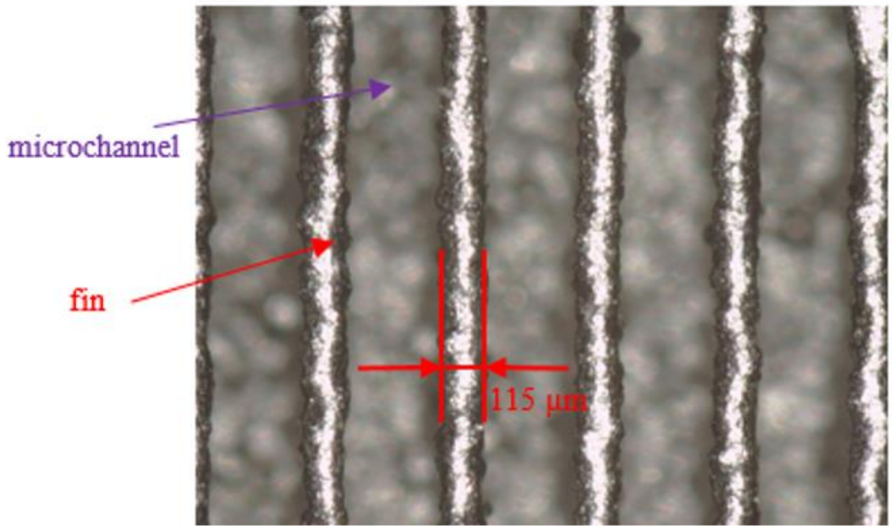

Figure 4-10: Microscopic image of the fins with 115 µm thickness

4.5 Base Thickness Study

In addition to the minimum printable fin thickness, another important design limitation is the minimum base thickness or separator plate (the distance between the microchannel base which separates the hot and cold flow streams) that is required to withstand the HX design operating pressures on the hot and cold sides. Ideally, the smaller the base thickness, the higher the HX performance, both in terms of thermal performance and mass reduction. Reducing the base thickness reduces the thermal resistance due to the conductive wall resistance, while also reducing the total mass of the HX. At the same time, a reduction in the base requirements positively affect the total mass of the HX. However, one of the biggest challenges with DMLS's application to HXs' fabrication is to deliver a leak-free product, which guarantees perfect sealing between the hot and cold sides as well as to the ambient. The minimum base thickness requires specific study considering the porosity issue of thin wall structure during the sintering process of DMLS.

In fact, there are some limitations faced when using AM: the part is obtained by sintering metal powder into a single structure and during this process some impurities can be trapped in the structure and porosity can affect the product quality. This may result in a final component that withstand pressure requirements differently, or less than the component fabricated conventionally from bulk material. As reported by Zhang *et al.* [120], the first M2HX fabricated for aerospace application through DMLS using Inconel 718 has a microchannel base thickness of 500 µm, and is leak-free under a system pressure of 4.5 bar.

To further investigate the minimum base thickness and reduce it without introducing leakage issues, several coupon designs were 3D printed. As shown in Figure 4-11, each coupon consists of a chamber whose testing walls are parallel to the x-z plane, while the other walls are 500 µm thick, which already proved to be leak free.

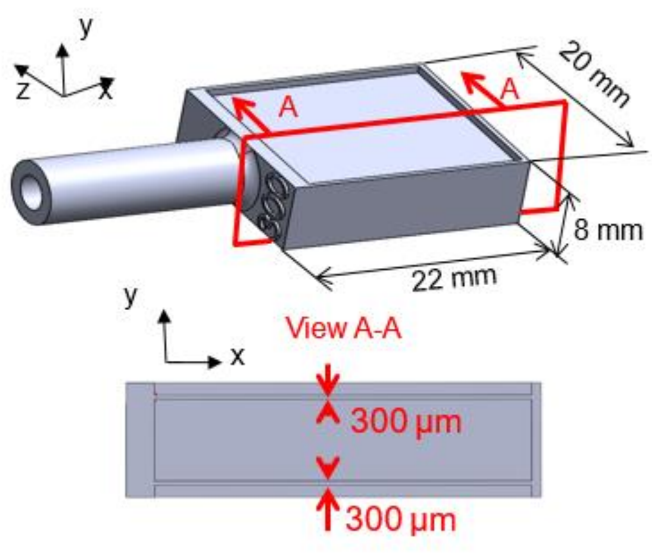

Figure 4-11: Coupon design for minimum microchannel base thickness investigation

Beside the chamber, each coupon was also designed with a pipe for connection to the pressurized system. The fittings were machined to guarantee perfect sealing during the pressure containment test. The printers selected for this study were the ones giving the most consistent results during the fin thickness study: ProX 300 (Inc718) and EOS M290 (20µm). Each machine printed three coupons, of chamber walls of respectively 300, 350 and 400 µm, as reported on each coupon (see Figure 4-12).

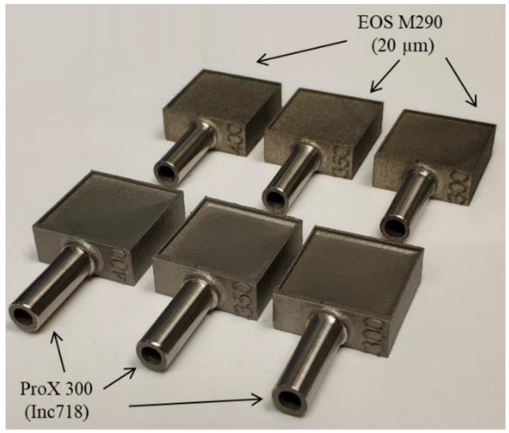

Figure 4-12: Pressure check coupon sets. Front line set: ProX 300 (Inc718), back line set: EOS M290 (20µm)

4.5.1 Layer Thickness Effect on Base Thickness

The six coupons were pressurized under the design condition reported in Table 3-2, using nitrogen as test medium. The test results are shown in the Table 4-3 below.

Table 4-3: Results of pressure containment check coupons

Design base thickness	ProX 300 (Inc718)	EOS M290 (20µm)
300 µm	Small leakage	No leakage
350 µm	No leakage	No leakage
400 µm	No leakage	No leakage

As reported in Table 4-3, EOS M290 (20µm) proved the capability of printing three pressure tight coupons, demonstrating dense structures for the three selected base thicknesses. ProX 300 (Inc718) failed in the smallest base thickness selected. As expected, moving from 40 -to 20-µm layer thickness proved to give better results. The requirement to lower the layer thickness to obtain leak proof HXs, varies based on the pressure selected. For the current study, the selected pressure of 340 kPa necessitated moving from 40 to 20 µm layer thickness, when printing base thickness smaller than 350 µm.

A direct measurement of the base thickness is not possible without cutting the coupons. The “indirect” method used to validate the printed base thickness was based on the volume check of the coupons. The volume of the coupons was measured using Archimede’s principle through a precision dynamometer. The liquid used for these measurements was ethyl-alcohol 200 proof. Having a lower surface tension than water, ethyl-alcohol 200 proof becomes a better choice, making sure that air microbubbles do not attach to the internal parts, thus compromising the results. The volume calculated was then compared to the design volume. For both printers, the deviation from design to actual volumes was in the order of 2-3%, which falls under the uncertainty of the measurements (in the order of 3%). The base thickness is so confirmed and the pressure containment results validated.

4.6 Surface Finish

One of the possible drawback of AM is the surface finish. Compared to conventional machining, in fact, the surface roughness can be higher and cause issues in some applications. Moreover, adopting a build angle different from the most common vertical one (as the suggested orientation for the M2HX implies) can cause the surface to be even rougher.

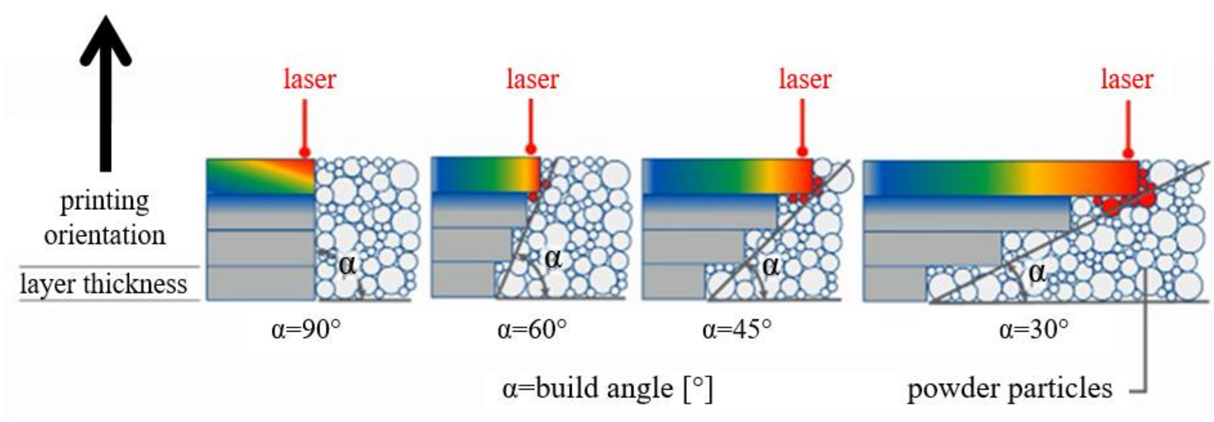

Figure 4-13: Surface roughness for AM part

As shown in Figure 4-13, in fact, the smaller build angles create larger layer to layer overhangs of solidified metal over the loose powder, causing the surrounding powder to be sintered or melted into the solid layer.

In the HXs field, higher roughness is usually connected to higher pressure drop. In the case of M2HXs, however, the flow in the microchannels is laminar and roughness does not affect the pressure drop in this region. On the contrary, rougher surface can be considered as surface augmentation and promotes breaking the boundary layers, thus increasing the thermal performance.

In order to evaluate the surface finish capability of the selected printers, the pressure test coupon surfaces were analyzed using Keyence 3D digital microscope at University of Maryland, AM Center.

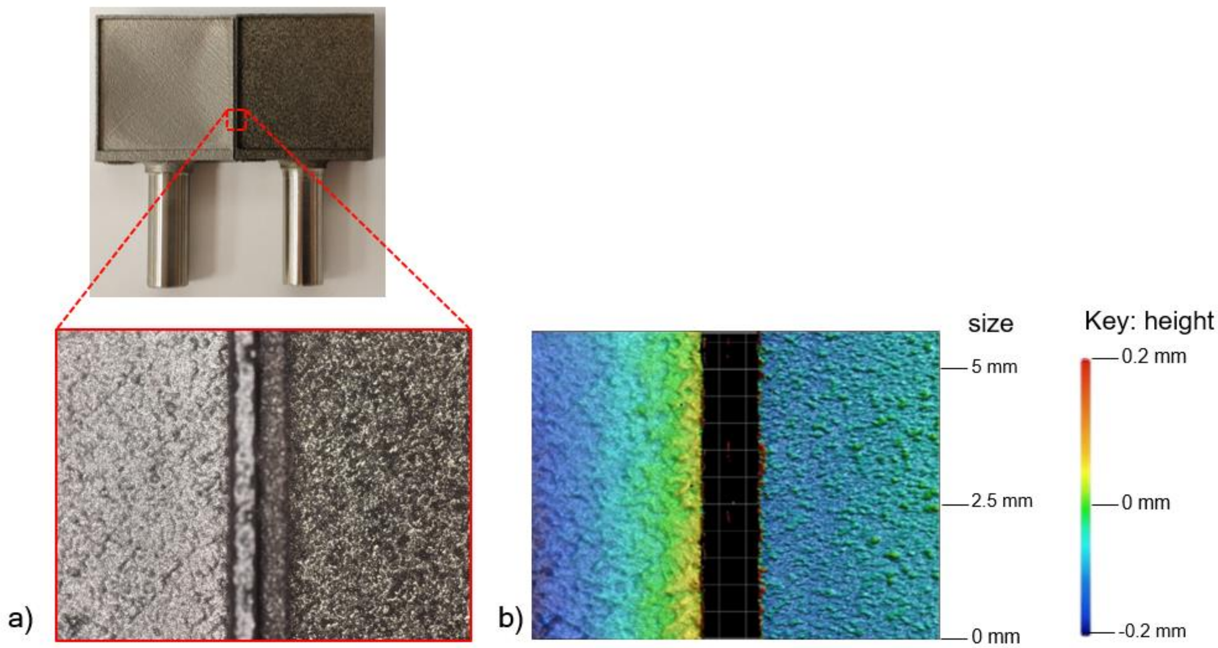

Figure 4-14: (a) Coupons roughness comparison: left - ProX 300 (Inc718), right -EOS M290 (20μm), (b) 3D rendering of the two coupons: left - ProX 300 (Inc718), right -EOS M290 (20μm)

Figure 4-14 shows the surface roughness of two coupons printed with ProX 300 (Inc718) and EOS M290 (20μm). The 3D rendering in Figure 4-14 shows that ProX 300 (Inc718)'s surface is smooth, but it is irregular closer to the edge. EOS M290 (20μm), on the contrary, is more uniform but spots with different height are visible throughout the surface, thus increasing the roughness. In order to quantify the surface finish, the two printers were evaluated on the basis of the following surface properties:

- Root mean square height (Sq), represents the root mean square value of ordinate values within the definition area.

- Arithmetic mean peak curvature (Spc) represents the arithmetic mean of the principal curvature of the peaks on the surface. A smaller value indicates that the points of contact with other objects have rounded shapes, while a larger value indicates that the points of contact with other objects have pointed shapes.
- Developed interfacial area ratio (Sdr) is expressed as the percentage of the definition area's additional surface area contributed by the texture as compared to the planar definition area. The Sdr of a completely level surface is 0, while when a surface has any slope, its Sdr value becomes larger.

Table 4-4: Surface finish results of the pressure check coupons

Printer	**Sq [mm]**	**Spc [1/mm]**	**Sdr [-]**
EOS M290 (20µm)	0.015	4.90	0.0138
ProX 300 (Inc718)	0.009	1.77	0.0049

The results of the study are reported in Table 4-4. As observed from Figure 4-14, ProX 300 (Inc718) surface is smoother and the points of contact with other objects have rounded shapes. On the other hand, EOS M290 (20µm) surface augmentation is slightly higher.

4.7 M2HX Units Fabrications

Based on the information collected, M2HXs fabrication was performed through multiple steps from small HX units till the subscale HX designed in the previous chapter.

4.7.1 Preliminary M2HX Units Fabrication

Figure 4-15 shows three M2HXs fabricated out of maraging steel using ProX 200 at the University of Maryland - College Park, AM Center.

Figure 4-15: Image of the (a) 1”×1"×1", (b) 2”×2"×2", (c) 3”×3"×3" M2HX unit fabricated out of maraging steel

Before fabricating the 3” x 3” x 3” size M2HX, which is the maximum build size capability of ProX 200, Multiple coupons were fabricated from small to larger size.

The role of these M2HXs is to study if the results applied at the coupons level can be extended to the real unit, which means that scaling-up does not affect the results. This consideration is crucial in the current study because proving that the subscale is printable can be used to assess that also the fabrication of the full-scale unit will be feasible.

To investigate whether the HX was leak free, the 1” x 1” x 1” M2HX was fabricated and leak tightness was proven through a leakage test, based on pressurizing the HX with nitrogen. Based on this promising result, two larger M2HXs with the size of 2” x 2” x 2” and 3” x 3” x 3”were fabricated.

In order to investigate the quality of the fabricated M2HX, the 2” x 2” x 2” M2HX was cut. The cut section image is shown in Figure 4-16. By analyzing the cross section view, it can be seen that the fins are successfully fabricated without clogging or defects.

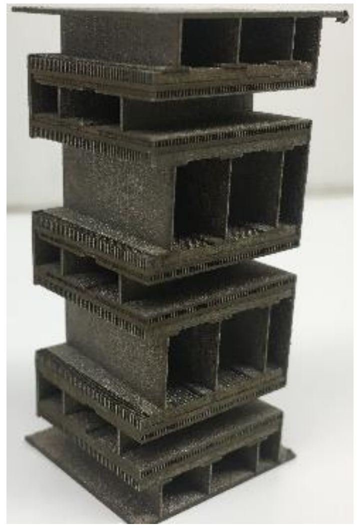

Figure 4-16: Cut view of 2” x 2” x 2” M2HX (Figure 4-15(b))

Based on the knowledge learned from the fin thickness study, the fins were designed at 0.100 mm. The fin size of the three maraging steel M2HXs were measured to be between 0.110 and 0.130 mm, which is consistent with the results of the fin thickness study.

The 3” x 3” x 3” size M2HX was used to study the support of the unit and the orientation with respect to the recoater direction. The support is the same as the one designed in Figure 4-4.

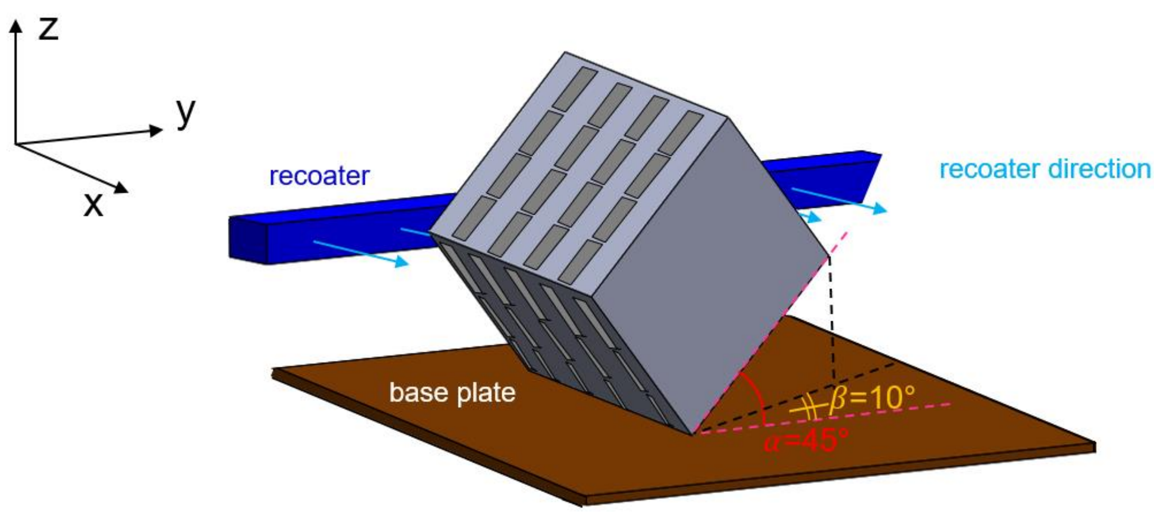

Figure 4-17: HX unit orientation with respect to the base plate

Figure 4-17 shows that beside the previously mentioned 45° angle in the y-z plane (identified with α in Figure 4-17), another 10° angles was given to the unit in the x-y plane (identified with β in Figure 4-17). The reason for this choice was to avoid that the recoater hits the entire size of the HX perpendicularly to the recoater direction, as shown in Figure 4-18. Introducing this angle β, the subsequent fronts in the recoater direction impact progressively larger portions of the unit, thus reducing the stress of the impact and increasing the chance of a successful print.

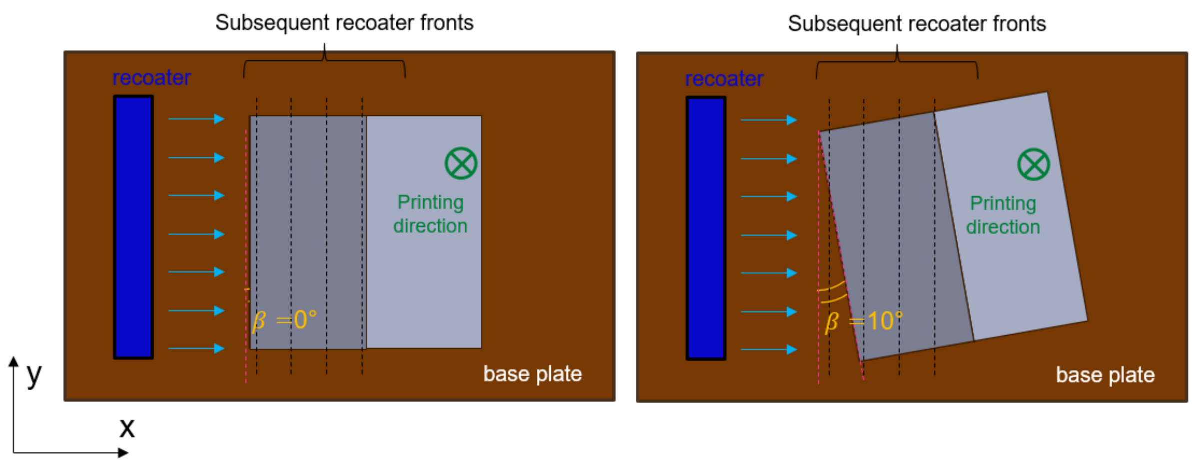

Figure 4-18: Top view of Figure 4-17 showing the effect of angle β during the printing (manifold openings are omitted to simplify the drawing)

4.7.2 Subscale 4” x 4” x 4” Unit Fabrication

Based on the successful scaled-up procedure demonstrated with ProX 200, the printer selected to fabricate the 4” x 4” x 4” subscale M2HX with high-temperature material (Inconel) is ProX 300 (Inc718). Despite having lower printing resolution compared to the EOS M290 (20µm), ProX 300 (Inc718) reduces fabrication time and cost, which are crucial factors to make M2HXs competitive in the aerospace market. The printing time of this M2HX using the ProX 300 (Inc718) was four days, 50% faster compared to the EOS M290 (20 µm). The same percentage was also reflected on the quoted cost of the HX.

The company to which the M2HX print was outsourced decided to add a third angle of orientation γ to the unit beside the previous two mentioned angles α and β, as shown in Figure 4-19.

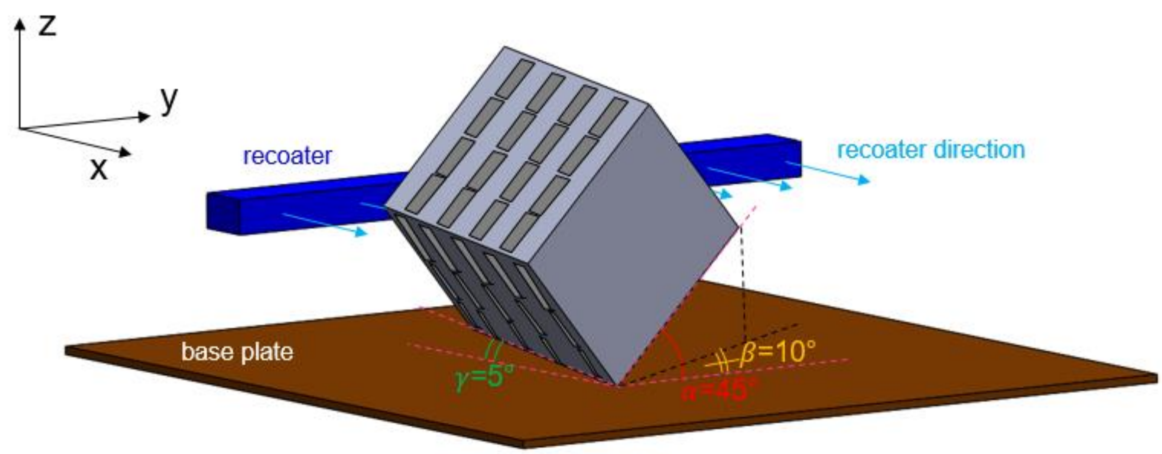

Figure 4-19: 4" x 4" x 4" M2HX unit orientation with respect to the base plate

Once more, the objective of the 5° angle given to the unit in the x-z plane was to reduce the cross-sectional area perpendicular to the recoater direction as shown by Figure 4-20.

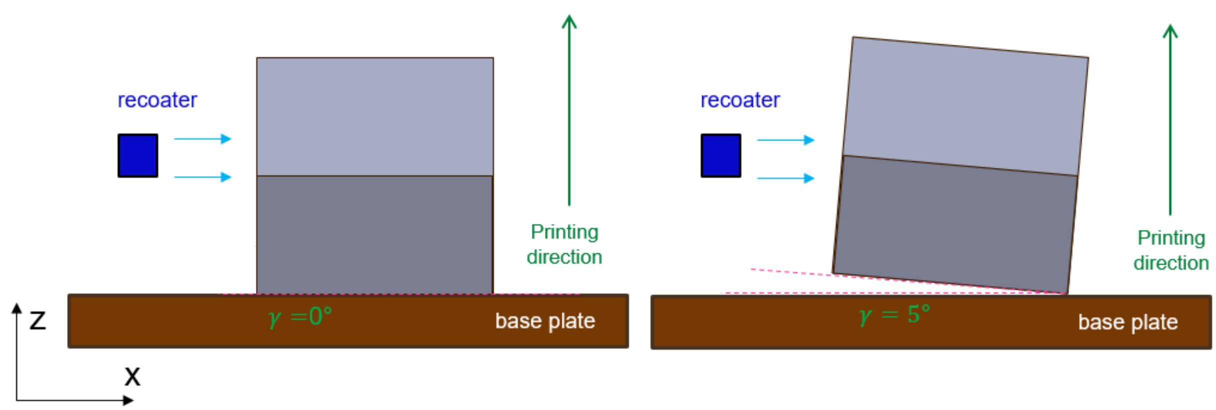

Figure 4-20: Side view of Figure 4-19showing the effect of angle γ during the printing (manifold openings are omitted to simplify the drawing)

Based on the results of the fin thickness study, in order to fabricate this M2HX with a minimum fin thickness, the designed fin thickness was set at 0.100 mm. The base thickness was set to 0.500 mm to ensure a leak-proof unit.

Two smaller sectional sample designs were also created for measuring internal structure dimensions, considering it would be very difficult to directly measure the features' dimensions inside the subscale unit. The printed parts, including support and orientation are shown in Figure 4-21.

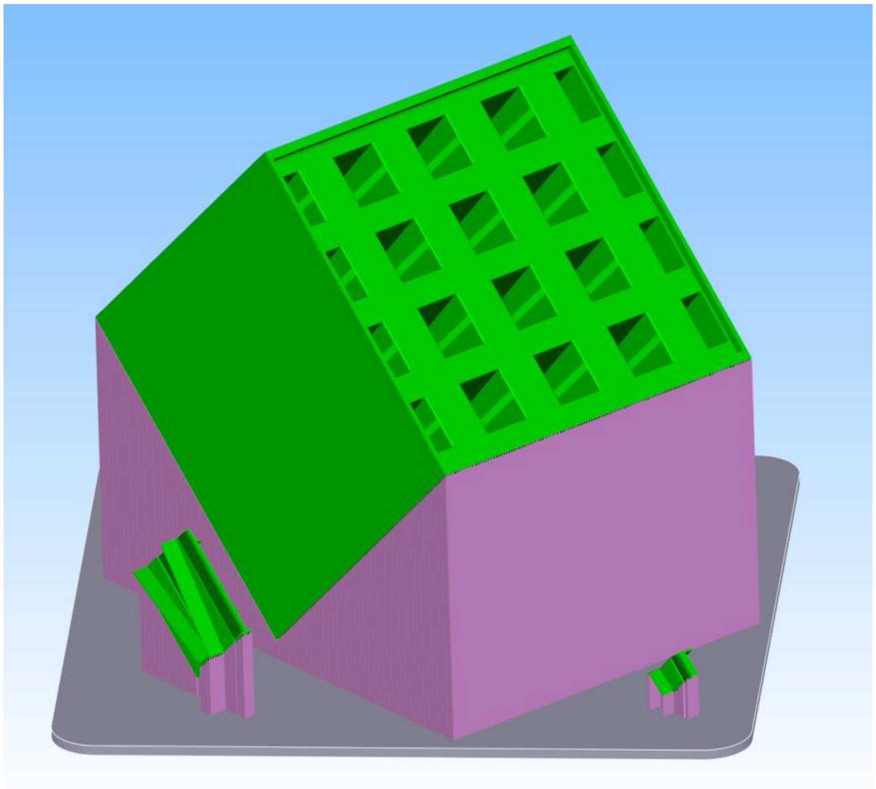

Figure 4-21: Printing rendering of the 4" x 4" x 4"M2HX unit and the two representative coupons

The total print time was 4 days, which is much less than the quoted lead time of any other conventional manufacturing techniques. Among the post process steps mentioned in Section, 2.5.2.2, the unit underwent powder removal, stress relief and removal from the base plate. Further high temperature treatment or high pressure treatment could be applied in case the unit leaked to reduce the porosity.

4.7.3 Subscale 4" x 4" x 4" Unit Evaluations

Once received from the company, the unit was cleaned multiple times using an ultrasonic cleaner to ensure there was no powder remaining. After cleaning, the first check was done comparing the actual mass to the theoretical one. The difference between the two was 3%.

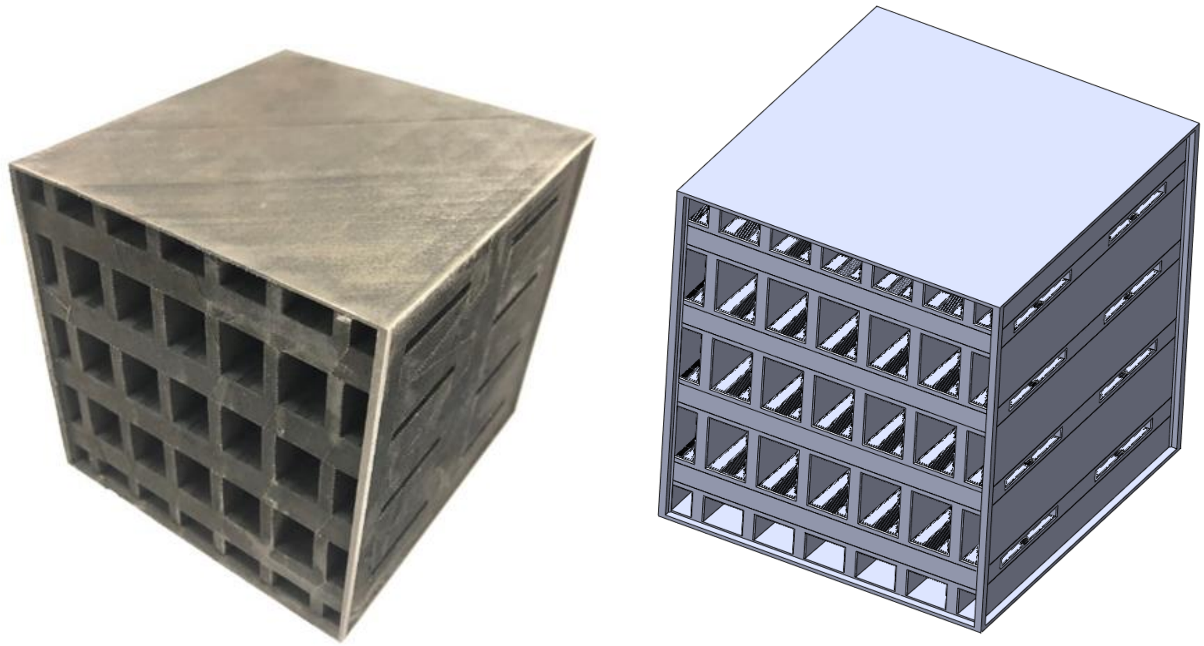

Figure 4-22: 4" x 4" x 4" Inconel 718 M2HX (a) AM printed unit (b) design rendering

Figure 4-22 shows the additively manufactured Inconel 718 subscale unit as compared to the design. The actual fin thickness of the 4" x 4" x 4" M2HX fabricated using ProX 300 (Inc718) was determined based on the measurements of the small section coupons. As expected from the fin study, the t_{fin} was confirmed to be 0.220 mm, which means +10% compared to the designed value of the optimization process.

The HX core was leak tested on both sides under design pressure. The unit was pressurized using nitrogen while being submerged into water. No leaks were observed, thus confirming that the separator plate selected meets the requirements. As a consequence, no additional post process e.g. HIP was needed.

4.8 Summary

Compared to state-of-the-art heat exchangers, manifold-microchannel heat exchangers have shown superior heat removal density (kW/kg) and with moderate pressure drops. However, manifold-microchannel heat exchangers made of Ni-based super alloys or other tough-to-machine materials often represent a challenge to fabricate using conventional fabrication methods. This is mainly because of the inherent manifold microchannel complex geometry, as well as the required small feature sizes (fin thicknesses) that should be comparable or smaller than state-of-the-art high performance metallic-based heat exchangers (~ 150 micron or smaller). In this chapter, direct metal laser sintering was used to fabricate compact high temperature manifold-microchannel heat exchangers. This technique allows the manifold-microchannel heat exchanger to be fabricated as a single object, which significantly simplifies the fabrication process. Three different machines were used to study the effect of geometries and printing parameters, such as laser power, powder size, and layer thickness, on the fin and channel sizes of the fabricated microchannel heat exchangers. Pressure containment tests were also performed to evaluate the minimum wall thickness that can hold the required design pressures. A wall thickness of 0.3 mm was shown to withstand 340 kPa and leakage-free. A detailed analysis of different printing orientations and their effect on the manifold-microchannel heat exchanger's design was also performed. Higher fin density was achieved by printing the units with a 45° inclination with respect to the base plate. Lastly, a 3" $\times$3" $\times$3" mm^3 size manifold microchannel heat exchanger was successfully fabricated with fin thickness of 0.133 mm out of maraging steel. A second unit with dimensions of 4"x4"x4" manifold microchannel heat exchanger was successfully fabricated with fin thickness of 0.220 mm out of Inconel 718. Cross-flow heat exchangers with straight fins on both sides were then successfully printed for the first time

Chapter 5 Performance Characterization of the 4” x 4” x 4” Subscale Unit

5.1 Introduction

This chapter discusses the design and fabrication of the metal headers used to connect the subscale unit to the experimental setup. Performance characterization of the 3D printed 4” x 4” x 4” subscale unit under low-temperature and high-temperature conditions was then presented. The experimental results were compared with the numerical predictions. CT scan analysis was performed on the unit to evaluate the printing quality. Lastly, the performance of the M2HX was compared to other conventional designs.

5.2 Metal Headers for Core Connection

The primary role of the headers is to connect the subscale unit to the existing piping connections of the experimental setup. In particular, the cold side is connected to a 2” circular piping system, while the hot side is connected to a 1” circular piping system. In order to test the 3D printed 4” x 4” x 4” subscale, custom designed metal headers were designed and fabricated using AM due to the complex design and to save fabrication time.

5.2.1 Metal Headers Design

Based on the work of Zhang [171], it was found that headers design is a crucial step during the experimental test because non-uniform flow induced by the header might create maldistribution at the core entrance and affect the performance when compared to the model prediction, that is based on uniform flow. In order to assess the need of flow defectors to improve the uniformity of the flow entering the subscale unit, a preliminary check was performed on the pressure ratio (P_r) between the dynamic pressure at the entrance of the header (P_{dyn}) and the pressure drop across the core of the HX (ΔP_{core}):

$$P_r = \frac{P_{dyn}}{\Delta P_{core}} \tag{12}$$

where:

$$P_{dyn} = \frac{1}{2}\rho v_{in,hdr}^2 \tag{13}$$

where $v_{in,hdr}$is the flow speed at the entrance of the headers and ρ is the density of the fluid at the inlet of the headers. A lower value of P_r suggests that the design of the header has a smaller impact on the flow distribution at the inlet of the core. Based on equation (12), $P_{r,cold} = 35.1\%$, while $P_{r,hot} = 12.8\%$. From this preliminary analysis, it is possible to conclude that the design of the cold side headers has a higher impact on the flow maldistribution analysis and deflectors might be needed to limit this effect.

5.2.1.1 Flow simulation for Headers

When simulating the flow distribution in the headers, it is important to include the back pressure effect of the core. However, if it is prohibitive to get a tridimensional full-CFD simulation of the core only, combining the headers makes it computationally infeasible. One possible approach shown by Zhang [171] is to substitute the real microchannel section of the core with a porous medium region. When properly calibrated, the porous medium region can provide the same pressure drop and combining the headers for a tridimensional full-CFD simulation become feasible. However, this approach requires time to calibrate the porous medium and every time the design of the header is changed, the entire assembly need to be generated, meshed and simulated.

For this study, the header flow distribution was simulated using the commercially available software COMSOL Multiphysics. The fluid within the header and the entrance to the core was designed as shown in Figure 5-1(a). For simplicity, only the hot inlet header design is shown, but the same approach is applied for the other three headers. As to the boundary conditions, mass flow rate and temperature were set at the inlet. For the outlet, instead, a customized pressure was assigned as boundary condition. In fact, one of the advantages of COMSOL Multiphysics is the capability to express boundary conditions as mathematical expression. In particular, for the current design it is possible to derive ΔP_{core} as a quadratic function of the mass flow rate ($\dot{m}_{in}$) from the simulations of the hybrid method. As stated in Section 3.4.1, one of the main assumptions of the hybrid method is the uniform flow at the inlet of each channel as well as at the inlet of every manifold channel. When shifting from core to header point of view, the inlet of the core becomes the outlet of the header, and in case of uniform flow, it is possible to define the ideal speed of the flow at the outlet of the header as:

$$v_{out,hdr,ideal} = \frac{\dot{m}_{in}}{\rho A_{opening}} \tag{14}$$

where $A_{opening}$ is the sum of the areas defined as 2 in Figure 5-1(b). If ΔP_{core} is a quadratic function of $\dot{m}_{in}$, Eq. (14) suggests that ΔP_{core} is a quadratic function of $v_{out,hdr,ideal}$ as well and it can be written as:

$$\Delta P_{core} = a\, v_{out,hdr,ideal}^2 + b\, v_{out,hdr,ideal} \tag{15}$$

where a and b are the two coefficients used to interpolate the simulated points of the hybrid method. In case of constant pressure at the outlet of the header, the flow does not automatically readjusts to reflect the physical behavior. However, the flow distribution is sensitive to the maldistribution: if less mass flow rate goes through a manifold channel, the pressure drop across this portion of HX will be smaller compared to the rest of the manifold channels. It happens then that the flow will tend to go the portion with lower mass flow rate, thus modifying the flow of the manifold channels in M2HX. To mimic this behavior, the back pressure at the header outlet is set as a function of the real speed at the exit of the header/ entrance of the core ($v_{out,hdr,real}$). The resulting pressure boundary condition (P_{bc}) can be written as:

$$P_{bc} = a\, v_{out,hdr,real}^2 + b\, v_{out,hdr,real} \tag{16}$$

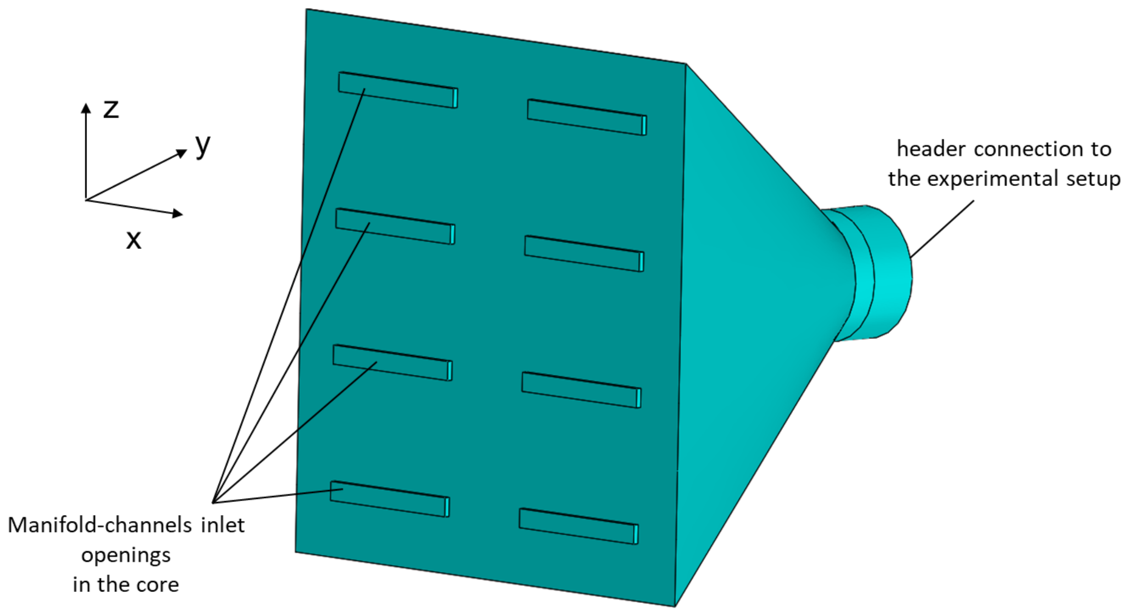

(a)

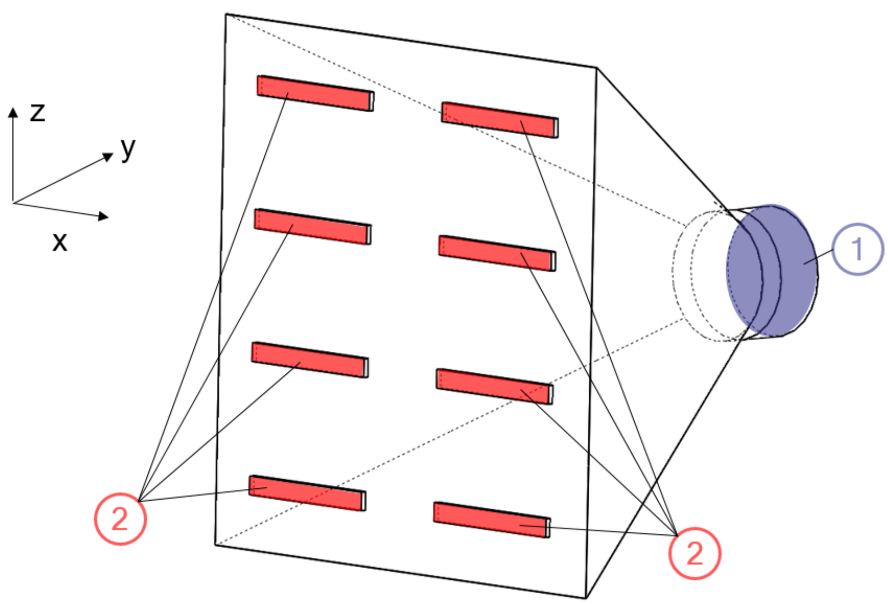

(b)

Figure 5-1: (a) Hot inlet model for CFD simulation (b) Computational domain and boundary condition: (1) header inlet surface with mass flow inlet and constant temperature, (2) HX core manifold channel inlet surface with condition expressed by equation (16).

The goal of the simulation is to identify the mass flow rate that enters every manifold channel and check if it is uniform, thus validating the assumption used in the predicting model. The level of uniformity is evaluated through the flow maldistribution value, defined as the ratio of the standard deviation of mass flow rate among all the manifold channels to the mean mass flow rate:

$$F = \frac{\sqrt{\frac{1}{r}\sum_{i=1}^{r}\left(\dot{m}_i - \dot{m}_{avg}\right)^2}}{\dot{m}_{avg}} \tag{17}$$

where

$$\dot{m}_{avg} = \frac{\sum_{i=1}^{r}\dot{m}_i}{r} \tag{18}$$

where, $\dot{m}_i$ is the mass flow rate entering each manifold channel opening and r is the number of openings. This definition is valid when all the openings have the same area as in the case of the hot inlet, as shown in Figure 5-2(a).

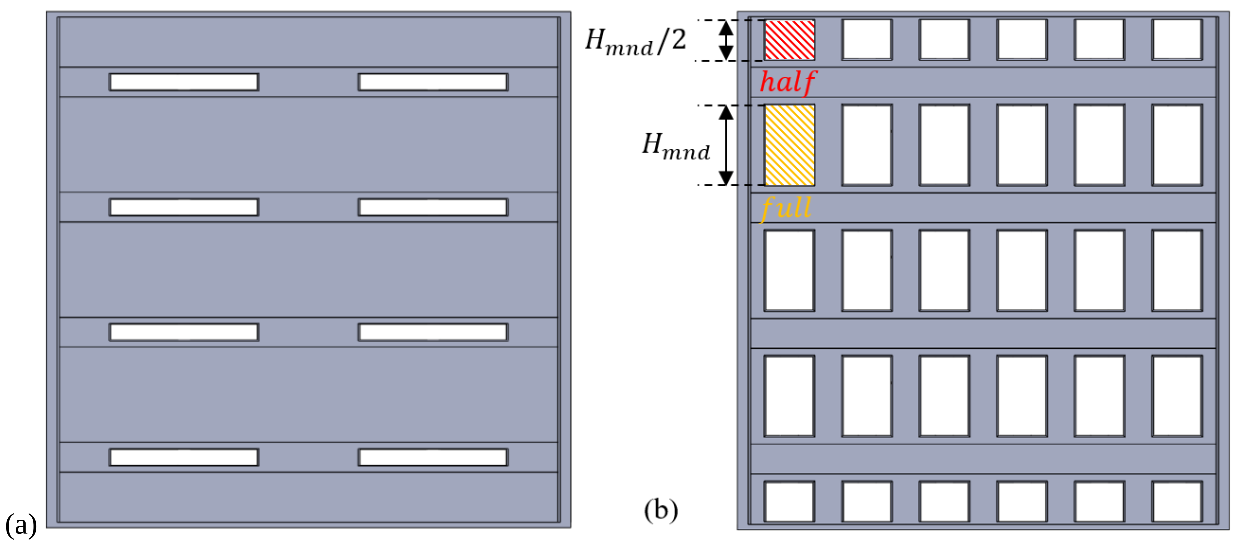

Figure 5-2: Manifold channels inlet opening: (a) hot side (b) cold side

When analyzing the cold inside, instead, the definitions need to be updated, based on the fact that some openings areas are half size of others (see Figure 5-2b). In this case the ratio of the standard deviation of mass flow rate among the manifold channels to the mean mass flow rate is split into two components:

$$F = \sqrt{\frac{\frac{1}{m}\sum_{i=1}^{m}\left(\dot{m}_i - \dot{m}_{avg,half}\right)^2}{\dot{m}_{avg,half}^2} + \frac{\frac{1}{r}\sum_{j=1}^{r}\left(\dot{m}_j - \dot{m}_{avg,full}\right)^2}{\dot{m}_{avg,full}^2}} \quad (19)$$

$$\dot{m}_{avg,half} = \frac{\sum_{i=1}^{m}\dot{m}_i}{m} \quad (20)$$

$$\dot{m}_{avg,full} = \frac{\sum_{j=1}^{r}\dot{m}_j}{r} \quad (21)$$

where, $\dot{m}_i$ is the mass flow rate entering the half size manifold channel openings and m is the number of those openings, while $\dot{m}_j$ and r refer to the full size openings. The lower F is, the more uniform the flow distributes among the manifold channels. Ideally this value should be 0%, but values below 5-10% are considered acceptable. The design of the headers without deflectors are analyzed and the speed profile at the outlet of the headers are shown in Figure 5-3 (a) and (b), for hot and cold respectively. Visually, the flow distribution of the hot sides looks more uniform than then the cold one. Figure 5-3 (b) shows that most of the mass flow rate is concentrated in the central area, while the mass flow rate is almost the same for all the openings of the hot header of Figure 5-3 (a).

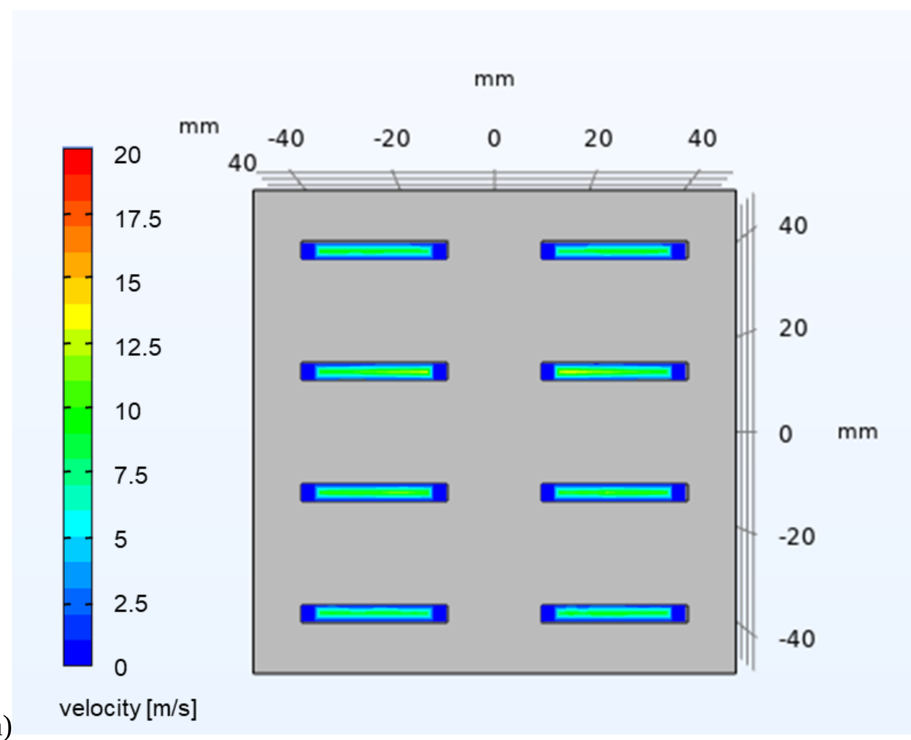

(a)

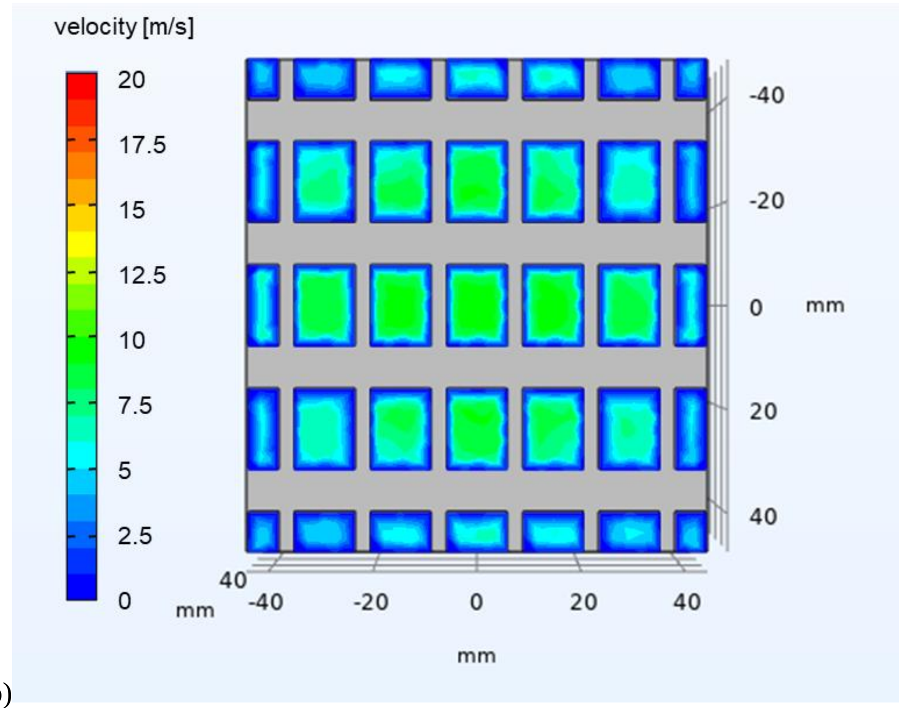

(b)

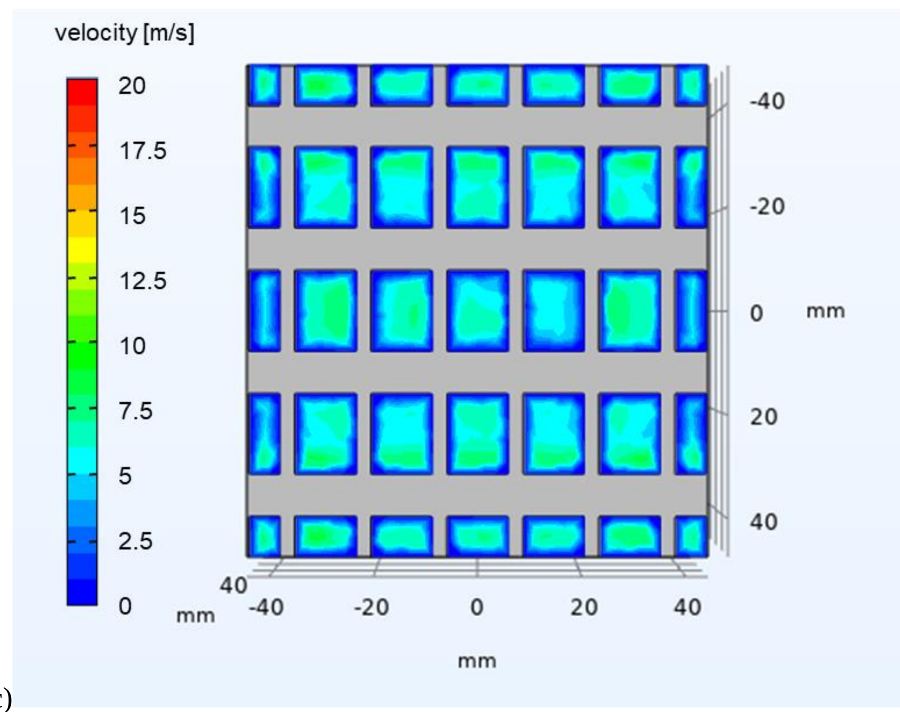

(c)

Figure 5-3: Speed profile at the outlet openings of (a) hot header without deflectors, (b) cold header without deflectors and (c) cold header with deflectors

The mass flow rates at the openings are also computed through the simulation. Using equation (17), $F_{hot} = 3\%$, while equation (19) leads to a value of $F_{cold} = 18\%$. As expected from the preliminary analysis and the speed profile of Figure 5-3 (b), cold side requires the introduction of deflectors to reduce the maldistribution to acceptable values. Based on the nominal flow rate, the design was updated by varying the position and angle of inclination of the deflectors. The optimized design has the speed profile shown in Figure 5-3 (b). Comparing Figure 5-3 (b) and (c), it is possible to notice a more uniform distribution of the flow. This configuration reduced the maldistribution to an acceptable value of $F_{cold} = 6\%$.

5.2.1.2 Mechanical stregth of the Headers

In order to estimate the thickness of the headers required to withstand the operative condition, a mechanical stress analysis was performed using the commercially available software Sledworks. The selected thickness of the headers is 2.0 mm. The simulation showed that the maximum von Mises stress on the hot side header under design system pressure is 6 times smaller than the yield strength of the material, thus providing enough safety factor.

In order to make sure that the size of the welding interface was sufficient to withstand the design pressure, the ratio (SF) between the welding joint resistance (FR_w) and the force applied to the header (FR_{hdr}) was calculated.

$$SF = \frac{R_w}{R_{hdr}} \tag{22}$$

where

$$FR_w = \Gamma_w \cdot W_w \cdot YS \tag{23}$$

$$FR_{hdr} = A_{hdr} \cdot n \cdot P_{sys} \tag{24}$$

where Γ_w and W_w are respectively the total perimeter and the thickness of the welding interface, YS is the yield strength of the Inconel, A_{hdr} is the projected area of the header, P_{sys} is the required system pressure and n is the design coefficient for system pressure which is set to 1.5 to increase the pressure requirement.

The resulting safety factor (SF) is 89, thus confirming that the designed welding interface is safe and reliable also under the design conditions.

5.2.2 Metal Headers Fabrication

Based on the flow simulation and mechanical stress analysis, the final design of the headers is shown in Figure 5-4. The flanges for the connection to the existing experimental setup are also shown in Figure 5-4 (a). The role of the flanges is to connect the assembled unit to the setup, in which similar flanges are already welded at the end of the piping system. Figure 5-4 (b) shows the inner design of the headers. It is possible to see the design of the deflectors of the cold header (right header, with reference to Figure 5-4 (b)) to which speed profile of Figure 5-3 (c) refers to. The flow has been divided into six sub flows to direct the fluid to the peripheral region of the core, thus reducing the maldistribution. Figure 5-4 (c) shows a cross-section view of the headers assembled to the core.

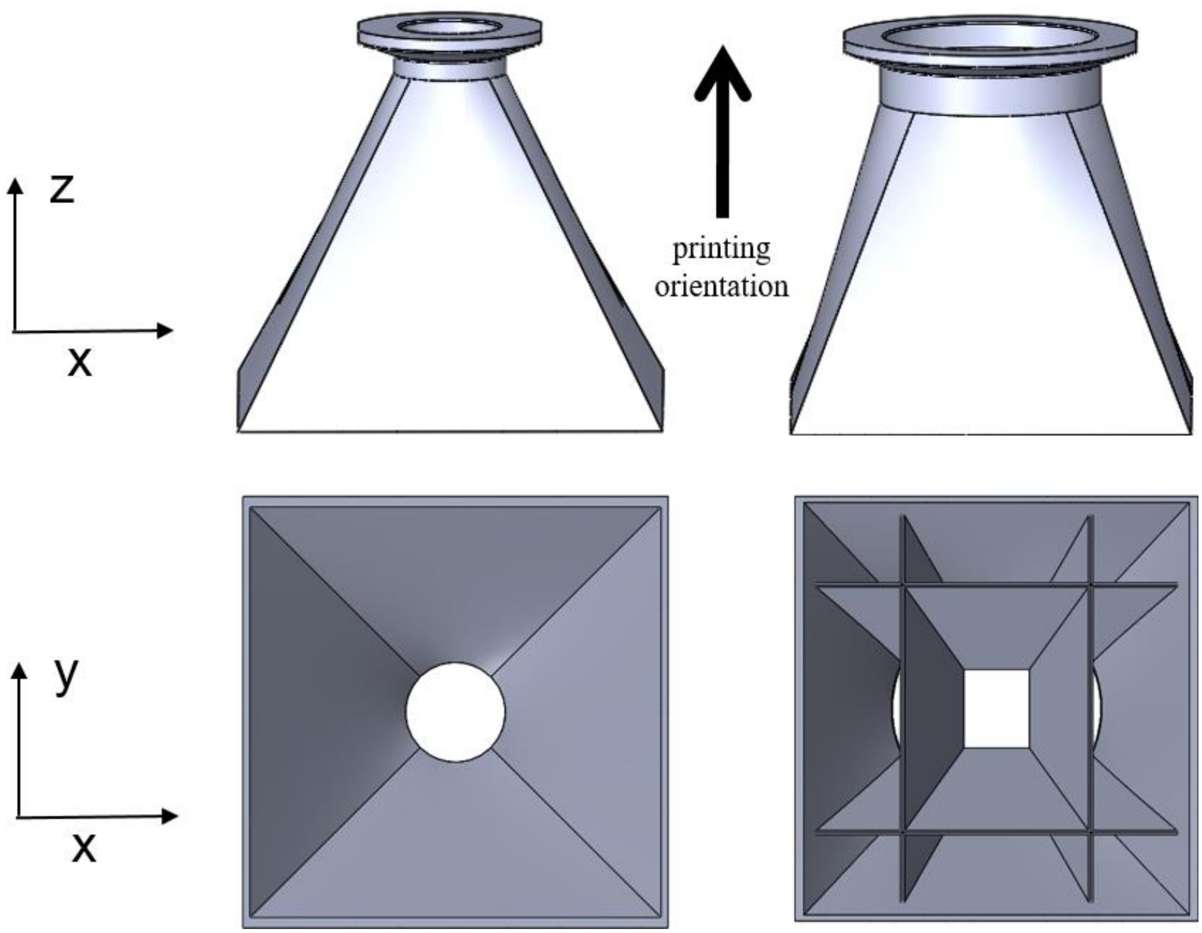

(a)

(b)

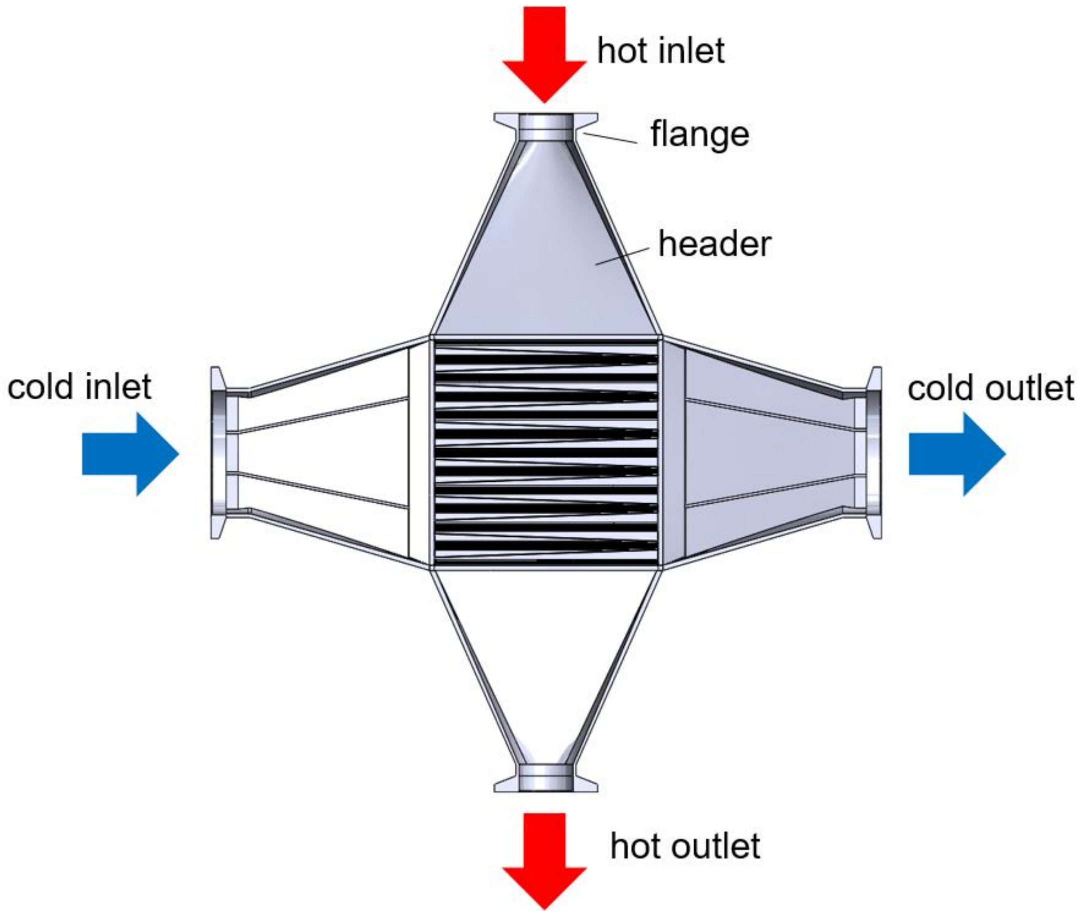

(c)

Figure 5-4: Headers design. (a) Frontal view. Left: hot side. Right: cold side. (b) Bottom view. Left: hot side. Right: cold side. (c) Cross section view of headers' design attached to the subscale unit

Since the metal header design does not have any small features and no overhanging surfaces are present in the design, all four headers were fabricated based on the printing orientation shown in Figure 5-4(a). The headers were printed using directly ProX 300 (Inc718), without the need of sampling coupons. Also the flanges were 3D printed using ProX 300 (Inc718), but unlikely the core and the headers, surface finish treatment was required to assure perfect contact at the interface with the existing flanges of the set-up.

5.3 Assembled Test Section

Hot- and cold-side headers and flanges were welded to the HX core as shown in the Figure 5-5.

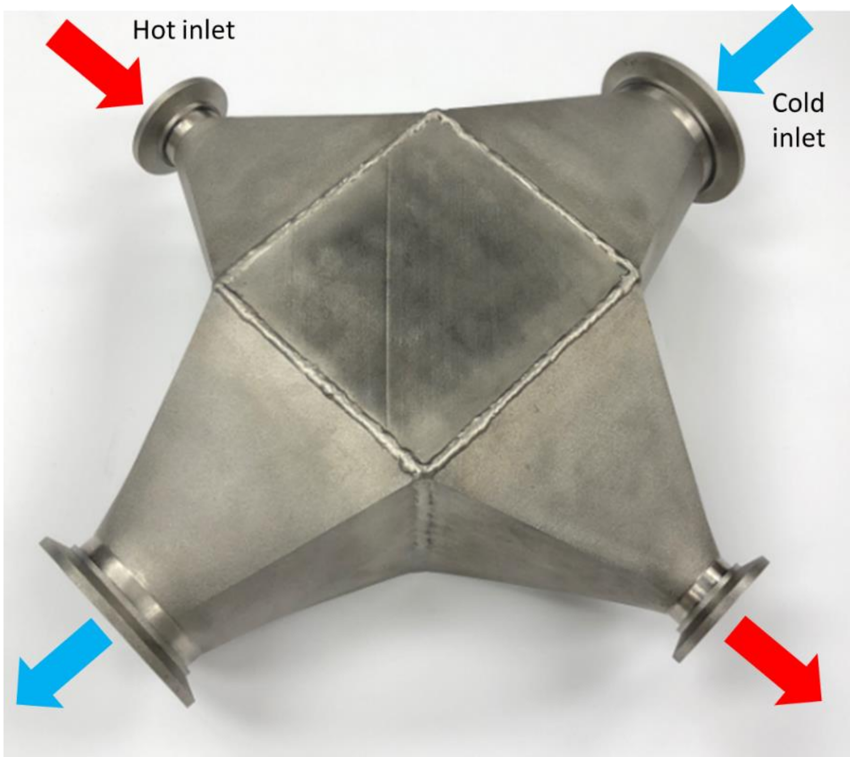

Figure 5-5: Assembled HX and headers

A specialist capable of welding the Inconel 718 HX core, headers, and flanges together was contacted to perform the work.

5.4 Experimental Setup Description

In order to assess the performance of the 4”x4”x4” subscale unit in terms of pressure drops and heat transfer, the assembled HX showed in Figure 5-5 was experimentally tested using pressurized N_2 on the hot side and air on the cold side. The schematic diagram of the test setup is shown in the Figure 5-6.

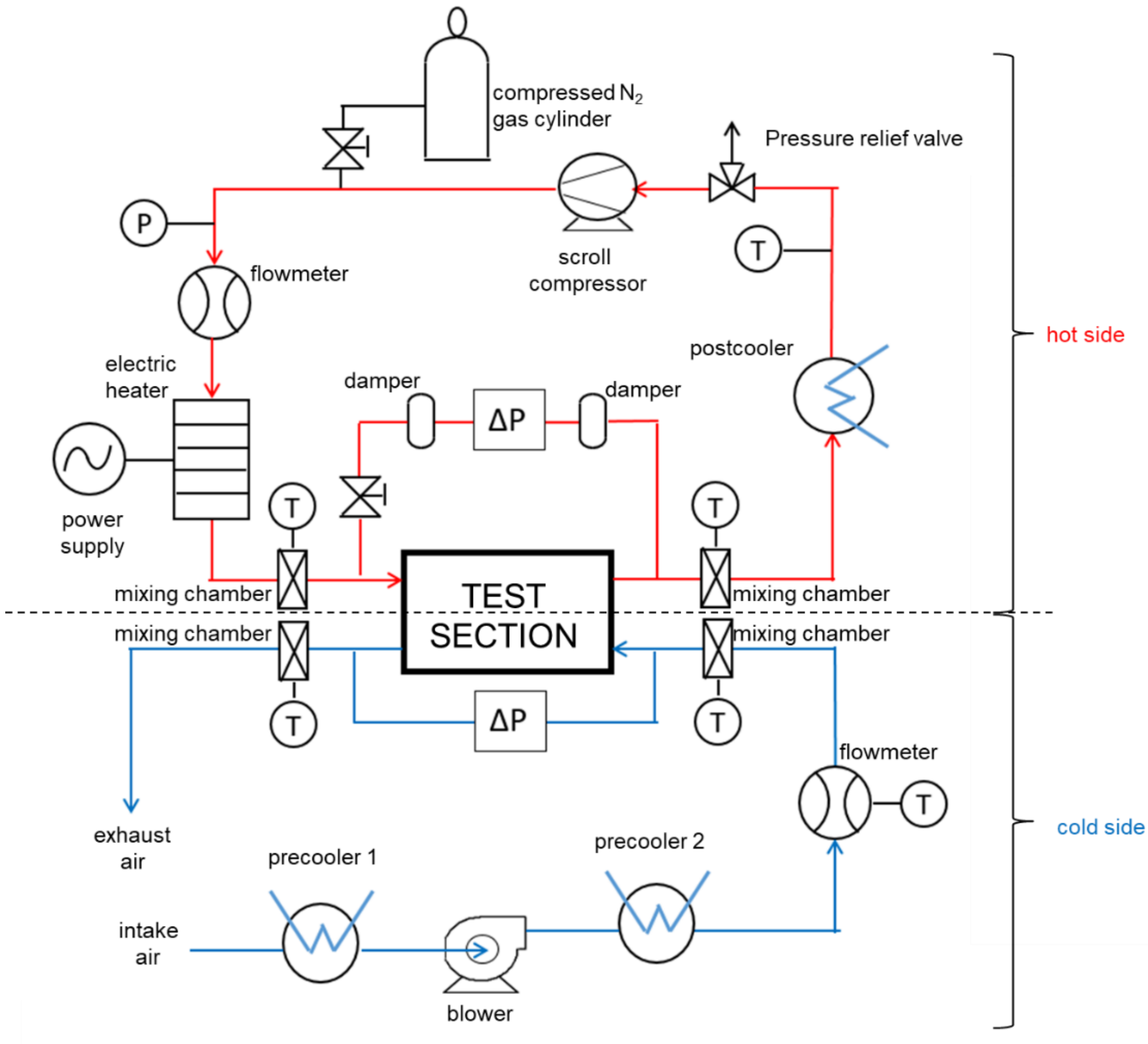

Figure 5-6: Schematic diagram of the experimental setup

The hot side consists of a closed loop, where a compressed N_2 gas cylinder was used to pressurize the system to the desired value. A pressure relief valve is installed as a safety measure. The total pressure was measured with a pressure gauge reader. A scroll compress, controlled by a variable speed controller, provided the desired flow. A 13-kW electric heater was used to increase the temperature in the system. A post-cooler (an air-to-water HX connected to a 20-kW chiller) was installed to cool down the flow from the outlet of the test section to the inlet of the compressor. The cold side is built as open loop with atmospheric system pressure. Air was used as working fluid and a blower, controlled by a variable speed controller, is used to provide the desired flow. Two precoolers were installed, before and after the blower, to make sure the temperature at the inlet of the test section was sufficiently low. Pressure transducers and high temperature thermocouples were used to measure the pressure drops and temperatures across the test section. On both sides, mixing chambers ensured uniform temperature measurements at both inlets and outlets of the test section. Coriolis flow meters were used to measure mass flow rates on both sides. All the measuring devices were connected to a data acquisition system (DAQ) to collect real-time values. Figure 5-7(a) shows the connection of the hot side of the unit to the rest of the setup. A series of flange-clamp connections with high temperature gaskets as interfacial elements was used to connect the different parts of the setup.

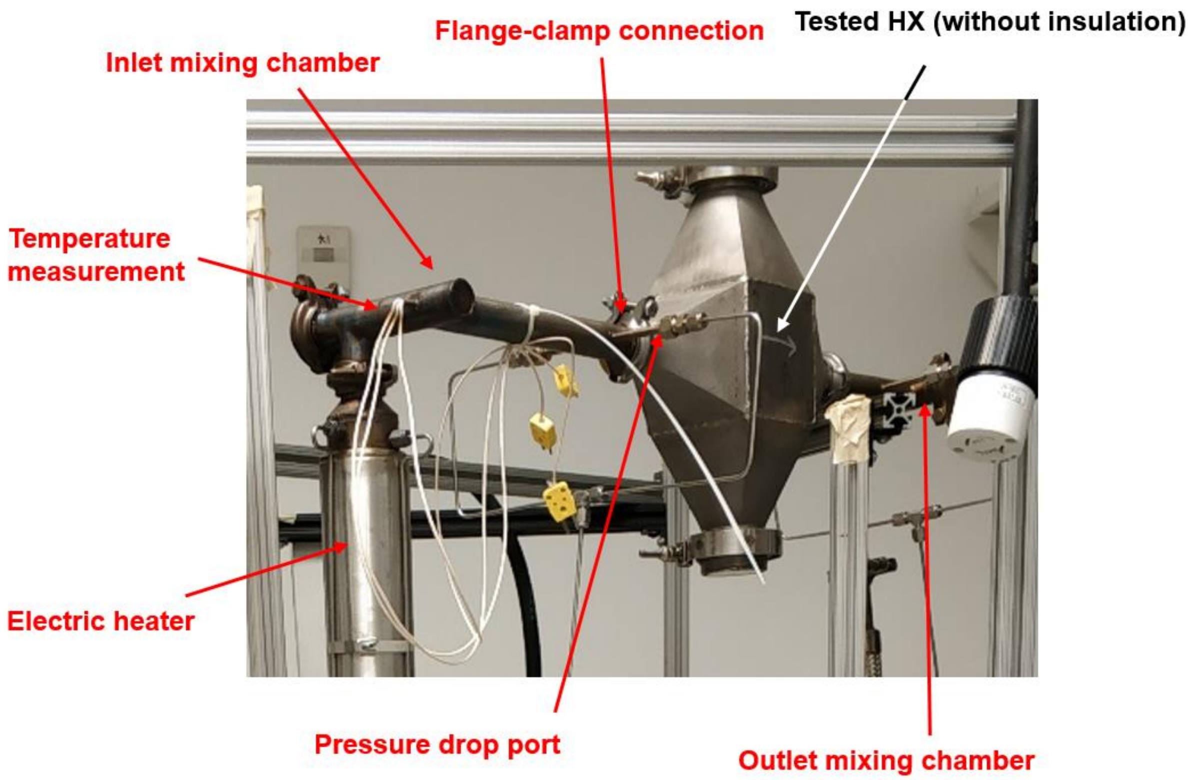

(a)

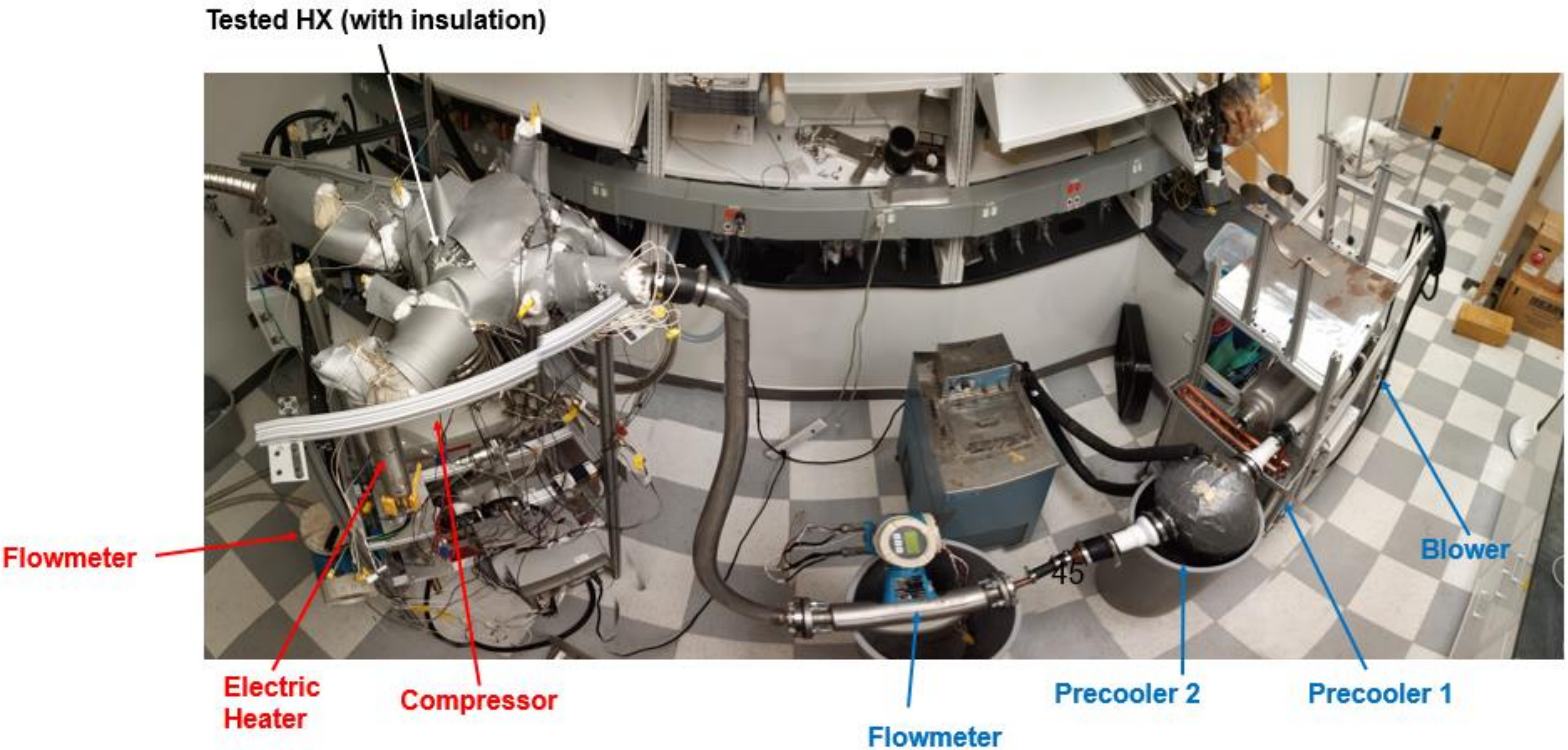

(b)

Figure 5-7: Experimental setup: (a) Zoom in view of the connections of the hot side of the test unit before insulation (b) overall experimental setup after insulation

Fiber glass insulation was applied to cover the HX, the headers and the mixing chambers to minimize heat losses as shown in the Figure 5-7(b). Infrared thermography was used to determine any heat loss sources. If heat loss sources were found, additional high temperature insulation was added. The insulation is ideally considered successful when operating the hot side only at high temperature, there is no difference across the unit:

$$T_{in,hot} - T_{out,hot} = 0 \tag{25}$$

where $T_{in,hot}$ and $T_{out,hot}$ are respectively inlet and outlet temperature of the hot side. Practically, this difference was considered acceptable below designed values that depend on the value of $T_{in,hot}$. Before testing was performed, all of the measurement devices were calibrated to ensure accurate measurement.

5.5 Low Temperature Testing

First, a low temperature testing was performed. The HX was tested by varying the cold-side mass flow rate ($\dot{m}_{cold}$) from 10 to 30 g/s while keeping the hot-side mass flow rate ($\dot{m}_{hot}$) constant. This procedure was repeated for five values of hot-side mass flow rates in the range of 7-13 g/s. For all the tested points, the inlet hot and cold temperatures were set constant at 100°C and 25°C, respectively, and the hot-side was pressurized at 340 kPa. A summary of the experimental test conditions is shown in Table 5-1.

Table 5-1: Low-temperature experimental test conditions of the 4" x 4" x 4" Subscale Unit

Temperature Boundary Conditions	
$T_{in,cold}$	25ºC
$T_{in,hot}$	100ºC
P_{hot}	340 kPa
P_{cold}	101 kPa
Mass flow rate Boundary Conditions	
$\dot{m}_{cold}$	10, 15, 20, 25, 30 g/s
$\dot{m}_{hot}$	7, 8.5, 10, 11.5,13 g/s

For all flow rate variations, inlet and outlet temperature (T_{in} and T_{out} respectively), pressure drop (ΔP), and mass flow rates were measured and recorded for both sides, while total system pressure (P_{hot}) was measured for the hot side only. For each temperature measurement, the final value is the average of the three thermocouples installed in each location.

5.5.1 Low-Temperature Experimental Procedure

First, the heat duty of the HX was evaluated on each side individually as shown in Eqs. (26)-(27), where, c_p is the N_2 or air specific heat for the hot- and cold-sides calculated at the average temperature of the inlet and outlet measurements.

$$Q_{hot} = \dot{m}_{hot} {c_p}_{hot} (T_{in,hot} - T_{out,hot}) \tag{26}$$

$$Q_{cold} = \dot{m}_{cold} {c_p}_{cold} (T_{out,cold} - T_{in,cold}) \tag{27}$$

Based on the measurements, the heat duty (Q) and the energy balance (EB) of the subscale HX were evaluated as:

$$Q = \frac{Q_{hot} + Q_{cold}}{2} \tag{28}$$

$$\Delta Q = |Q_{hot} - Q_{cold}| \tag{29}$$

$$EB = \frac{\Delta Q}{Q} \tag{30}$$

ΔQ is the absolute value of the difference between the heat duties obtained independently on the two sides. Ideally, the heat leaving the hot side should be equal to the heat received by the cold side, thus leading to $\Delta Q = 0$ and $EB = 0$. The average energy balance between the hot- and cold-side was found to be 5%, with standard deviation of 3% for all tested points. The deviation from the ideal case of perfect energy balance can be explained by a small heat leakage to the ambient, non-perfectly mixed temperature condition at the thermocouple locations, and uncertainty of the measurements. The average value of Q_{hot} and Q_{cold} is used to evaluate the performance of the HX, as shown in Eq. (28). From the collected measurements it is also possible to define the HX's effectiveness (ε), as:

$$\varepsilon = \frac{Q}{C_{min}(T_{in,hot} - T_{in,cold})} \tag{31}$$

where C_{min} = min($\dot{m}_{cold}c_{p,cold}$; $\dot{m}_{hot}c_{p,hot}$).

5.5.2 Uncertainty Analysis

Uncertainty propagation analysis was performed to calculate the uncertainty of the M2HX performance parameters (Q, ε). A list of measurement equipment is shown in Table 5-2 with the corresponding accuracies.

Table 5-2: List of measurement equipment and its accuracy

Equipment function	Equipment name	Accuracy
Hot-side flow rate	Coriolis flow meter (0.5-inch size)	± 0.5% of measurement
Cold-side flow rate	Coriolis flow meter (1-inch size)	± 3% of measurement
Temperature	K type thermocouple	± 2.2°C or 0.75% of measurement
Hot-side pressure drop	Pressure transducer	± 0.25% FS of 5.5 kPa
Cold-side pressure drop	Pressure transducer	± 0.25% FS of 5.5 kPa

The uncertainty of the calculated quantity Y, which is a function of $X_1, X_2, \ldots, X_N$ with uncertainty of $Un_{X_1}, Un_{X_2}, \ldots, Un_{X_N}$ can be calculated using the method explained in NIST Technical Note 1297 [178], defined as:

$$Un_Y = \sqrt{\sum_i \left(\frac{\partial Y}{\partial X_i}\right)^2 Un_{X_i}^2} \tag{32}$$

This method was implement in the EES software and used to calculate the uncertainties of the derived performance parameters. The maximum uncertainties in Q and ε were evaluated as ±13.5% and 10.0% respectively and the error bars are included in the results presented in the next section.

5.5.3 Low-temperature experimental results and discussion

The subscale unit's pressure drops (ΔP) for both sides is shown in Figure 5-8 as a function of $\dot{m}$, including the numerical trend obtained with the hybrid method. For the cold side (Figure 5-8(a)), the cold side mass flow rate was changed while keeping the mass flow rate constant at 10 g/s. Similarly, the pressure drop on the hot side (Figure 5-8(b)) was studied while keeping the cold side flow rate at the value of 25 g/s.

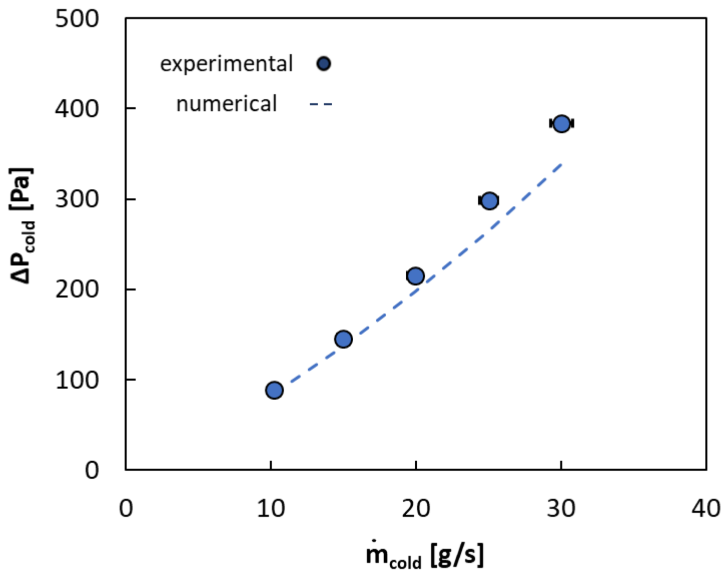

(a)

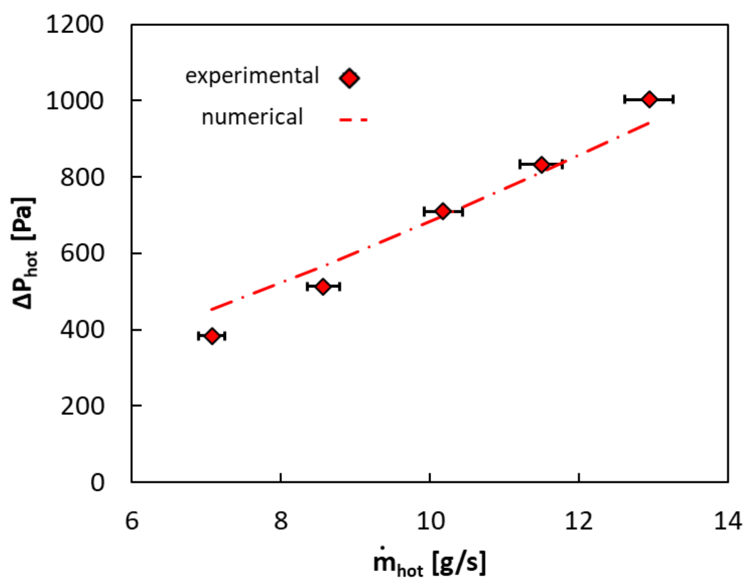

(b)

Figure 5-8: Low temperature testing result – Pressure drop (a) Cold-side (b) Hot-side of the 4" x 4" x 4" Subscale Unit

Both Figure 5-8 (a) and (b) show the expected trend: a quadratic pressure drop increase with increase in flow rate. Compared to the hybrid method, there is a good agreement between the predicted and tested pressure drop. The numerical prediction of the pressure drop is within 10% of the experimental results for both the hot- and cold- sides.

Figure 5-9, instead, shows the effectiveness (ε) as a function of the mass flow rate of the hot side ($\dot{m}_{hot}$), for all the tested conditions. Also Figure 5-8 shows the comparison between the experimental results and the predicted results obtained using the hybrid method.

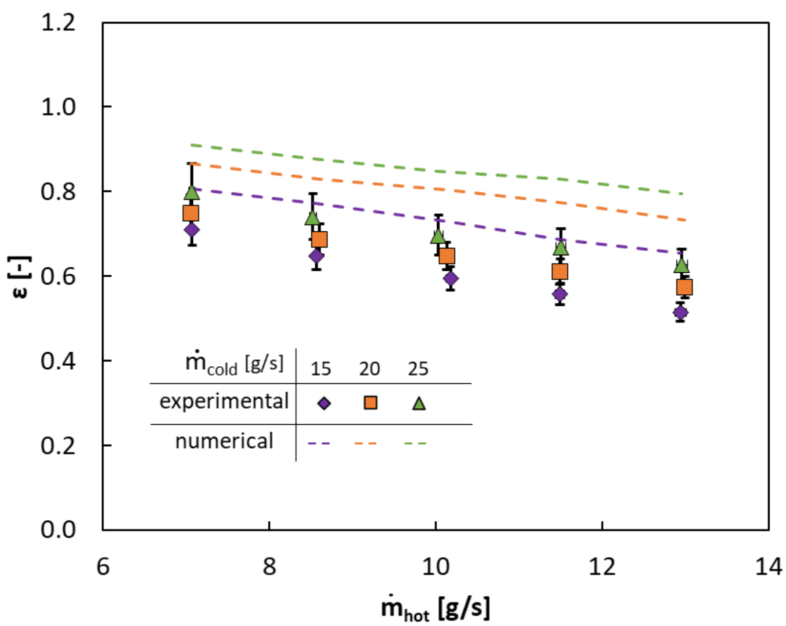

Figure 5-9: Low temperature testing result – Heat exchanger effectiveness of the 4" x 4" x 4" Subscale Unit

The deviation between the predicted and tested effectiveness is larger (up to 20%) compared to the results of the pressure drop. Among the possible causes of the deviation, the main reason for such a deviation could be predominantly due to printing defects during the AM manufacturing process. .

In order to assess the fabrication quality, CT scanning was performed on the 4" x 4" x 4" HX. The scans were performed twice.

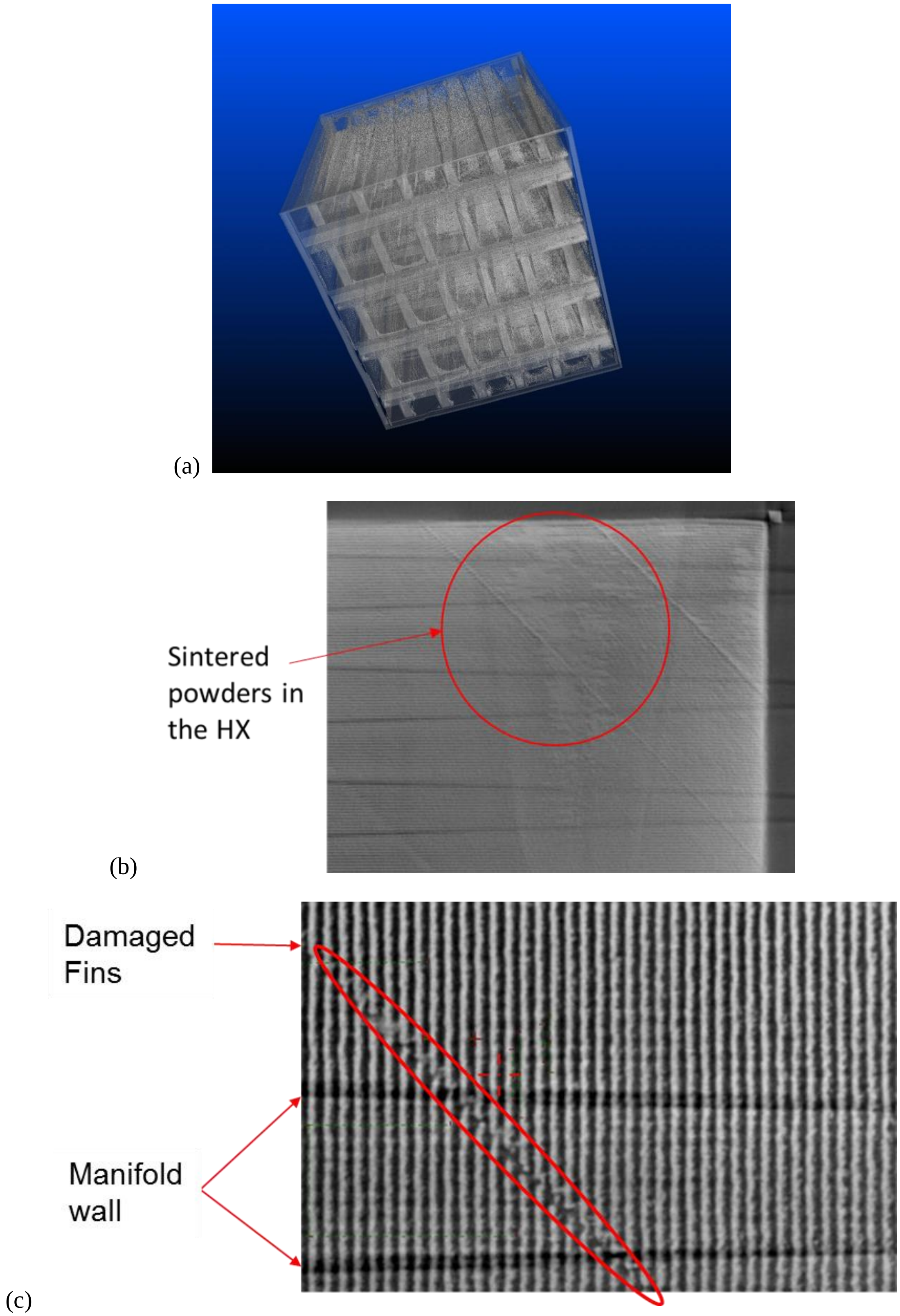

Figure 5-10: CT scan result of the 4" x 4" x 4" Subscale Unit (a) Full scan of the HX (b) CT scan result on the cold side fins (Top View) (c) Detailed scan on the cold side fins (Top View)

The first scan was a full size scan of the heat exchanger as shown in the Figure 5-10(a). This CT scan imaging had a resolution of 70 - 80µm. Analyzing the full-scale result, no crack was found between the hot and cold streams. However, leftover powder was observed blocking some of the channels as shown in the Figure 5-10 (b). Despite using the ultrasonic cleaner, not all of the powder could be removed as some of the powder might have been sintered during the stress relieve process. A more detailed scan was performed on a portion of the HX (1.5” x 1.5” x 1.5”) to analyze the fins quality. The detailed scan had a resolution of 35 µm. From the scan result, the fins were measured as 0.220 mm, confirming once more the expected value, but 0.020 mm bigger compared to the requested of 0.200 mm. Moreover, a small portion of the cold side’s fins were found to show traces of some defects, as shown in Figure 5-10 (c). This could be because of an interruption in printing as due to the need to refill the powder in the middle of the print. Since the defects did not cause any leaking between the hot and cold streams, they were not considered detrimental to the extent that would make the unit not-testable.

Beside this printing defects, another possible cause of the deviation between the numerical and experimental data in the heat transfer performance (Figure 5-9) could be the printing defects in the manifold base as shown in Figure 5-11.

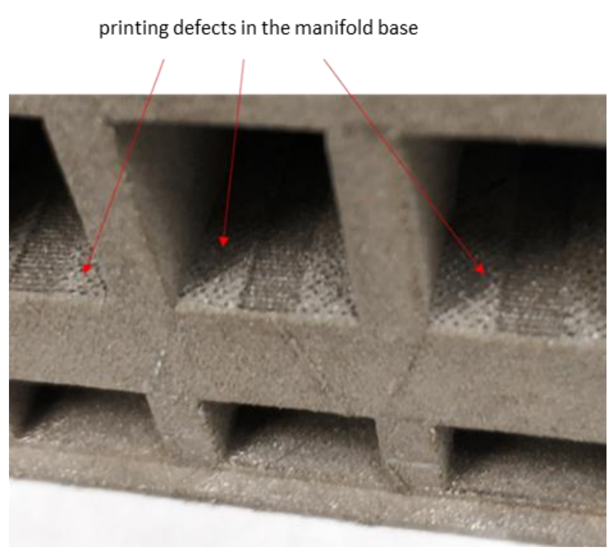

Figure 5-11: Printing defects in the manifold base of the 4” x 4” x 4” subscale unit

As explained in Section 2.4.4.1, the manifold base is placed on top of the microchannel, and it determines the flow length of the fluid in the microchannels, as shown in Figure 5-12(a). It is desirable to have the manifold base as thin as possible to minimize its mass. However, a very thin manifold base may result in a failed structure. When setting $H_{mnd,base}$=0.150 mm, the manifold base shows printing defects that alter the flow in the microchannel. Those defects cause a portion of the flow to take a shortcut path in the microchannels, as depicted in Figure 5-12(b). This causes a portion of the heat transfer area to be not fully utilized and the heat transfer performance to be significantly reduced.

The combination of the defects in the manifold base, the damage of few of the microchannels and the partial clogging of the unit is the cause of the deviation in both the pressure drop and heat transfer performance. However, it is not possible to create a numerical model that can reproduce the same behavior as the printed HX due to the complexity of those defects. For this reason, the comparison is confirmed to be between the experimental performance and the predictions made with the hybrid method based on the ideal design.

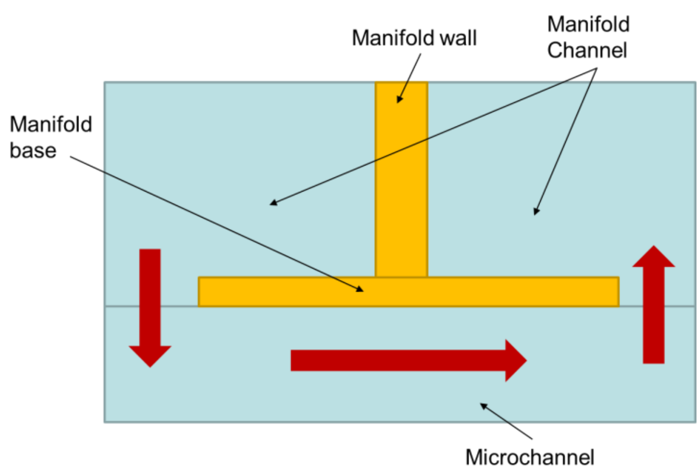

(a)

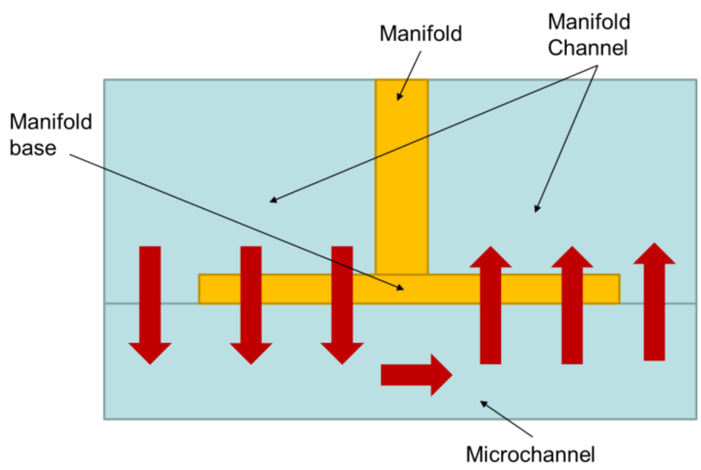

(b)

Figure 5-12: Flow direction in the microchannels (a) Solid manifold base – No bypass flow (b) Manifold base with printing defects– With bypass flow

5.6 High Temperature Testing

Once completed the test at the low-temperature and analyzed the results, it is also necessary to test the subscale unit at higher temperature to assess the performance of the HX at the designed conditions. The high temperature testing was performed under the conditions shown in Table 5-3.

Table 5-3: High-temperature experimental test conditions

Temperature Boundary Conditions	
$T_{in,cold}$	25ºC
$T_{in,hot}$	300ºC
p_{hot}	340 kPa
p_{cold}	101 kPa
Mass flow rate Boundary Conditions	
$\dot{m}_{cold}$	15, 20, 25 g/s
$\dot{m}_{hot}$	7-13 g/s

With higher temperature, the time for the system to reach steady-state is longer and the pressure drop is higher for the same mass flow rate due to the lower density of the fluids. For those reasons, the range for the cold side cold side of flows is smaller compared to the low-temperature one to minimize overheating of the blower.

5.6.1 High-Temperature Experimental Procedure and Data Reduction

The method of running the experiments and collecting the data is the same as the one described for the low temperature test. Beside the subscale's performance parameters mentioned for the low temperature, new parameters are introduced in the high temperature test. Once the effectiveness (ε) is determined with Eq. (31), it is possible to obtain the NTU from the correlation for cross-flow HW with both fluids unmixed [179]:

$$\varepsilon = 1 - exp\left[\frac{NTU^{0.22}}{C_R}\{exp(-C_R NTU^{0.78}) - 1\}\right] \tag{33}$$

where, C_R is defined as the ratio of C_{min} and C_{max}= max($\dot{m}_{cold}c_{p,cold}; \dot{m}_{hot}c_{p,hot}$). Since it is not possible to analytically determine NTU given ε, EES is used to get the value of the NTU. From the NTU definition, the overall heat transfer coefficient (U) can be obtained, which includes the convection on both sides and the conduction though the base (separating plate):

$$U = \frac{C_{min}NTU}{A_{ht}} \tag{34}$$

where A_{ht} is the heat transfer area, that can be obtained by multiplying the fins area on the two sides of the base plate by half the number of stacks N (4 for this case). Beside the thermal performance, it is also important to evaluate the pressure drop of the M2HX using non dimensional parameter. Therefore, it is possible to express the mean friction factor (f) as:

$$f = \frac{\Delta P}{L_{flow}}\frac{2}{\rho}\frac{D_{H,chn}}{v_{chn}^2} \tag{35}$$

where ρ is the density of the fluid, v_{chn} is the velocity of the fluid in the microchannel. $D_{H,chn}$ and L_{flow} are defined as (with reference to Figure 3-3):

$$D_{H,chn} = \frac{2H_{chn}W_{chn}}{H_{chn} + W_{chn}} \tag{36}$$

$$L_{flow} = L + \frac{H_{mnd}}{2} + 2H_{mnd,base} + H_{chn} + W_{mnd-chn} - \frac{W_{in}}{2} \tag{37}$$

where L_{flow} is the average flow path of the fluid from the entrance to the exit of the HX. It can be split into three terms corresponding to three directions in which the fluid flows in a M2HX. Using Figure 3-3 as reference, the flow path in the $\pm x$-axis corresponds to the flow length in the manifold-channel, while the flow path in the $\pm z$-axis represents the average distance travelled by the fluid to reach the microchannel from the manifold and conversely return from the microchannel $2\times(\frac{H_{mnd}}{4} + H_{mnd,base} + \frac{H_{chn}}{2})$. The third term of Eq. (37) is the flow path in the $\pm y$-axis pertaining to the average flow length in the microchannel.

5.6.2 High Temperature Experimental Results and Discussion

5.6.2.1 Heat transfer performance

The heat transfer performance testing results are shown in Figure 5-13 for different values of cold-side mass flow rates, while varying the hot-side mass flow rate. The results are plotted as a function of the Reynolds number (Re) of the flow in the microchannel, which is defined as

$$Re_{chn} = \frac{\rho \, v_{chn} \, D_{chn}}{\mu} \tag{38}$$

where μ is the viscosity of the fluid. Figure 5-13(a) and Figure 5-13(b) show, respectively, the effectiveness of the HX and the heat duty (Q) as a function of the hot-side Reynolds number ($Re_{chn,hot}$) and the overall hot-side mass flow rate at the HX's inlet ($\dot{m}_{hot}$) (top x-axis). The graphs show the results for the three values of $\dot{m}_{cold}$ tested: 15, 20 and 25 g/s and their corresponding $Re_{chn,cold}$.

Figure 5-13(a) shows that maximum effectiveness of 80% was achieved for $\dot{m}_{cold}$=25 g/s and $\dot{m}_{hot}$=7 g/s, which are respectively the highest value of $\dot{m}_{cold}$ and the lowest value of $\dot{m}_{hot}$ in the range of tested flow rates. This point corresponds, therefore, to the experimental condition with the lowest C_r. Considering that

C_{min} always corresponds to the hot side for all the tested points, the definition of effectiveness given in Eq. (31) can be rewritten as:

$$\varepsilon = \frac{T_{in,hot} - T_{out,hot}}{T_{in,hot} - T_{in,cold}} \tag{39}$$

By increasing the hot-side mass flow rate, $T_{out,hot}$ increases, and a decrease in effectiveness is observed as justified by Eq. (39). The same result is obtained when the cold-side mass flow rate is decreased, as shown in Figure 5-13(a). When evaluating an HX, however, it is important to determine the heat duty that can be transferred. Figure 5-13(b) shows that increasing the cold and hot side mass flow rates has a positive impact on Q, with a maximum value of 2,200 W at $Re_{chn,cold}$= 79 and $Re_{chn,hot}$=132. Moreover, it is interesting to notice that increasing the hot side has a higher effect on heat duty than increasing the cold side. Increasing $\dot{m}_{hot}$ by 28.5% from 7 g/s to 9 g/s increases Q by 11.3%, while increasing $\dot{m}_{cold}$ by 66.7% from 15 g/s to 25 g/s increases Q by 6.3%. This is because the hot-side mass flow rate is significantly lower than the cold, resulting in a higher thermal resistance on hot side that acts as the limiting factor.

The overall heat transfer coefficient as a function of $Re_{chn,hot}$ for the different cold-side flow rates is presented in Figure 5-13(c). It is observed that that increasing the mass flow rate of either of the two sides increases the overall heat transfer coefficient. Overall heat transfer coefficient as high as 49 W/m^{2}K was recorded for $Re_{chn,cold}$=79 and $Re_{chn,hot}$=132. The high value of the overall heat transfer is due to the high fin density (thanks to the small size of the fins) and the short flow path in the microchannel (thanks to the manifold on top), allowing the fluid to exploit the high heat transfers of the entry region. The base thickness is also minimized to reduce the thermal resistance, while guaranteeing the gas tightness under the operating conditions.

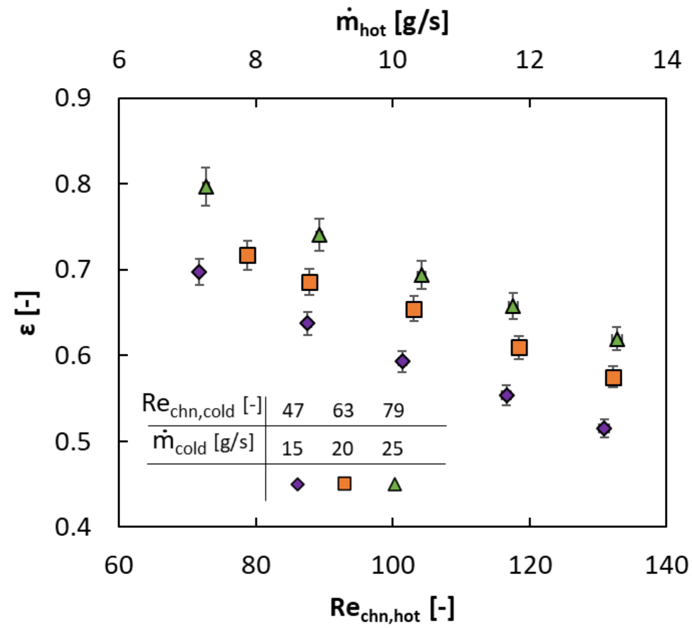
ṁhot [g/s]
6 8 10 12 14
0.9 0.8 0.7 0.6 0.5 0.4
ε [-]
Rechn,cold [-] 47 63 79
ṁcold [g/s] 15 20 25
60 80 100 120 140
Rechn,hot [-]

(a)

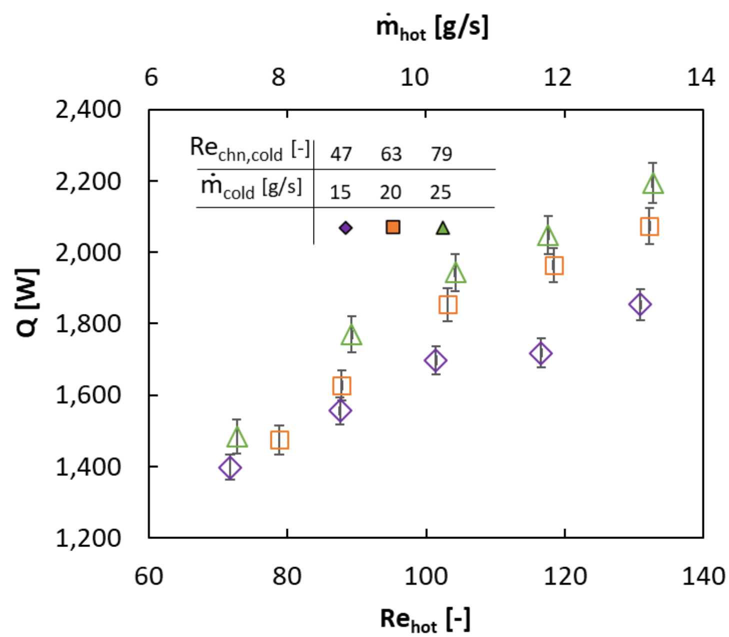
ṁhot [g/s]
6 8 10 12 14
2,400 2,200 2,000 1,800 1,600 1,400 1,200
Q [W]
Rechn,cold [-] 47 63 79
ṁcold [g/s] 15 20 25
60 80 100 120 140
Rehot [-]

(b)

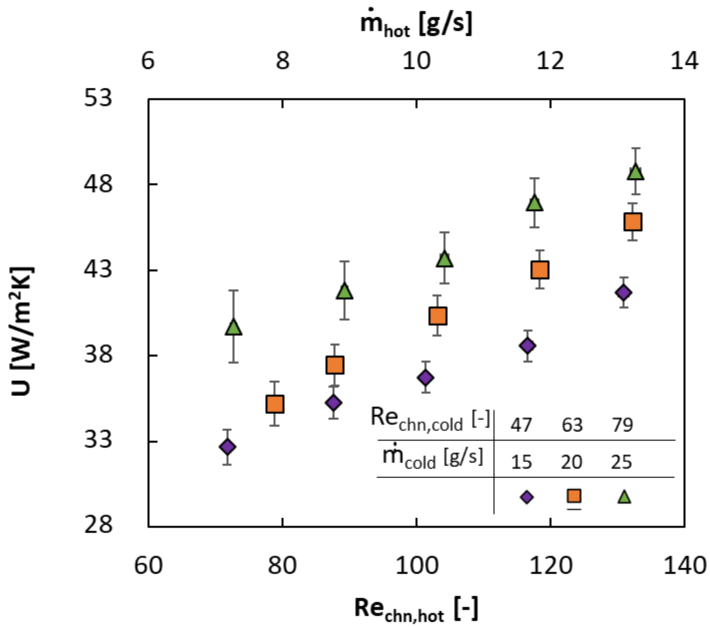

(c)

Figure 5-13: Heat transfer performance results of the 4" x 4" x 4" Subscale Unit: (a) effectiveness of the HX, (b) heat duty, (c) overall heat transfer coefficient

5.6.2.2 Pressure Drop Performance

The pressure drop (ΔP) for both sides is shown in Figure 5-14 (left y-axis) as a function of the Re_{chn} (bottom x-axis) and $\dot{m}$ (top x-axis). Both Figure 5-14(a) and Figure 5-14(b) show the expected trend: a quadratic pressure drop increase with increase in flow rate as shown by the data trending line. The difference in ΔP between the hot and cold side is due to the problem statement of the HX's design. However, using for both sides a pressure transducer with the same uncertainty results in a bigger uncertainty on the cold side. Also for the mass flow rates, the flowmeter used for the cold side has a bigger uncertainty, which is reflected in the reported graphs. Figure 5-14 also shows the trend of the friction factor f, as defined in Eq. (35) (right y-axis). The friction factor f decreases with the increase in flow rates, which corresponds to an opposite trend as compared to ΔP. The different values of f on the two sides is due to the different geometries, as shown in Table 3-4.

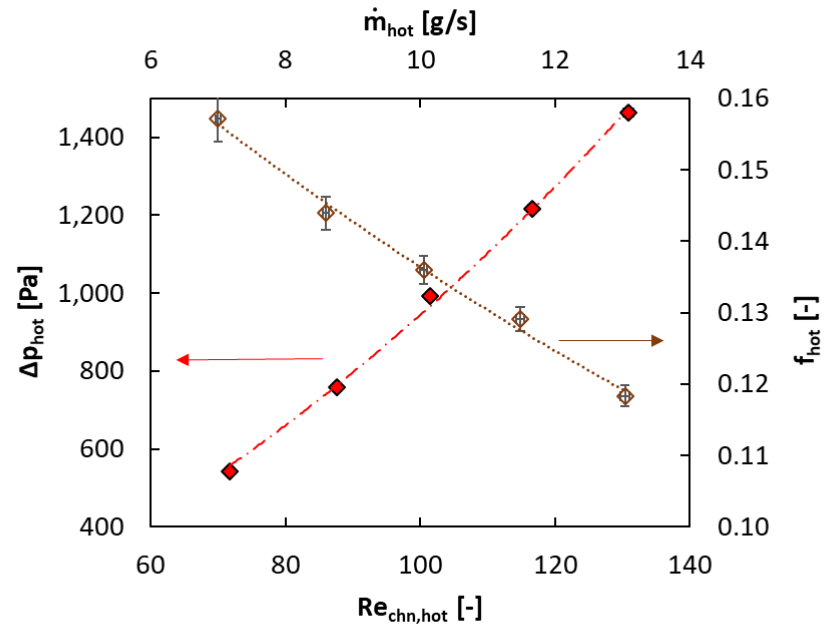

(a)

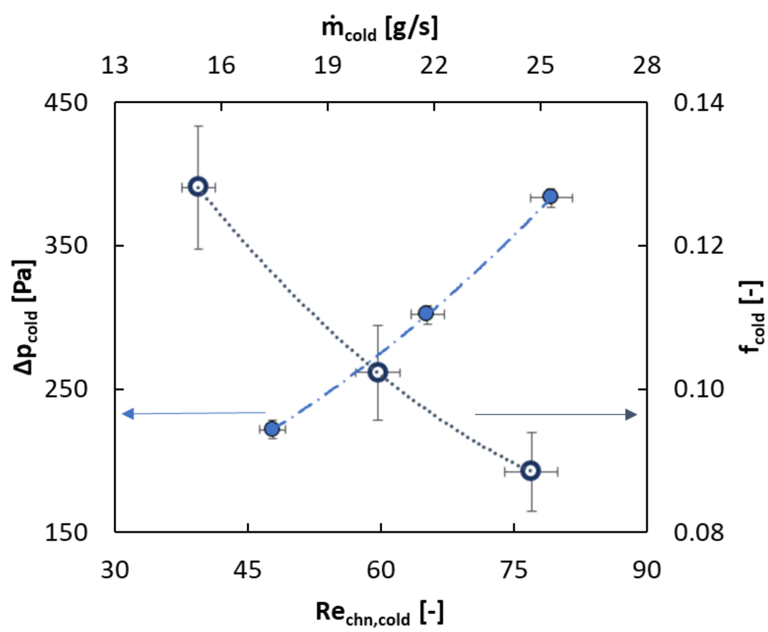

(b)

Figure 5-14: Pressure drop results of the 4" x 4" x 4" Subscale Unit (a) Hot-side pressure drop and friction factor; (b) Cold-side pressure drop and friction factor

5.6.3 Comparison with numerical model

The comparison between the numerical prediction obtained numerically (with the hybrid method and heat spreading model) and the experimental results is presented in Figure 5-15. Compared to the numerical data (shown as dotted lines), the average percentage error between the numerical and experimental results is calculated as 17% for the heat transfer performance (Figure 5-15(a)). For the pressure drops, the deviation between numerical and experimental is on average 9% and 4% for hot (Figure 5-15(b)) and cold (Figure 5-15(b)) sides, respectively. The causes of the deviation are the same as the ones mentioned for the low temperature test: printing defects in the manifold base, damage of few of the microchannels and partial clogging of the unit.

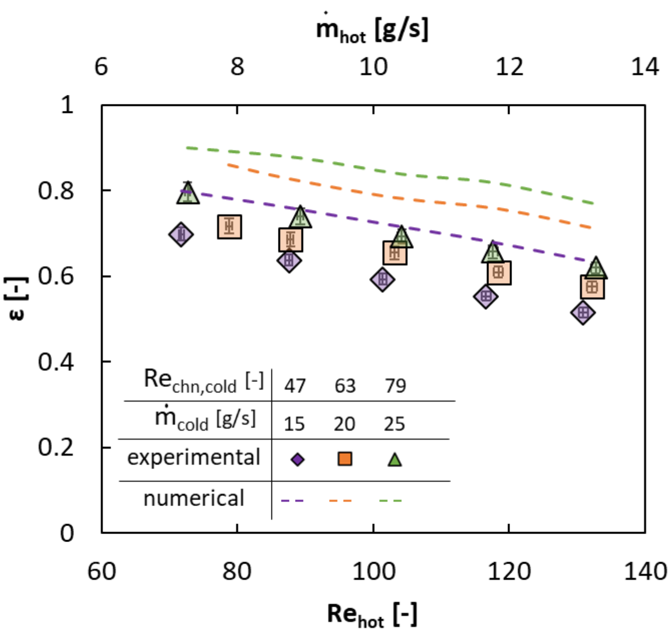

(a)

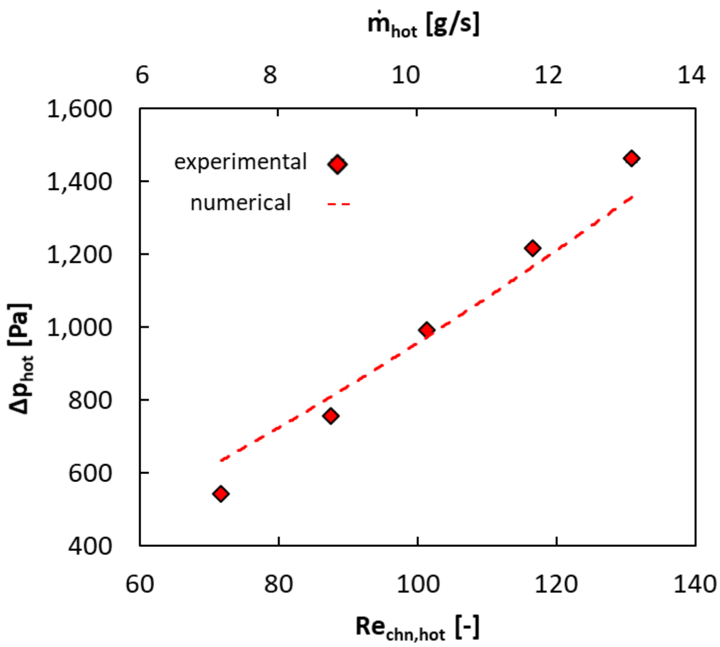

(b)

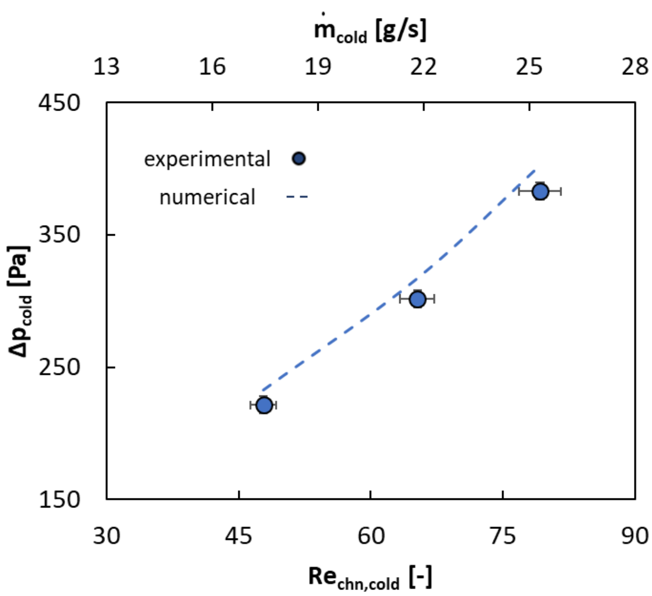

(c)

Figure 5-15: Comparison between experimental and numerical results of the 4" x 4" x 4" Subscale Unit: (a) Heat flow rate; (b) Hot-side pressure drop, (c) Cold-side pressure drop

5.7 Comparison of Low and High Temperature Results and Discussion

Dimensionless quantities can also be used for a comparison between low- and high temperature results. Figure 5-16 shows the friction factor (f) as a function of the Reynolds number in the channel (Re_{chn}). Hot- and cold side are shown in Figure 5-16(a) and Figure 5-16(b), respectively.

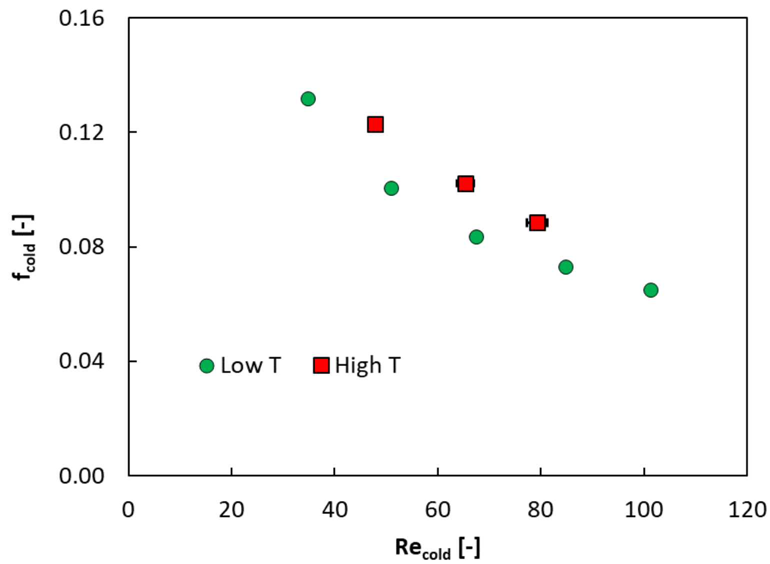

(a)

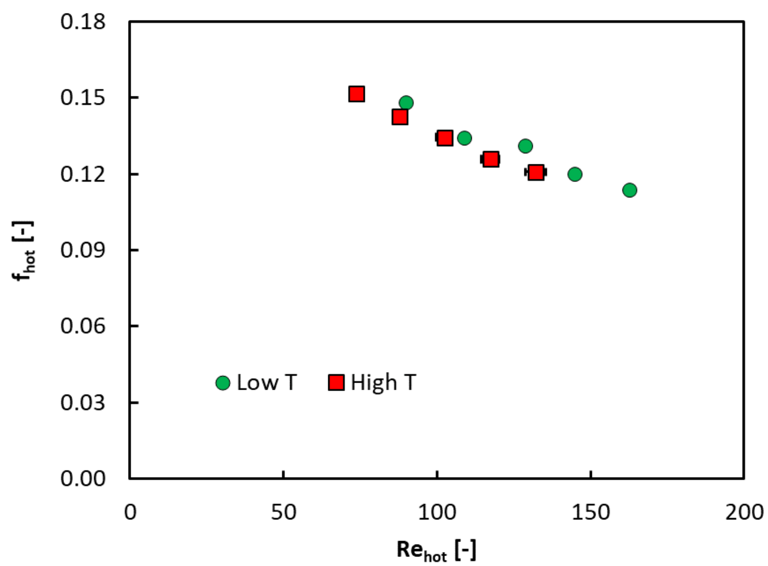

(b)

Figure 5-16: Comparison between high and low temperature results in terms of f vs Re_{chn} of the 4" x 4" x 4" Subscale Unit for (a) Cold-side (b) Hot-side

Figure 5-16 shows that a similar friction factor (f) was observed for the same Reynold numbers (Re_{chn}), thus proving consistency within the experimental results at the two different levels of temperature. Figure 5-17 shows the measured effectiveness of the HX for the two tests as a function of the hot mass flow rate ($\dot{m}_{hot}$) for the different values of cold mass flow rate ($\dot{m}_{cold}$).

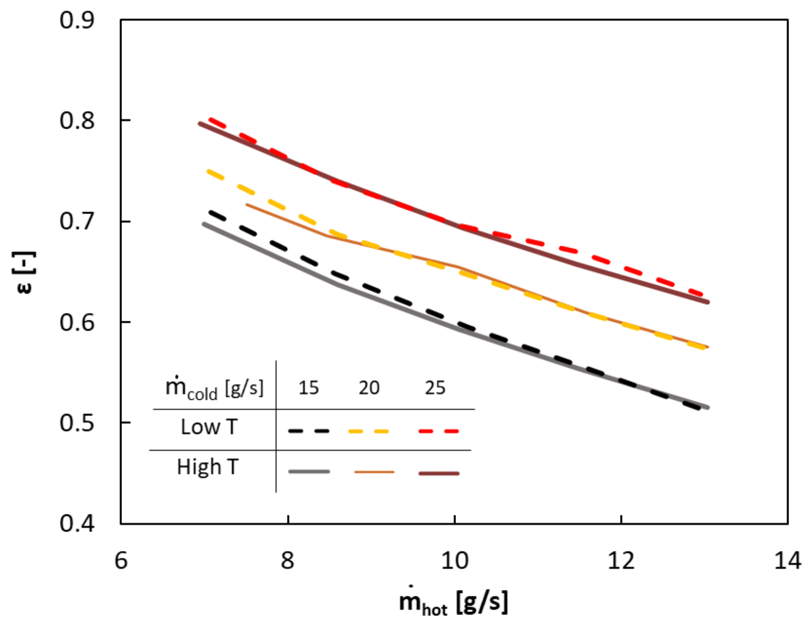

Figure 5-17: Comparison between high and low temperature results of the 4" x 4" x 4" Subscale Unit in terms of ε vs $\dot{m}_{hot}$

The same trend is also observed for the case of heat exchanger effectiveness. Once more, also from the thermal point, consistent experimental results are shown between the low temperature and high temperature testing.

5.8 Comparison with State of the Art

To rate M2HXs against conventional design HXs, the experimental results obtained during the performance testing are compared with the performance of conventional HXs. Based on a database provided in Ref. [6] and collected by EES software, several commercially available PFHXs are selected. The key geometrical specification of the selected PFHX surfaces are shown in Table 5-4.

Table 5-4: Key geometrical specification of conventional PFHX surface[6]

Name	Fin pitch [fin/cm]	Plate spacing (cm)
S1027T	4.04	1.38
S1477	5.82	0.838
S1110	4.37	0.635
S1508	5.94	1.06

The sizing process is performed by matching the heat duty (Q), HX effectiveness (ε), coefficient of performance (COP), and inlet temperature for both sides of the plate fins HXs to the corresponding values in the M2HX. The COP is evaluated considering pumping power on both sides of the HX, as

$$COP = \frac{Q}{\Delta P_{tot,hot}\dfrac{\dot{m}_{hot}}{\rho_{hot}} + \Delta P_{tot,cold}\dfrac{\dot{m}_{cold}}{\rho_{cold}}} \tag{40}$$

where

$$\Delta P_{tot} = \frac{\rho}{2}\left[\underbrace{v_{mnd}^2(k_c + 1 - \sigma_{in}^2)}_{\text{Entrance pressure loss}} + \underbrace{f\,\frac{v_{chm}^2 L_{flow}}{D_{H,chn}}}_{\text{Core pressure loss}} + \underbrace{v_{mnd}^2(1 - \sigma_{exit}^2 - k_e)}_{\text{Exit pressure loss}}\right] \tag{41}$$

where v_{mnd} is the velocity in the manifold channel, k_c is coefficient of contraction, k_e is coefficient of expansion, and σ is area ratio of minimum free flow area over frontal area. It must be noted that, as the cold-side loop is an open circuit with exit air facing the ambient, the coefficient of expansion is approximately 1 and exit area ratio (σ_{exit}) is assumed to be 0. Thus, the exit pressure loss in Eq. (41) is equal to zero. A more detailed description of the conventional surfaces geometries and the sizing method can be found in Ref. [60].

Figure 5-18 shows the performance comparison between the M2HX to PFHXs in terms of gravimetric heat transfer density ($Q/M\Delta T$) as a function of COP, where M is the overall mass of the HX and ΔT is the temperature difference between the hot and cold inlet temperatures. As expected, increasing COP decreases the heat transfer density because the smaller pressure drops negatively affect the heat transfer performance and the heat duty as a consequence. It is possible to see that for the same COP, M2HX yields more than 60% improvement in gravimetric heat transfer density ($Q/M\Delta T$) compared to PFHXs. When dealing with the aerospace industry, light weight and compactness is vital for HXs to break into the market.

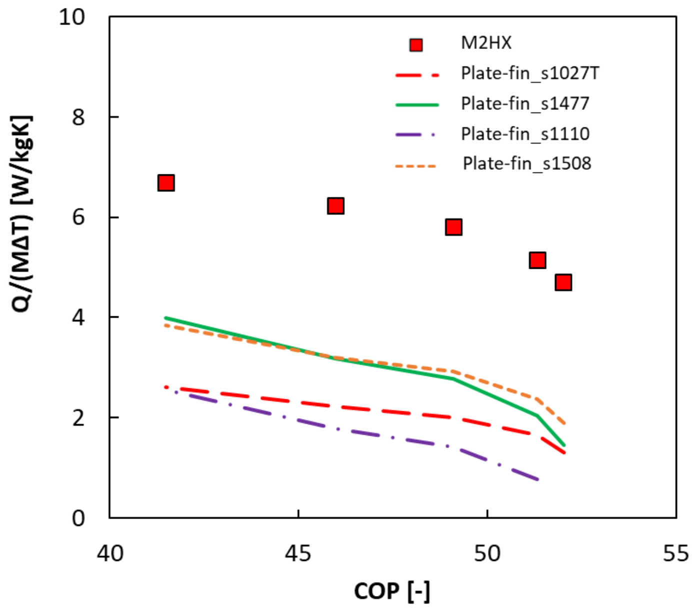

Figure 5-18: Performance comparison between the 4" x 4" x 4" Subscale Unit and PFHXs in terms of gravimetric heat transfer density

A very similar trend is also observed in Figure 5-19, which shows the performance comparison between the M2HX to PFHXs in terms of volumetric heat transfer density ($Q/V\Delta T$) as a function of COP, where V is the overall volume of the HX. Also in this case, M2HX yields more than 60% improvement in volumetric heat transfer density ($Q/V\Delta T$) compared to PFHXs The result shows that despite the fabrication imperfections, which reduces its performance, the performance of the printed M2HX is still superior to conventional PFHXs, warranting further investment in this technology.

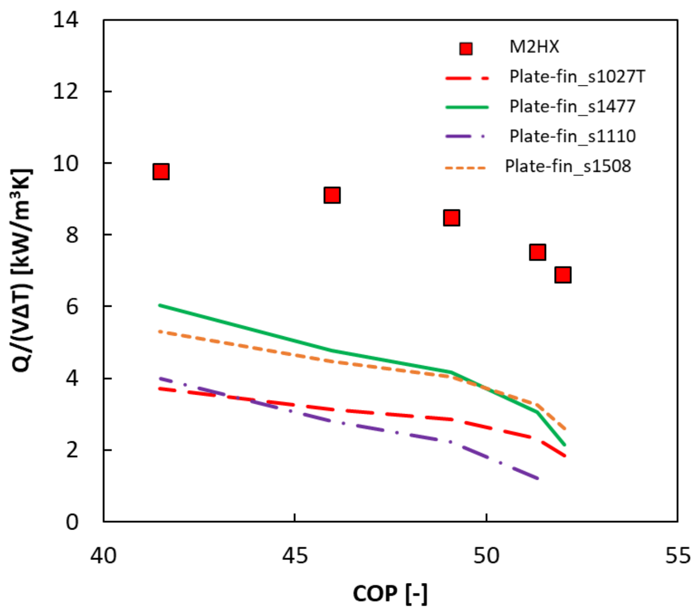

Figure 5-19: Performance comparison between the 4" x 4" x 4" Subscale Unit and PFHXs in terms of volumetric heat transfer density

Besides M2HXs, other HXs have been developed for both high temperature and high-pressure conditions. As mentioned in the introduction, PCHXs are a state-of-the-art design due to their structural strength under the high temperature and high pressure conditions. Despite the thermo-mechanical strength resulting from the fabrication process, PCHXs designs are usually limited, and the feature sizes are less compact than those of other HXs. Therefore, it is important to compare the performance of the M2HX and PCHXs. The performance results of the M2HX are those obtained experimentally. They are compared to a PCHX designed to have the same volume and to operate in the same range of COP shown in Figure 5-18 and Figure 5-19, with the same mass flow rates and inlet temperatures as those for the M2HX (see Table 5-3). It is important to emphasize that during the fabrication of the PCHX, the photo-chemical etching causes the channel cross section to have a semicircular geometry. The common correlations used for rectangular or circular channels can only approximate the actual performance. In order to avoid such approximations, a State-of-the-Art PCHX with zigzag channels as described by Liu et al. [180] is used for the comparison. The geometry of the PCHX described in [180] accounts for channel diameter ($D_{chn,PC}$), fin thickness, base plate height ($H_{base,PC}$) and also the specific fin efficiency ($\eta_{fin,PC}$). The performance of the PCHX is evaluated using the Nusselt number (Nu_{PC}) and friction factor (f_{PC}) correlation for the PCHX as derived by Kim and No [181].

First, the pressure drop of the PCHX core (ΔP_{PC}), which corresponds to the middle term of Eq.(41), is evaluated as:

$$\Delta P_{PC} = f_{PC} \frac{L_{flow,PC}}{D_{h,PC}} \frac{1}{2} \rho v_{chn,PC}^2 \tag{42}$$

where f_{PC} is the friction factor for the PCHX, $L_{flow,PC}$ is the average flow length of the channel in the PCHX, $v_{chn,PC}$ is the speed of the fluid in the channel, and $D_{h,PC}$ is the hydraulic diameter of a PCHX, defined as:

$$D_{h,PC} = \frac{D_{chn,PC}}{1 + \frac{2}{\pi}} \tag{43}$$

The definition of $D_{h,PC}$ is due to the semicircular nature of the PCHXs' channels. The heat duty (Q_{PC}) is obtained using the inverse process described in the experimental data analysis: the output of the experiments, in fact, was the heat duty, and overall heat transfer coefficient was the derived quantity. In this section, instead, the initial point is the UA and the final result is the heat duty of the PCHX. Starting from UA, it is possible to identify three steps in the heat transfer from the hot to cold side: convective conductance on both sides of the PCHX and conductive conductance across the base plate. For the convective term, it possible to adopt the values of $\eta_{fin,PC}$ of the PCHX described in [180]; and h_{PC} for each side of the HX is obtained from the correlations obtained by Kim and No [181] in terms of Nu_{PC} and substituting the thermo-physical properties of the fluids into the definition for the Nusselt number. For the conductive term, instead, the base plate height is described in [180], and the thermal conductivity of the solid (k_s) is that of Inconel 718 for a fair comparison with the M2HX. The UA value is then obtained as:

$$\frac{1}{UA_{PC}} = \underbrace{\frac{1}{\eta_{fin,PC,cold} \cdot h_{PC,cold} \cdot A_{PC,cold}}}_{\text{Convective term of the cold side}} + \underbrace{\frac{1}{\eta_{fin,PC,hot} \cdot h_{PC,hot} \cdot A_{PC,hot}}}_{\text{Convective term of the hot side}} + \underbrace{\frac{1}{\frac{k_s}{H_{base,PC}}}}_{\text{Conductive term across the base plate}} \tag{44}$$

where A_{PC} is the overall heat transfer area per side of the PCHX. From UA_{PC} it is then possible to calculate NTU_{PC} by the definition of NTU and using the operative conditions of Table 5-3:

$$NTU_{PC} = \frac{UA_{PC}}{C_{min}} \tag{45}$$

Using NTU_{PC} as input to the correlation for cross-flow HW with both fluids unmixed (see Eq. (33)), it is possible to obtain the effectiveness (ε_{PC}) of the PCHX. From ε_{PC}, the desired Q_{PC} is computed using the definition of effectiveness of an HX:

$$Q_{PC} = \varepsilon_{PM} C_{min}(T_{in,hot} - T_{in,cold}) \tag{46}$$

As to the overall mass, the volume of the solid part was multiplied by the density of Inconel 718.

Figure 5-20 shows the gravimetric heat transfer density of a PCHX as a function of COP, compared to the M2HX tested. For the trend shown in Figure 5-20, the observations discussed for Figure 5-18 still hold for both HXs. In particular, it can be seen that the performance of PCHX is comparable to some of the less enhanced PFHXs analyzed in Figure 5-18. As expected, a PCHX has a fairly simple design due to the fabrication limitations, and so the heat transfer area is not significantly increased, nor does the heat transfer coefficient benefit from small features. In a PCHX, in fact, the channel size is on the order of 1-2 mm [180], thus negatively affecting the compactness of the HX. Despite the outstanding structural performance, the bulkiness of the PCHX results in half the thermal performance of the M2HX, further emphasizing the superiority of the M2HX in case of ECS, where the lightness of the component is crucial.

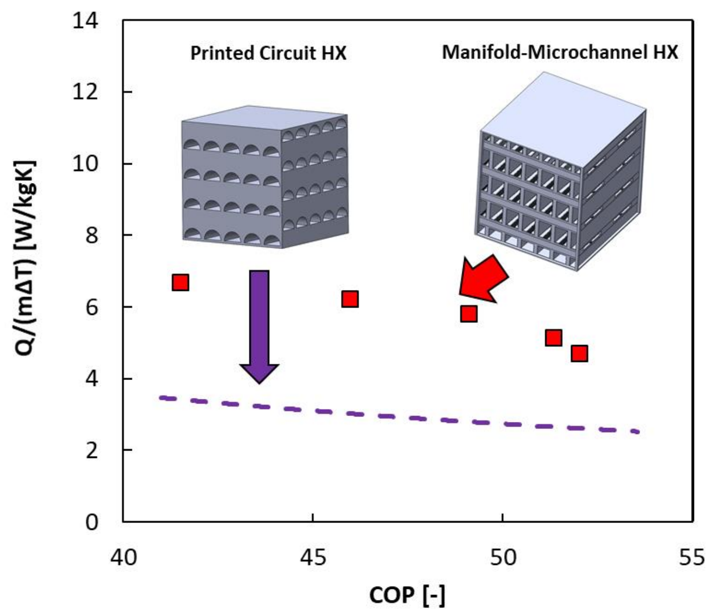

Figure 5-20: Performance comparison between M2HX with printed circuit HXs

5.9 Summary

In summary, the model used to design the metal headers was introduced and the final design of the metal headers reduced the maldistribution to 3% and 6% for hot- and cold-side respectively. Based on the design obtained, the headers were 3D printed out of Inconel 718 and welded to the core. The assembled unit was then installed in the experimental setup and tested under low and high temperature. Consistency in the data between the low and high temperature was observed. For the high temperature test, an overall heat transfer of 49 W/m^2K was obtained for Reynolds number values of 132 and 79 for cold and hot sides, respectively. Gravimetric heat transfer density ($Q/M\Delta T$) of 4.7-6.7 W/kgK and volumetric heat transfer density ($Q/V\Delta T$) of 6.9-9.8 kW/m^3K were recorded for this heat exchanger with coefficient of performance value that varies from 42 to 52, over the operating conditions studied. The maximum heat exchanger capacity was 2.2 kW for a temperature difference of almost 300°C between hot- and cold-side inlets. The experimental pressure drop results were within 10% of the numerical predictions, while the heat transfer results deviated up to 17%, from the numerical prediction. The deviation was mainly due to the imperfections in the fabrication process. Despite this penalty, the performance of the tested heat exchanger was superior to the conventional plane plate-fin heat exchangers: more than 60% improvement in both gravimetric and volumetric heat transfer densities was recorded for the entire range of experimental data.

Chapter 6 : 4.5” x 4” x 3.5” Unit Design and Fabrication

6.1 Introduction

This chapter presents the quality assessment of the printer at the University of Maryland additive manufacturing center. Test coupons were printed to verify the printer capability to fabricate thin fins and leak proof separating walls. Based on the outcome of this study, a new optimization was run and a new optimized set of parameters obtained. The full-scale heat exchanger was then scaled down to match the build size capability of the printer.

6.2 In-House Printing Capability

Despite the positive results obtained by the 4” x 4” x 4” HX, two crucial limits were observed that need to be addressed to fabricate a more enhanced unit. First, the fin thickness obtained using outsourced printers was not as small and accurate as the one fabricated with the in-house printer with customized printing parameters. Second, defects were found in the unit after the fabrication, thus causing deviation from the predicted performance. A possible way to overcome those limitations is to directly control the process of the unit fabrication. In order to verify this option, the material used for the ProX 200 at University of Maryland was changed from maraging steel into Inconel 625.

6.2.1 Printing Orientation

The first parameter that needs to be defined is the printing orientation. As shown in Table 4-1, ProX 200 has a smaller build volume compared to the outsourced printers. Due to the limitation in the build size (5” x 5” x 4”) of ProX 200, the orientation of the M2HX becomes crucial to determine the volume of the unit. Figure 6-1 shows the two possible printing orientations and the resulting dimensions of the unit. A 2.8” x 2.8” x 2.8” HX can be fabricated if the HX is printed with the orientation of α=45°, as shown in Figure 6-1(a). Printing with an orientation of α=0°, instead, allows for a 4”x4”x4” unit. Comparing the resulting volumes, it can be observed that adopting the orientation of α=0° increases the volume by more than 100%. Although α=45° can provide higher performance, α=0° has an optimized space utilization, resulting in significantly bigger HX, while having similar printing time and cost, which are dominated by the vertical height in the printing direction (the same for both the orientations).

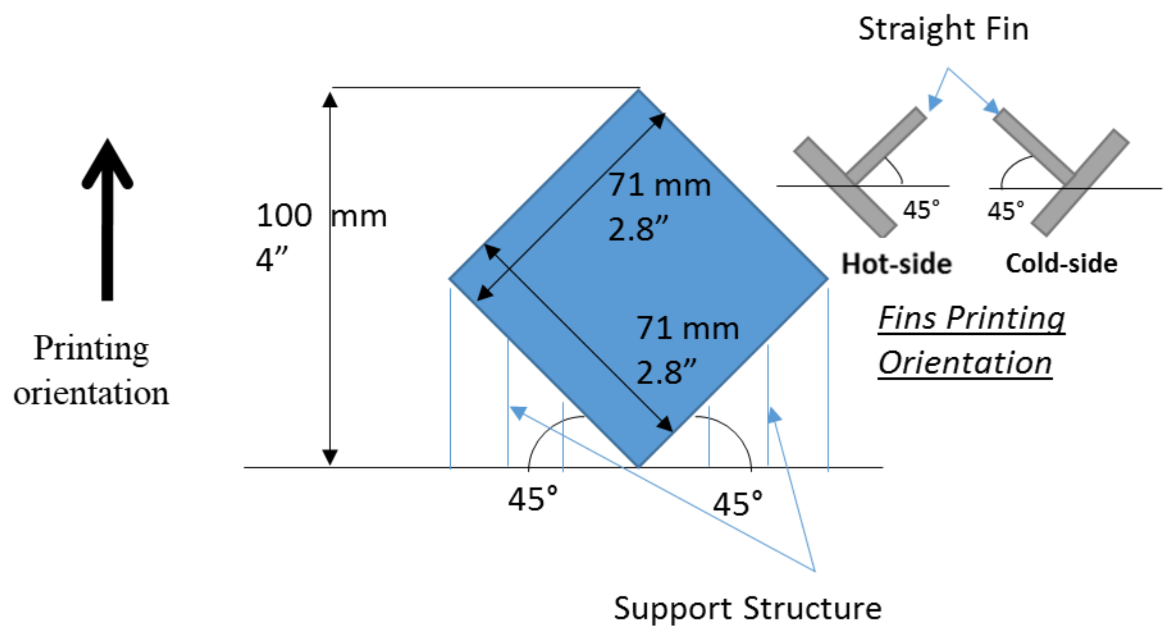

(a)

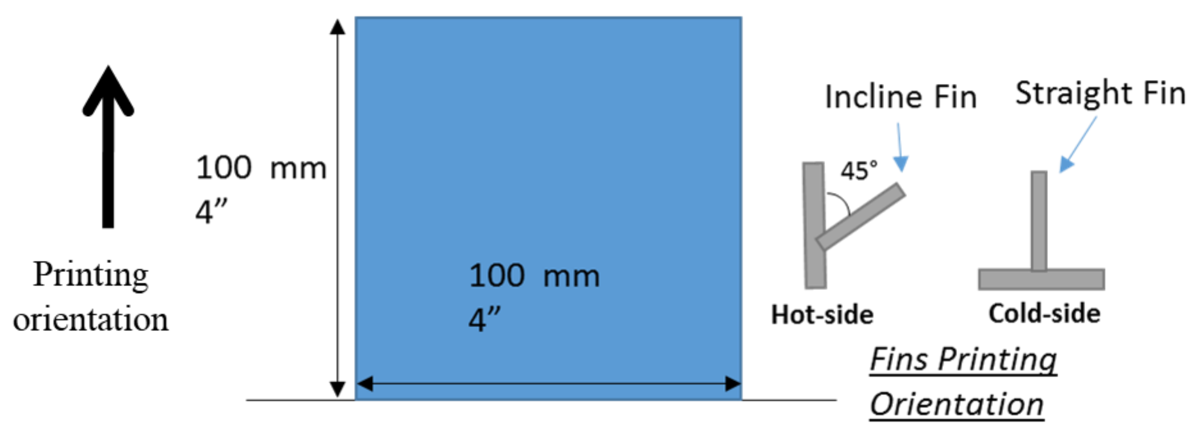

(b)

Figure 6-1:Second HX Unit Printing orientation options and resulting dimensions

6.2.2 Fin Thickness Study

As discussed in Section 4.4, one of the most important factors that significantly impacts the performance of a M2HX is the fin thickness. Figure 6-2 shows a series of coupons that were printed with the printing orientation shown in Figure 6-1 (b). Inclined and vertical straight fins are shown in Figure 6-2(a) and Figure 6-2(b), respectively. The fin study coupons were used to check printer resolution for different design values (fin thickness of 150, 125, 100 and 75 μm), different fin height (1 mm and 0.259 mm) and different laser powers (300 W and 225 W).

(a)

(b)

Figure 6-2: Printed fins test coupons using ProX 200 for (a) inclined fin study, (b) straight fins study

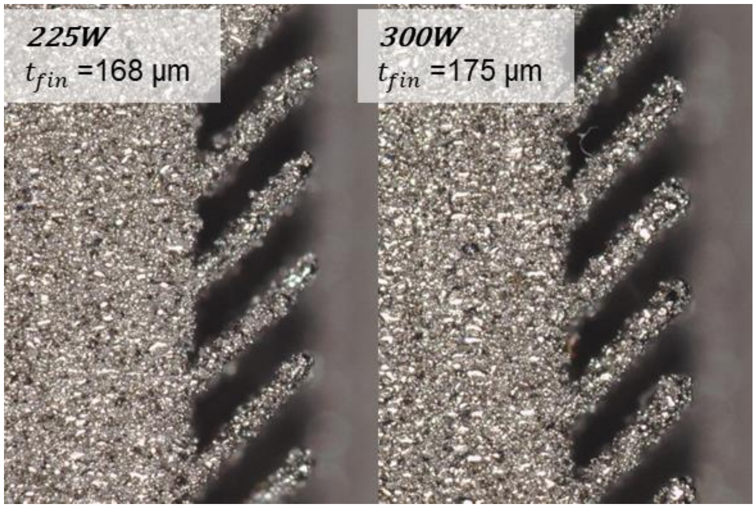

(a)

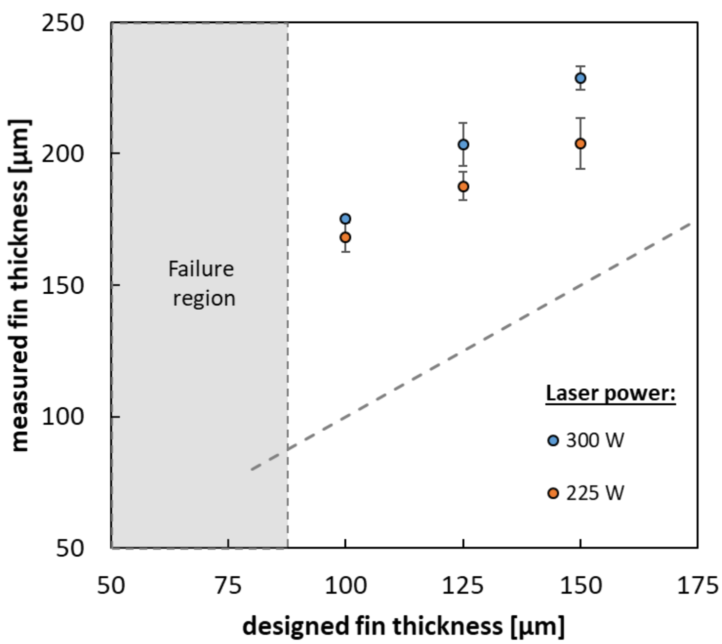

(b)

Figure 6-3: Inclined fins study results (a) Zoom in view of the fins with a design fin thickness of 100µm and laser power of 225W (left) and 300W (right), (b) Measured fin thickness vs design fin thickness comparison

Figure 6-3 shows the inclined fins' fabrication results for design fins of 100 µm. A deviation of 70-80 µm from the design to the actual print size was measured, when the laser power was set to the default value of 300 W. When lowering the laser power to 225 W, instead, the difference reduced to 65-70 µm. As shown in Figure 6-3 (a), fins as small as 168 and 175 were observed for 225 and 300 W, respectively. Designing fin thickness smaller than 100 μm resulted in failed print. The comparison between measured fin thickness and design fin thickness is summarized in Figure 6-3 (b). Based on the outcomes of the fin thickness study, a laser power of 225 W is preferable compared to the default 300 W.

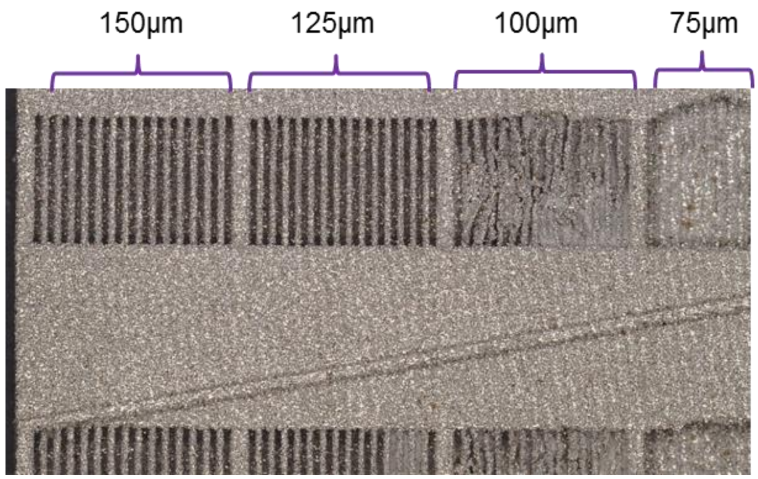

(a)

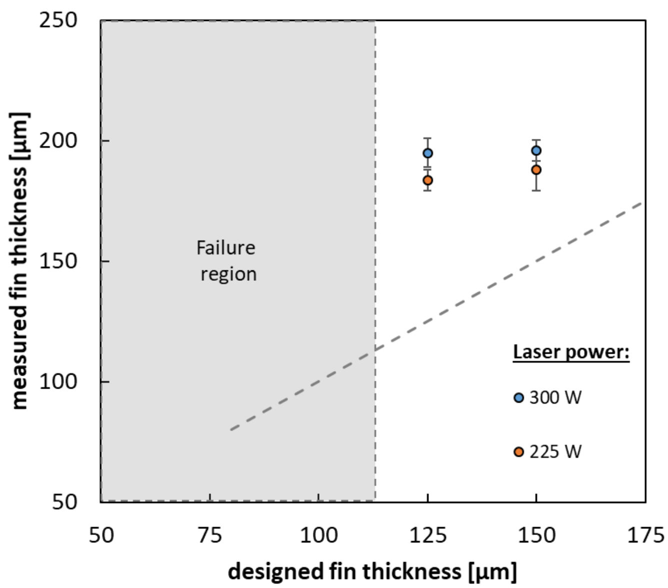

(b)

Figure 6-4: Vertical fin results (a) Zoom in view of the fins (b) Measured fin thickness vs design fin thickness comparison

Figure 6-4 shows the straight vertical fins' fabrication results. Only fins with design value of 125 μm or bigger were successfully fabricated, as shown in the Figure 6-4(a). A fin thickness of 195 μm for both design values (125 and 150 μm) was measured when the laser power was set to the default value of 300 W. When lowering the laser power to 225 W, instead, the value reduced to 185 μm. The comparison between measured fin thickness and design fin thickness of the vertical straight fins is summarized in in Figure 6-4 (b). Laser power of 225 W confirmed to provide lower fin thickness compared to the default 300 W.

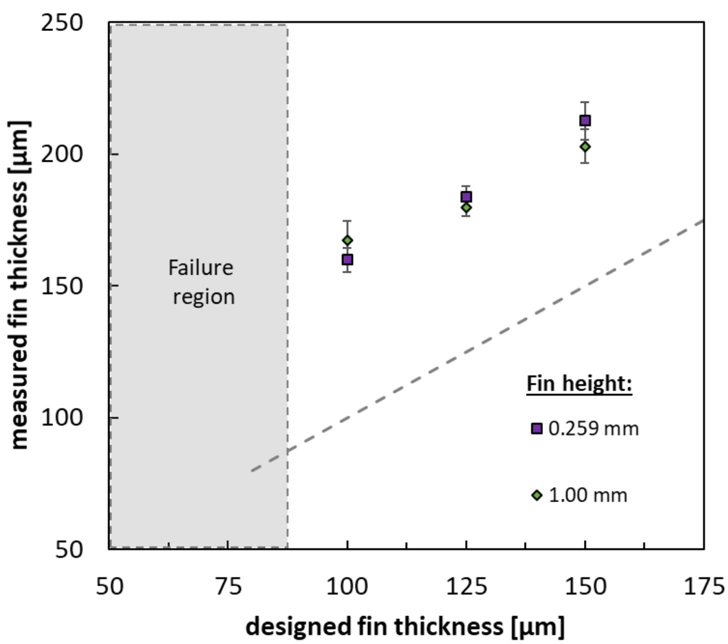

Figure 6-5: Measured fin thickness vs design fin thickness comparison for different fin heights

Figure 6-5 shows the comparison of the fin thickness for two values of fin heights (1.00 mm and 0.259 mm). The measurements of the fin thickness for the two different heights were very close. It can be observed that in range of fin height studied, fin thickness is not affected by the height of the fin.

6.2.3 Manifold Wall Study

When printing with an orientation of 0°, the design of the manifolds of the M2HX has also to be carefully considered. As shown in Figure 4-3, the manifold of the side with straight vertical channels has to be inclined in order to avoid the presence of supports inside the HX. Therefore, it is necessary to verify that the thickness of the manifold wall (t_{wall}) is properly sized. Manifold wall thickness of 300 μm was designed for manifold height of 3.0 mm. Figure 6-6 shows the CAD design and the successful print of the inclined tapered manifold.

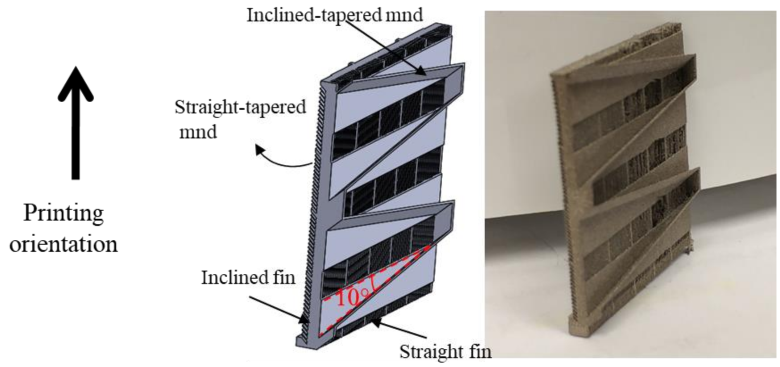

Figure 6-6: Design and printed coupon of an inclined-tapered manifolds

6.2.4 Base Thickness Study

As discussed in Section 4.5, another important design parameter that significantly impacts the performance of a M2HX is the base thickness. The same approach described in Section 4.5 was followed to assess the minimum wall thickness that can withstand the design pressure. The pressure containment coupons were designed based on Figure 4-11 with three wall thicknesses: 300 μm, 350 μm, and 400 μm. All three coupons shown in Figure 6-7 were pressurized up to 390kPa.

(a)

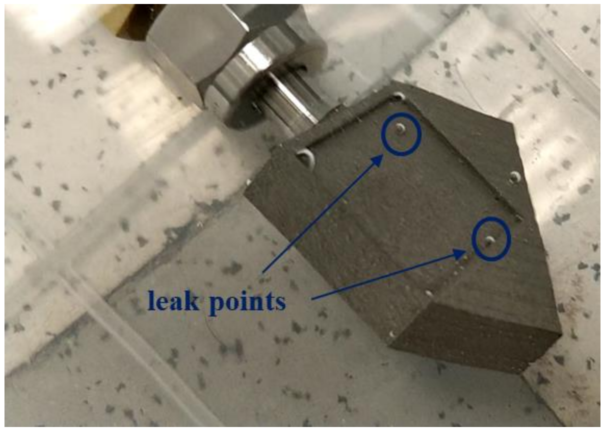

(b)

Figure 6-7: (a) Pressure containment coupons machined, (b) leak test results for a designed wall thickness of 300 µm

Table 6-1 summarizes the result of the pressure containment study. No leakage was observed on the 400 µm coupon. However, a small leak was observed on the 300 µm (as shown in Figure 6-7(b)) and 350 µm coupons. These results show that 400 µm is the minimum base thickness that allows to fabricate a leak free HX.

Table 6-1: Results of pressure containment check coupons of the ProX 200 unit

Design base thickness	Leak test outcome
300 µm	Small leakage
350 µm	Small leakage
400 µm	No leakage

6.2.5 Manifold Base Study

One of the printing defects observed in the first unit was the presence of printing defects in the manifold base, which could cause flow bypass and negatively affect the HX performance as a consequence. Figure 6-8 shows the zoom in view of the manifold base of the fin study coupons. Compared to the first unit, printing defects are not visible.

Figure 6-8: Zoom in view of the manifold base

6.2.6 Surface Finish

As explained Section 4.6, in order to evaluate the surface finish capability of the ProX 200 with Inconel 625, the pressure test coupon surface was analyzed using Keyence 3D digital microscope at University of Maryland, AM Center. Figure 6-9 shows that the surface is not uniform, with a concentration of roughness on the left side of the sample.

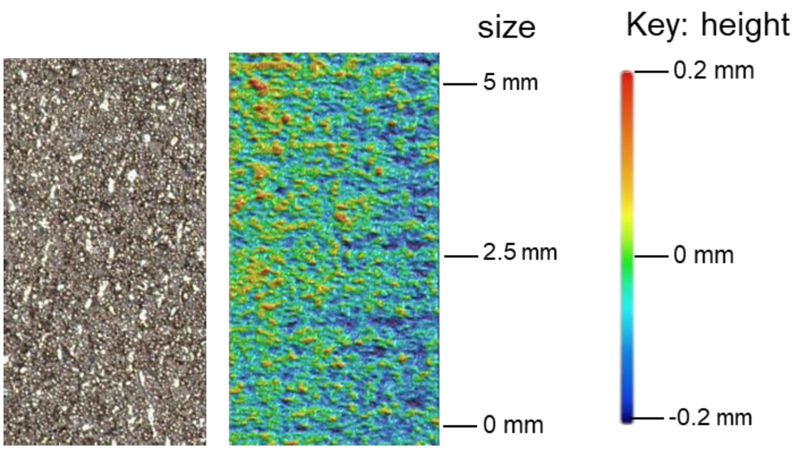

Figure 6-9: Coupon roughness ProX 200 (Inconel 625) (a) microscope image (b) 3D rendering

In order to characterize and quantify the level of roughness, the value of root mean square height (Sq), arithmetic mean peak curvature (Spc) and developed interfacial area ratio (Sdr) are listed in Table 6-2.

Table 6-2: Surface finish results of the ProX 200 using Inconel 625

Printer	**Sq [mm]**	**Spc [1/mm]**	**Sdr [-]**
ProX 200 (Inc625)	0.008	3.488	0.0082

Comparing the results of Table 6-2 and Table 4-4, it is possible to notice that the value of Sq obtained with the ProX 200 is similar to ProX 300 and lower than EOS M290, thus suggesting a superior quality of the surface finish that 3D System machines can print. The values of Spc and Sdr, instead, fall between ProX 300 and EOS M290. As a consequence of this analysis, switching to ProX 200 provides surface finish similar to the other printers analyzed for the fabrication of the first unit.

6.3 Full-Scale Unit Design

Despite the fabrication defects that limited the performance of the first unit, M2HXs design proved to be competitive with the other design. For this reason, the design selected for the second unit is again M2HX.

6.3.1 Optimization Process

The optimization process to obtain the design of the second unit follows the same steps as the one described in 3.5.2: design of experiment, metamodel creation, single-objective optimization and metamodel validation. Out of those four steps, the single-objective optimization is the one only one that needs to be updated.

Using the final problem definition of Eq. (7) as reference, design requirements (Table 3-1) and operative conditions (Table 3-2) are the same. Moreover, also the geometrical constraints of M2HXs described by Eqs. (8)-(9) need to be imposed. As to the optimization costraints based on the AM capibility, instead, the outcomes of the coupons study of ProX 200 need to included. The differences compared to the constraints mentioned in Table 3-3 are summarized in Table 6-3.

Table 6-3: AM optimization constraints for the second HX

Parameter	Constraint	Improvement over first unit
$W_{mnd-chn}$	2-45 mm	80% longer
t_{fin}	$\geq$ 0.150 mm	25% smaller
$H_{chn,base}$	$\geq$ 0.400 mm	20% smaller

Table 6-3 shows the significant improvement of two of the most important parameters of M2HX: fin thickness and base thickness can be reduced respectively by 25% and 20% compared to the first unit. Moreover, based on the successful outcomes observed during the powder removal process of the coupons, it was chosen to allow for longer microchannels. Based on pressure drop requirements and the high effectiveness (ε =90%), having longer microchannels can enhance the performance.

6.3.2 Optimization Results

Based on the updated optimization process, the optimal set of variables for the second unit is shown in Table 6-4. It has to be mentioned that the side with the inclined fins is the hot one. The description of fin thickness, channel with and channel height with respect to an inclined fin is shown in Figure 6-10.

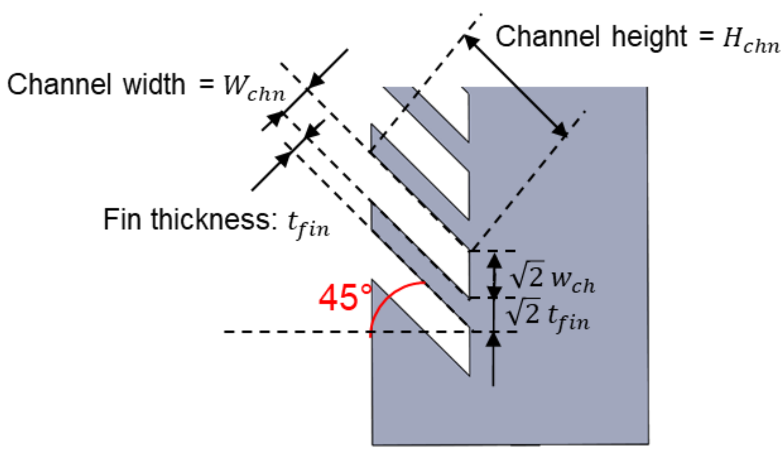

Figure 6-10: Nomenclature for inclined fins

Table 6-4: Full-scale parameters obtained from single objective optimization for the second unit

Parameter		Unit	Value
Cold side	W_{chn}	mm	0.27
	t_{fin}	mm	0.165
	H_{chn}	mm	1.25
	W_{in}	mm	2.5
	$W_{mnd-chn}$	mm	8.67
	$H_{mnd,base}$	mm	0.150
	H_{mnd}	mm	14.0
	N_{mnd}	-	76
	N_{chn}	-	205
Hot side	W_{chn}	mm	0.23
	t_{fin}	mm	0.150
	H_{chn}	mm	1.00
	W_{in}	mm	2.00
	$W_{mnd-chn}$	mm	44.74
	$H_{mnd,base}$	mm	0.150
	H_{mnd}	mm	8.6
	N_{mnd}	-	2
	N_{chn}	-	1,268
H_{base}		mm	0.400
N_{stack}		-	20

6.3.3 Full-Scale M2HX Projected Performance

The HX with the parameters described in Table 6-4 is the full-scale M2HX used to compare the performance of the current design with the requirements of the problem statement. The results of this comparison, including the first full-scale M2HX of Table 3-5, are shown in Table 6-5.

Table 6-5: Performance comparison between target and second full-scale M2HX

	Unit	Target	Full-scale M2HX	Second Full-scale M2HX
COP	-	>47.6	53	52
ε	-	>0.9	0.9	0.9
L_{cold}	mm	--	94	90
L_{hot}	mm	--	686	682
$L_{no-flow}$	mm	--	257	266

V	L	--	16.6	16.2
M	kg	<21.5	19.4	16.75

Table 6-5 shows that all the requirements of the problem statement are matched, with a 22,1% mass reduction of the second M2HX, compared to the target.

6.4 Subscale 4.5” x 4” x 3.5” Unit Design

As mentioned in Section 3.6, due to the limitation of the building volume of the current 3D printers, the designed HX was scaled down to a size compatible with the printing capability of ProX 200. The procedure followed was the same as the one mentioned in Section 3.6. The results of the scale-down procedure are reported in Table 6-6.

Table 6-6: Scale down procedure outcomes of the 4.5” x 4” x 3.5” unit

Parameter	**Full-scale**	**Subscale**	**Deviation**
N_{stack}	20	10	-55.6%
$N_{mnd,cold}$	94	6	-92.1%
$H_{mnd,cold}$	14.0 mm	14.0 mm	0%
$N_{chn,cold}$	205	205	0%
$N_{mnd,hot}$	2	2	0%
$H_{mnd,hot}$	8.6 mm	3.0 mm	-65.1%
$N_{chn,hot}$	1,268	101	-92.0%
L_{cold}	0.090 m	0.090 m	0%
L_{hot}	0.682 m	0.055 m	-92.0%
$L_{no-flow}$	0.266 m	0.115 m	-56.8%
M	16.75 kg	0.67 kg	-96.0%

6.4.1 4.5” x 4” x 3.5” M2HX Unit

For fabrication, the full-scale M2HX was scaled down to 4.5” x 4” x 3.5”, as shown in Figure 6-11(a). The cross section view of the hot-side with inclined fins and straight manifolds is shown in Figure 6-11(b). The cross section view of the cold-side with straight fins and inclined tapered manifolds is shown in Figure 6-11(c).

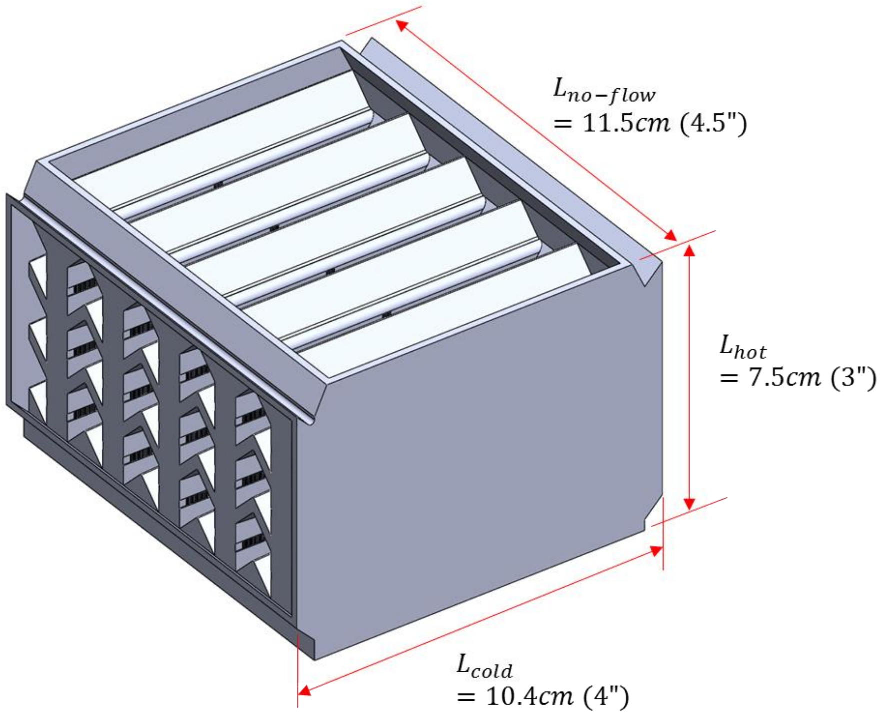

(a)

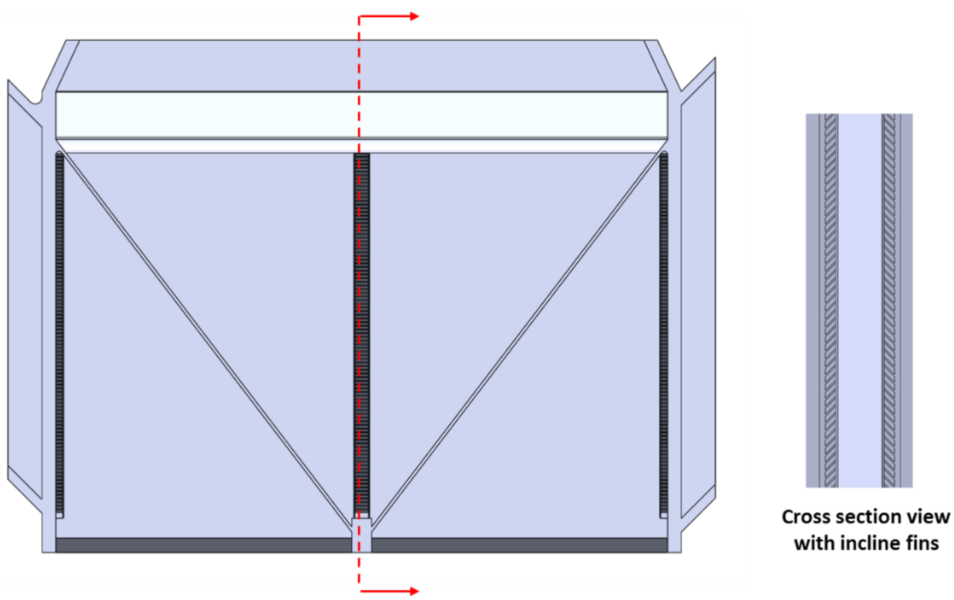

(b)

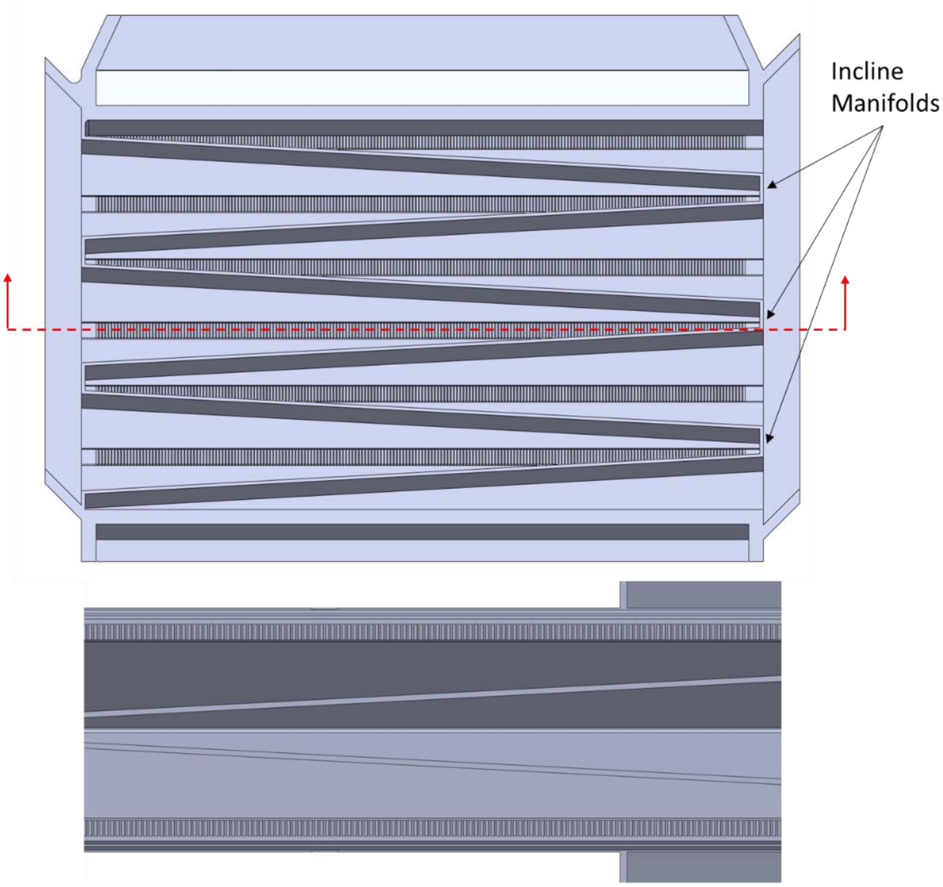

(c)

Figure 6-11: : 4.5" x 4" x 3.5" M2HX unit (a) isometric view, (b) hot-side with inclined fins and straight manifolds, (c) cold-side with straight fins and incline manifolds

6.5 4.5" x 4" x 3.5" Unit Fabrication and Evaluation

Following the same criterion explained in Section 4.7.1, the unit was oriented with an angle β=10° with respect to the axis perpendicular to the direction of the recoater (see Figure 6-12(a)). Figure 6-12(a) also shows the support added to facilitate the preliminary powder removal process required before removing the part from the base plate. This second unit was successfully fabricated at University of Maryland's AM facility, the excessive powder removed and EDM wire cutting was used to separate the unit from the base plate, as shown in Figure 6-12(b).

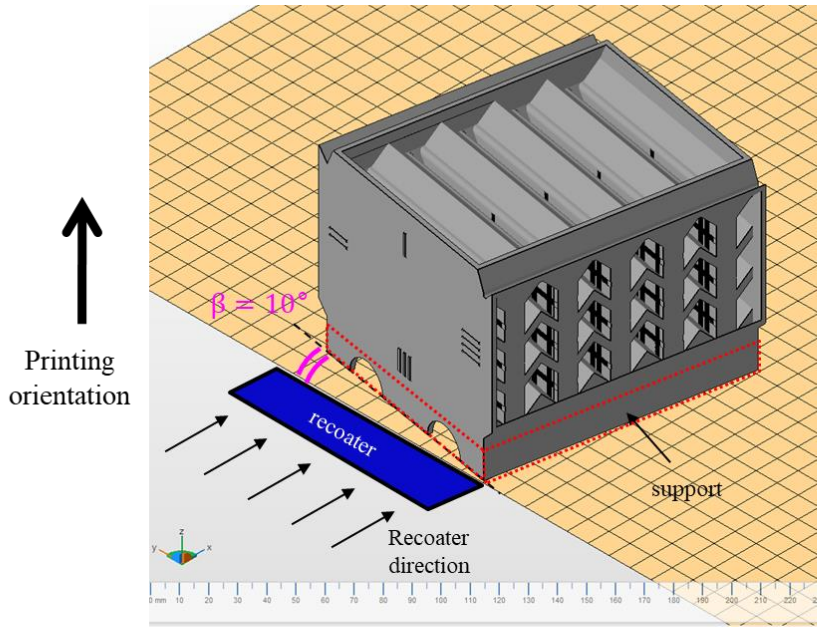

(a)

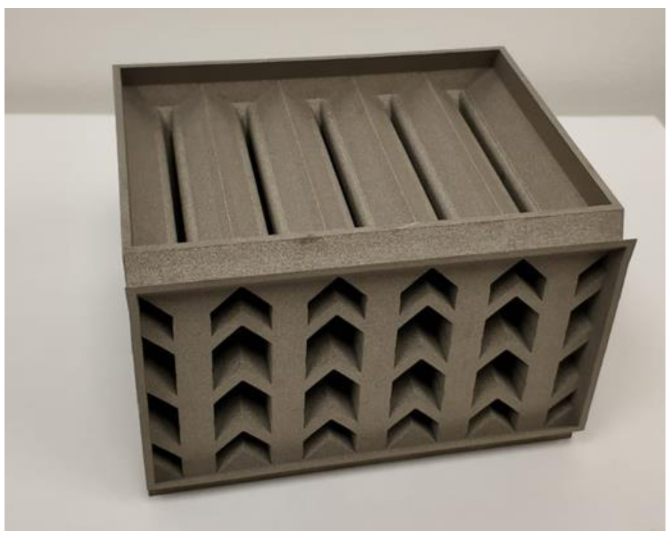

(b)

Figure 6-12: 4.5" x 4" x 3.5" Inconel 625 M2HX (a) printing orientation (b) fabricated unit

The ultrasonic cleaner was then used to remove the remaining non-sintered powder. After repeating the powder removal procedure multiple times, the mass of the unit was measured and confirmed to be within 2% of the design mass, thus excluding the chance of significant clogging in the microchannels. A coupon representative of the internal features of the HX was also printed together with the unit. The measurements of the hot- and cold-side fins were measured as 0.17 mm and 0.185 mm, respectively, thus confirming the outcomes of the fin thickness study.

When tested on both sides under the design pressure, the HX showed a small internal leakage. The unit was then sent to an outside company to undergo HIP process to improve its microstructure and eliminate porosity. The HX was processed at a temperature of 1,163°C and a pressure of 15,000 psi for four hours. After the HIP process, the leak test was repeated at the designed pressure. No leakage was observed this time, thus confirming the success of the HIP process. Although recognizing the possible effect of the HIP on closed feature, CT scan was not performed before and after the treatment. Therefore, it is not possible to evaluate the consequences directly. However, the experimental results will indirectly confirm the design or highlight possible major deviations.

6.5.1 Preliminary Isothermal Pressure Drop Test

A preliminary isothermal pressure drop test was performed on both sides of the HX in order to assess the quality of the printed unit. A significant deviation from the expected values would occur in case of presence of clogging, misaligned fins, features size different from the design ones or other important printing defects.

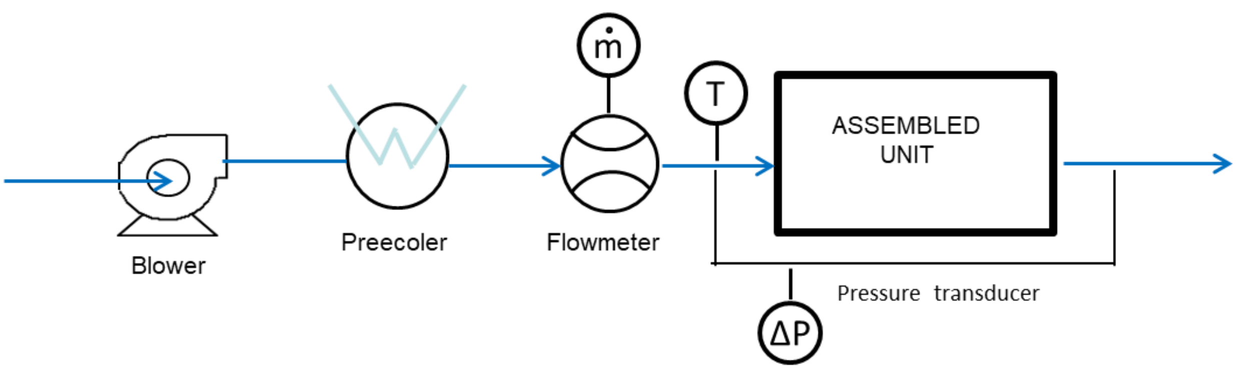

Figure 6-13: Schematic diagram of the experimental setup for the preliminary isothermal pressure drop

The schematic diagram of the experimental setup is shown in Figure 6-15. The blower was used to provide the desired flow, while the temperature at the inlet of HX was controlled with the precooler. Plastic headers were 3D printed and a system of rods and nuts with silicone gaskets as interfacial elements was used to connect the unit to the rest of the setup, as shown in Figure 6-14.

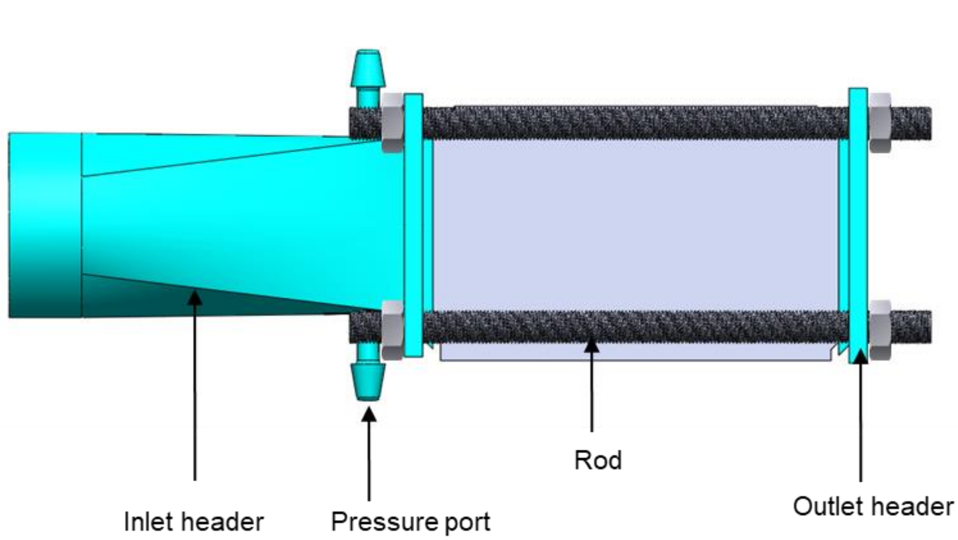

Figure 6-14: Assembled unit with plastic headers

Mass flow rate was measured by Coriolis flow meter, while the pressure transducer measured the pressure drop between the pressure port at the inlet of the HX and the ambient. Three thermocouples were used to measure the temperature at the inlet. All the measuring devices were connected to a data acquisition system (DAQ) to collect real-time values.

Isothermal testing was performed on both sides of the HX and the experimental data were compared to the numerical prediction, as shown in Figure 6-15. The hot side pressure drop was within 16% of the numerical prediction (see Figure 6-15(a)), while the cold-side pressure drop was within 9% of the numerical prediction (Figure 6-15(b)). Despite small leaks noticed at the interface between plastic header and HX, the results are sufficiently close to the numerical model, thus further validating the absence of significant printing defects in the HX due to sintering or HIP treatment.

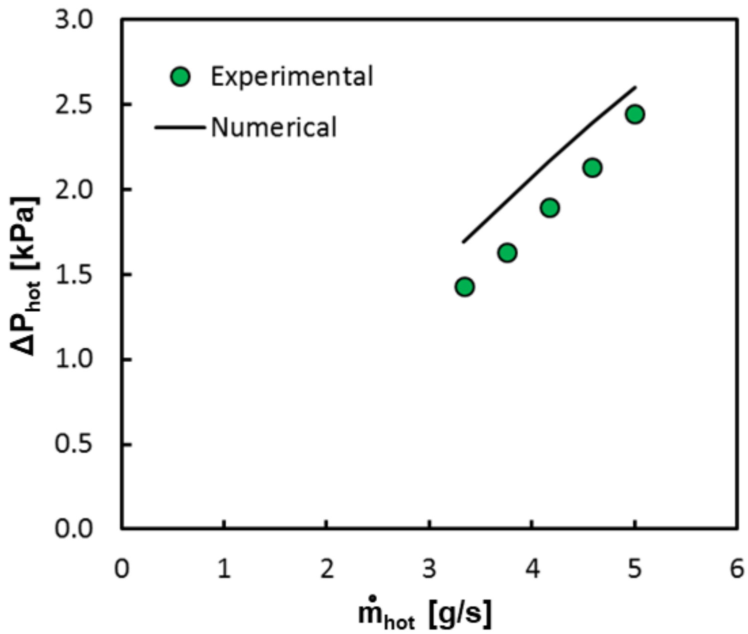

(a)

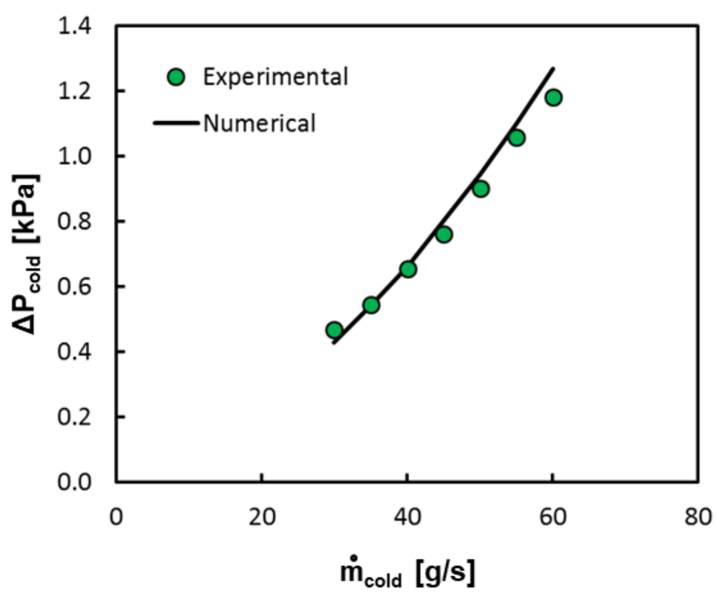

(b)

Figure 6-15: Preliminary isothermal testing results (a) Hot-side pressure drop (b) Cold-side pressure drop

6.6 Metal Header Design and Fabrication

In preparation for testing, cold- and hot-side headers were designed as shown in Figure 6-16. The headers of the cold side were designed to connect the cold side of the HX to the 2” piping system of the setup. For the hot side, instead, the connection was made for the 1” piping system of the hot side of the setup.

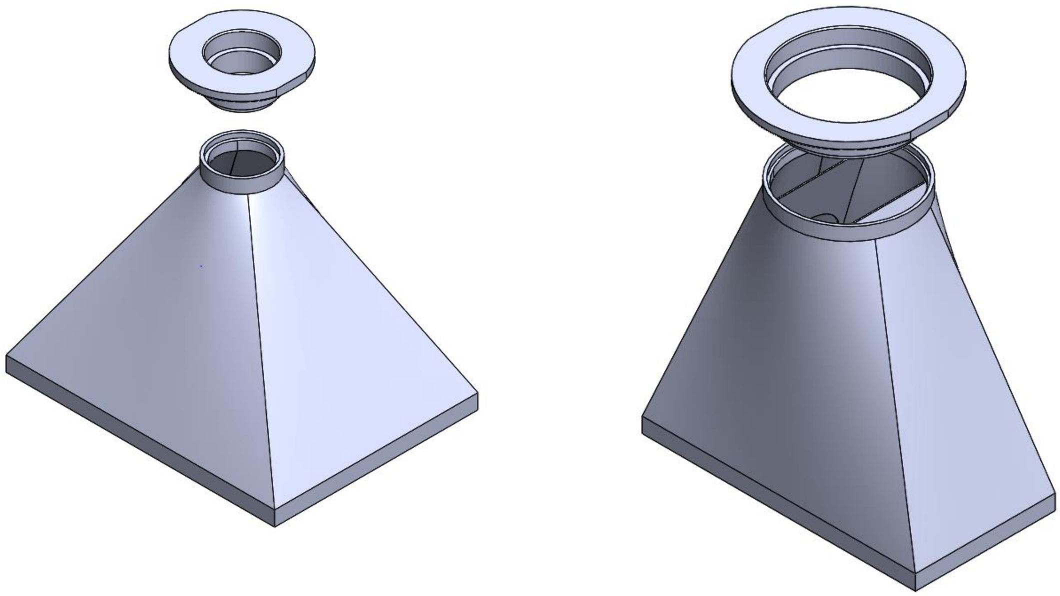

(a) (b)

Figure 6-16: Header and flange design: (a) hot-side (b) cold-side

The procedure described in Section 5.2.1.1 was followed to perform the CFD simulation to evaluate the pressure drop and flow maldistribution in cold-side headers. Flow deflectors were added into the design in order to reduce the flow maldistribution. The cold-side header pressure drop is estimated to be 20% of the core pressure drop with the flow maldistribution of 10%. For the hot-side, as the dynamic pressure is calculated to be less than 3% of the expected pressure drop, a uniform flow is expected.

Headers and flanges were successfully fabricated by the ProX 200 at the University of Maryland’s AM facility out of Inconel 625. Headers and flanges were fabricated out of the same material as the HX core to allow for the different parts to be welded together. As a matter of fact, the flanges needed to be fabricated separately from the headers to avoid overhanging structures that require support material, as shown in

Figure 6-16. The fabricated hot- and cold-side headers and flanges are shown in Figure 6-17(a) and Figure 6-17(b), respectively. Figure 6-18, instead, shows the complete assembly, including core, headers and flanges.

(a) (b)

Figure 6-17: Fabricated headers and flanges (a) cold side (b) hot side

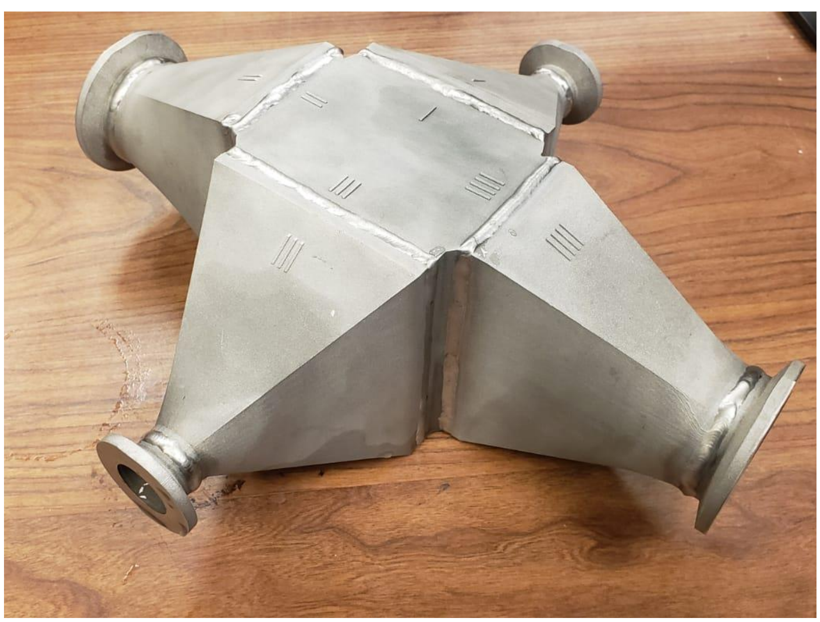

Figure 6-18: 4.5" x 4" x 3.5" unit with headers and flanges

6.7 Summary

In summary, the printing capability of the printer at the University of Maryland's Additive Manufacturing Center was studied. Based on the measurements of the printed coupons, fin thickness of 170 μm was obtained, which represents a 20% reduction compared to the outcome of the first unit. Similarly, a base thickness of 400 μm proved to be leak free at the design pressure, resulting in a further 20% reduction compared to the first unit. After updating the problem definition on the basis of the coupons' study, the single-objective optimization was performed and a new design obtained, leading to a 17% mass reduction compared to the base case heat exchanger unit. The full-scale of the second unit was then scaled-down to the size of the build capability of the printer. Lastly, the heat exchanger core unit and its headers were successfully printed and welded.

Chapter 7 Performance characterization of the 4.5” x 4” x 3.5” Unit

7.1 Introduction

This chapter discusses the performance characterization of the new 3D printed unit under different levels of temperature. The experimental data and numerical prediction were then compared and the numerical model was updated to reflect the outcomes of the experimental data. A second model based on fluid properties dependence on temperature was developed and compared with the previous model and the experimental data collected. Lastly the comparison with the performance of conventional heat exchanger is presented.

7.2 Experimental Results of the 4.5” x 4” x 3.5” Unit

In order to assess the experimental performance of the 4.5” x 4” x 3.5” M2HX, the assembled unit was installed in the setup shown in Figure 5-7. Based on the numerical prediction, the pressure drop transducer of the hot-side was changed with another transducer with a bigger range (up to 22.0 kPa, uncertainty equals to 0.25% of FS). The experiments were performed under adiabatic conditions and under different levels of temperature, as shown in Table 7-1. For the adiabatic tests, first the hot-side flow rate was varied between 2.5 and 13 g/s, then the cold side was tested between 5 and 36 g/s. For the test involving the heat transfer, instead, two sets of data were collected for each level of temperature (100°C, 300°C and 600°C), that corresponds to the value of the inlet temperature of the hot-side ($T_{in,hot}$). The three levels are referred either by the value of the temperature or as low, medium and high temperature, respectively. For every level of temperature, first, the hot-side flow rate was varied, while keeping the cold side constant at 20 g/s. Then, in the second test, the cold-side flow rate was varied while keeping the hot side at 9 g/s. The measurements collected during the experiments were the same as the one described for the first M2HX (see Chapter 5).

Table 7-1: Low-temperature experimental test conditions of the 4.5" x 4" x 3.5" subscale unit

Test		Hot Side	Cold Side
Adiabatic	Temperature Condition	15°C	15°C
	System Pressure	340 kPa	101 kPa
	Varying Hot Side Flow Rate	5-13 g/s	0 g/s
	Varying Cold Side Flow Rate	0 g/s	5-36 g/s
Heat Transfer	Temperature Condition	100/300/600°C	15°C
	System Pressure	340 kPa	101 kPa
	Varying Hot Side Flow Rate	7-13 g/s	20 g/s
	Varying Cold Side Flow Rate	9 g/s	10-30 g/s

7.3 Heat Transfer Performance

The heat transfer performance of the 4.5" x 4" x 3.5" M2HX results are plotted in terms of total heat duty (Q) as function of the mass flow rate, as shown in Figure 7-1. Figure 7-1(a) shows the heat duty variation with the cold-side mass flowrate ($\dot{m}_{cold}$), while keeping the hot side flowrate at 9 g/s for the three levels of temperature. As expected, increasing the mass flowrate and/or the temperature at the inlet of the hot side $T_{in,hot}$ increases the heat exchanged by the two streams. Up to 663 W, 2,297 W and 4,787 W heat duties were achieved for low, medium and high temperature test respectively. The points correspond to the value of Q for $\dot{m}_{cold}$=30 g/s. Similarly, Figure 7-1(b) shows the heat duty variation for the three levels of temperature when the cold-side flow rate is kept at 20 g/s and the hot-side mass flow rate ($\dot{m}_{hot}$) is varied. For this sets of data, up to 755 W, 2,568 Q and 5,368 W heat duties were achieved for low, medium and high temperature. The points correspond to the value of Q for $\dot{m}_{hot}$=13 g/s. It is important to notice that an extra point at $\dot{m}_{hot}$=13 g/s and $\dot{m}_{cold}$=30 g/s was tested for the high temperature set. A heat duty of 6,329 W was measured, corresponding to a gravimetric heat duty (Q/M) of 9.4 kW/kg for an effectiveness (ε) of 78%.

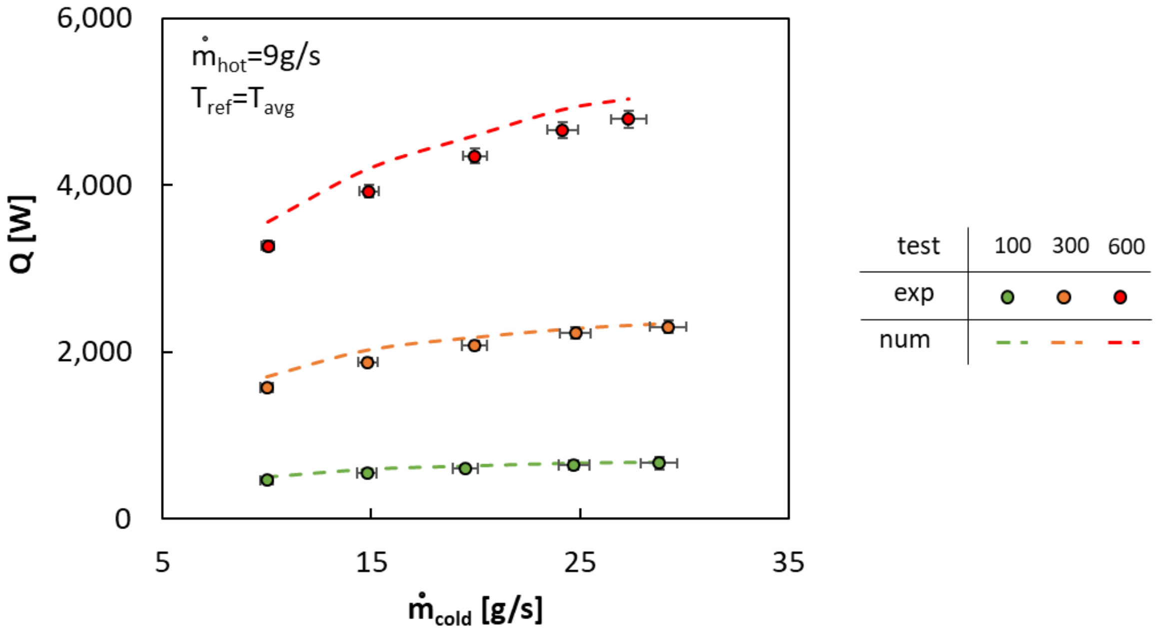

(a)

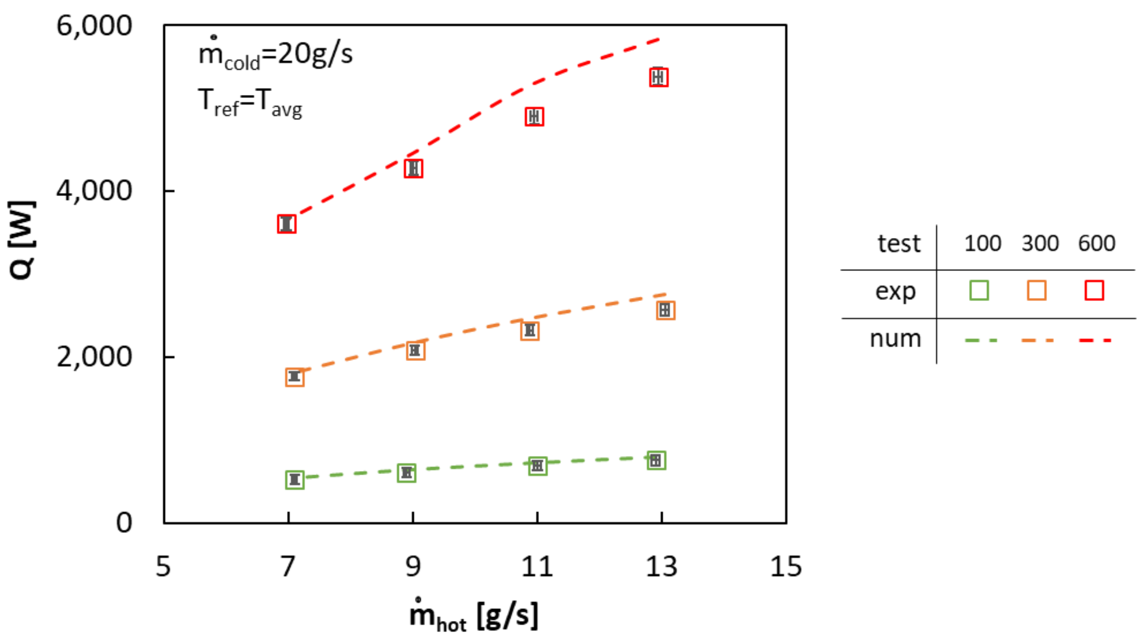

(b)

Figure 7-1: Comparison between experimental and numerical results of heat duty (Q) of the 4.5" x 4" x 3.5" subscale unit as a function of (a) mass flow rate of the cold side ($\dot{m}_{cold}$) for constant hot-side of 9 g/s, (b) mass flow rate of the hot side ($\dot{m}_{hot}$) for constant cold-side of 9 g/s

Moreover, comparing the results of Figure 7-1(a) and Figure 7-1(b), it is possible to notice that increasing the hot side has a higher effect on heat duty than increasing the cold side. Using the 600°C test as reference, increasing $\dot{m}_{hot}$ by 22% from 9 g/s to 11 g/s increases Q by 12.7%, while increasing $\dot{m}_{cold}$ by 25% from 20 g/s to 25 g/s increases Q by 7.0%. Compared to the numerical data (shown as dotted lines), the average percentage error between the numerical and experimental results is calculated as 6%. Compared to the first unit tested, a significant improvement in the agreement between the numerical model and the experimental data is observed. It has to be noticed that the properties of the fluids are evaluated at the average temperature (T_{avg}), which is then defined as:

$$T_{avg} = \frac{T_{in,hot} + T_{in,cold}}{2} \tag{47}$$

In order to compare the performance at the different levels of temperature, the experimental data are shown in terms of effectiveness of the M2HX (ε) as a function of the mass flow rate on the cold-side and hot-side, in Figure 7-2(a) and Figure 7-2 (b), respectively. It is possible to notice that the value of the effectiveness is mainly affected by the mass flow rate, while the dependence on the level of temperature is almost negligible.

When compared to the numerical model, the deviation decreases with the increase of the effectiveness. A deviation up to 9% is observed for the lower ε, while it reduces to 3% for the higher values. This trend can be explained when compared to the NTU-ε plots. For higher values of ε, a decrease in NTU has a smaller impact on the ε.

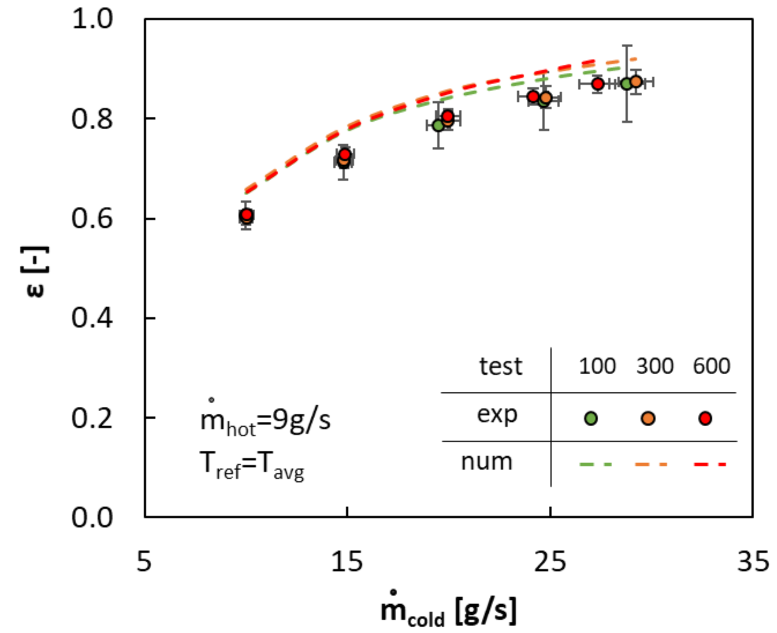

(a)

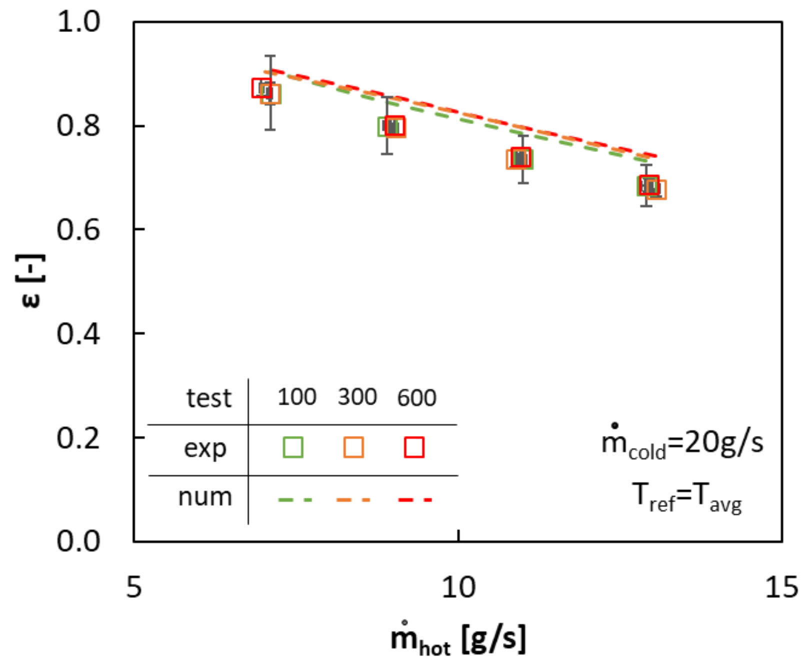

(b)

Figure 7-2: Comparison between experimental and numerical results of the effectiveness (ε) of the 4.5" x 4" x 3.5" subscale unit as a function of (a) mass flow rate of the cold side ($\dot{m}_{cold}$) for constant hot-side of 9 g/s, (b) mass flow rate of the hot side ($\dot{m}_{hot}$) for constant cold-side of 9 g/s

Calculating the overall heat transfer coefficient (U) of the M2HX is then necessary to complete the heat transfer performance analysis. Following the same procedure described in Section 5.6.1, the values of U is plotted with respect to the mass flow rate as shown in Figure 7-3. It is observed that that increasing the mass flow rate of either of the two sides increases the overall heat transfer coefficient. Overall heat transfer coefficient as high as 94.4 W/m^{2}K was recorded for $\dot{m}_{cold}$=28 g/s and $\dot{m}_{hot}$=9g/s, which corresponds to $Re_{chn,cold}$=99 and $Re_{chn,hot}$=265. Compared to the first unit tested, the value of U is almost double, thus proving a significantly improvement in the performance.

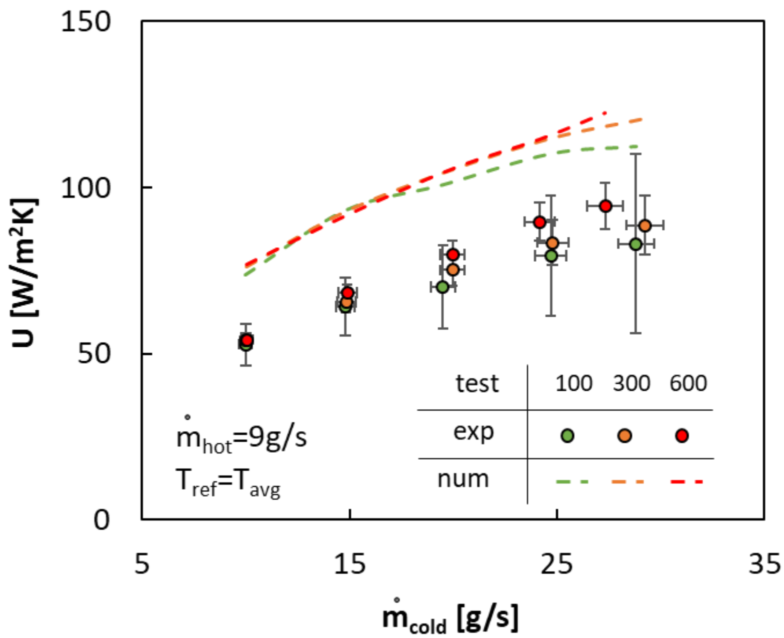

(a)

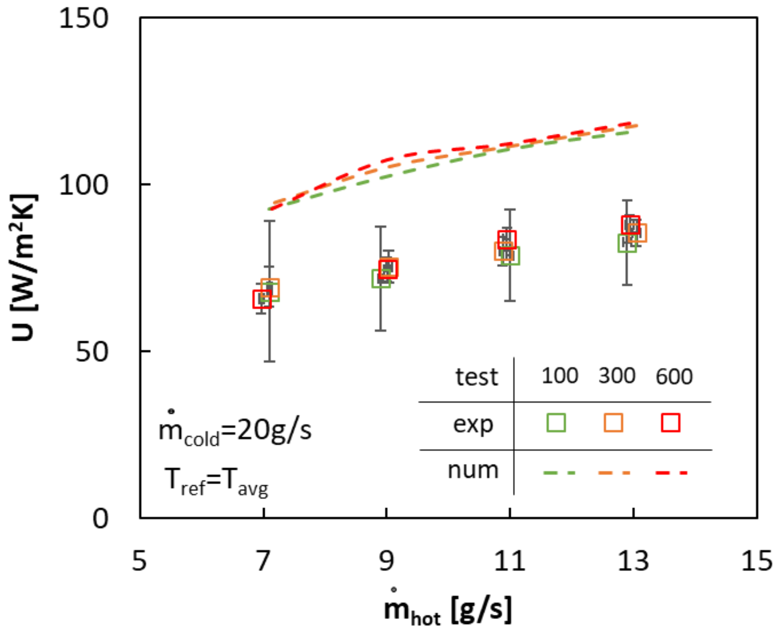

(b)

Figure 7-3: Comparison between experimental and numerical results of the overall heat transfer coefficient (U) of the 4.5" x 4" x 3.5" subscale unit as a function of (a) mass flow rate of the cold side ($\dot{m}_{cold}$) for constant hot-side of 9 g/s, (b) mass flow rate of the hot side ($\dot{m}_{hot}$) for constant cold-side of 9 g/s

As expected from the analysis of the effectiveness, the deviation between the experimental overall heat transfer coefficient and the numerical prediction is constant across the different values of mass flow rate, effectiveness and temperature. The value of U obtained experimentally corresponds to 70-80% of the expected values. Reasons for the deviation between the numerical and experimental values can be losses to the ambient (the energy balance is guaranteed within 5%) and small defects in the print that can cause different sizes of the microchannel or partially obstructing the flow: Moreover, in case of a cross-flow HX, the role of the thermal conductivity of the solid plays a crucial role on the effectiveness of the M2HX. For high thermal conductivity, the heat spreading in the base plate becomes dominant and limits the effectiveness of the HX. When the thermal conductivity is low, instead, the high conductive resistance across the base plate negatively affects the heat transfer. For the numerical model, values of 10.8, 12.0 and 13.3 W/mK were assumed for low, medium and high temperature test, respectively.

7.4 Pressure Drop Performance

The pressure drop of the cold side (ΔP_{cold}) is shown in Figure 7-4 as a function of the mass flow rate of the cold side ($\dot{m}_{cold}$), for all the four sets of data in which the mass flow rate was varied on the cold-side. The graph also includes the numerical prediction of the hybrid method, where the fluid properties are calculated using the average temperature (T_{avg}).

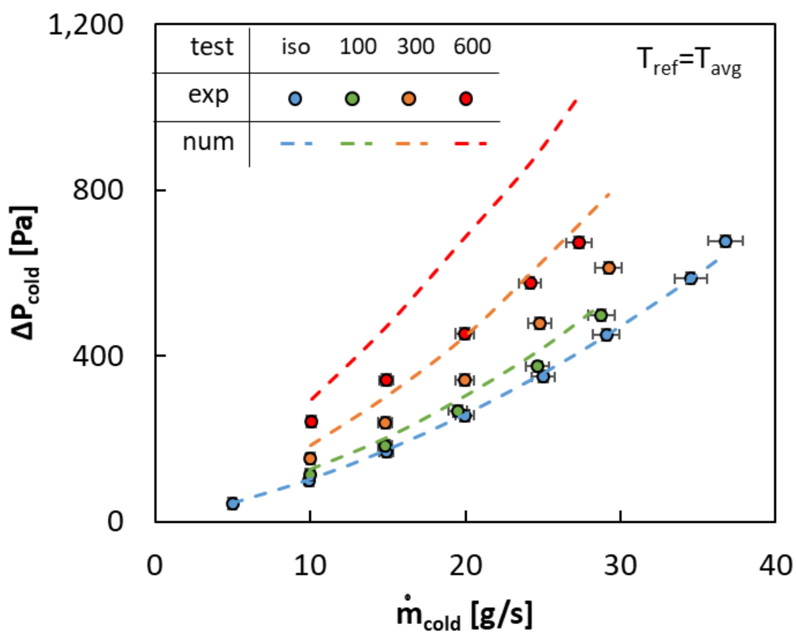

Figure 7-4: Comparison of the cold-side pressure drop between experimental data and numerical prediction of the 4.5" x 4" x 3.5" subscale unit using T_{avg}

Although very convenient, it can be observed that the choice of T_{avg} is not realistic for some data since T_{avg} exceeds the range of temperatures of the cold-side. In case of low temperatures (e.g., 100°C), the difference in the fluid properties is so small that it does not result in a significant deviation of the prediction. However, when moving to high temperature (e.g. 600°C), this effect becomes dominant. As shown in Figure 7-4, the deviation between the experimental data and the numerical prediction increases when increasing the level of temperature of the experimental set. It can be noticed that the numerical prediction of the isothermal test matches the experimental data within 5%, thus suggesting that the model successfully replicates the actual performance. In order to compare the pressure drop at different operative conditions, it is useful to characterize the pressure drop in terms of non-dimensional quantities. Figure 7-5 shows the mean friction factor (f_{cold}) as a function of the Reynolds number of the microchannel in the cold-side ($Re_{chn,cold}$) for the three different levels of temperature. The fluid properties used for the definition of f_{cold} and $Re_{chn,cold}$ were evaluated at T_{avg}.

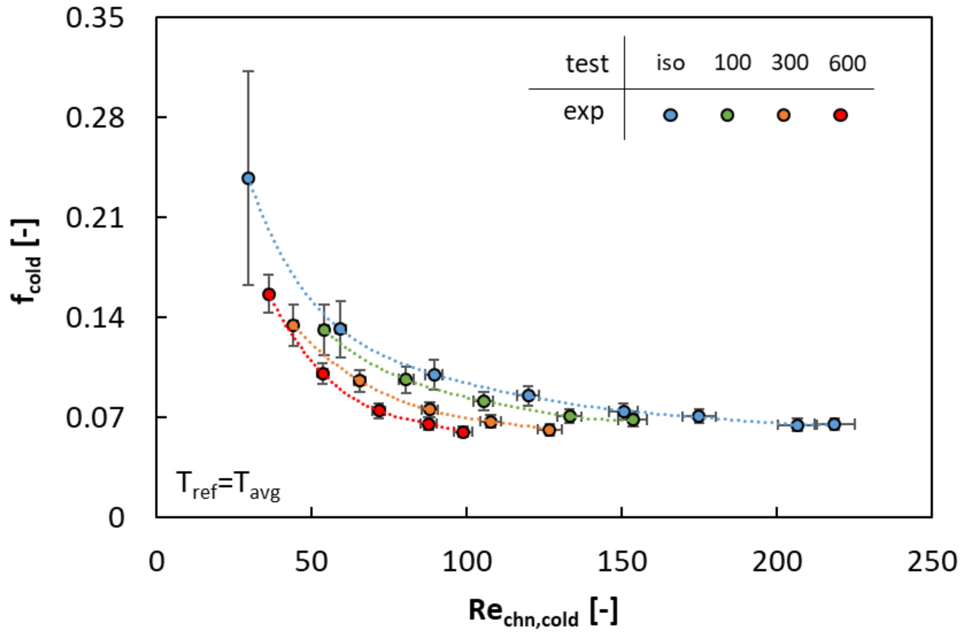

Figure 7-5; Comparison of the cold-side pressure drops of the 4.5" x 4" x 3.5" subscale unit using $T_{avg}$for the definition of f vs Re

As expected, Figure 7-5 shows that the trends of f_{cold} vs $Re_{chn,cold}$ for the different data sets are not consistent. Unlike the tests involving heat transfer (tests at 100°C, 300°C and 600°C), the isothermal test was conducted at a constant temperature across the entire HX. For this reason, the trend given by the experimental data of the isothermal test does not carry any uncertainty in the definition of the fluid properties. Based on this consideration, it is possible to assume the trend of the isothermal test as reference. The reference temperature for the fluid properties of each of the other data points can then be adjusted so that the pressure drop of the equivalent microchannel with constant properties equals the real microchannel, thus matching the curve fitting of the isothermal $f$vsRe trend. In order to perform the curve fitting, it has been demonstrated by Yuruker *et al*. [182] that the pressure drop of an U-shaped microchannel in case of laminar flow can be described by the linear interpolation:

$$(fRe)_{chn} = aRe_{chn} + b \tag{48}$$

where f_{chn} is the friction factor defined on the pressure drop in the microchannel and a and b are coefficients depending on the geometric parameters. It is then needed to verify that also the pressure drop in the manifold can be characterized by a similar formulation. Based on the definition of f and Re and omitting the geometrical parameters, it can be observed that f and Re can be described as proportional to $\frac{\rho\Delta P}{\dot{m}^2}$ and $\frac{\dot{m}}{\mu}$, respectively. Provided that viscosity and density are constant for the isothermal test, it is possible to visualize the plot of (fRe)vsRe as $\frac{\Delta P}{\dot{m}}$ vs $\dot{m}$. Even though the pressure drop in manifolds ($\Delta P_{mnd,cold}$) can not be directly measured, the close match between numerical prediction and experimental data allows the use of the model to obtain the value of $\Delta P_{mnd,cold}$. Figure 7-6 shows that a linear interpolation exists between (fRe) and Re for the cold side manifold. The level of accuracy of the interpolation can be quantified with a root mean square error equal to 0.99998.

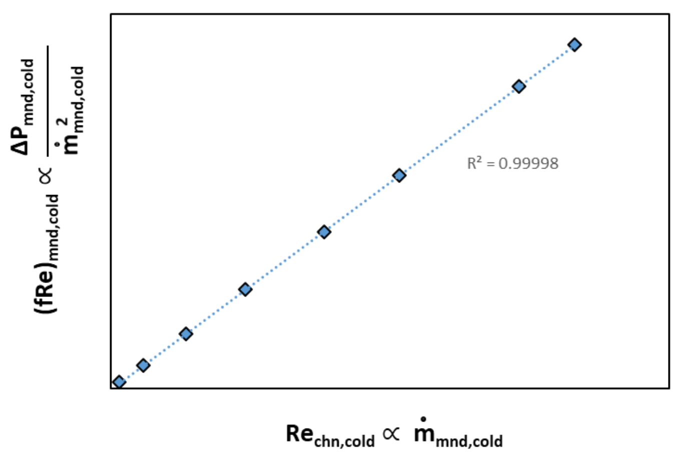

Figure 7-6: fRe vs Re correlation of the numerical prediction of the isothermal test

Since both terms of the pressure drop in the core can be written in the form $(fRe) = aRe + b$ and the ratio of the Reynolds numbers in the microchannel and manifold $\left(\frac{Re_{chn}}{Re_{mnd}}\right)$ is constant when the fluid properties are constant for the entire HX, it can be concluded that also the pressure drop of the entire HX can be expressed in terms of:

$$f_{cold}Re_{chn,cold} = a'Re_{chn,cold} + b' \tag{49}$$

where a' and b' are again coefficients depending solely on the geometric parameters. Provided that mass flow rate and pressure drop need to be treated as given values, it can be observed that the effect of the temperature on the data points is expressed in terms of proportionality of (fRe) to the density of the fluid $(fRe \propto \rho)$ and proportionality of Re to the inverse of the viscosity of the fluid $(Re \propto 1/\mu)$. Changing the temperature used for defining the properties then results in a translation of the experimental point in both the directions of the fRe vs Re plot.

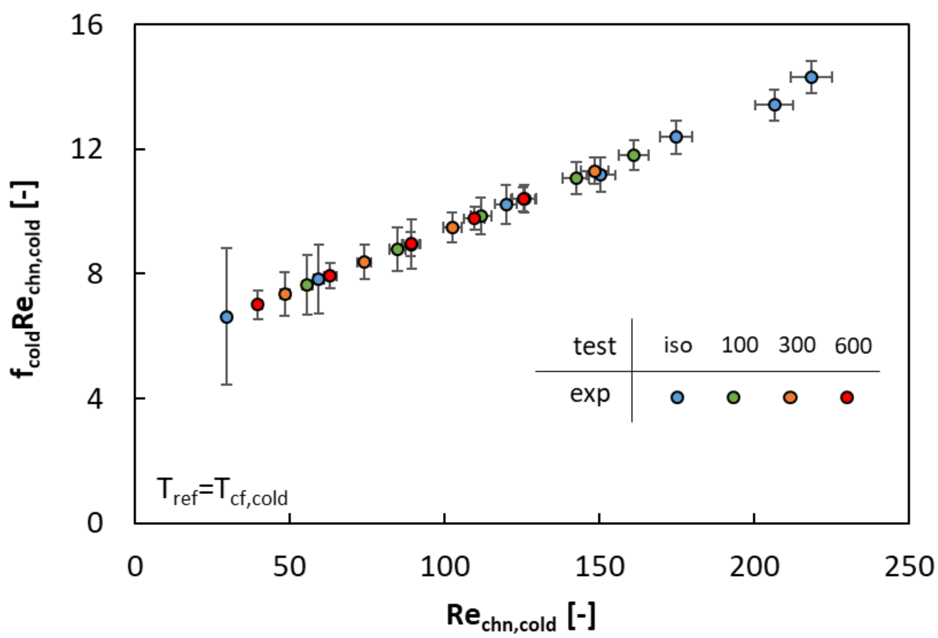

(a)

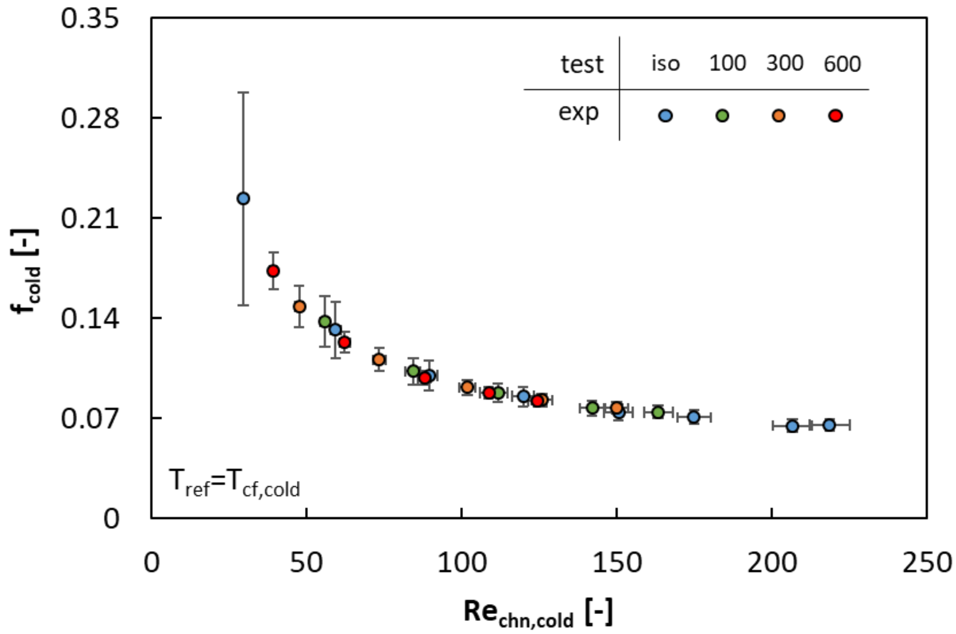

(b)

Figure 7-7: Curve fitting of the cold-side pressure drop of the experimental data to the isothermal data of the 4.5" x 4" x 3.5" subscale unit in terms of (a) (fRe) vs Re and (b) f vsRe

Figure 7-7 shows the results of the curve fitting of the experimental data (pressure drop performance of the tests at 100°C, 300°C and 600°C) to the isothermal data both in terms of (fRe)vsRe and $f$vsRe analysis. Figure 7-7(a) shows the linear interpolation used to perform the curve fitting of the different sets of data, while Figure 7-7(b) can be studied in comparison to Figure 7-5-. The experimental points now lie on the same curve. The resulting temperature that satisfies the curve fitting of the cold-side is defined as curve fitting temperature ($T_{cf,cold}$). From the physical point of view, it can be considered as the constant temperature in the microchannel that causes the same pressure drop as the real case with varying properties. It is important to highlight that the definition of $T_{cf,cold}$ is based on the experimental data. It is then interesting to rerun the hybrid method using $T_{cf,cold}$ as reference for the fluid properties.

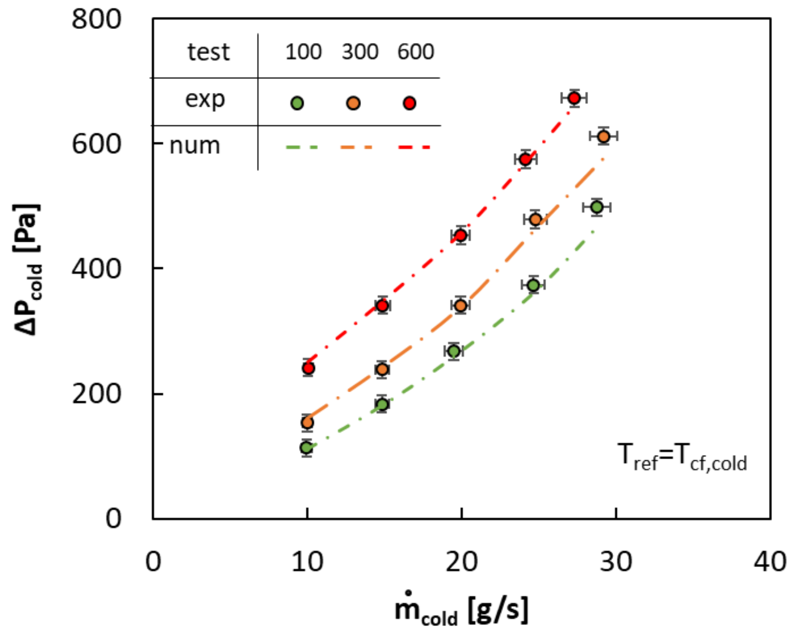

Figure 7-8: Comparison of the cold-side pressure drop between experimental data and numerical prediction of the 4.5" x 4" x 3.5" subscale unit using $T_{cf,cold}$

Figure 7-8 shows the comparison between the experimental data and the numerical prediction of the hybrid method obtained using $T_{fc,cold}$. A significant improvement of the performance prediction can be observed comparing the results of Figure 7-4 and Figure 7-8. The deviation between numerical and experimental data is reduced from 10% to 6% for the low temperature test, from 24% to 4% for the medium temperature test and from 35% to 6% for the high temperature test. The numerical prediction is then consistent among the different sets of data, including the isothermal test. Based on the accuracy of the numerical prediction, the hybrid model can also be used to analyze the pressure drop in the microchannels, compared to the entire core of the HX. The microchahannels region contributes to 75-90% of the overall pressure drop of the HX. As expected in a properly designed M2HX, the pressure drop in the manifolds is quite limited. Differently from the microchannels, the manifolds do not contribute to the heat transfer in the HX and the minimization of the pressure drop is then critical to achieve high values of COP.

Similarly to the approach used for the cold-side, the pressure drop performance analysis is started by plotting the pressure drop of the hot-side (ΔP_{hot}) as a function of the mass flow rate of the hot-side ($\dot{m}_{hot}$), for all the four sets of data in which the mass flow rate was varied on the hot-side, as shown in Figure 7-9. The graph also includes the numerical prediction of the hybrid method, where the fluid properties are calculated at T_{avg}. It can be noticed that the reference temperature has the same value for both cases when T_{avg} is used as reference. However, the properties on the two sides are not the same because the working fluids and the pressure values are different (N_2 is pressurized in the closed-loop of the hot side).

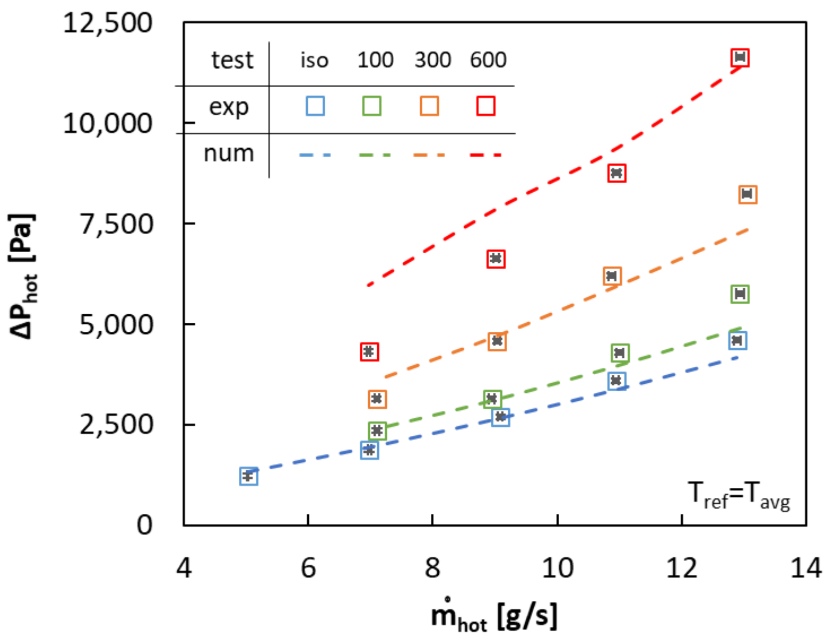

Figure 7-9: Comparison of the hot-side pressure drop between experimental data and numerical prediction of the 4.5" x 4" x 3.5" subscale unit using T_{avg}

The comparison between Figure 7-9 with Figure 7-4 shows that the deviation between the numerical model and the experimental data is smaller for the hot-side. Analyzing the temperature of the hot-side, in fact, it is possible to notice that T_{avg}.always lies between the temperatures at the inlet and the outlet. Following the same procedure of the cold-side, Figure 7-10 shows the non-dimensional analysis of the pressure drop (f_{hot}) of the hot-side as a function of the Reynolds number in the hot microchannel ($Re_{chn,hot}$). Compared to the deviation that the choice of T_{avg} led to for the cold side, Figure 7-10 shows closer trends for the four conditions. The only set of data that significantly diverges from the isothermal test is the one at high temperature. Based on this closer agreement between numerical and experimental data, running the curve fitting is expected to return temperature that are close to the initial guess of T_{avg}.

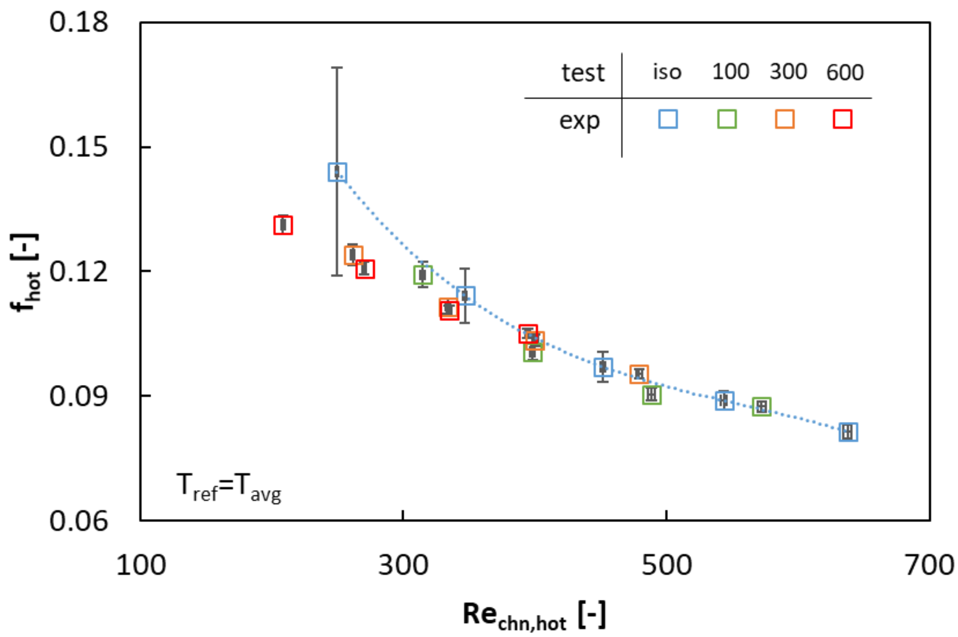

Figure 7-10: Comparison of the hot-side pressure drops of the 4.5" x 4" x 3.5" subscale unit using T_{avg} as reference of f vs Re

In order to perform the curve fitting of the experimental data, the first step was to study the role of the pressure drop of in the manifold channels. Based on the model prediction, the pressure drop in the microchannels accounts for 96-98% of the pressure drop in the hot-side of the HX. It is then possible to conclude that the role of the manifold channels can be neglected and the linear trend of fRe vs Re that characterizes the behavior of the pressure drop in the microchannel can be extended to the entire unit.

Figure 7-11shows the results of the curve fitting of the experimental data (pressure drop performance of the tests at 100°C, 300°C and 600°C) to the isothermal data both in terms of (fRe)vsRe and $f$vsRe analysis. Differently from the cold-side, the values of $T_{fc,hot}$ are both higher and lower than T_{avg}. In particular, it is possible to observe a good agreement between the trend of $T_{fc,hot}$ and the deviation of the numerical method using T_{avg}: $T_{fc,hot}$>T_{avg} is observed for the cases in which the numerical model is under predicting the experimental data, while $T_{fc,hot}$<T_{avg} occurs in case of over prediction.

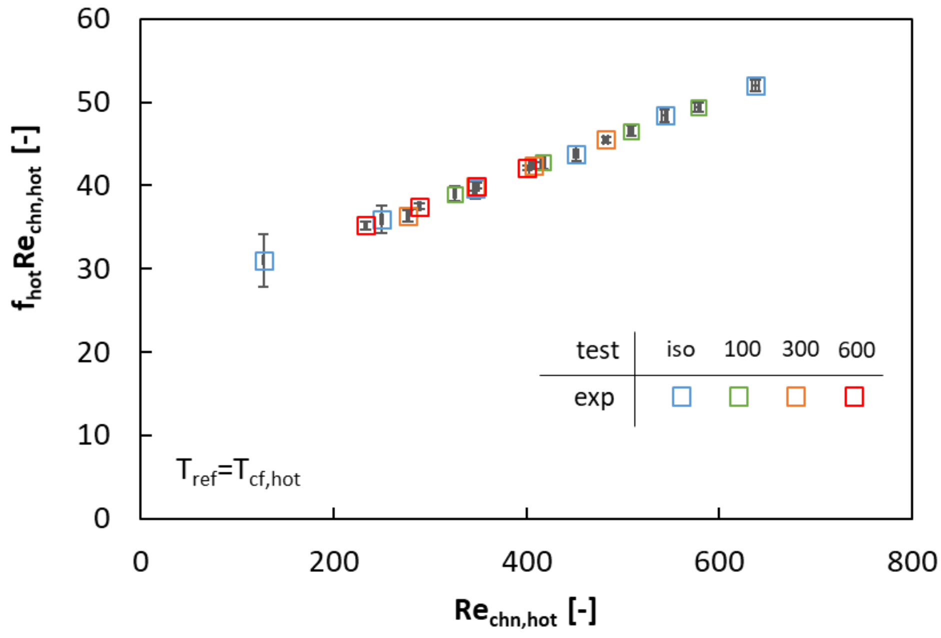

(a)

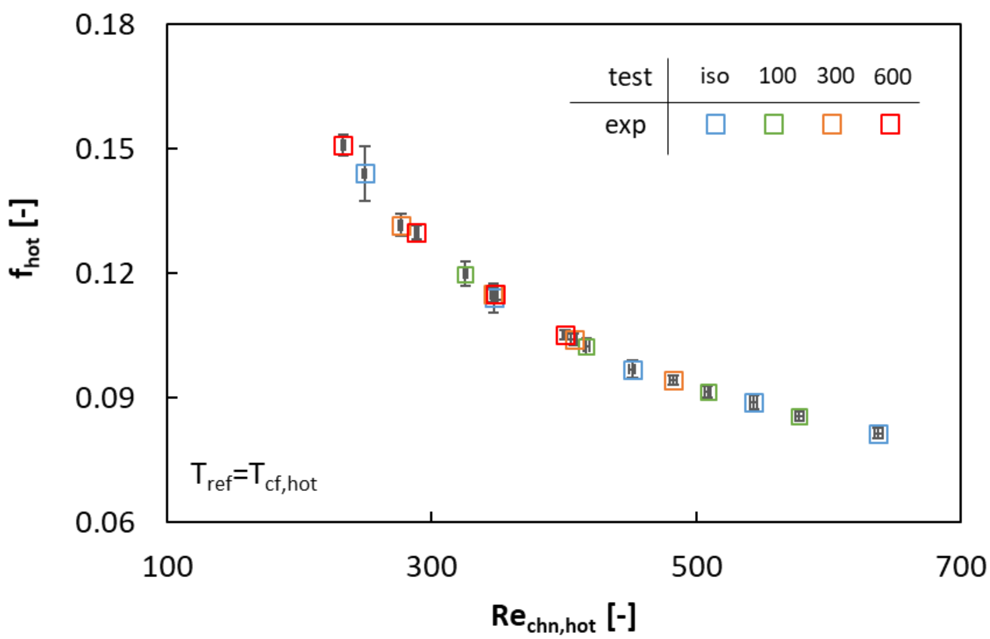

(b)

Figure 7-11: Curve fitting of the hot-side pressure drop of the experimental data to the isothermal data of the 4.5" x 4" x 3.5" subscale unit in terms of (a) (fRe) vs Re and (b) f vsRe

Figure 7-12 shows the comparison between the experimental data and the numerical prediction of the hybrid method obtained using $T_{fc,hot}$ for the hot-side. The improvement of the prediction is significant for the high temperature case, where the deviation is decreased from 28% to 5%. For the low and medium temperature, the deviation decreases from 10% to 4%. The numerical prediction is then consistent among the different sets of data, including the isothermal test.

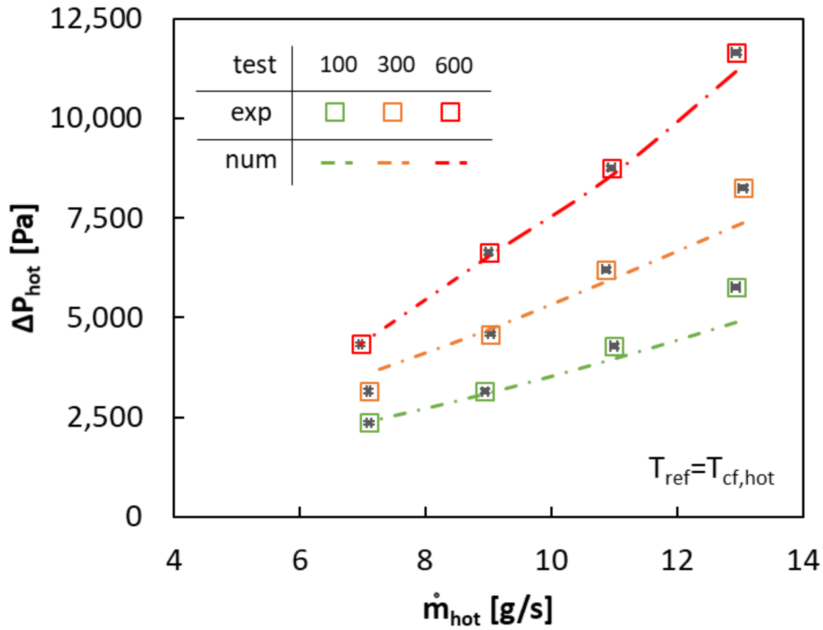

Figure 7-12: Comparison of the cold-side pressure drop between experimental data and numerical prediction of the 4.5" x 4" x 3.5" subscale unit using $T_{cf,hot}$

7.4.1 Curve Fitting Temperature Effect on Heat Transfer Performance

Based on the significant improvement of the curve fitting temperature (T_{fc}) definition in the model prediction of the pressure drop, it is then necessary to study the effect of T_{fc} on the heat transfer performance. The hybrid model and the heat spreading model were rerun using the new temperature and the results are plotted in Figure 7-13, in terms of effectiveness as a function of the mass flow rate.

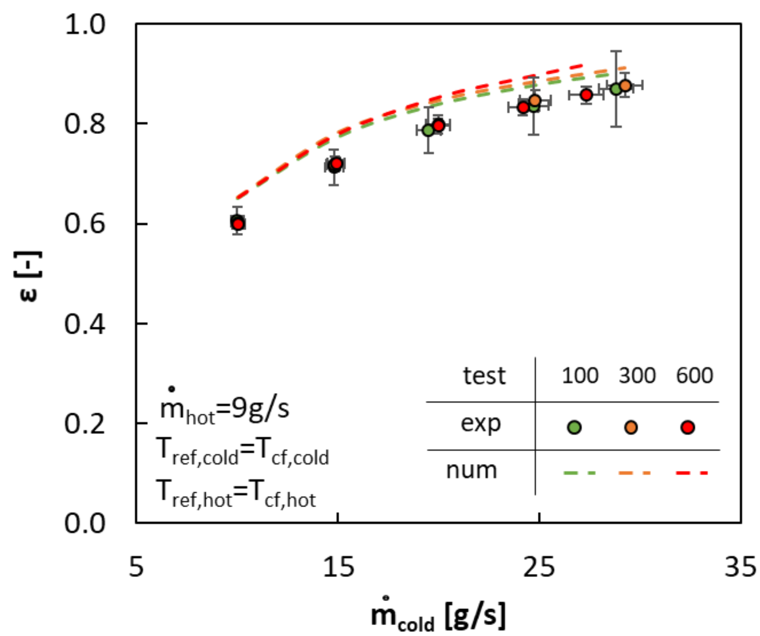

(a)

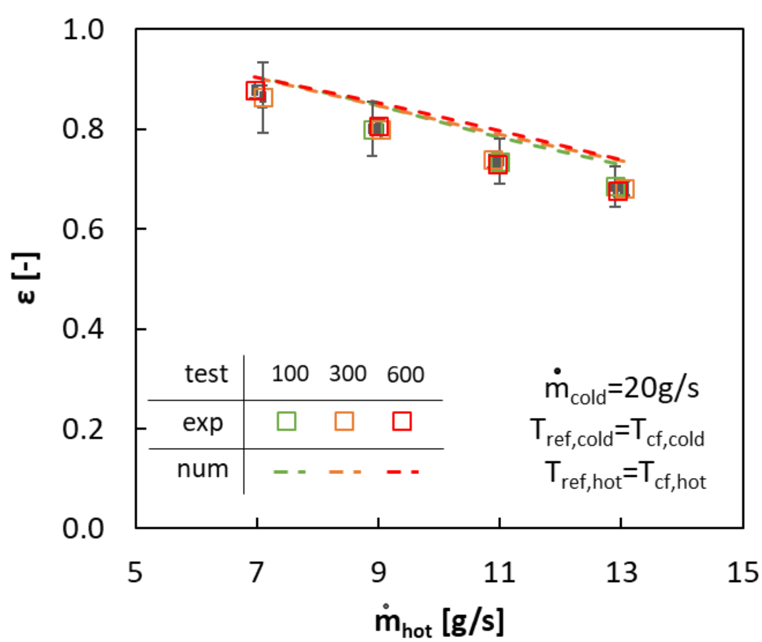

(b)

Figure 7-13: Comparison between experimental and numerical results using T_{fc} of the effectiveness (ε) of the 4.5" x 4" x 3.5" subscale unit as a function of (a) mass flow rate of the cold side ($\dot{m}_{cold}$) for constant hot-side of 9 g/s, (b) mass flow rate of the hot side ($\dot{m}_{hot}$) for constant cold-side of 9 g/s

Comparing the results of Figure 7-13 and Figure 7-2, it can be concluded that the deviation between numerical models and the experimental data is the same. Unlike the case of the pressure drop, the change of fluid properties on the heat transfer performance required several steps. First, the Nusselt numbers was recalculated using the SMM. Second, the effective hot- and cold-side conductances between the hot- and cold-side fluids were redefined. Third, the heat spreading model recomputed the heat transfer process in the cross-flow M2HX. During this process, the effect of the temperature on the heat transfer becomes less relevant. Starting with the correlation between Nusselt number (Nu) and Re for laminar flow in a U-shaped microchannel, it was demonstrated by Yuruker *et al.* [182]that it can be described with the formulation:

$$Nu = kRe^{0.4}\mathrm{Pr}^{0.5} + \mathrm{n} \tag{50}$$

where k and n are the curve fitting parameters and Pr is the Prandtl number. When changing the temperature, the effect on Re and Pr is flattened out by the exponents 0.4 and 0.5. Moreover, the presence of the coefficient n offsets the variation, thus decreasing the impact on the value of Nu. The heat spreading model then reduces the effect of the temperature because it has a low sensitivity on the effective hot- and cold-side conductances. It can be concluded that changing the reference temperature in the heat transfer model does not affect the outcome of the prediction as much as in the case of pressure drop. Since heat transfer and pressure drop are connected, it is suggested to use the same temperature as reference to avoid incongruities in the definition of the properties.

7.5 Curve Fitting Temperature Characterization

Despite the improvement in the performance prediction obtained using T_{fc} as reference for the fluid properties, the quantification of this new variable is based on the extrapolation of the experimental data. It is then necessary to find a method that allows to predict T_{fc} at the design stage. The first approach is to find significant trends from the experimental data collected. It is then useful to introduce few key parameters of the HX analysis and verify if constant pattern can be identified when mapping the experimental data. In order to quantify the magnitude of the driving temperature difference between the two streams, it is useful to introduce the logarithmic mean temperature difference (ΔT_{LM}), which is defined as:

$$\Delta T_{LM} = F\frac{\Delta T_2 - \Delta T_1}{\ln\left(\frac{\Delta T_2}{\Delta T_1}\right)} \tag{51}$$

where, in case of a cross-flow HX:

$$\Delta T_2 = T_{in,hot} - T_{out,cold} \tag{52}$$

$$\Delta T_1 = T_{out,hot} - T_{in,cold} \tag{53}$$

and F is a correcting factor that needs to be introduced to adjust the definition of logarithmic mean temperature difference of a parallel flow to more complex flow distributions. F is commonly presented as a function of two non-dimensional parameters: the ratio of the thermal capacities of the two streams (R) and the effectiveness, which is typically identified with P in the contest of the F factor method. In a cross-flow HX, the ratio of the thermal capacities of the two streams (R) is defined as:

$$R = \frac{T_{in,hot} - T_{out,hot}}{T_{in,cold} - T_{out,cold}} \tag{54}$$

When curve fitting the pressure drop on the two sides of the M2HX, it can be observed that the two temperatures $T_{cf,hot}$ and $T_{cf,cold}$ are defined for each experimental data. It is then possible to define the difference between those two temperatures as:

$$\Delta T_{cf} = T_{cf,hot} - T_{cf,hot} \tag{55}$$

Similarly to the concept of logarithmic mean temperature difference, this temperature difference defines the magnitude of the driving difference of the curve fitted temperatures. It is then possible to compare ΔT_{LM} and ΔT_{cf} to establish possible patterns. Figure 7-14 shows the comparison between ΔT_{LM} and ΔT_{cf} for the three different levels of temperature.

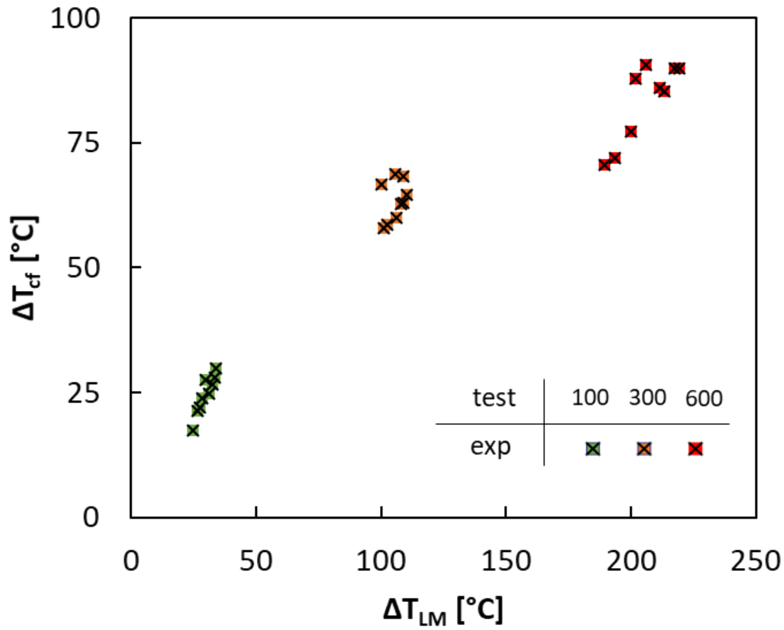

Figure 7-14: ΔT_{cf} vs ΔT_{LM} for the different levels of temperature

Observing the trends, the ratio between ΔT_{LM} and ΔT_{cf} seems to be constant for each of the data point at the same level of temperature. In order to normalize the comparison, it is possible to introduce the ratio of temperatures (RT), defined as:

$$RT = \frac{\Delta T_{cf}}{\Delta T_{LM}} \tag{56}$$

Figure 7-15 shows the ratio of temperatures (RT) as a function of the heat capacities (C_R) for the three different levels of temperature. As expected from Figure 7-14, RT is shown to be constant with the level of temperature for different values of C_R. As a matter of fact, the effect of C_R is already included in the definition of ΔT_{LM}. Moreover, it can be observed that the ratio RT decreases with temperature. From the physical point view, the outcomes of Figure 7-14 implies that the difference between the equivalent thermal temperatures increases faster with the temperature level compared to the difference between the equivalent fluid dynamic ones. This can be explained by recalling that the change in fluid properties has a direct impact on the pressure drop (as shown in the fRe analysis), while the change of properties for the heat transfer performance is flatted out (as shown in the thermal analysis).

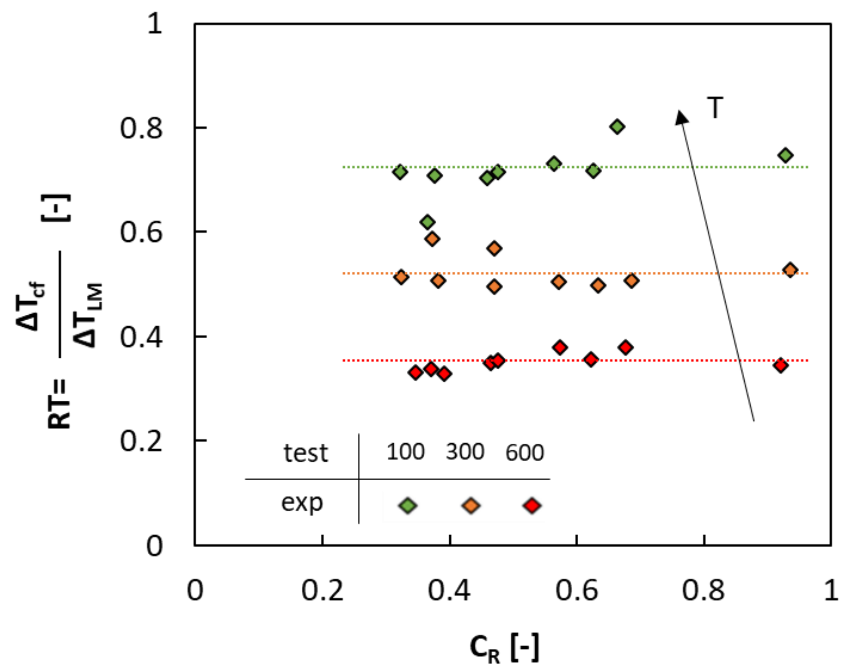

Figure 7-15: RT vs C_R for the different levels of temperature

Once quantified the magnitude of ΔT_{cf}, it is then necessary to predict the actual values of the temperatures. A possible way to identify T_{cf} is by defining the value of T_{cf} with respect to the overall temperature difference experienced across the side of the M2HX. It is then possible to introduce the parameter B, defined as:

$$B = \frac{T_{in} - T_{cf}}{T_{in} - T_{out}} \tag{57}$$

It can be observed that the same definition can be applied to both hot- and cold-side. As shown in Figure 7-16, the parameter B varies between 0 and 1, where a value of B=1 means that the curve fitting temperature should be equal to the temperature of the outlet, while B=0 corresponds to the situation in which the curve fitting temperature equals the inlet temperature.

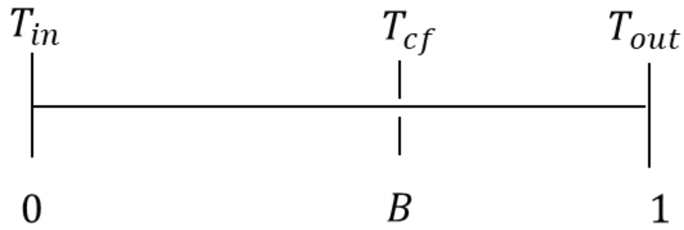

Figure 7-16: Schematic representation of the parameter B

Moreover, it is possible to define the effectiveness of each of the side of the M2HX as:

$$\varepsilon_{hot} = \frac{T_{in,hot} - T_{out,hot}}{T_{in,hot} - T_{in,cold}} \tag{58}$$

$$\varepsilon_{cold} = \frac{T_{out,cold} - T_{in,cold}}{T_{in,hot} - T_{in,cold}} \tag{59}$$

Figure 7-17 shows the plot of the paramater B of the HX as a function of the effectiveness of the same side of the HX. In particular, Figure 7-17(a) shows B_{cold} as a function of ε_{cold} for the data obtained varying the cold-side at different values of temperature. Similarly, Figure 7-17(b) shows the correlation between B_{hot} and ε_{hot} for the data obtained varying the cold-side at different values of temperature. As expected, the higher is the effectiveness of the HX side, the higeer is the value of B, thus meaning the the T_{cf} tends to be closer to the outlet temperature. It is also possible to notice that for the same value of ε, B increases with the level of temperature. This trend can be explained by the variation of the fluid properties with the temperature. Having a quadratic trend with temperatuee, the higher the level of the temperature is, the higher the reference temperature needs to be. Figure 7-17(c) then shows the results obtained combining Figure 7-17(a) and Figure 7-17(b). When plotted on the same chart in terms of B as a function of the effectiveness of the corresponding side, it is possible to notice that a common trend between the two sides exsists. In particular, the paramater B tends to increase rapidly for the low values of effectiveness, while it flattens out for the higher values.

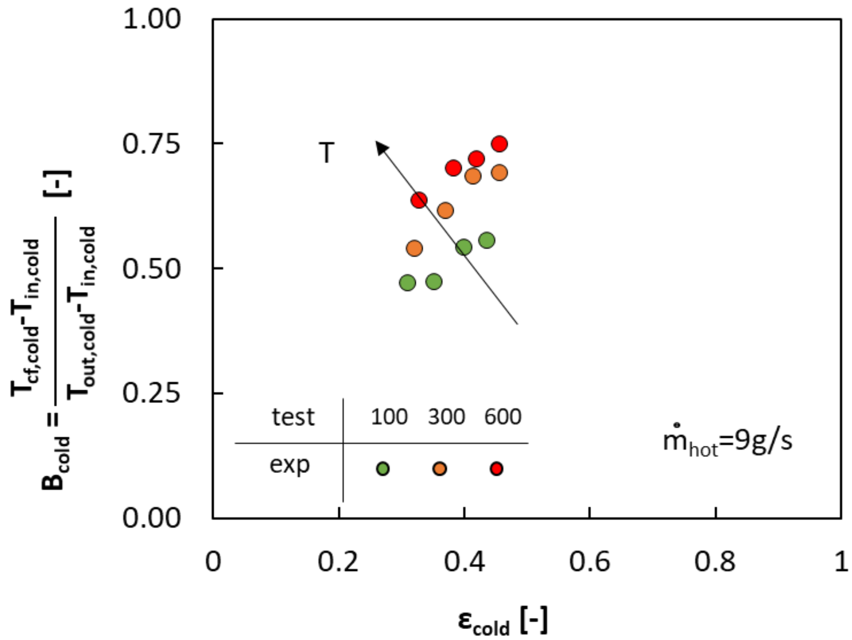
1.00
0.75
0.50
0.25
0.00
0
0.2
0.4
0.6
0.8
1
T
test
100
300
600
exp
ṁhot=9g/s
εcold [-]
Bcold = (Tcf,cold-Tin,cold)/(Tout,cold-Tin,cold) [-]

(a)

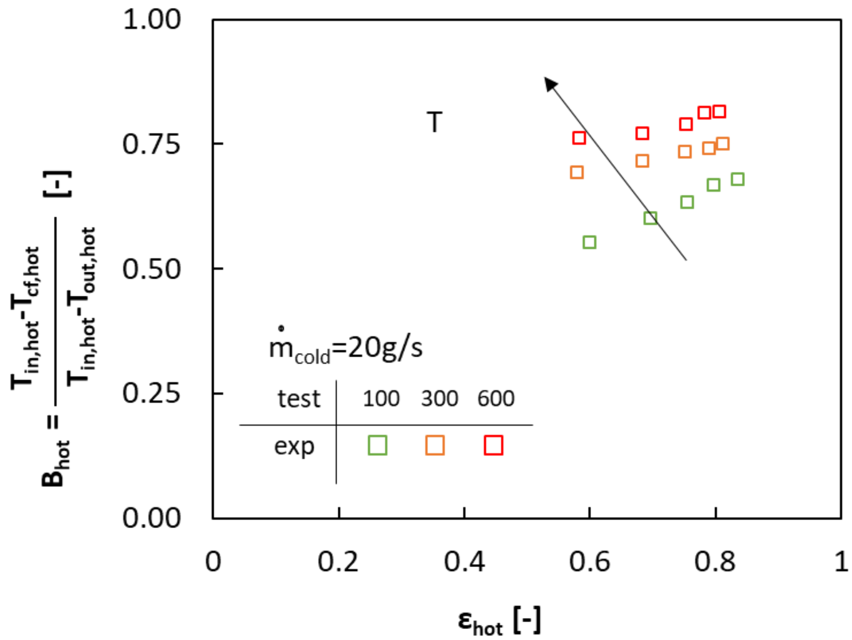
1.00
0.75
0.50
0.25
0.00
0
0.2
0.4
0.6
0.8
1
T
ṁcold=20g/s
test
100
300
600
exp
εhot [-]
Bhot = (Tin,hot-Tcf,hot)/(Tin,hot-Tout,hot) [-]

(b)

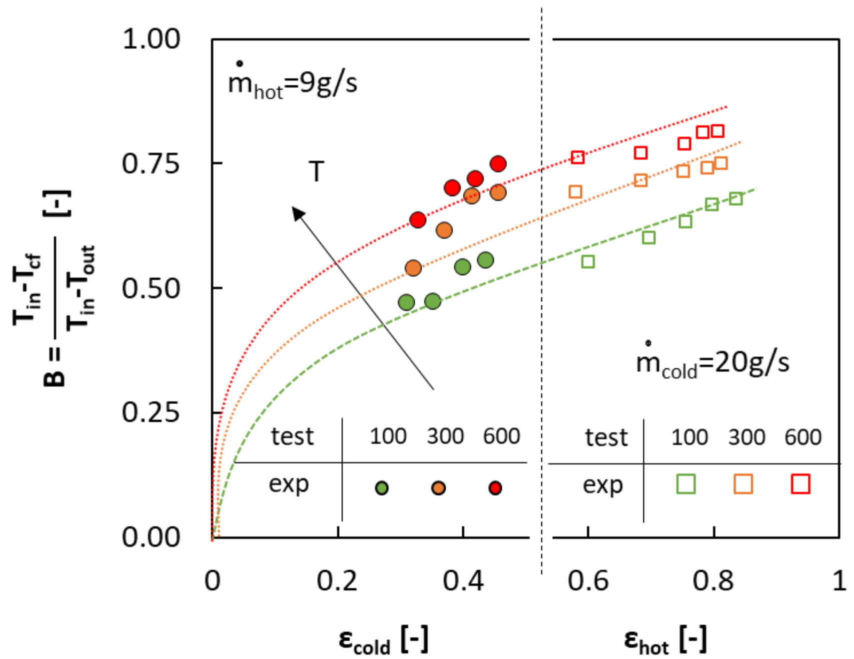

(c)

Figure 7-17: (a) B_{cold} vs ε_{cold} for the data obtained varying the cold-side at different values of temperature, (b) B_{hot} vs ε_{hot} for the data obtained varying the hot-side at different values of temperature, (b) combination of figure (a) and (b)

Despite the trends observed, it is not possible to establish a correlation due to the limited number of experimental data collected.

7.6 3D -Thermal Unit Cell

In order to have a more robust method to predict the temperatures that need to be used in the hybrid method, it would be useful to perform a 3D-CFD simulation of one stack of the M2HX, including the fluid properties and the solid properties dependence on temperature. Despite the validity of this approach, the complexity of the geometry and the computational effort to create the mesh and perform the simulation make this approach not feasible. However, it was observed by Mandel *et al.* [165] that, provided the following assumptions:

- the flow distribution among the microchannels is uniform

- the temperature at the inlet of the microchannel is the same along the entire length of the manifold channel for both hot- and cold-side (which equals to the assumption that heat transfer does not occur in the manifold channels)

it is possible to scaled-down the heat transfer in a M2HX to the smaller Thermal Unit Cell (TUC) of the HX shown in Figure 7-18. The size of this region is defined by the width of $W_{mnd-chn,cold}$ and $W_{mnd-chn,hot}$, while the z-directions includes the base plate and the microchannels of both sides.

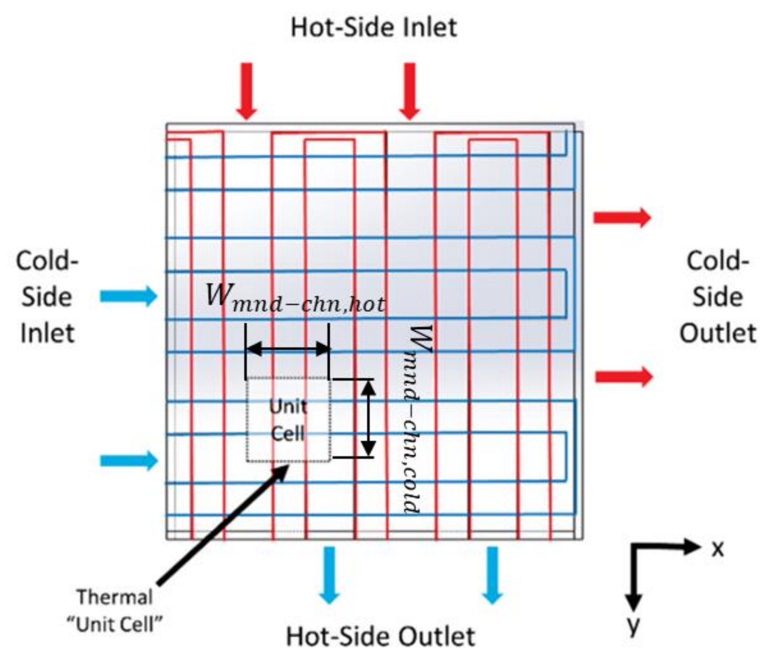

Figure 7-18: Double-sided cross-flow manifold-microchannel unit-cell pattern

When applied to the geometry of the 4.5" x 4" x 3.5" M2HX tested, the 3D-TUC computational domain and the boundary conditions are defined as shown in Figure 7-19. Moreover, the properties of air and N_2 are defined with respect to the temperature. The same approach is also used for the solid region made of Inconel 625.

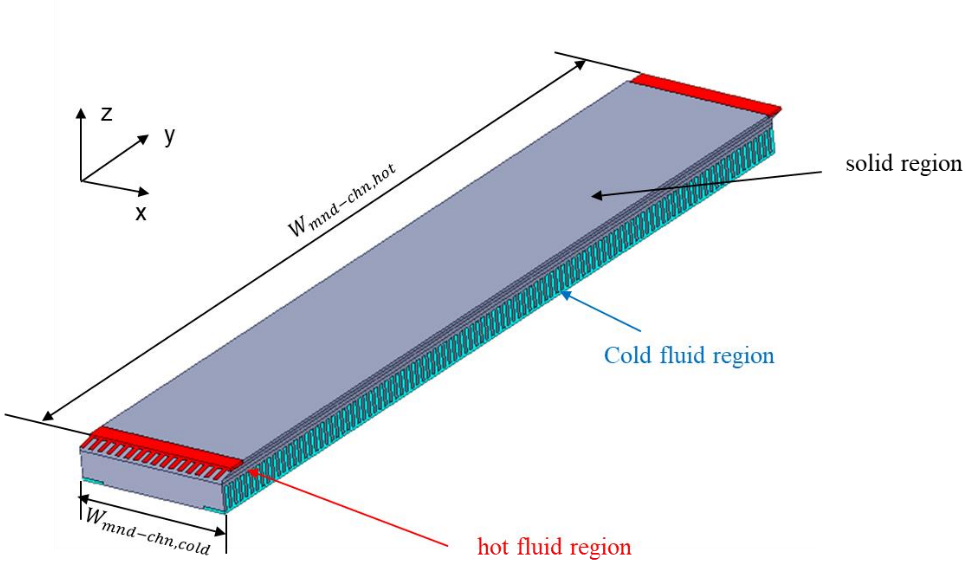

(a)

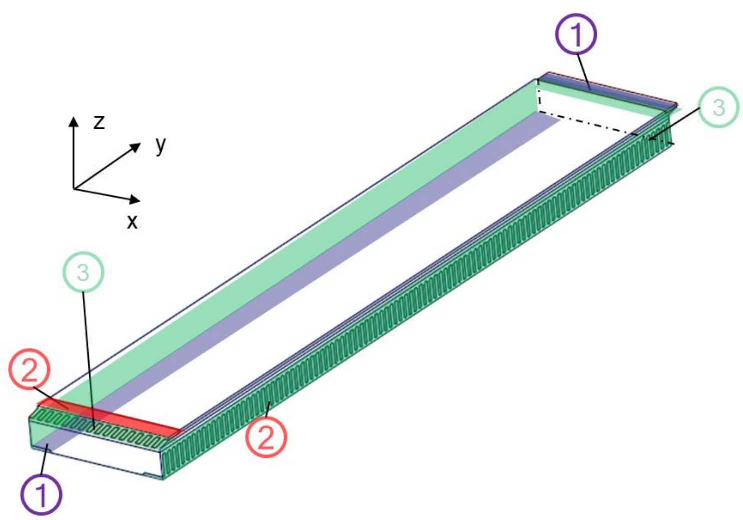

(b)

Figure 7-19: (a) 3D-TUC model of the 4.5" x 4" x 3.5" M2HX (b) Boundary conditions of the 3D-TUC: (1) mass flow rate and inlet temperature, (2) constant outlet pressure, (3) symmetry, (-) wall

7.6.1 3D Thermal Unit Cell Analysis

The goal of this model is to use CFD to obtain the temperature at the outlet of the mictrochannels, as well as the mass averaged properties of the working fluid and compare the results with the curve fitting temperatures obtained from the experimental analysis. One of the advantages of the 3D-TUC is the possibility to obtain the temperature distribution of the fluid region. Figure 7-20, for example, shows the temperature contour of the fluid in five microchannels on the cold-side for the case with $\dot{m}_{in,cold}$=10g/s and $\dot{m}_{in,hot}$=9g/s and $T_{in,hot}$=600°C.

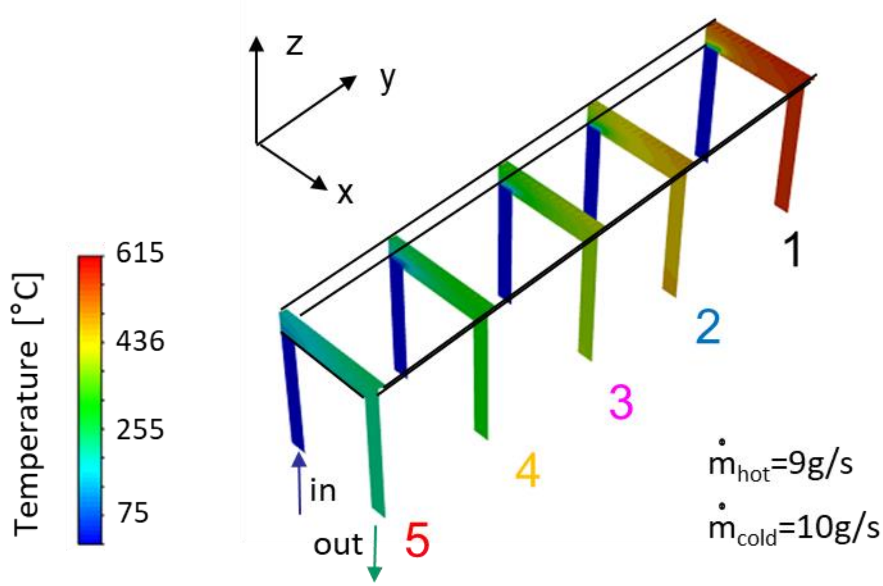

Figure 7-20: temperature contour of the fluid in five microchannel on the cold side for the case with $\dot{m}_{in,cold}$=10g/s and $\dot{m}_{in,hot}$=9g/s and $T_{in,hot}$=600°C.

It is then possible to map the temperature profile in the microchannel and plot the change in temperature along the microchannels (direction of the x-axis with reference to Figure 7-20), as shown in Figure 7-21 (a). The profile of the temperature was taken at half the height of the microchannel. The drop in temperature in first portion of the microchannel corresponds to the region where the fluid enters from the manifold channel into the microchannel through the opening W_{in}. It is also possible to notice that the temperature distribution in the cold-side microchannels with respect to the direction of the y-axis (with reference to

Figure 7-20) is linear. The corresponding fluid properties are also plotted in Figure 7-21 (b) and Figure 7-21 (b) for density and viscosity, respectively.

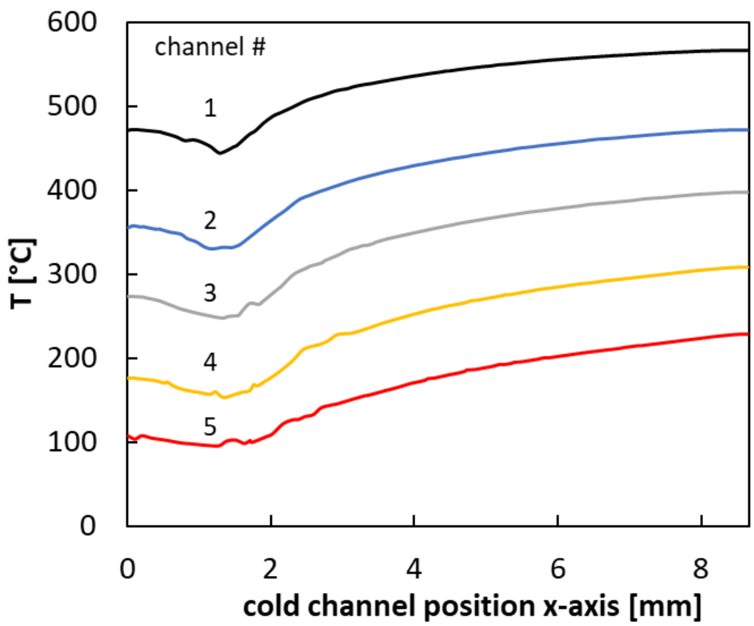

(a)

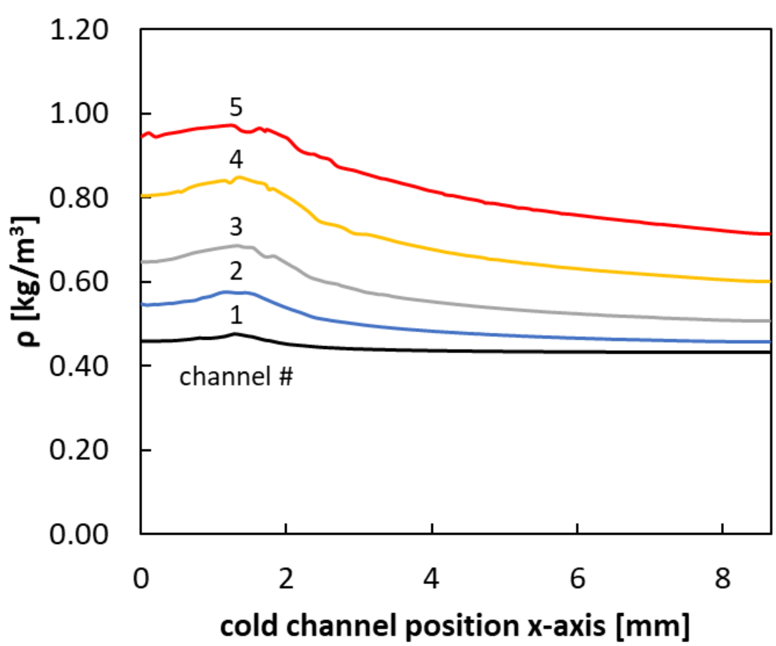

(b)

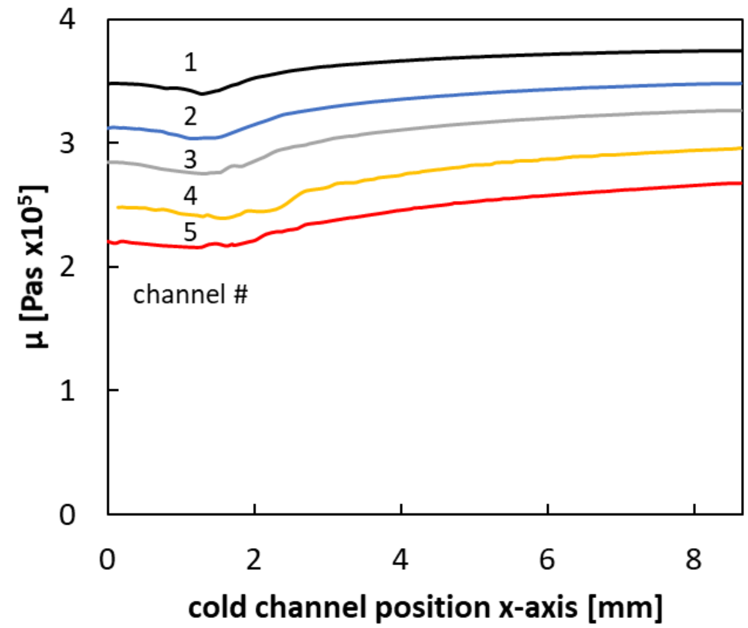

(c)

Figure 7-21: (a) temperature (b) density) (c) viscosity of the working fluid in the five microchannel shown in Figure 7-20 with respect to the channel position on the x-axis

It is interesting to notice that despite the linear trend of the temperature in the y-axis, the density is significantly affected by the effect of the temperature and the role of the high temperature is dominant in defining the mass-averaged density of 0.64 kg/m^3. On the contrary, the profile of the viscosity is linear across the M2HX and the resulting mass-averaged viscosity of 2.93 10^{-5} Pas reflects this trend. The case analyzed highlights that defining one reference temperature to be representative of the complexity in the change of the fluid property with temperature can introduce some approximation. Figure 7-22 shows the correlation between the fluid properties calculated at the temperature obtained by curve fitting the experimental data (x-axis) and the fluid properties obtained by mass averaging the fluid domain in the 3D-TUC simulation (y-axis). A good agreement can be observed, as the points tend to lie on the 45° line, which correspond to the case in which the two methods have the same output. The outcome of this study shows that 3D-TUC analysis can be used in defining the curve fitting temperature required by the initial model (hybrid model + heat spreading model) to provide accurate predication of the performance of the M2HX.

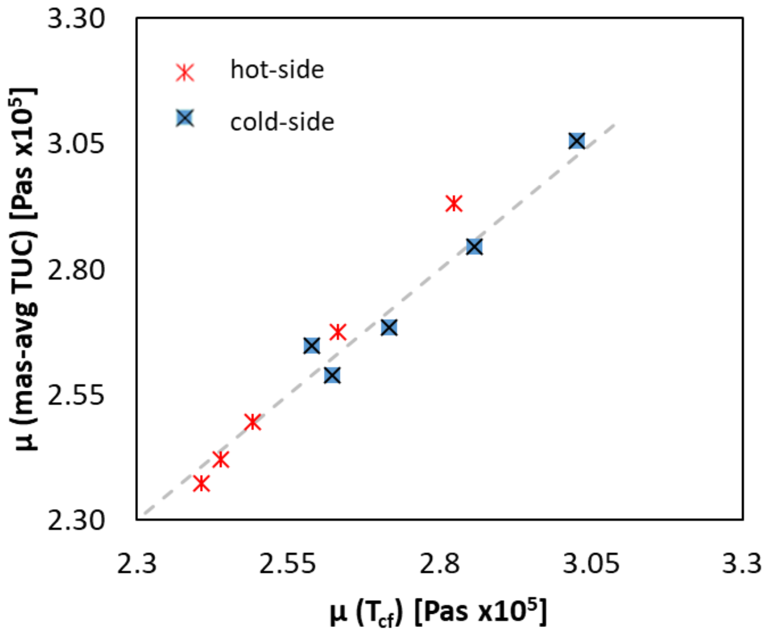

(a)

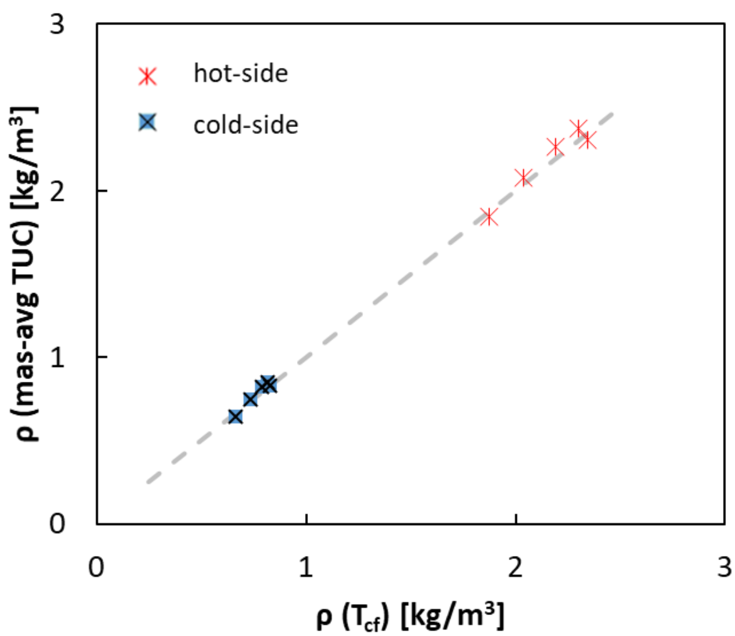

(b)

Figure 7-22: Comparison between the curve fitting method and the 3D –TUC with respect to the (a) viscosity (b) density

7.6.2 3D Thermal Unit Cell Performance Prediction

Besides using the 3D-TUC as a tool to predict the curve fitting temperature for the hybrid model, it is also possible to compare the performance of the two models with respect to the experimental data. As starting point, it is important to verify the prediction of the pressure drop across the microchannel. In this case, experimental data are not available to directly verify the quality of the simulation. However, due to the close match between the experimental data and the hybrid method, it is possible to compare the prediction of the 3D-TUC with the values of the pressure drop in the microchannels predicted by the SMM with T_{cf}. The comparison for the high temperature set of data of the pressure drops in the microchannel between the 3D-TUC model and the SMM model is shown in Figure 7-23. Figure 7-23(a) shows a good agreement between the two models in predicting the pressure drop of the cold microchannel, with a maximum deviation of 7% for the highest flow rate. For the hot side, the comparison between the two models presents a maximum deviation of 5% in the pressure drop of the hot-side microchannel for the lowest flow rate, as shown in Figure 7-23(b).

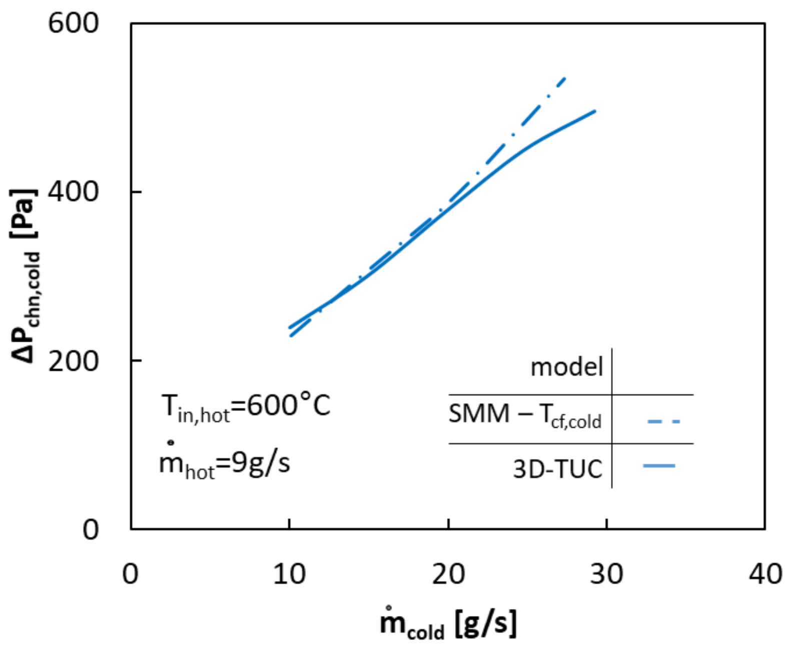

(a)

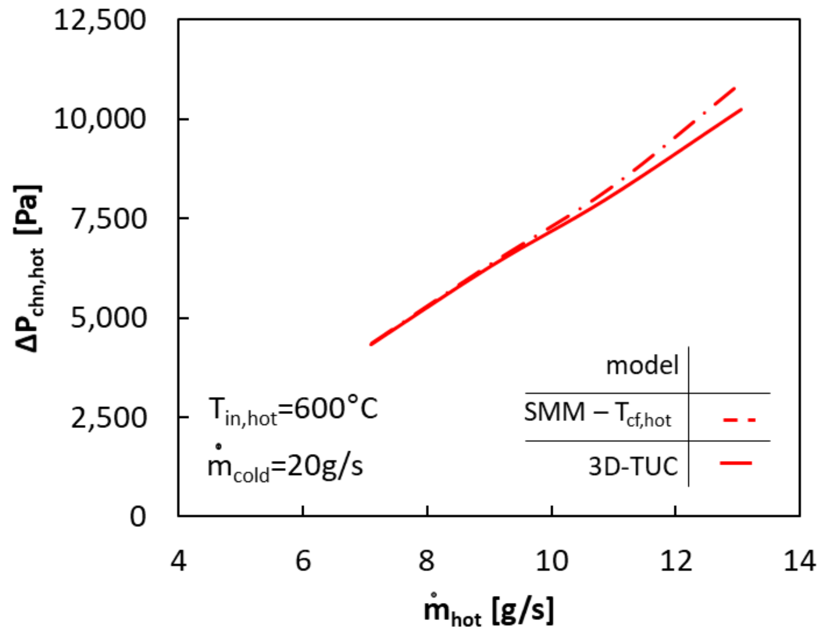

(b)

Figure 7-23: Comparison between the 3D-TUC model and the SMM (using T_{cf})in terms of pressure drop in the microchannel as a function of the mass flow rate for (a) the cold-side, while varying the cold-side mass flow rate and keeping the hot side at 9/g/s and (b) the hot-side, while varying the hot-side mass flow rate and keeping the cold-side at 20/g/s

Based on these positive outcomes, the prediction of the 3D-TUC model is indirectly validated, as the pressure drop in the manifold is computed with the same model. As to the heat transfer performance, the comparison of the effectiveness for the high temperature set of data between the 3D-TUC model and the combination of hybrid model and heat spreading model (HM+SP) is shown in Figure 7-24 as a function of the mass flow rate. The experimental data are also included in the graphs. Both Figure 7-24 (a) and Figure 7-24(b) show a small improvement in the performance prediction when using the 3D-TUC, with the average deviation from the experimental data that reduced from 7 to 6%. It is interesting to notice that the highest difference between the two models occurs for the highest values of effectiveness. Those are the instances when the difference between inlet and outlet temperature is the highest and the change in fluid properties is the most significant. The limit of defining the properties of one temperature only can cause the deviation shown in the graph. Another possible reason of the difference in the prediction can be the definition of the

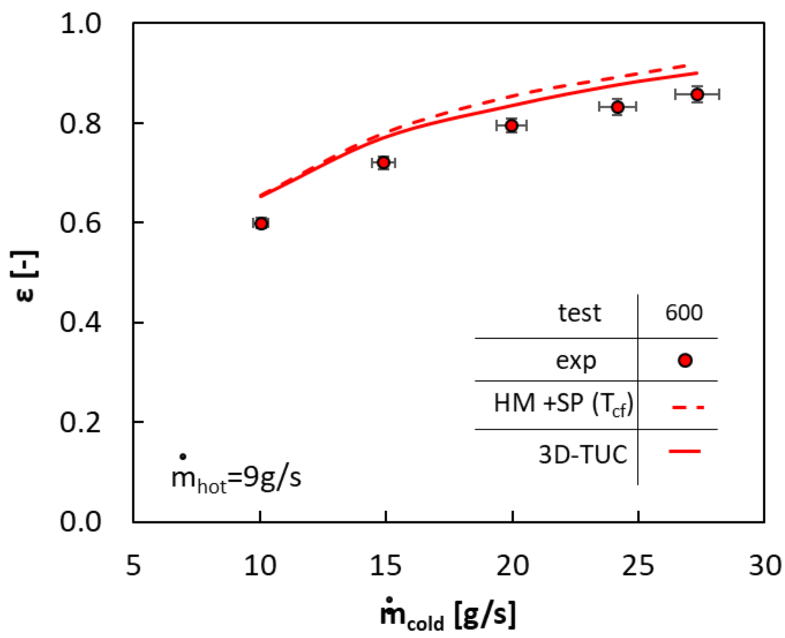

(a)

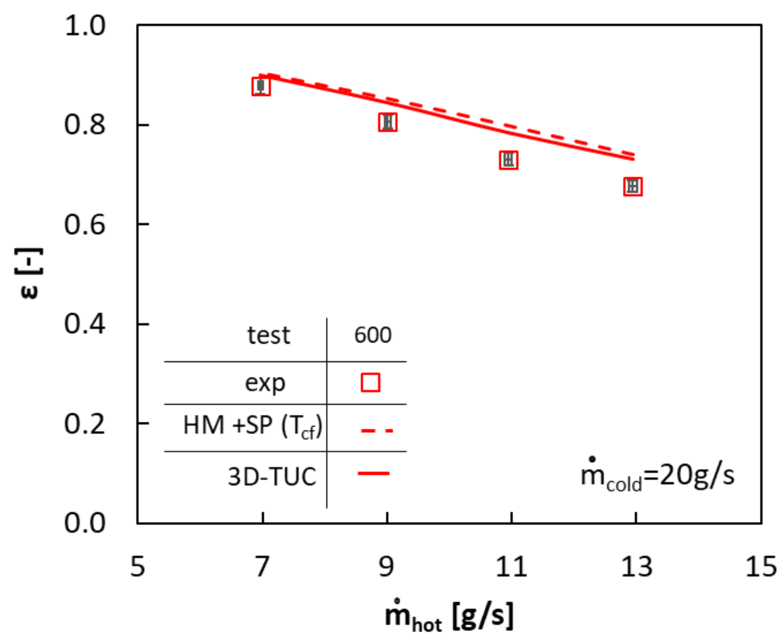

(b)

Figure 7-24: Comparison between the 3D-TUC model and the SMM (using T_{cf})in terms of effectiveness as a function of the mass flow rate for (a) the cold-side, while varying the cold-side mass flow rate and keeping the hot side at 9/g/s and (b) the hot-side, while varying the hot-side mass flow rate and keeping the cold side at 20/g/s thermal conductivity of the solid. In case of the combination of the hybrid and the heat spreading models, the thermal conductivity is given as a constant value. In reality, the thermal conductivity of the solid also vary across the HX, due to the different temperature, thus resulting in different thermal resistance according to the location of the M2HX. This effect is included in the 3D-TUC model by defining the thermal conductivity as a function of the temperature.

7.7 Comparison with State of the Art

To rate the performance of the 4.5” x 4” x 3.5” M2HXs against conventional design HXs, the experimental results obtained during the performance testing were compared with the performance of conventional HXs. Beside the PFHXs mentioned in Table 5-4, a series of commercially available PFHXs using wavy fins and louvered fins were added to the analysis, based on a database provided in Ref. [6] and collected by EES software. The key geometrical specification of the selected PFHX surfaces are shown in Table 7-2.

Table 7-2: Key geometrical specification of conventional PFHX surface[6]

Name	Fin Type	Fin pitch [fin/cm]	Plate spacing (cm)
S38a-606	Louvered	2.38	0.635
S12-606	Louvered	2.39	0.635
S34-111	Louvered	4.37	0.635
S1986	Plane	7.82	0.636
S1144-38W	Wavy	4.50	1.019

The procedure conducted to evaluate the performance of those HXs was the same as the one described in Section 5.8. Figure 7-25 shows the performance comparison between the M2HX and PFHXs in terms of gravimetric heat transfer density ($Q/M\Delta T$) as a function of COP, where M is the overall mass of the HX and ΔT is the temperature difference between the hot and cold inlet temperatures. It is possible to see that for the same COP, the second M2HX yields more than 50% improvement in gravimetric heat transfer density ($Q/M\Delta T$) compared to the wavy and louvered PFHXs. This deviation increases furtherly when comparing with the plane PFHXs used as a term of comparison in Figure 5-18. Figure 7-25 also includes the comparison with PCHXs. As observed during the analysis of the first M2HX, PCHXs have performance similar to the one of the plane PFHXs. The second M2HX then represents a significant improvement in mass reduction compared to the other solutions available.

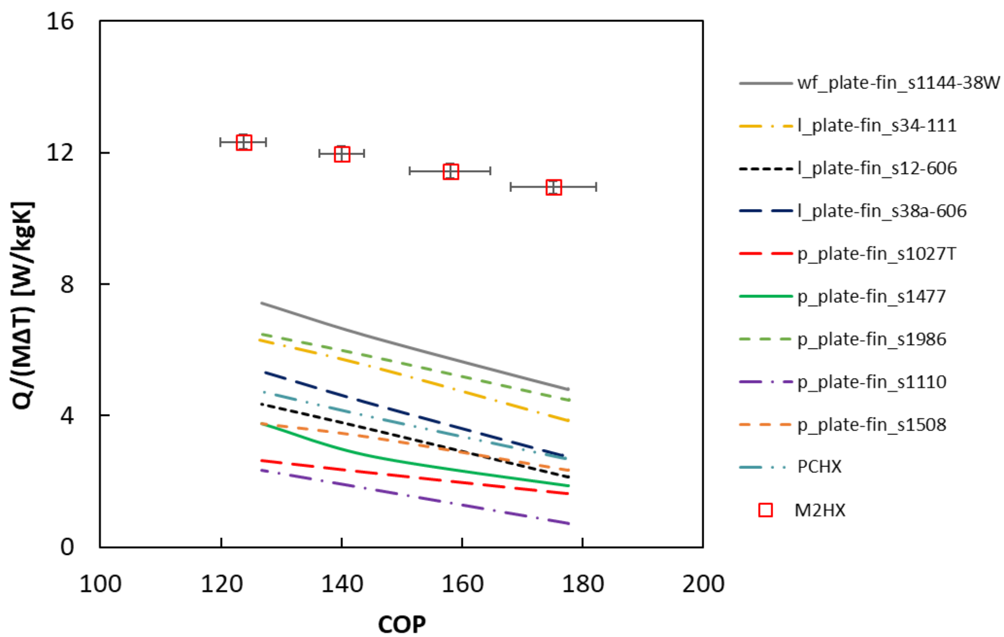

Figure 7-25: Performance comparison between the 4.5" x 4" x 3.5" subscale unit with PFHXs and PCHX and in terms of gravimetric heat transfer density

The performance comparison between the 4.5" x 4" x 3.5" M2HX and the PFHXs was also performed in terms of volumetric heat transfer density ($Q/V\Delta T$) as a function of COP, where V is the overall volume of the HX. As shown in Figure 7-26, even though reduced, the second M2HX still yields improvement in volumetric heat transfer density ($Q/V\Delta T$) compared to plane PFHXs. The reason of the difference in the level of improvement between gravimetric and volumetric heat transfer density is the objective function used for the optimization of the second M2HX. As a matter of fact, the goal of the design was to achieve mass reduction at a fixed volume and fixed heat duty. The design obtained for the second M2HX was then characterized by relatively tall manifold channels that are beneficial in terms of HX performance and mass reduction, but adversely affect the compactness in terms of volume.

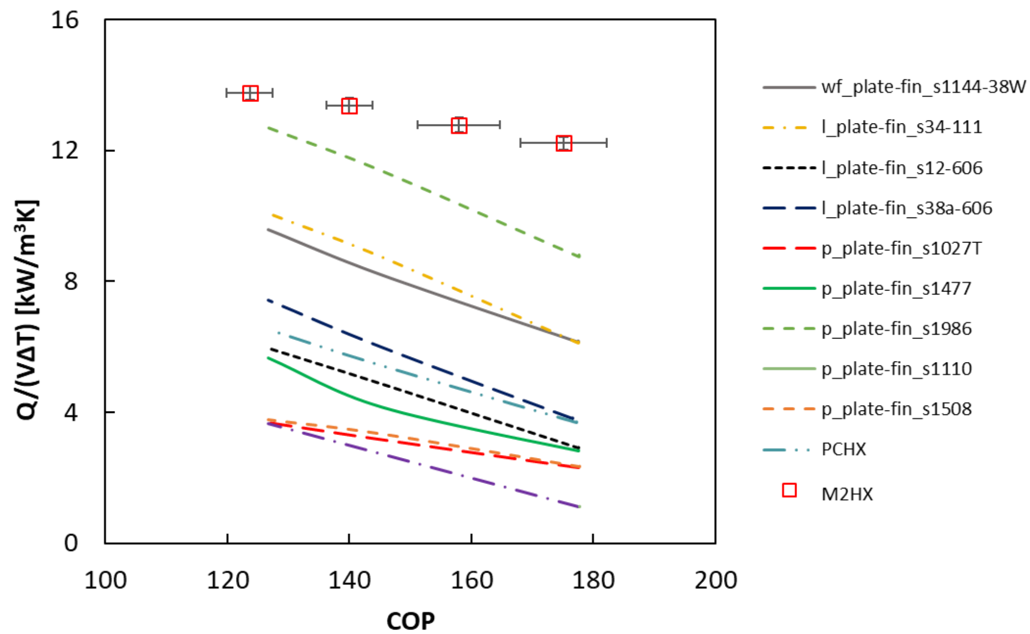

Figure 7-26: Performance comparison between the 4.5" x 4" x 3.5" subscale unit with PFHXs and PCHX and in terms of volumetric heat transfer density

7.8 Summary

In summary, the fabricated and assembled 4.5" x 4" x 3.5" M2HX was installed in the experimental setup and tested under isothermal conditions, as well as three different levels of temperature: low, medium and high temperature. A significant deviation was observed between numerical and experimental data for the high temperature test (inlet temperature of the hot side set to 600°C). A recalibration of the model was then performed to allow for improved performance prediction. The experimental pressure drop results were within 10% of the numerical values, while the corresponding heat transfer results were within 7%. Despite the success of the updated model, the procedure to calibrate the model was based on the experimental data. In order to predict the performance at the design level, a new model was developed, in which change of fluid properties with temperature was accounted for and replaced the previous approach of using constant properties during the analysis. The deviation between the new model and the experimental data was reduced to less than 7% for both pressure drop and heat transfer performance. Moreover, no prior knowledge of the experimental results was needed with this new model.

For the high temperature test, an overall heat transfer of 94.4 W/m^{2}K was recorded for $\dot{m}_{cold}$=28 g/s and $\dot{m}_{hot}$= 9g/s, which corresponds to $Re_{chn,cold}$=99 and $Re_{chn,hot}$=265. Gravimetric heat transfer density (Q/MΔT) of 13.5 W/kgK and volumetric heat transfer density (Q/VΔT) of 15 kW/m^{3}K were recorded for this heat exchanger for a coefficient of performance of 120. The performance of the tested heat exchanger was superior to the conventional plate-fin heat exchangers, by as much as greater than 50% improvement in gravimetric heat transfer densities for the entire range of experimental data when compared to louvered and wavy fins.

Chapter 8 Thermo-mechanical Analysis

8.1 Introduction

This chapter first discusses the importance of thermo-mechanical analysis for high temperature heat exchangers. A detailed explanation of the model used, including the assumptions, is then provided. The results of the combined effect of the thermal and pressure stresses are presented in terms of deformation and Von Mises stress. Lastly, the upgraded design features for manifold-microchannel to be suitable for high temperature and high pressure applications are presented.

8.2 Thermo-mechanical Analysis Model

As mentioned in the introduction, one of the main challenges of HTHPHX is the combined effect of thermal and mechanical stresses to which the HX is simultaneously subjected to. During the test of the M2HX, the maximum temperature of the fluid at the inlet is 600°C, with a pressure difference of 240 kPa across the two sides of the HX. As discussed in the material choice (Section 2.3), when the operational temperate is increased, the mechanical properties of the metals degrade and the levels of pressure that can be tolerated at low temperature cannot be withstood by the HX anymore. Moreover, the difference of temperature between the inlets of the two sides is in the order of 580°C, which creates a big temperature gradient across the HX. Therefore, assessing the deformation of the part and the magnitude of the stresses on the HX becomes crucial in determining the performance of M2HX. Although recognizing the importance of the effect of the combination of high temperature and pressure over a long period of time that can lead to creep was not included in this study.

The thermo-mechanical modelling of the HX involves a coupled CFD/FEM approach. For this analysis, ANSYS Workbench is used to couple the effect of temperature and pressure on the HX. The geometry is first created in SpaceClaim and shared by both CFD and FEM software. The fluid-dynamic profile and the thermal distribution are then solved using FLUENT. From the solution obtained with FLUENT, the temperature distribution is imported into the Static Structural analysis of ANSYS Workbench as thermal load. Once the pressures and the fixed structures are added, the combined thermal and mechanical stress analysis is solved using the Static Structural analysis of ANSYS Workbench. In this procedure, the hypothesis is that the solution of the flow and thermal fields are not affected by the mechanical stresses. Therefore, both simulations can be decoupled and run sequentially. This assumption is valid provided that the deformation obtained as a result of the thermo-mechanical analysis does not significantly alter the geometry of the HX.

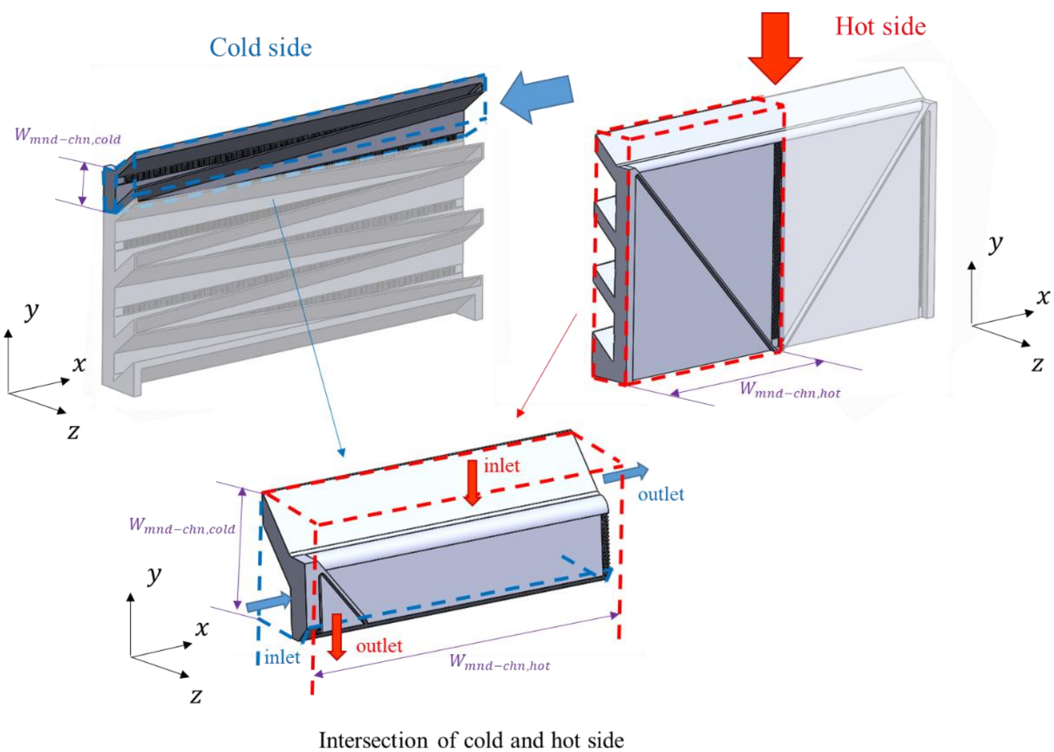

Figure 8-1: Geometrical identification of the representative portion of the M2HX

8.2.1 Geometry Identification

The overall size of the HX combined with the small features of the microchannels make the analysis of the entire HX computationally prohibitive. The first step of the thermo-mechanical analysis is then to identify a representative portion of the M2HX that can capture the real geometry of the HX (including both sides), without incurring in computational capability limitations. To have both sides of the HX in the representative portion of the HX, the most obvious choice is to select one stack. However, in this case, the HX complexity is simplified to only 1/10th of the M2HX, with a minimum estimated mesh with more than 60 million cells. Therefore, it is necessary to furtherly simplify the model. A possible option is to consider half manifold on the cold side (as shown in the top left corner of Figure 8-1) and half manifold on the hot side (as shown in the top right corner of Figure 8-1) and analyze the zone of the intersection of those two regions. Compared to the volume of the tested M2HX, the region analyzed is 1/120th in size, which allows for a detailed analysis without incurring in computational limitations (mesh cell count in the order of 5 million). As highlighted in Figure 8-1, the resulting sample includes the fluid on both sides of the HX, as well as the metal part. It can be noticed that this domain is very similar to the one of the 3D-TUC model. In this case, however, the manifold channels have to be included as they play a crucial role in the structural analysis of the HX.

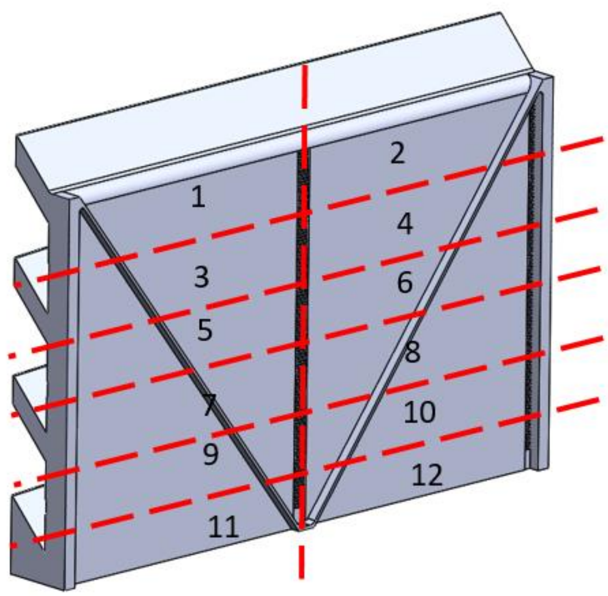

Figure 8-2: Possible alternatives in selecting the representative portion of the M2HX

However, with tapered manifold walls, the choice of the representative portion of the HX needs to be carefully addressed. As shown in Figure 8-2, each of the 12 parts in which the HX can be subdivided has a different geometry. It is then suggested to choose the one that is expected to have the biggest deformation. With reference to Figure 8-2, regions 1 and 2 are the one that need to be chosen because they are the portions where the distance between the manifold walls is the longest.

8.2.2 CFD Analysis

The second step of the thermo-mechanical analysis is the computational fluid dynamic modelling, in which the thermal and flow fields are numerically simulated using the CFD software. As shown in Figure 8-1, the portion of HX selected, includes the manifold-channels. It can be observed that in cases where the number of microchannels considered is a small fraction of the total number of the microchannels of the full design, it might become problematic to simulate the fluid flow in the manifold channels. As shown in Figure 8-3, the tapered shape of the manifold on the hot side (whose inclination is based on the full side length) creates a flow distribution that does not mimic the full-size HX. In order to avoid this problem, the flow in the manifold-channels is not modeled, as it is does not contribute to the heat transfer. The flow is then directed vertically into the microchannels, as in the 3D-TUC model. The definition of the boundary conditions is also the same as the one in 3D-TUC model (see Section 7.6). Fluid and solid properties dependence on temperature are also implemented. The geometry is created in SpaceClaim, exported to FLUENT Meshing for the mesh generation and the mesh is imported into FLUENT for the computation. The resulting flow and thermal fields are obtained by solving the governing continuity, momentum, and energy equations to a tolerance of 1e-4 for continuity and momentum, and 1e-10 for energy.

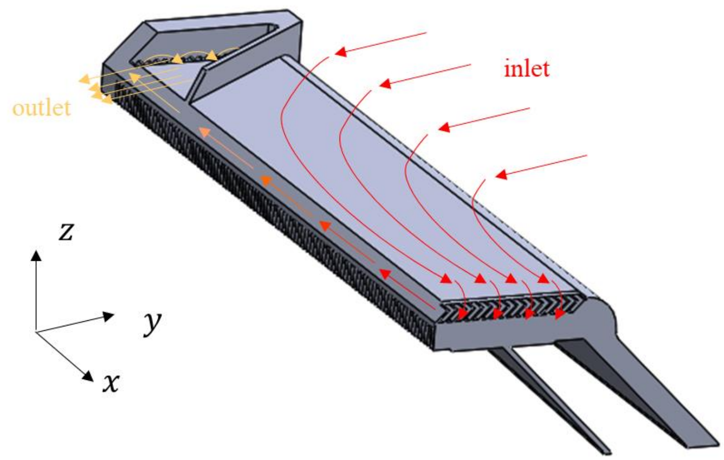

Figure 8-3: Fluid flow visualization in the manifold channel with tapered manifold

8.2.3 Finite Element Modelling

The third step is to import the thermal field results obtained from the CFD simulation into the computational solid mechanics modelling to study the behavior of the HX at the operational conditions and assess the level of stress and deformation. The geometry created in SpaceClaim is also used for the FEM analysis. In this case, however, the presence of the two fluid regions is not needed and they are suppressed during the analysis. The focus is then moved to the solid body. The properties of the material of the solid body are based on the information provided by the library of Workbench for the additive manufactured Inconel 625. Moving to the setup of the Static Structural analysis of ANSYS Workbench, it requires to determine the connection and the loads on the body. As shown in Figure 8-4, the external frame extensions used to weld the core to the headers are considered fixed.

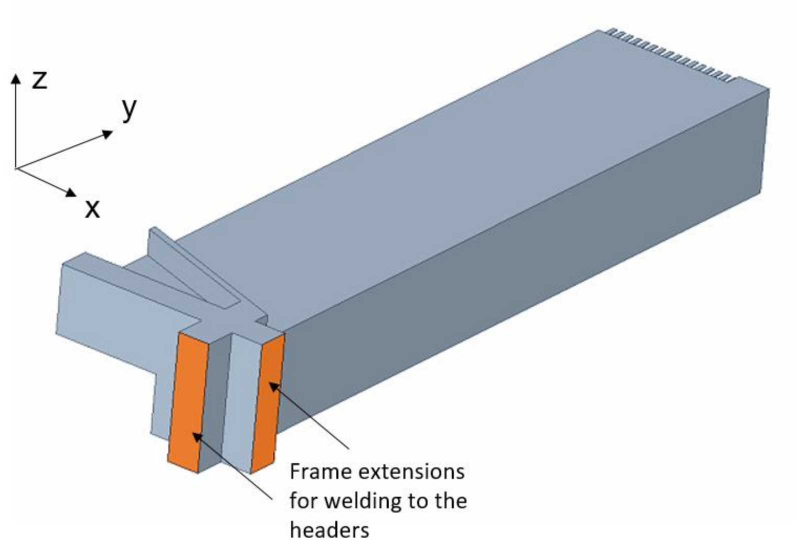

Figure 8-4: Fixed surface for the finite element modelling

For the loads, the effect of the pressure on the two sides is defined by imposing the value of the pressure on the surfaces facing the two different pressures. Figure 8-5 shows that the pressure on the two sides of the manifold wall is the same. To be accurate, the pressure of the side facing the outlet is equal to the pressure at the inlet subtracted by the pressure drop across the microchannels. However, as the system pressure difference between the inlet and exit manifold is only 2% or less, the same pressure can be assumed on both sides of the manifold wall without affecting the final result. . For the thermal stress, the profile obtained with the CFD simulation in FLUENT is imported into the structural analysis of ANSYS. A dedicated mesh for stress analysis is then generated and the combined effect of thermal and mechanical stresses is simulated. The results are expressed in terms of von Mises stress and deformation of the component during the thermo-mechanical analysis.

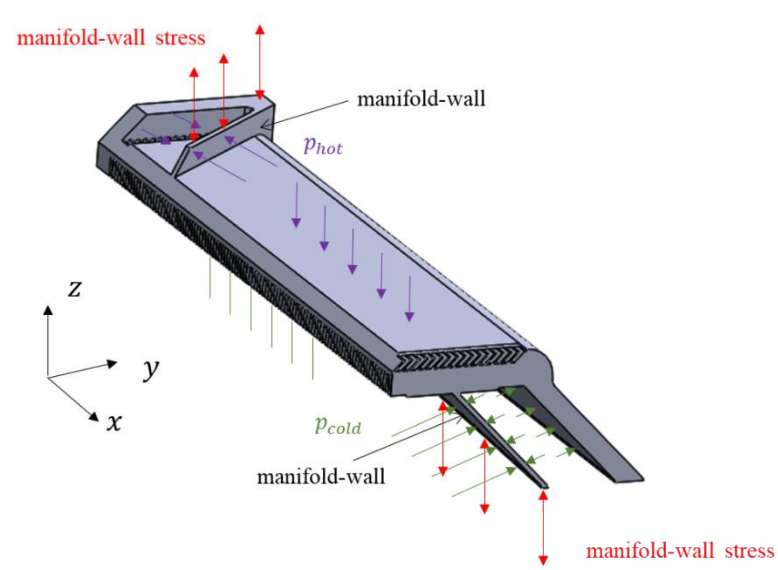

Figure 8-5: Pressure definitions for the finite element modelling

8.3 Thermo-Mechanical Analysis Results

The first condition that needs to be studied is the one where the HX is pressurized at the design pressures, under isothermal conditions. The pressures are then set to be 340 kPa and 100 kPa for hot- and cold-side respectively. Figure 8-6(a) shows the deformation of the part. As expected, the higher pressure on the hot side causes a deformation in the vertical direction (z-direction with reference to Figure 8-6(a)). However, the magnitude of the deformation is in the order of few microns at most, thus becoming almost negligible.

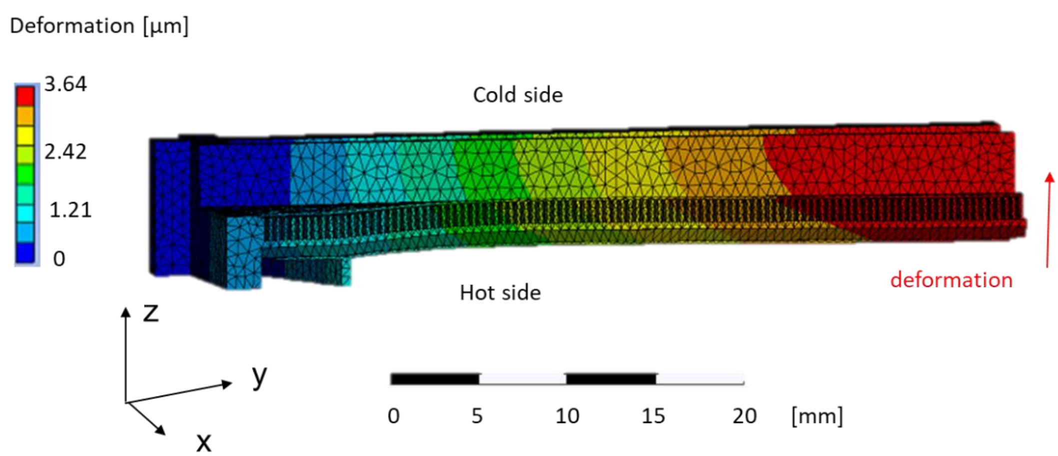

(a)

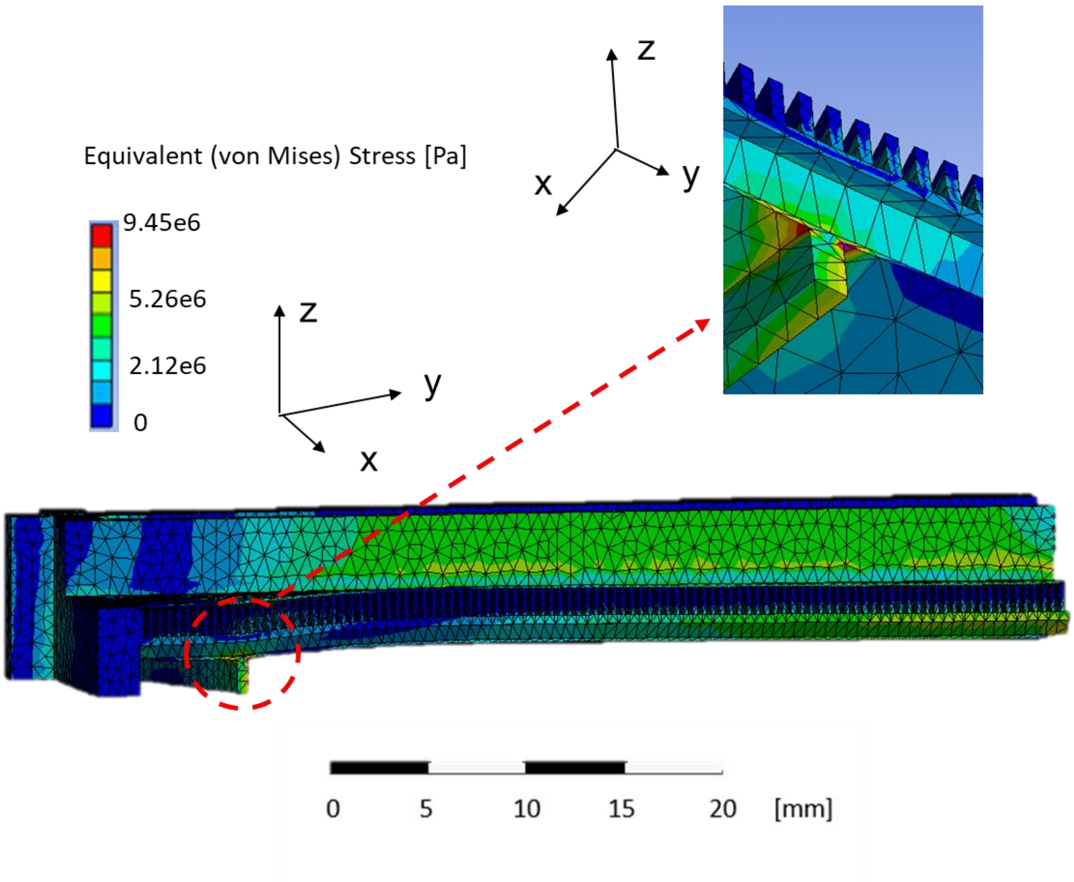

(b)

Figure 8-6: Stress analysis under 340kPa for the hot-side and 101kPa for the cold side in terms of (a) deformation, (b) equivalent (Von Mises) stress

The same outcome can also be obtained studying the contour plot of the equivalent (Von Mises) stresses shown in Figure 8 6(b). In order to evaluate the level of stress that the material needs to withstand, the equivalent (Von Mises) stresses need to be compared with the yield strength of the material. For the additive manufacture Inconel 625, the yield strength in the database of the software is given as a function of the temperature. For the isothermal case (temperature equals to 24°C), the yield strength of Inconel 625 is 655 MPa. When compared to the level of stresses shown in Figure 8 6(b), it can be observed that the part is working at less than 2% of the yield stress. In particular, it is possible to notice that the pick of the stresses is found at the intersection between the manifold wall and manifold base. This is the point where most of the stress caused by the deformation is concentrated.

Once demonstrated that the HX can withstand the level of pressure determined by the operational conditions in terms of mechanical strength, it is then possible to move to the thermal analysis. The thermal profile obtained from the CFD analysis is imported in the structural analysis. As shown in Figure 8-7, the typical temperature distribution of a cross-flow HX is observed. The temperature varies from 570°C at the inlet of the hot side to 160°C at the inlet of the cold side, for a total difference of temperature across the HX of 400°C, thus resulting in thermal expansion of the unit.

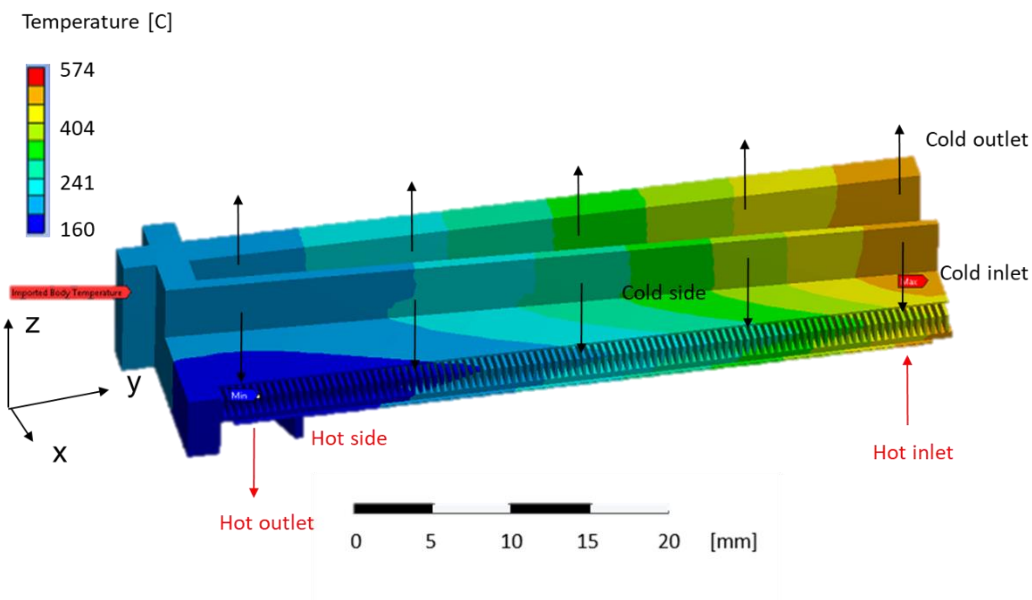

Figure 8-7: Imported temperature profile in the mechanical analysis

Pressure and thermal stress are then applied to the model and stress analysis of the combined effects performed.

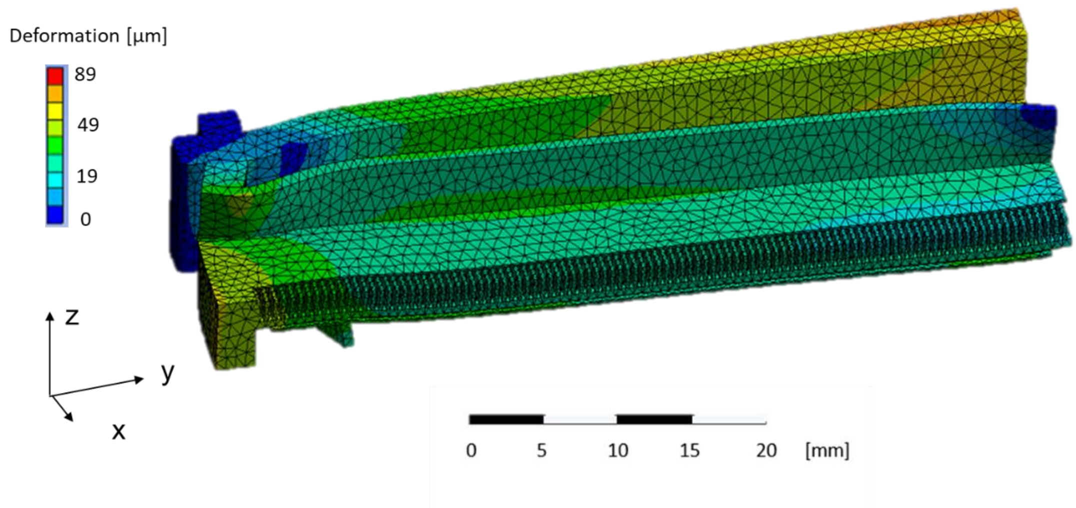

(a)

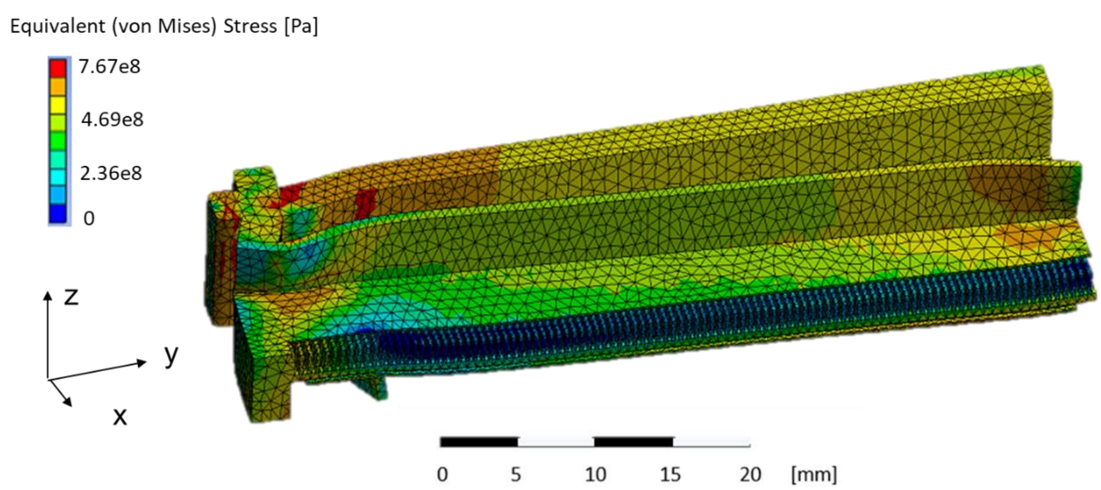

(b)

Figure 8-8: Thermo-mechanical analysis under 340kPa for the hot-side and 101kPa for the cold side with $T_{in,hot}$=600°C in terms of (a) deformation, (b) equivalent (Von Mises) stress

Figure 8-8(a) shows the deformation of the part. Compared to the case where only the pressure was applied, the deformation is increased due to the thermal expansion given by the temperature difference across the HX. Although increased, the value of the deformation remains very small and can be neglected in the CFD analysis. Moving to the equivalent (Von Mises) stresses is shown in Figure 8-8(a) a significant increase in stresses was observed. In particular the area in the proximity to the frame extensions for the welding are subjected to the highest stress. Few pick points are found where the stress level equals the yield strength of the material. The area that need to be improved is then the one around the frame. The manifold wall, instead, is subjected to medium stresses, while microchannels and base plate have the lowest stresses.

Besides studying thermo-mechanical performance at the operational conditions, it is also possible to see the effect of pressure and temperature when increased to more demanding conditions. The first case that can be analyzed is the one in which the pressure on the hot side is increased to 100 bar. This value corresponds then to situation of an HX operating at high pressure conditions. Figure 8-9 (a) shows the deformation of the part. Compared to the results of Figure 8-6(a), it is possible to see that increasing the pressure level from 3 bar to 100 bar does not change the distribution of the deformation, but the magnitude is significantly improved. In this case the maximum deformation is in the order of 100 µm, compared to the few microns of the 3bar test. However, also in this case, the deformation does not significantly affect the geometry, thus not having an impact on performance.

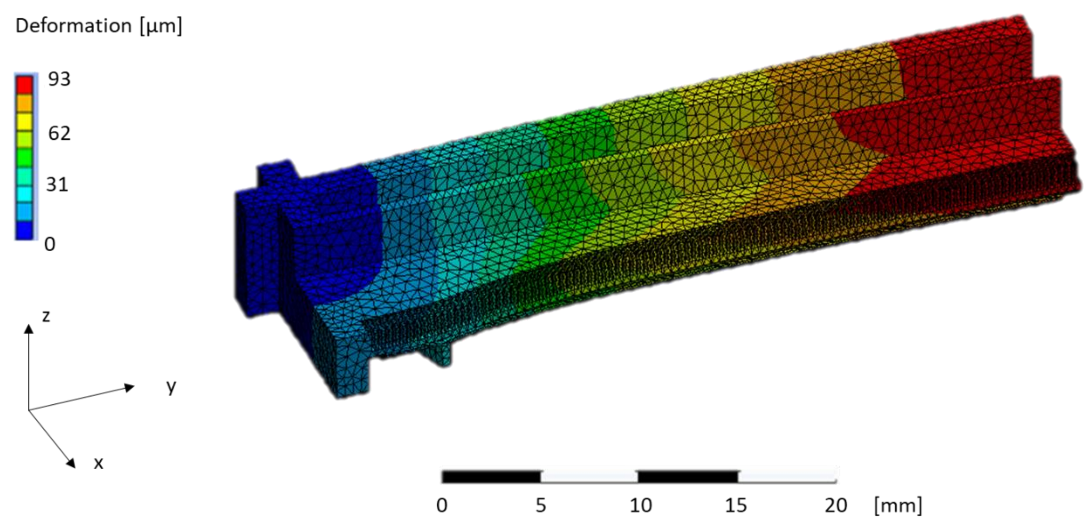

(a)

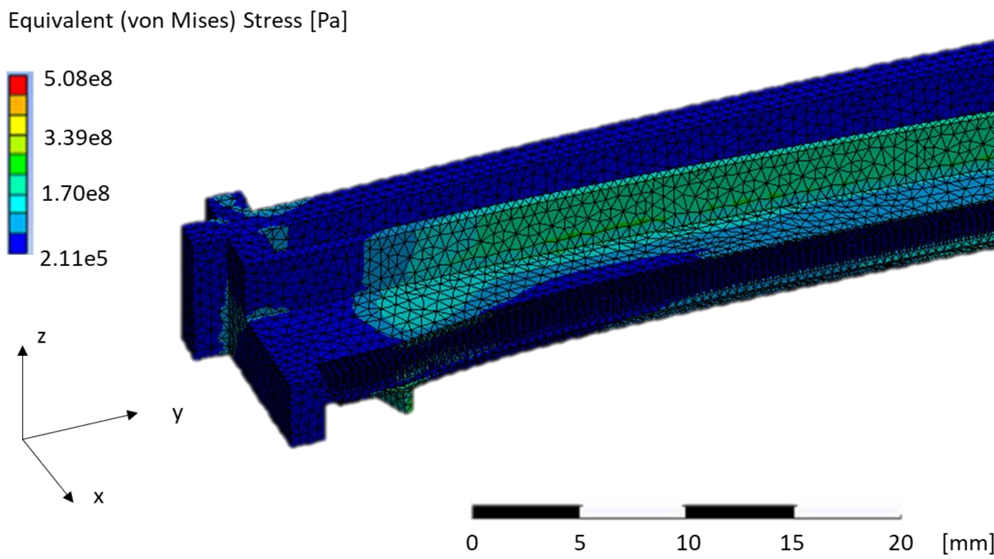

(b)

Figure 8-9: : Thermo-mechanical analysis under 100 bar for the hot-side and 1 bar for the cold side in terms of (a) deformation, (b) equivalent (Von Mises) stress

A similar conclusion can also be obtained studying the contour plot of the equivalent (Von Mises) stresses shown in Figure 8-9 (b). As observed in the case of 3 bar, when the temperature is not involved in the analysis, the areas that suffer from the highest levels of stress are the manifold walls. In this case, however, the magnitude of the stress is very close to the yield strength of the material. With the current design, a pressure of 100 bar generates stresses close to the part failure.

The second case that can be studied is the presence of high pressure and high temperature combined. In this case study, pressure and inlet temperature of the hot-side are assumed to be 100 bar and 1,000°C, respectively. For the cold-side, instead, 1 bar and 15°C are used for the analysis. With this condition, the temperature across the HX varies from 255°C to 855°C, thus resulting in a thermal gradient of 600°C across the unit. Figure 8-10(a) shows that the deformation of the unit is significantly higher compared to the previous cases. In this case the effect of the high pressure and high temperature generates deformation of similar magnitude. In particular, the pressure causes deformation in the z-axis, while the thermal deformation is dominant in the x-axis. The juxtaposition of those two effects causes a deformation that is higher than the single ones.

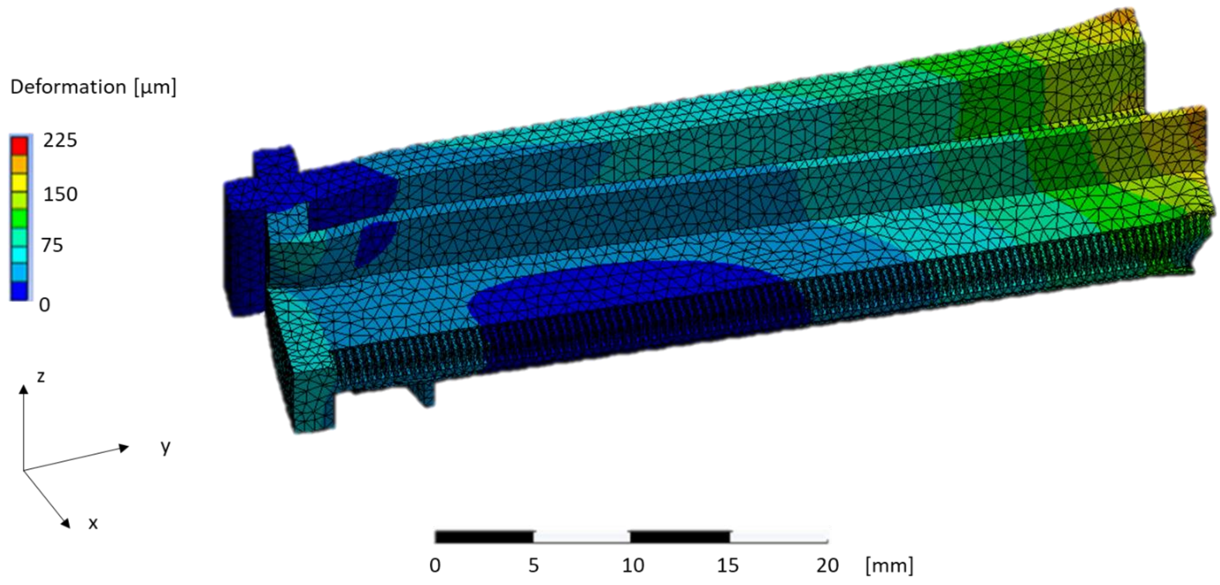

(a)

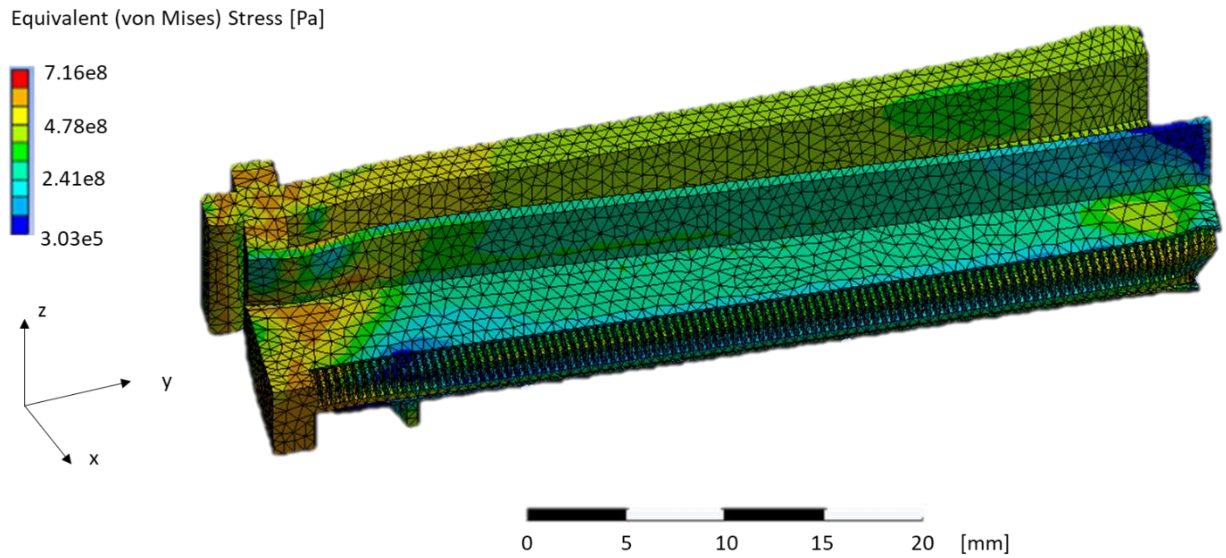

(b)

Figure 8-10: Thermo-mechanical analysis under 100 bar for the hot-side and 1 bar for the cold side with $T_{in,hot}$=1,000°C in terms of (a) deformation, (b) equivalent (Von Mises) stress

When converted in terms of stress analysis, Figure 8-10(b) shoes that stresses are uniform throughout the sample region. The stress concentrated at the frame extensions for the welding to the headers is mainly caused by the thermal expansion, while the stresses in the base and manifold channels are mainly driven by the pressure levels. Compared to yield strength of the material, the stress to which the unit is subjected to is close to the limit of the material, with peaks that exceed the resistance of the material and can cause the unit to fail during operation.

8.4 Summary

The thermo-mechanical model was developed to study the combined effect of pressure and temperature gradient on the HX. In order to simplify the analysis, a representative portion of the HX was selected for this study. CFD was initially performed to obtain the flow field and the temperature distribution in the solid. The temperature profile was then used as input to the stress analysis, combined with the effect of the pressure. It was noticed that the stresses due to the design pressure of 340kPa were almost negligible at room temperature. When increasing the temperature to the operational conditions (600°C), significantly higher equivalent (Von Mises) stresses were observed in the area around the frame extensions used to weld the core to the headers. The rest of the heat exchanger was subjected to lower stresses.

Chapter 9 A Porous medium approach for single-phase flow and heat transfer modeling in manifold microchannel heat

9.1 Introduction

This chapter presents the preliminary results of adopting porous medium in the analysis of M2HX. The model is described, including details of the calibration procedure for the parameters defining pressure drop and heat transfer. Few case studies were also simulated to access the quality of the model.

9.2 Model Description

Because of this, design of a manifold-microchannel heat exchanger requires the design of the manifold and microchannel. In some situations, a sequential design approach, where one first designs the microchannel and then the manifold—is sufficient to meet the requirements of the problem statements. The more demanding requirements of contemporary applications require manifold microchannel design to evolve and become more complex. In particular, reducing the volume and pitch of the manifold has become necessary. Reducing the volume of the manifold results in a higher flow maldistribution, and the ability to predict how maldistribution affects heat transfer rate is critical. Similarly, reducing the pitch of the manifold increases the effect of axial conduction in the solid, and understanding the effect on heat transfer is important. To those ends, it would beneficial to develop a porous medium approach for single-phase flow in manifold microchannel, which allows to predict pressure drop, maldistribution, axial conduction, and heat transfer rate with a much smaller computational demand when compared to a full 3D simulation, while guaranteeing very similar results.

9.2.1 Unit-Cell with Fluid and Fin

The model used in this study to describe the behavior of the real microchannel is based on the unit-cell shown in Figure 9-1. It consists of one microchannel segment, including the contraction/expansion at the entrance and exit of the microchannel, which result in pressure losses. As shown in Figure 9-1, the domain includes two regions: the fluid and the solid. The solid section represents the fin and the base, while the fluid section characterizes the microchannel and the two extensions at the inlet and outlet of the microchannel. It is also worth noting that the thickness of the fin (t_{fin}) and the microchannel (W_{chn}) in the y-axis are half the actual dimensions due to the symmetry conditions imposed on both sides of the geometry. The same explanation can be used to justify the use of half the width of the entrance from the manifold to the microchannel (W_{in}) in the x-axis. It is assumed in this model that entrance and exit have the same width. Temperature and mass flowrate are the boundary conditions at the inlet, while the pressure is imposed at the outlet of the microchannel. The rest of the geometry is treated as wall with a dedicated boundary condition to the bottom of the solid base, which is set to constant temperature.

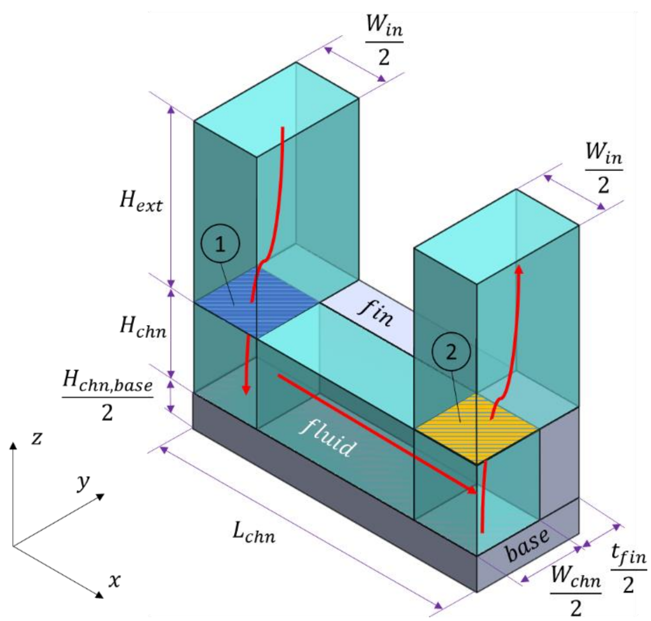

Figure 9-1: Schematic drawing of the unit-cell with fin, base and fluid.

As shown in Figure 9-1, the fluid region of the microchannel is divided into three parts to better characterize the mesh resolution: the region in which the fluid turns 90° to enter the microchannel, the straight portion of the microchannel and the second 90° turn that the fluid undergoes before leaving the microchannel. The mesh is generated in GAMBIT and imported to FLUENT for the computation. The governing continuity, momentum, and energy equations are solved to a tolerance of 1e-4 for continuity and momentum, and 1e-

10 for energy. The pressure is then computed directly in the CFD software and used to calculate the pressure drop in the microchannel (between plane 1 and 2 with reference to Figure 9-1).

$$\Delta P_{chn} = P_{1,} - P_2 \tag{60}$$

The mass-averaged fluid temperature on the microchannel outlet (T_2 with reference to the plane 2 of Figure 9-1) is also computed in the CFD software. It is used to calculate the effectiveness of the heat transfer process (ε) as

$$\varepsilon = \frac{T_2 - T_{in}}{T_{base} - T_{in}} \tag{61}$$

and, in case of constant temperature, it is possible to derive the NTU from the effectiveness through [17]

$$NTU = -\ln(1 - \varepsilon) \tag{62}$$

Once determined the NTU, it is possible to calculate the heat transfer coefficient at the bottom of the base (h_base) as [17]

$$h_{base} = NTU \frac{\dot{m} c_p}{A_{base}} \tag{63}$$

where, $\dot{m}$ is the mass flow rate in the microchannel, c_p is the specific heat capacity of the fluid and A_{base} is the surface area at the bottom of the base:

$$A_{base} = L_{chn} \left(\frac{t_{fin} + W_{chn}}{2} \right) \tag{64}$$

In case of a very conductive material, the temperature at the bottom of the base (T_{base}) is the same as the one at the wall between solid and liquid (T_{wall}), thus resulting in a fin efficiency (η_{fin}) of 1. The corresponding heat transfer coefficient (h_{wall}) can then be obtained from Eq. (64), replacing A_{base} with A_{wall}, which is the total surface area of the solid in contact with the fluid, defined as:

$$A_{wall} = L_{chn}\left(H_{chn} + \frac{W_{chn}}{2}\right) \tag{65}$$

In real applications, the material has such values of thermal conductivity that cause a different thermal profile at A_{wall}. It is possible to compute the temperature of this area with the CFD. However, when the microchannel is long and the mass flow limited, it can happen that $T_2 > T_{wall}$. This inequality creates a mathematical incongruity when substituting T_{base} with T_{wall} in Eq. (59) and trying to obtain the corresponding NTU with ε>1. In order to avoid this issue, an effective η_{fin} is introduced [17]

$$\eta_{fin} = \frac{tanh\,(m\,H_{chn})}{m\,H_{chn}} \tag{66}$$

where m is the fin parameter:

$$m = \sqrt{\frac{2\,h_{wall}}{k_s\,H_{chn}}} \tag{67}$$

with k_s defined as the thermal conductivity of the solid. It can be observed that it is not possible to quantify η_{fin} since it is a function of h_{wall}, which is also unknown. The problem can be solved by introducing an iterative procedure where the overall thermal resistance at the base has to the same either calculated using h_{base} or as a sum of the thermal resistances of the fin and base. This equality can be summarized as:

$$\underbrace{\frac{H_{base}}{h_{base}A_{base}}}_{\text{overall thermal resistance at the base}} = \underbrace{\frac{H_{base}}{k_s A_{base}}}_{\text{conductive resistance through}} + \underbrace{\frac{1}{h_{wall}A_{wall}\eta_o}}_{\text{overall fin thermal resistance}} \tag{68}$$

:

where η_o is the overall surface efficiency:

$$\eta_o = 1 - \frac{H_{chn}}{H_{chn} + \frac{W_{chn}}{2}}\left(1 - \eta_{fin}\right) \tag{69}$$

The main outcome of this iterative procedure is the heat transfer coefficient h_{wall}, as a generalization of the fin efficiency effect.

9.2.2 Unit-Cell with PM

When implementing the PM in place of the real design, the microchannel fluid and fin zones are replaced with one zone, which is treated as PM, with the exception of the fin base. As a consequence of this choice, length and height of the PM region are the same as the real channel, while the width is half the sum of the fin and channel width (see):

$$W_{PM} = \frac{W_{chn} + t_{fin}}{2} \tag{70}$$

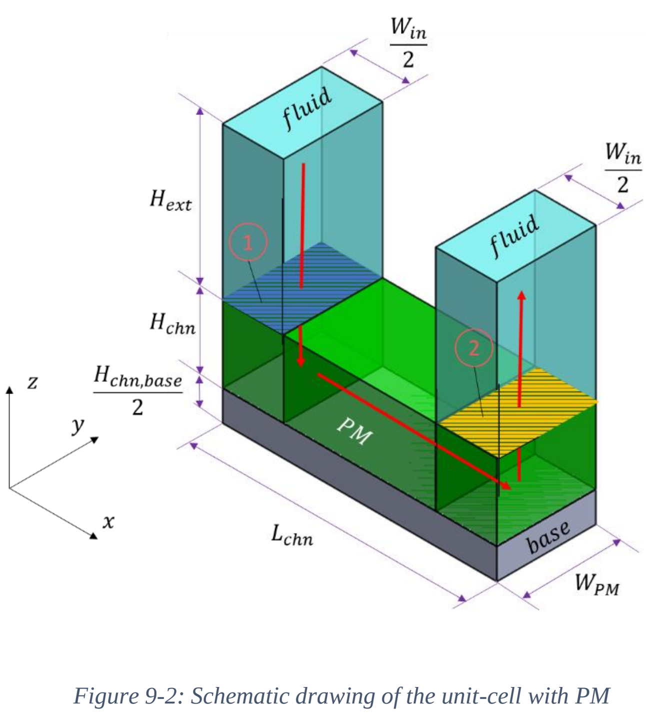

Figure 9-2: Schematic drawing of the unit-cell with PM

Introducing the PM approach, however, requires the definition of new terms that are used to concentrate the complexity of the real geometry into fewer variables. FLUENT is the CFD software used to compute also the performance of the unit-cell with the PM.

As to the momentum equations, the PM region is treated as a fluid part with the introduction of a source term (S) which is composed of two parts: a viscous loss term and an inertial loss term. In case of a simple homogeneous PM like the one under study, the source term for each of the directions (ith stands for x, y and z) is defined as

$$S_i = -\left(\underbrace{\frac{\mu_f}{\alpha} v_i}_{\substack{\text{viscous} \\ \text{loss term}}} + \underbrace{C_2 \frac{1}{2} \rho_f |v| v_i}_{\substack{\text{inertial} \\ \text{loss term}}} \right) \tag{71}$$

where μ_f and ρ_f are the viscosity and density of the fluid respectively and v is its velocity. The two terms that need to be defined are α and C_2, which are the permeability and the inertial resistance factor, respectively. Their calibration and role will be discussed in the PM calibration section.

As to the model energy transport in PM, FLUENT has two different approaches: Local Thermal Equilibrium (LTE) and Local Thermal Non-Equilibrium (LTNE). In LTE, the PM and the fluid are assumed to be in thermal equilibrium, which means that solid region and fluid region have the same temperature. In case of MMHX, this condition is not valid, and it is required to adopt the LTNE method. The conservation equations of energy for fluid and solid are respectively:

$$\frac{\partial}{\partial t}\left(\gamma \rho_f E_f\right) + \nabla\left(\vec{v}\left(\rho_f E_f + p\right)\right) = \nabla\left[\gamma k_f \nabla \mathrm{T_f} - \left(\sum_i h_i J_i\right) + (\bar{\bar{\tau}}\vec{v})\right] + S_f^h + h_{fs} A_{fs}(T_s - T_f) \tag{72}$$

$$\frac{\partial}{\partial t}\left((1-\gamma)\rho_s E_s\right) = \nabla\left((1-\gamma) k_s \nabla \mathrm{T_s}\right) + S_s^h + h_{fs} A_{fs}(T_s - T_f) \tag{73}$$

where E_f is total fluid energy, E_s is total solid medium energy, k_f is the fluid thermal conductivity, ρ_s and k_s are solid density and thermal conductivity, respectively. γ is the porosity of the PM and it is defined as the ratio of the volume of the fluid over the total volume replaced by the PM. In this work the porosity is directly obtained from the geometry as

$$\gamma = \frac{W_{chn}}{W_{chn} + t_{fin}} \tag{74}$$

It is possible to notice that the total energy terms and k_f are corrected with the porosity. $\sum_i h_i J_i$ stands for the effect of enthalpy transport due to the diffusion of species, $(\bar{\bar{\tau}}\vec{v})$ for the effect of viscosity, and S^h is the energy source term. The last term in both the Eq. (72) and (73) is the coupling term which models heat transfer between the fluid and the solid domains of the porous region. Two new parameters are introduced to simulate the heat transfer between fluid and solid. First, the interfacial area density (A_{fs}) is defined as the ratio of the wetted surface area over the sample volume of the PM. With the given geometry, the definition results in

$$A_{fs} = \frac{A_{wall}}{L_{chn} H_{chn} \left(\frac{W_{chn} + t_{fin}}{2} \right)} \tag{75}$$

Second, the heat transfer coefficient of the wetted area of the porous zone (h_{fs}), which combined with A_{fs}, needs to provide the same heat transfer behavior as the real microchannel.

9.2.3 PM Region Calibration

The first terms that need to be calibrated are the one regarding the fluid flow: α and C_2 in the three directions. The goal is to set them so that the pressure drop in the unit-cell with PM is within an acceptable deviation from the pressure of the unit-cell with fluid and fin. It is worth noting that also in the case of the unit-cell with PM the pressure drop is defined at the same planes (see Figure 9-2).|

$$\Delta P_{chn,PM} = P_{1,PM} - P_{2,PM} \tag{76}$$

The calibration of the PM is set to a level of acceptance such that

$$\frac{\left|\Delta p_{chn} - \Delta p_{chn,PM}\right|}{\Delta p_{chn}} \leq 1\% \tag{77}$$

As to the directions of the PM region, they are selected to be parallel to the x, y and z axis (see Figure 9-2). In order to prevent the flow in the y-direction i.e. through the fin, the values of α and C_2 in y are 1,000 times bigger than then one of x and z directions, which are assumed to be the same value. In order to determine the value of α of the x and z components, the pressure drop in the unit-cell with fluid and fin is computed for multiple flow rates characterized by low Re numbers (less than 100). For the given geometry, Re_{chn} can be defined as

$$Re_{chn} = \frac{\rho_f v D_{h,chn}}{\mu_f} \tag{78}$$

where:

$$D_{h,chn} = \frac{2H_{chn}W_{chn}}{H_{chn} + W_{chn}} \tag{79}$$

In case of low Re, in fact, the inertial losses are dominated by the viscous ones and the effect of the extra source term in the momentum equations due to C_2 can be neglected. Once calibrated α to follow the criterion of Eq. (78) the pressure drop is computed for flow rates that result in Re_{chn} on the high end of the laminar region (more than 1,500). In those cases, the inertial losses effect is present and needs to be added to the momentum equations. When plotting the Δp_{chn} vs Re_{chn} graph (see Figure 9-3), in fact, the curve has the typical quadratic trend due to inertial effect. When the Re_{chn} increases, however, the Re_{mnd} can transition to turbulent even when Re_{chn}<2,300. Re_{mnd}, in fact, is defined as

$$Re_{mnd} = \frac{\rho_f v_{mnd} D_{h,mnd}}{\mu_f} \tag{80}$$

where:

$$D_{h,mnd} = W_{in} \tag{81}$$

When designing MMHX, Re_{chn} is typically set for laminar region but if the geometry is such that $\frac{2}{W_{chn}+W_{fin}} > \frac{2H_{fin}W_{chn}}{(H_{fin}+W_{chn})^2}$, e_{mnd}> $Re_{chn}$and can transition to turbulent. In those cases, the solver needs to be switched to a model that introduces the turbulence. The model adopted in those cases is the k-ε and the equations are solved to a tolerance of 1e-4. This approach is applied to both real and PM cases. In both instances, the zone identified between planes 1 and 2 in Figure 9-1 and Figure 9-2 is set to laminar region in FLUENT, since Re_{chn}<2,300. The value of C_2 of the x and z components are then calibrated to match the criterion of Eq. (78). It is worth noting that once obtained both α and C_2, it is recommended to rerun also the cases for low Re_{chn} and confirm that the deviation is still acceptable. Once calibrated the fluid flow, heat transfer parameters need to be tuned so that the thermal performance of the two unit-cells is the same. In particular:

$$1 - \left|\frac{T_{2,PM} - T_{in}}{T_{2,} - T_{in}}\right| \leq 0.25\% \tag{82}$$

where $T_{2,PM}$ is the mass-averaged temperature at plane 2 with reference to Figure 9-2. In order to achieve this condition, the following procedure is defined:

$$h_{fs} = h_{wall} \tag{83}$$

$$A_{fs,PM} = \beta A_{fs} \tag{84}$$

where β is a corrective factor introduced to hold the criterion of Eq. (83).

9.3 Case Study

9.3.1 Pressure Drop Calibration

In this section, a case study with a real MMHX design is presented. The geometry and operational conditions are given in Table 1, where T_f and P_f are the temperature and pressure of the fluid used to calculate the fluid's properties.

Table 9-1: Case study geometry, operational conditions and materials

$\boldsymbol{W_{fin}}$ **[mm]**	0.146
$\boldsymbol{W_{chn}}$ **[mm]**	0.220
$\boldsymbol{L_{chn}}$ **[mm]**	25.875
$\boldsymbol{L_{in}}$ **[mm]**	5.372
$\boldsymbol{T_f}$ **[°C]**	23
$\boldsymbol{P_f}$ **[kPa]**	101.325
fluid material	Air
solid material	Inconel 625

The results from the case study are shown in Figure 9-3. Figure 9-3(a), in particular, shows the calibration for α. The range used for this first study is 20<Re_{chn}<80 and the pressure drop for three different values of 1/α is plotted with the pressure drop obtained from the unit-cell with fluid and fin. It is possible noting that the trend is linear for all the three α studied and for 1/α=4e+8 the deviation between $\Delta p_{chn,real}$ and $\Delta p_{chn,PM}$ is within 1%. A similar approach is also done for C_2. In this case the range is 900<Re_{chn}<1,500. It is interesting to notice that when C_2=0, the pressure drop follows a linear trend and deviates from the quadratic trend of the pressure drop obtained from the real geometry. Also, in this case, as shown in Figure 4b, the deviation is limited within 1%. The same approach has also been repeated with other microchannels, always satisfying the criterion of Eq. (78). It is, therefore, demonstrated that it is possible to use PM approach at the microchannel level in MMHX without sacrificing the accuracy of the performance in terms of pressure drop.

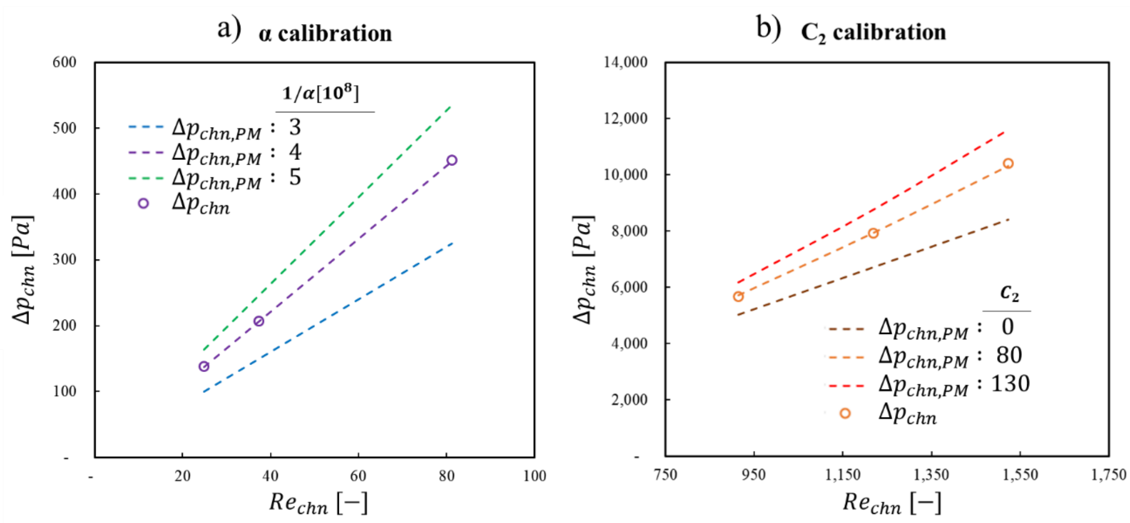

Figure 9-3: PM calibration procedure plotted as ΔP_{chn} vs Re_{chn}: a) low Re_{chn} to determine viscous resistance coefficient, b) high Re_{chn} to determine inertial resistance factor

9.3.2 Computational Reduction with PM Approach

Beside accuracy, another important point that needs to be addressed is the level of simplification that the mesh can reach while providing reliable results. Using the geometry and operational conditions given in Table 1, the number of cells in the PM mesh is progressively reduced while monitoring the pressure drop and the computational time required to solve the case. As shown in Figure 9-4, the number of cells is reduced from 108,900 to 2,000 following several steps. For all those cases, the values of Re, α and C_2 are kept the same. It is possible to notice that the deviation from the targeted pressure drop (left y-axis of Figure 9-4) fluctuates without a specific trend-line, thus excluding mesh-independency concerns. It is worth mentioning that the calibration is performed using the highest number of cells, and for this reason, it is the one with the smallest deviation. Although this choice, the deviation is always acceptable for the different mesh levels.

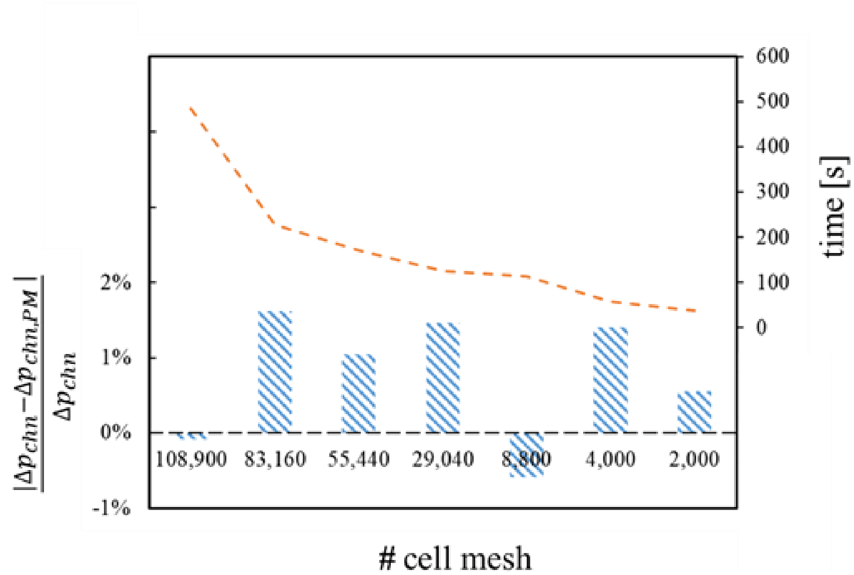

Figure 9-4: Effect of mesh resolution on accuracy (left y-axis) and computational time (right y-axis)

Figure 9-4 also shows (with reference to the right y-axis) the time needed for the solution convergence. A time saving of 92% is achieved for the coarsest mesh, with a deviation in the pressure drop that is still within the threshold of 1%. The results obtained confirms that, when dealing with PM, it is possible to reduce considerably the mesh resolution.

9.3.3 Model Validity for Different Operational Conditions

As mentioned in the introduction, one of the assumptions in the MMHX models developed so far is the use of constant properties for the fluid during the calculation. When combing the two sides of a cross-flow MMHX, however, this limitation can be avoided, provided temperature dependence of the properties of the fluid is implemented. This statement is true in case of the real geometry. However, it is necessary to study the behavior of the unit-cell with PM when the operational conditions change. To address this point, the geometry described in is studied at three different operational conditions, whose fluid properties are reported in Table 9-2.

Table 9-2: Case study properties for model robustness at change of operational conditions

Case #	ρ_f $[kg/m^3]$	μ_f *[Pa s]*
1	1.2	0.00001896
2	2.745	0.00002435
3	1.006	0.00002322

The pressure drop is calculated for six different flow rates to cover the range of possible Re_{chn}. In particular, three flow rates are selected for the low Re_{chn} to study the effect of α, while the other three address the region in which C_2 can not be neglected. The values in the middle are assumed to follow the trend once demonstrated it holds for the extreme values. Similarly to Figure 9-3, Figure 9-5 reports the pressure drop for both the unit-cells as a function of Re_{chn}. In this case, the entire range is shown, with a dedicated zoom for the region where the inertial losses are negligible as compared to the viscous ones. For all three the cases, α and C_2 are the same, and the PM replicates the behavior of the real microchannel and guarantees a deviation within the 1% for all 18 points. This result demonstrates the goodness of this model: first, once calibrated for one operational condition, the PM region can be used for all the other operational conditions that need to be tested. Second, when combining the two sides of the HX and defining the temperature dependence of the fluid properties, the model adjusts simultaneously pressure drop and heat transfer.

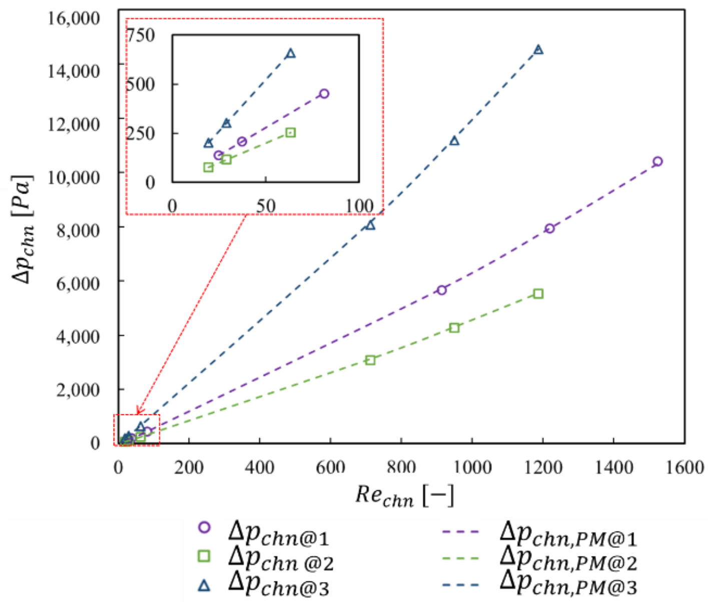

Figure 9-5: PM performance as Δp_chn vs Re_chn for different operational conditions with the same calibration

9.3.4 Heat transfer calibration

Once addressed the fluid flow, the other crucial aspect of the model is the calibration of the PM to satisfy the condition of Eq. (83). The study is performed using the geometry described in Table 1, and the operational condition 2 (with reference to Table 9-2).The rest of the information are reported in Table 9-3.

Table 9-3: Case study fluid and solid properties

	Fluid	**solid**
$\boldsymbol{k}\ \left[\frac{\boldsymbol{W}}{\boldsymbol{mK}}\right]$	0.03552	14.1
$\boldsymbol{C_p}\left[\frac{\boldsymbol{J}}{\boldsymbol{kgK}}\right]$	1020	471
$\boldsymbol{\rho}\ \left[\frac{\boldsymbol{kg}}{\boldsymbol{m^3}}\right]$	2.745	8,400

The temperature conditions imposed as boundary conditions are T_{in}=200K and T_{base} =100 K for both unit-cells. This choice is arbitrary since it does not affect the thermal characterization of the microchannel. In particular h_wall is independent of the temperature chosen. It is also important to underline that for the heat transfer calibration, only the higher mass flow rates are considered. When the flow rate was too small, in fact, T_2=T_{base} and limitations to the calibration are obtained as a consequence. Although those precautions, when imposing Eq. (83) and (84) with β=1 in the software, as suggested by FLUENT User's Guide, the deviation between expected and computed temperatures is significant. An explanation of this behavior can be obtained by observing the velocity contours for both unit-cells of Figure 9-6(a). It is possible to notice how the two unit-cells show locally different profile of velocity. Differently from the straight microchannel for which Eq. (83) and (84) hold to satisfy the thermal calibration, in case of manifold-microchannel, the U-shape with the PM shows a different velocity field compared with the real U-shape channel. A possible solution found to overcome this limitation is keeping h_{fs} constant, while changing β to satisfy Eq. (82). Figure 9-6(b) shows the temperature profile obtained with this method. Also for the thermal profile, the temperature are locally different when comparing the PM results with the real microchannel, while keeping the same performance overall. This is inherent of PM and it is the main sacrifice of the model. Although the results are only shown for one mass flow rate, it is important to underline that for the given geometry, the same value of β is necessary to calibrate the heat transfer at the three given flow rates. As a consequence, even if not following the guidelines, the model still holds its validity when changing the mass flow rate.

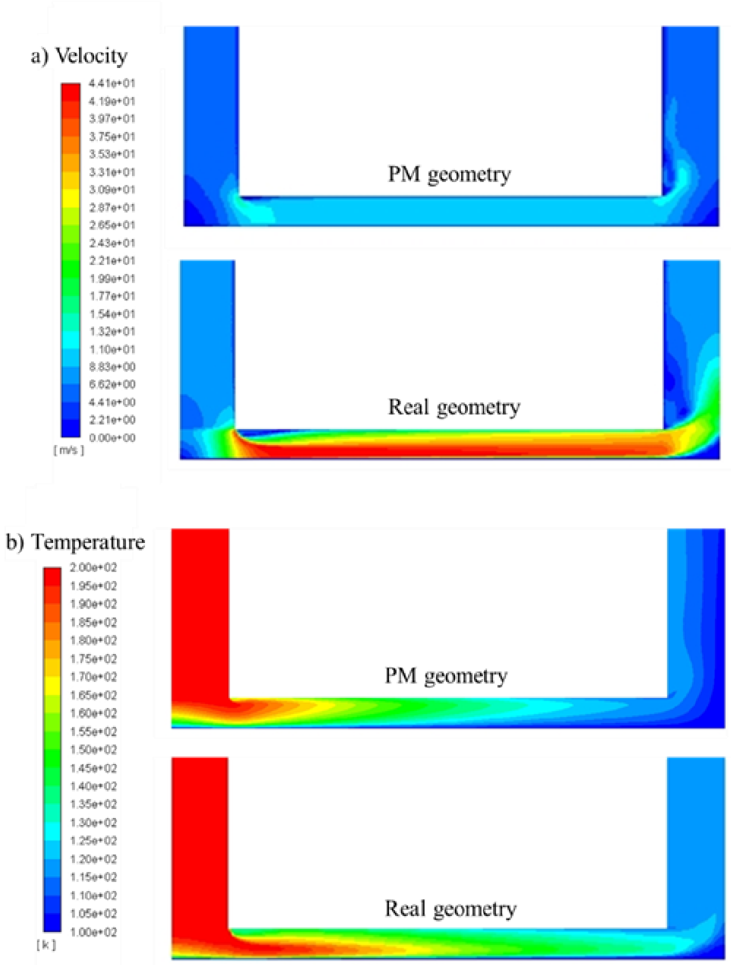

Figure 9-6: Comparison between PM and real unit-cells of the local distribution of a) velocity and b) temperature for the same operational conditions and mass flow rate

9.3.5 Parametric Fin Study

In order to determine if β can be valid for other cases, a parametric study is performed, varying γ. The operational conditions are the one of the case 2 from Table 9-2with the additional information of Table 9-3. As to the geometry, instead, L_{chn}, W_{in} and $t_{fin} + W_{chn}$ are the one reported by Table 9-1. As shown in Eq. (15), changing γ means changing the size of W_{chn}. For the parametric study, the porosities selected are: 0.95, 0.77, 0.6 and 0.4. Going beyond this value, ε~1 and it becomes difficult to calibrate the heat transfer properly. For each of this case, the same three mass flow rates selected for the heat transfer calibration are used and α and C_2 are initially determined to generate the fluid flow, while the different values of h_{wall} are obtained from the real unit-cell.

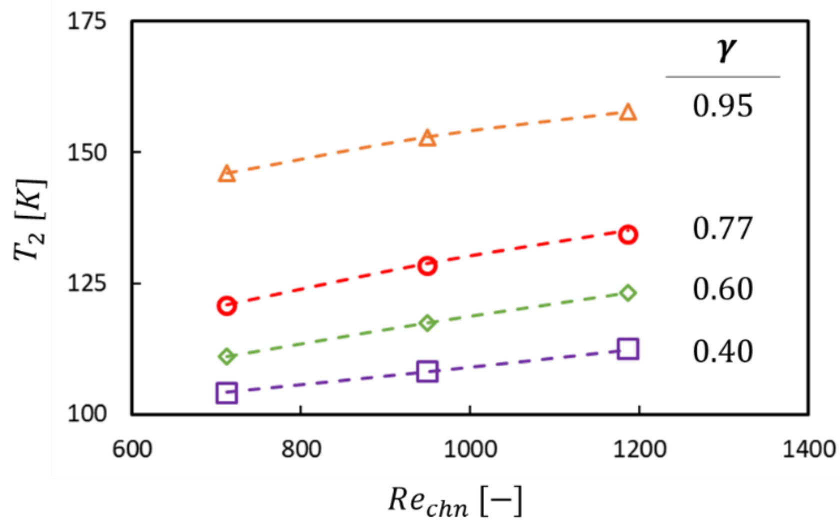

(a)

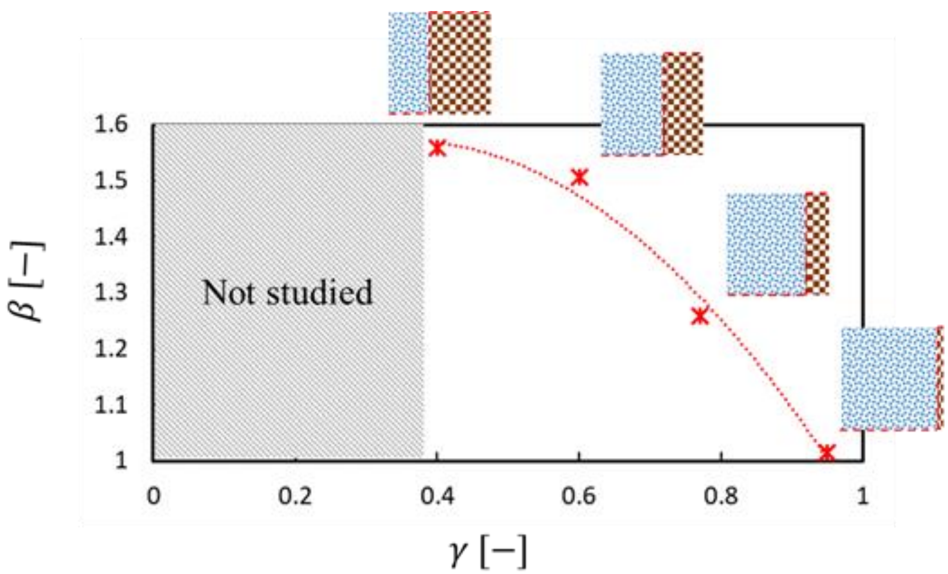

(b)

Figure 9-7: (a) PM performance as T_2 vs Re_{chn} for different porosities; (b) β-γ relation for different porosities used to fix the $A_{fs,Pm}$ in FLUENT

Figure 9-7(a) shows the T_2 for both unit-cells for different values of γ for the three prescribed flow rates. γ=0.6 represents the case used for the heat transfer calibration study. As described above, also for each of the other three porosities it is possible to determine a single value of β that satisfies Eq. 23. In fact, porous media outlet temperature matches the targeted temperature. However, as shown in Figure 9-7 (b), β changes with γ to satisfy the heat transfer calibration. In particular it is possible to notice a quadratic trend between the two parameters. This trend may suggest that as the difference in flow field between the PM approach and the real microchannel increases, the corrective factor β increases as a consequence. It has to be mentioned this is only a preliminary observation on the deviation between the theoretical and actual values of $A_{fs,PM}$, but demonstrates that there is a rule in the relation that still needs to be identified.

9.4 Summary

The main reason for the introduction of the PM in place of the real geometry was to reduce the complexity of modelling manifold microchannel heat exchanger without losing accuracy: for the case study, the deviation between the real geometry and the PM could be quantified within 1% for the pressure drop and 0.25% for the temperature at the outlet. Saving in computational time could be up to 92% for the desired criteria of accuracy. For the case study, the PM calibration was demonstrated to be independent of the operational conditions, thus showing its robustness. It can therefore be used to calculate the pressure drop when temperature dependent properties are considered, such as in a heat exchanger.

Chapter 10 Conclusions and Proposed Future Work

10.1 Conclusion

While manifold microchannel heat exchangers provide localized and optimum distribution of the flow among the heat transfer surface micro channels, offering superior heat transfer performance and heat removal density (kW/kg) and low pressure drops for the HX, they present fabrication and joining/assembly challenges when attempting to use conventional fabrication techniques. This work studied the feasibility of using additively manufactured manifold microchannel heat exchangers made of Ni-based super alloys as a possible alternative for current gas-to-gas heat exchangers in high-temperature applications, such as those used in the environmental control systems for aircrafts. When applied to the aerospace applications, the application focus of the present study, the main objective is to develop heat exchangers that while offer attractive gravimetric heat exchange density (kW/kg), they offer the required life cycle durability and reliability, while also meeting reasonable product life cycle cost targets.

Two advanced metallic manifold microchannel heat exchangers made of Ni-based super alloys suitable for high temperature and high pressure conditions were successfully designed, optimized, and fabricated using the AM manufacturing technique. Nearly 10% ~~m~~ass reduction for first generation, and 22% mass reduction for the second generation HX was realized, when compared to the baseline heat exchanger unit. This result was possible due to the improved fabrication quality of DMLS via printer settings adjustment: fabrication of fin size of 115μm and leak-proof wall thickness of 300 μm was successfully demonstrated.

Performance characterization of the heat exchanger was tested up to 600°C. Gravimetric heat duty of 9.4 kW/kg at an effectiveness (ε) of 78% was achieved, which corresponds to up to 60% increase in gravimetric heat transfer density over conventional heat exchangers. Moreover, the work validated the performance prediction model used to obtain the design. Lastly, thermo-mechanical analysis of the unit was numerically simulated. The modeling results demonstrated excess stress in the joining areas where the heat exchanger connects to the headers for high temperature and pressure operating conditions.

The importance of the outcomes and the observations resulting from the study is supported by the fact that high temperature heat exchangers are key to the success of emerging high-temperature, high-efficiency solutions in energy conversion, power generation and waste heat recovery applications.

10.2 Proposed Future Work

To furtherly enhance the study of additive-manufacture manifold microchannel heat exchangers in the field of high temperature-high pressure applications, a series of possible improvements are listed.

10.2.1 Numerical Modeling

For the future work, the first upgrade is to develop a correlation between the curve fitting temperature and the expected performance of the heat exchanger. Even though the new model proved to be matching the experimental data, it is not possible to use it during the process of optimization, as it would significantly increase the computational time. However, the new model can be used as reference for the creation of the correlation, saving the time and the resources required to collect experimental data.

Another possible enhancement is to include heat exchanger roughness in the model prediction. All the models developed for manifold microchannels are based on the assumption of neglecting the roughness. If this hypothesis can be consider valid in case of conventionally fabricated manifold-microchannel heat exchanger, when using additive manufacturing the surface is rougher and this can play a key role in the actual performance projection.

A possible approach that can help improving the porous media approach analysis of U-shaped channels is to switch from superficial velocity to physical velocity in FLUENT. In this way, the discrepancy between the fluid fields should reduce and the calibration of the heat transfer can be improved as a consequence.

It is also suggested to experimentally measure the material properties of the additively manufactured parts. In particular, the thermal conductivity value is essential in the model prediction of cross-flow air-to-air heat exchangers, like the ones studied in this dissertation. The knowledge of the mechanical properties would also be beneficial when running the thermo-mechanical analysis of the unit.

10.2.2 Design Improvement

As to the heat exchanger design, future works should concentrate on designing a manifold-microchannel heat exchanger that can withstand high temperature and high pressure. It becomes then crucial to combine the optimization process with the thermo-mechanical analysis developed in this dissertation. The optimized shape of the heat exchanger should minimize pressure drop, maximize the heat transfer and minimize the weight of the heat exchanger without compromising the life cycle duration reliability. To achieve this goal, a simulation using conventional approach may become prohibitive. Topology optimization might be considered as the best option. Once given all the constraints of the problems, the optimum solution is found using machine learning technique applied to fluid flow and heat transfer. The resulting geometry has also to be physically realizable. In this regard, additive manufacturing flexibility would allow to fabricate non-trivial designs, where, for example, the material thickness is increased only where structurally needed.

10.2.3 Additive Manufacturing

In the field of additive manufacturing, more work is needed to improve the fabrication quality of DMLS. In this study, only few printing parameters were analyzed and their role characterized in terms of fin thickness and base thickness. As future recommendation, it is suggested to develop a printing protocol that is able to fully characterize the entire range of parameters. (e.g., scanning speed, hatch angle, etc). A different set of parameters could be used for different parts of the heat exchanger. Using the laser power as an example, it could be reduced when printing the fins to minimize the risk of sintering unwanted powder, while it could be increased when printing the base plate to minimize the risk of porosity.

Another crucial aspect is the capability to print bigger units with the same level of printing resolution. As shown in this study, increasing the build size of the printer often resulted in thicker fins, assuming the same set of parameters was applied to the different printers. However, demonstrating the feasibility of scaling-up to full-size heat exchanger is crucial to allow this technology to be applied in fabrication of industrial-size heat exchangers. To address this point, 3D printers should be modified to assure constant distance between the laser and the layer of sintered powder. This could be achieved, for example, by allowing the laser header to move vertically in the printing direction. In this way, build size and printer resolution would be decoupled.

References

[1] B. Sundén, *Introduction to heat transfer*. WIT Press, 2012.

[2] C. F. McDonald and D. G. Wilson, "The utilization of recuperated and regenerated engine cycles for high-efficiency gas turbines in the 21st century," *Appl. Therm. Eng.*, vol. 16, no. 8–9, pp. 635–653, Aug. 1996.

[3] B. SUNDÉN and J. FU, *HEAT TRANSFER IN AEROSPACE APPLICATIONS*. 2017.

[4] S. Wright, G. Andrews, and H. Sabir, "A review of heat exchanger fouling in the context of aircraft air-conditioning systems, and the potential for electrostatic filtering," *Appl. Therm. Eng.*, vol. 29, no. 13, pp. 2596–2609, Sep. 2009.

[5] I. Martinez, "Aircraft environmental control system."

[6] W. M. (William M. Kays and A. L. (Alexander L. London, *Compact heat exchangers*. McGraw-Hill, 1984.

[7] O. Majeed, "Aircraft Environmental Control Systems A Presentation of Current Systems and New Developments," 2010.

[8] D. Aquaro and M. Pieve, "High temperature heat exchangers for power plants: Performance of advanced metallic recuperators," *Appl. Therm. Eng.*, vol. 27, no. 2–3, pp. 389–400, 2007.

[9] Y. Ahn, J. Lee, S. G. Kim, J. I. Lee, J. E. Cha, and S. W. Lee, "Design consideration of supercritical CO2 power cycle integral experiment loop," *Energy*, vol. 86, pp. 115–127, 2015.

[10] A. Banerjee, R. Bala Chandran, and J. H. Davidson, "Experimental investigation of a reticulated porous alumina heat exchanger for high temperature gas heat recovery," *Appl. Therm. Eng.*, vol. 75, pp. 889–895, Jan. 2015.

[11] X. Liu, Y. D. Deng, K. Zhang, M. Xu, Y. Xu, and C. Q. Su, "Experiments and simulations on heat exchangers in thermoelectric generator for automotive application," *Appl. Therm. Eng.*, vol. 71, no. 1, pp. 364–370, Oct. 2014.

[12] T. Daisuke and N. Shigeaki, "Thermal Performance of Intermediate Heat Exchanger during High-Temperature Continuous Operation in HTTR," *J. Nucl. Sci. Technol.*, vol. 48, no. 11, pp. 1361–1368, 2011.

[13] K. Hada, I. Nishiguchi, Y. Muto, and H. Tsuji, "Developments of metallic materials and a high-temperature structural design code for the HTTR," *Nucl. Eng. Des.*, vol. 132, no. 1, pp. 1–11, Dec. 1991.

[14] L. Magistri, A. Traverso, A. F. Massardo, and R. K. Shah, "Heat Exchangers for Fuel Cell and Hybrid System Applications," *J. Fuel Cell Sci. Technol.*, vol. 3, no. 2, p. 111, May 2006.

[15] C. F. McDonald, A. F. Massardo, C. Rodgers, and A. Stone, "Recuperated gas turbine aeroengines, part I: early development activities," *Aircr. Eng. Aerosp. Technol.*, vol. 80, no. 2, pp. 139–157, Mar. 2008.

[16] C. F. McDonald, A. F. Massardo, C. Rodgers, and A. Stone, "Recuperated gas turbine aeroengines, part II: engine design studies following early development testing," *Aircr. Eng. Aerosp. Technol.*, vol. 80, no. 3, pp. 280–294, May 2008.

[17] C. F. McDonald, A. F. Massardo, C. Rodgers, and A. Stone, "Recuperated gas turbine aeroengines. Part III: engine concepts for reduced emissions, lower fuel consumption, and noise abatement," *Aircr. Eng. Aerosp. Technol.*, vol. 80, no. 4, pp. 408–426, Jul. 2008.

[18] B. Sunden, "High temperature heat exchangers (HTHE)," *Enhanc. Compact Ultra-Compact Heat Exch. Sci. Eng. Technol.*, no. September, pp. 226–238, 2005.

[19] M. F. Ashby, *Materials selection in mechanical design*. Butterworth-Heinemann, 1999.

[20] A. Sommers, Q. Wang, X. Han, C. T'Joen, Y. Park, and A. Jacobi, "Ceramics and ceramic matrix composites for heat exchangers in advanced thermal systems-A review," *Appl. Therm. Eng.*, vol. 30, no. 11–12, pp. 1277–1291, 2010.

[21] P. F. Peterson, H. Zhao, F. Niu, W. Huang, J. Schmidt, and J. Schulte-Fischedick, "Development of C-SiC ceramic compact plate heat exchangers for high temperature heat transfer applications."

[22] M. M. Ohadi and S. G. Buckley, “High temperature heat exchangers and microscale combustion systems: applications to thermal system miniaturization,” *Exp. Therm. Fluid Sci.*, vol. 25, no. 5, pp. 207–217, Nov. 2001.
[23] San Jose Delta Inc., “Ceramics for Strength.” [Online]. Available: https://www.sanjosedelta.com/ceramics_strength.html. [Accessed: 03-Mar-2019].
[24] MakeItFrom.com, “Silicon Carbide (SiC).” [Online]. Available: https://www.makeitfrom.com/material-properties/Silicon-Carbide-SiC. [Accessed: 03-Mar-2019].
[25] “Ceramic Heat Exchangers HTI 4-Pass Ceramic Heat Exchanger.”
[26] C. A. Lewinsohn, M. A. Wilson, J. R. Fellows, and H. S. Anderson, “Fabrication and Joining of Ceramic Compact Heat Exchangers for Process Integration,” *Int. J. Appl. Ceram. Technol.*, vol. 9, no. 4, pp. 700–711, Jul. 2012.
[27] R. J. Kee *et al.*, “The design, fabrication, and evaluation of a ceramic counter-flow microchannel heat exchanger,” *Appl. Therm. Eng.*, vol. 31, no. 11–12, pp. 2004–2012, Aug. 2011.
[28] C. Lewinsohn, “High-efficiency, ceramic microchannel heat exchangers,” *Am. Ceram. Soc. Bull.*, vol. 95, no. 4, pp. 26–31, 2015.
[29] U. Scheithauer, E. Schwarzer, T. Moritz, and A. Michaelis, “Additive Manufacturing of Ceramic Heat Exchanger: Opportunities and Limits of the Lithography-Based Ceramic Manufacturing (LCM),” *J. Mater. Eng. Perform.*, vol. 27, no. 1, pp. 14–20, Jan. 2018.
[30] J. Schulte-Fischedick, V. Dreißigacker, and R. Tamme, “An innovative ceramic high temperature plate-fin heat exchanger for EFCC processes,” *Appl. Therm. Eng.*, vol. 27, no. 8–9, pp. 1285–1294, Jun. 2007.
[31] J. Haunstetter, V. Dreißigacker, and S. Zunft, “Ceramic high temperature plate fin heat exchanger: Experimental investigation under high temperatures and pressures,” *Appl. Therm. Eng.*, vol. 151, pp. 364–372, Mar. 2019.
[32] H. Takegami, A. Terada, and Y. Inagaki, “Development of strength evaluation method for high-pressure ceramic components,” *Nucl. Eng. Des.*, vol. 271, pp. 253–256, May 2014.
[33] R. K. Shah, “Compact Heat Exchangers for Microturbines,” *Int. Conf. Enhanc. Compact Ultra-Compact Heat Exch. Sci. Eng. Technol.*, no. September, pp. 247–257, 2005.
[34] S. Dewson and X. Li, “Selection criteria for the high temperature reactor intermediate heat exchanger,” *Proc. ICAPP*, pp. 1–8, 2005.
[35] G. Subbaraman, S. Kung, and H. Saari, “Materials for Supercritical CO 2 Applications A Tutorial,” in *6 th International sCO2 Power Cycles Symposium*, 2018.
[36] X. Zhang *et al.*, “Recent developments in high temperature heat exchangers: A review,” *Front. Heat Mass Transf.*, vol. 11, 2018.
[37] T. Allison, G. Beck, J. Bennett, K. Hoopes, and L. Miller, “Development of a Thin Film Primary Surface Heat Exchanger for Advanced Power Cycles,” Pittsburgh, PA, and Morgantown, WV (United States), Jun. 2016.
[38] B. S.-J. Kang, L. Ogawa, L. Ma, M. A. Alvin, N. Wu, and G. Smith, “Materials and Components Development for Advaced Turbine Systems - ODS Alloy Development.”
[39] A. . Spierings, B. T., K. Dawson, A. Colella, and K. Wegener, “Processing ODS Modified IN625 Using Selective Laser Melting.”
[40] K. Brun, P. Friedman, and R. Dennis, *Fundamentals and applications of supercritical carbon dioxide (sCO2) based power cycles.* Woodhead Publishing an imprint of Elsevier, 2017.
[41] C. F. McDonald, “Recuperator considerations for future higher efficiency microturbines,” *Appl. Therm. Eng.*, vol. 23, no. 12, pp. 1463–1487, Aug. 2003.
[42] R. A. Wolf, “Carbon-Carbon Composites as Recuperator Materials for Direct Gas Brayton Systems,” 2006.
[43] R. D. Stevenson and D. L. Vrable, “Development of an Intermediate Temperature Carbon-Carbon Heat Exchanger for aircraft applications,” in *SAMPE 1999*, 1999, p. 1.
[44] L. Chordia, M. A. Portnoff, and E. Green, “High Temperature Heat Exchanger Design and Fabrication for Systems with Large Pressure Differentials,” Pittsburgh, PA, and Morgantown, WV

(United States), Mar. 2017.
[45] Q. Li, G. Flamant, X. Yuan, P. Neveu, and L. Luo, "Compact heat exchangers: A review and future applications for a new generation of high temperature solar receivers," *Renew. Sustain. Energy Rev.*, vol. 15, no. 9, pp. 4855–4875, Dec. 2011.
[46] A. E. Kabeel, M. H. Hamed, Z. M. Omara, and S. W. Sharshir, "Water Desalination Using a Humidification-Dehumidification Technique—A Detailed Review," *Nat. Resour.*, vol. 04, no. 03, pp. 286–305, Jun. 2013.
[47] Sondex, "The simple choice for demanding liquids Spiral Heat Exchangers."
[48] "Scambiatori di calore a piastre e industria galvanica." [Online]. Available: https://www.impianto.it/scambiatori-a-piastre-e-galvanica/. [Accessed: 26-Feb-2019].
[49] "1009 Supermax® Shell and Plate Heat Exchangers from Tranter, Inc." [Online]. Available: https://www.thomasnet.com/catalogs/item/10039051-9807-1008-1009/tranter-inc/supermax-174-shell-and-plate-heat-exchangers/. [Accessed: 26-Feb-2019].
[50] "EXTREME PERFORMANCE FOR EXTREME CONDITIONS."
[51] "Alfa Laval Packinox."
[52] "APV Hybrid - Welded Heat Exchanger."
[53] "Hybrid - Fully Welded Plate Heat Exchanger - VAU Thermotech GmbH & Co. KG - PDF Catalogs | Technical Documentation | Brochure." [Online]. Available: http://pdf.directindustry.com/pdf/vau-thermotech-gmbh-co-kg/hybrid-fully-welded-plate-heat-exchanger/105877-405297.html. [Accessed: 26-Feb-2019].
[54] Kelvion, "A New Dimention of Efficiency adn Flexibility - K°Flex." 2018.
[55] H. Strumpf and Z. Mirza, "Development of a Microchannel Heat Exchanger for Aerospace Applications," in *ASME 2012 10th International Conference on Nanochannels, Microchannels, and Minichannels*, 2012, p. 459.
[56] R. L. Webb and N.-H. Kim, *Principles of enhanced heat transfer*. Taylor & Francis, 2005.
[57] U. Brockmeier, T. Guentermann, and M. Fiebig, "Performance evaluation of a vortex generator heat transfer surface and comparison with different high performance surfaces," *Int. J. Heat Mass Transf.*, vol. 36, no. 10, pp. 2575–2587, Jul. 1993.
[58] L. Sheik Ismail, R. Velraj, and C. Ranganayakulu, "Studies on pumping power in terms of pressure drop and heat transfer characteristics of compact plate-fin heat exchangers—A review," *Renew. Sustain. Energy Rev.*, vol. 14, no. 1, pp. 478–485, Jan. 2010.
[59] E. Cetegen, "Force Fed Microchannel High Heat Flux Cooling Utilizing Microgrooved Surfaces," University of Maryland, 2010.
[60] M. A. Arie, "Air Side Heat Transfer Enhancement in Heat Exchangers Utilizing Innovative Designs and the Additive Manufacturing Technique," University of Maryland, 2016.
[61] M. Williams, A. Muley, J. Bolla, and H. Strumpf, "Advanced Heat Exchanger Technology for Aerospace Applications," *SAE Tech. Pap. Ser.*, vol. 1, 2010.
[62] M. A. Wilson, K. Recknagle, and K. Brooks, "Design and Development of a Low-Cost, High Temperature Silicon Carbide Micro-Channel Recuperator," in *Volume 1: Turbo Expo 2005*, 2005, pp. 1029–1034.
[63] Marlin Steel, "4 Inconel Machining Tips You Need to Know," 2016. [Online]. Available: https://www.marlinwire.com/blog/inconel-machining-tips. [Accessed: 04-Mar-2019].
[64] C. F. McDonald, "The Role of the Ceramic Heat Exchanger in Energy and Resource Conservation," *J. Eng. Power*, vol. 102, no. 2, p. 303, Apr. 1980.
[65] Y. Fan and L. Luo, "Recent Applications of Advances in Microchannel Heat Exchangers and Multi-Scale Design Optimization," *Heat Transf. Eng.*, vol. 29, no. 5, pp. 461–474, May 2008.
[66] S.-J. Yoon, P. Sabharwall, and E.-S. Kim, "Analytical Study on Thermal and Mechanical Design of Printed Circuit Heat Exchanger," 2013.
[67] Hyprotech, "Introduction to Heat Exchangers," *2002*. [Online]. Available: https://www.scribd.com/doc/183898110/Introduction-to-Heat-Exchangers-ppt. [Accessed: 27-Feb-2019].

[68] C. H. Phillips and K. T. Symonds, "DEVELOPMENT OF A NOVEL INTEGRATED CHEMICAL REACTOR-HEAT EXCHANGER."
[69] N. Tsuzuki, Y. Kato, and T. Ishiduka, "High performance printed circuit heat exchanger," *Appl. Therm. Eng.*, vol. 27, no. 10, pp. 1702–1707, Jul. 2007.
[70] J. E. Hesselgreaves, *Compact heat exchangers : selection, design, and operation*. Pergamon, 2001.
[71] J. Delgado, J. Ciurana, and C. A. Rodríguez, "Influence of process parameters on part quality and mechanical properties for DMLS and SLM with iron-based materials," *Int. J. Adv. Manuf. Technol.*, vol. 60, no. 5–8, pp. 601–610, May 2012.
[72] S. L. Sing, J. An, W. Y. Yeong, and F. E. Wiria, "Laser and electron-beam powder-bed additive manufacturing of metallic implants: A review on processes, materials and designs," *J. Orthop. Res.*, vol. 34, no. 3, pp. 369–385, Mar. 2016.
[73] D. Jafari and W. W. Wits, "The utilization of selective laser melting technology on heat transfer devices for thermal energy conversion applications: A review," *Renew. Sustain. Energy Rev.*, vol. 91, pp. 420–442, 2018.
[74] "HiETA Technologies chooses Simufact Additive for the Simulation of Metal Additive Manufacturing Processes | Additive Manufacturing (AM)." [Online]. Available: http://additivemanufacturing.com/2018/07/04/hieta-technologies-chooses-simufact-additive-for-the-simulation-of-metal-additive-manufacturing-processes/. [Accessed: 06-Mar-2019].
[75] A. Hussein, "Additive Manufacturing of Compact Heat Exchangers," 2017.
[76] "Postprocessing Steps and Costs for Metal 3D Printing: Additive Manufacturing Magazine." [Online]. Available: https://www.additivemanufacturing.media/blog/post/postprocessing-steps-and-costs-for-metal-3d-printing. [Accessed: 13-Mar-2019].
[77] Z. Gobetz, A. Rowen, C. Dickman, K. Meinert, and R. Martukanitz, "Utilization of Additive Manufacturing for Aerospace Heat Exchangers Enabling Additive Manufacturing Technologies for Industry Insertion Project," 2016.
[78] "Chemical Vapor Deposition (CVD) | Ultramet." [Online]. Available: https://ultramet.com/chemical-vapor-deposition/. [Accessed: 13-Mar-2019].
[79] "High Power LED Light: MOCVD Metal-organic Chemical Vapor Deposition - LED Wiki." [Online]. Available: http://high-power-led-light.blogspot.com/2013/10/mocvd-metal-organic-chemical-vapor.html. [Accessed: 13-Mar-2019].
[80] A. A. Mohamad, "Heat transfer enhancements in heat exchangers fitted with porous media Part I: constant wall temperature," *Int. J. Therm. Sci.*, vol. 42, no. 4, pp. 385–395, Apr. 2003.
[81] W. Liu, K. Yang, A. Nakayama, C. Yang, and Z. F. Huang, "Enhancing heat transfer in the core flow by using porous medium insert in a tube," *Int. J. Heat Mass Transf.*, vol. 53, no. 5–6, pp. 1164–1174, Feb. 2009.
[82] S. Mahjoob and K. Vafai, "A synthesis of fluid and thermal transport models for metal foam heat exchangers," *Int. J. Heat Mass Transf.*, vol. 51, no. 15–16, pp. 3701–3711, Jul. 2008.
[83] D. L. Youchison, M. G. Izenson, C. B. Baxi, and J. H. Rosenfeld, "High-Heat-Flux Testing of Helium-Cooled Heat Exchangers for Fusion Applications," *Fusion Technol.*, vol. 29, no. 4, pp. 559–570, Jul. 1996.
[84] A. . Raffray and J. . Pulsifer, "MERLOT: a model for flow and heat transfer through porous media for high heat flux applications," *Fusion Eng. Des.*, vol. 65, no. 1, pp. 57–76, Jan. 2003.
[85] A. SHERMAN, R. TUFFIAS, and R. KAPLAN, "Refractory ceramic foams- A novel, new high-temperature structure," *Am. Ceram. Soc. Bull.*, vol. 70, pp. 1025–1027, 1991.
[86] A. Muley, C. Kiser, B. Sundén, and R. K. Shah, "Foam Heat Exchangers: A Technology Assessment," *Heat Transf. Eng.*, vol. 33, no. 1, pp. 42–51, Jan. 2012.
[87] R. K. (Ramesh K. . Shah and D. P. Sekulić, *Fundamentals of heat exchanger design*. John Wiley & Sons, 2003.
[88] "Welded plate heat exchangers | Ziemex." [Online]. Available: http://www.ziemex.com/en/technologie-produit/echangeurs-a-plaques-soudees/. [Accessed: 26-Feb-2019].

[89] R. A. Wirtz, "A Semi-Empirical Model for Porous Media Heat Exchanger Design."
[90] J. D. Lindstrom, "Design and evaluation of compact heat exchangers for hybrid fuel cell and gas turbine systems," Montana State University - Bozeman, College of Engineering, 2005.
[91] Y. Takeuchi, C. Park, K. Noborio, Y. Yamamoto, and S. Konishi, "Heat transfer in SiC compact heat exchanger," *Fusion Eng. Des.*, vol. 85, no. 7–9, pp. 1266–1270, Dec. 2010.
[92] B. Alm, U. Imke, R. Knitter, U. Schygulla, and S. Zimmermann, "Testing and simulation of ceramic micro heat exchangers," *Chem. Eng. J.*, vol. 135, pp. S179–S184, Jan. 2008.
[93] I. Southgate Process Equipment, "Shell & Tube Heat Exchangers." .
[94] "Alfa Laval - Olmi shell-and-tube exotic metallurgy." [Online]. Available: https://www.alfalaval.us/products/heat-transfer/tubular-heat-exchangers/process-shell-and-tube-heat-exchangers/olmi-shell-and-tube-exotic-metallurgy/. [Accessed: 05-Mar-2019].
[95] "Thermo-T ™ Construction."
[96] "Alfa Laval spiral heat exchangers Problem solvers for tough applications."
[97] "GEABloc ®-Fully Welded Plate Heat Exchangers."
[98] "Schmidt-Bretten All-Welded Plate Heat Exchangers | API Heat Transfer." [Online]. Available: http://www.apiheattransfer.com/Product/103/SIGMAWIG-All-Welded-Plate-Heat-Exchangers. [Accessed: 26-Feb-2019].
[99] "All Welded Plate And Frame Heat Exchanger Manufacturer - Accessen." [Online]. Available: https://www.accessen.com/products-and-solutions/all-welded-plate-and-frame-heat-exchanger.html. [Accessed: 26-Feb-2019].
[100] "FUNKE Heat Exchangers USA - welded." [Online]. Available: https://www.funke.de/en-us/produkte-en-us/plattenwaermetauscher-en-us/funkebloc-en-us.html. [Accessed: 26-Feb-2019].
[101] "Performance through thick and thin Alfa Laval Compabloc welded heat exchangers."
[102] "Welded plate heat exchanger : remarkable efficiency, unique design and compactness." [Online]. Available: https://www.nexson-group.com/products/welded-plate-heat-exchanger/. [Accessed: 26-Feb-2019].
[103] "MAXCHANGER® Mini-Welded Heat Exchanger - Tranter." [Online]. Available: http://www.tranter.com/products/maxchanger-mini-welded-heat-exchanger/. [Accessed: 26-Feb-2019].
[104] R. C. Sanders and G. C. Louie, "Development of the WR-21 Gas Turbine Recuperator," in *Volume 4: Manufacturing Materials and Metallurgy; Ceramics; Structures and Dynamics; Controls, Diagnostics and Instrumentation; Education; IGTI Scholar Award; General*, 1999, p. V004T07A001.
[105] J. Kesseli, T. Wolf, J. Nash, and S. Freedman, "Micro, Industrial, and Advanced Gas Turbines Employing Recuperators," in *Volume 3: Turbo Expo 2003*, 2003, pp. 789–794.
[106] H. Schoenenborn, E. Ebert, B. Simon, and P. Storm, "Thermomechanical Design of a Heat Exchanger for a Recuperative Aeroengine," *J. Eng. Gas Turbines Power*, vol. 128, no. 4, p. 736, 2006.
[107] J. K. Min, J. H. Jeong, M. Y. Ha, and K. S. Kim, "High temperature heat exchanger studies for applications to gas turbines," *Heat Mass Transf.*, vol. 46, no. 2, pp. 175–186, Dec. 2009.
[108] J. J. Murray, C. M. Hempsell, A. Bond, and I. A. Federation, "An Experimental Precooler for Airbreathing Rocket Engines," in *49th, International astronautical congress*, 1998, p. ALL.
[109] R. Nacke, B. Northcutt, and I. Mudawar, "Theory and experimental validation of cross-flow micro-channel heat exchanger module with reference to high Mach aircraft gas turbine engines," *Int. J. Heat Mass Transf.*, vol. 54, no. 5–6, pp. 1224–1235, Feb. 2011.
[110] "Chemical Etching - Complex Flow Paths for Any Process | Heatric." [Online]. Available: https://www.heatric.com/heat-exchangers/features/chemical-etching/. [Accessed: 28-Feb-2019].
[111] "Materials - High Spec Materials for Extreme Duties - Heatric." [Online]. Available: https://www.heatric.com/heat-exchangers/features/materials/. [Accessed: 28-Feb-2019].
[112] "Characteristics of Diffusion Bonded Heat Exchangers | Heatric." [Online]. Available: https://www.heatric.com/heat-exchangers/features/characteristics/. [Accessed: 28-Feb-2019].

[113] "Alfa Laval - PCHE." [Online]. Available: https://www.alfalaval.us/products/heat-transfer/plate-heat-exchangers/printed-circuit-heat-exchangers/pche/. [Accessed: 28-Feb-2019].

[114] K. Kanlayasiri and B. K. Paul, "A Nickel Aluminide Microchannel Array Heat Exchanger for High-Temperature Applications," *J. Manuf. Process.*, vol. 6, no. 1, pp. 72–80, Jan. 2004.

[115] H. Song, "Investigations of a printed circuit heat exchanger for supercritical CO2 and water," 2007.

[116] M. Chen, X. Sun, R. N. Christensen, I. Skavdahl, V. Utgikar, and P. Sabharwall, "Pressure drop and heat transfer characteristics of a high-temperature printed circuit heat exchanger," *Appl. Therm. Eng.*, vol. 108, pp. 1409–1417, Sep. 2016.

[117] M. Chen, X. Sun, R. N. Christensen, I. Skavdahl, V. Utgikar, and P. Sabharwall, "Dynamic behavior of a high-temperature printed circuit heat exchanger: Numerical modeling and experimental investigation," *Appl. Therm. Eng.*, vol. 135, pp. 246–256, May 2018.

[118] S. Mylavarapu, X. Sun, J. Figley, N. Needler, and R. Christensen, "Investigation of High-Temperature Printed Circuit Heat Exchangers for Very High Temperature Reactors," *J. Eng. Gas Turbines Power*, vol. 131, no. 6, p. 062905, Nov. 2009.

[119] D. Reay and Centre for the Analysis and Dissemination of Demonstrated Energy Technologies., *Learning from experiences with compact heat exchangers*. CADDET, 1999.

[120] X. Zhang, R. Tiwari, A. H. Shooshtari, and M. M. Ohadi, "An additively manufactured metallic manifold-microchannel heat exchanger for high temperature applications," *Appl. Therm. Eng.*, vol. 143, pp. 899–908, Oct. 2018.

[121] I. L. Collins, J. A. Weibel, L. Pan, and S. V. Garimella, "A permeable-membrane microchannel heat sink made by additive manufacturing," *Int. J. Heat Mass Transf.*, vol. 131, pp. 1174–1183, Mar. 2019.

[122] M. A. Arie, A. H. Shooshtari, and M. M. Ohadi, "Experimental characterization of an additively manufactured heat exchanger for dry cooling of power plants," *Appl. Therm. Eng.*, vol. 129, pp. 187–198, Jan. 2018.

[123] "Evaluation of Additively Manufactured Microchannel Heat Sinks," *IEEE Trans. Components, Packag. Manuf. Technol.*, pp. 1–1, 2018.

[124] F. Romei, A. N. Grubišić, and D. Gibbon, "Manufacturing of a high-temperature resistojet heat exchanger by selective laser melting," *Acta Astronaut.*, vol. 138, pp. 356–368, Sep. 2017.

[125] A. J. Robinson, W. Tan, R. Kempers, J. Colenbrander, N. Bushnell, and R. Chen, "A new hybrid heat sink with impinging micro-jet arrays and microchannels fabricated using high volume additive manufacturing," in *2017 33rd Thermal Measurement, Modeling & Management Symposium (SEMI-THERM)*, 2017, pp. 179–186.

[126] A. J. Robinson, W. Tan, R. Kempers, J. Colenbrander, N. Bushnell, and R. Chen, "An ultra high performance heat sink using a novel hybrid impinging microjet — Microchannel structure," in *2017 16th IEEE Intersociety Conference on Thermal and Thermomechanical Phenomena in Electronic Systems (ITherm)*, 2017, pp. 482–490.

[127] B. J. Hathaway, K. Garde, S. C. Mantell, and J. H. Davidson, "Design and characterization of an additive manufactured hydraulic oil cooler," *Int. J. Heat Mass Transf.*, vol. 117, pp. 188–200, Feb. 2018.

[128] M. A. Arie, A. Shooshtari, and M. Ohadi, "Air side enhancement of heat transfer in an additively manufactured 1 kW heat exchanger for dry cooling applications," in *2017 16th IEEE Intersociety Conference on Thermal and Thermomechanical Phenomena in Electronic Systems (ITherm)*, 2017, pp. 1–8.

[129] D. Saltzman *et al.*, "Experimental Comparison of a Traditionally Built versus Additively Manufactured Aircraft Heat Exchanger."

[130] K. Kasim, A. Muley, M. Stoia, and F. Ladeinde, "Advanced Heat Transfer Devices for Aerospace Applications," in *Volume 8: Heat Transfer and Thermal Engineering*, 2017, p. V008T10A027.

[131] W. D. Gerstler and D. Erno, "Introduction of an additively manufactured multi-furcating heat exchanger," in *2017 16th IEEE Intersociety Conference on Thermal and Thermomechanical Phenomena in Electronic Systems (ITherm)*, 2017, pp. 624–633.

[132] W. D. Gerstler, D. J. Erno, M. T. Kenworthy, J. D. Rambo, and N. K. Sabo, "Heat exchanger including furcating unit cells," 22-Mar-2016.
[133] D. Bacellar, V. Aute, Z. Huang, and R. Radermacher, "Design optimization and validation of high-performance heat exchangers using approximation assisted optimization and additive manufacturing," *Sci. Technol. Built Environ.*, vol. 23, no. 6, pp. 896–911, Aug. 2017.
[134] M. A. Arie, A. H. Shooshtari, S. V Dessiatoun, and M. M. Ohadi, "Performance Characterization of an Additively Manufactured Titanium (Ti64) Heat Exchanger for an Air-Water Cooling Application," *Conf. ASME 2016 Heat Transf. Summer Conf. collocated with ASME 2016 Fluids Eng. Div. Summer Meet. ASME 2016 14th Int. Conf. Nanochannels, Microchannels, Minichannels*, pp. 1–13.
[135] S. Vanapalli, R. Keijzer, P. Buitelaar, and H. J. M. ter Brake, "Cryogenic flat-panel gas-gap heat switch," *Cryogenics (Guildf).*, vol. 78, pp. 83–88, Sep. 2016.
[136] K. L. Kirsch and K. A. Thole, "Heat Transfer and Pressure Loss Measurements in Additively Manufactured Wavy Microchannels," *J. Turbomach.*, vol. 139, no. 1, p. 011007, Sep. 2016.
[137] J. C. Snyder, C. K. Stimpson, K. A. Thole, and D. Mongillo, "Build Direction Effects on Additively Manufactured Channels," in *Volume 5A: Heat Transfer*, 2015, p. V05AT11A034.
[138] P. Dupuis, Y. Cormier, M. Fenech, and B. Jodoin, "Heat transfer and flow structure characterization for pin fins produced by cold spray additive manufacturing," *Int. J. Heat Mass Transf.*, vol. 98, pp. 650–661, Jul. 2016.
[139] P. Dupuis, Y. Cormier, M. Fenech, A. Corbeil, and B. Jodoin, "Flow structure identification and analysis in fin arrays produced by cold spray additive manufacturing," *Int. J. Heat Mass Transf.*, vol. 93, pp. 301–313, Feb. 2016.
[140] K. Wong *et al.*, "Title Convective Heat Transfer Performance Of Staggered Heat Sink Arrays Fabricated By Selective Laser Melting," 2016.
[141] "3ders.org - Plunkett Associates uses 3D printing to build high performance heat sinks | 3D Printer News & 3D Printing News." [Online]. Available: https://www.3ders.org/articles/20160115-plunkett-associates-uses-3d-printing-to-build-high-performance-heat-sinks.html. [Accessed: 06-Mar-2019].
[142] E. M. Dede, S. N. Joshi, and F. Zhou, "Topology Optimization, Additive Layer Manufacturing, and Experimental Testing of an Air-Cooled Heat Sink," *J. Mech. Des.*, vol. 137, no. 11, p. 111403, Oct. 2015.
[143] M. Norfolk and H. Johnson, "Solid-State Additive Manufacturing for Heat Exchangers," *JOM*, vol. 67, no. 3, pp. 655–659, Mar. 2015.
[144] S. M. Thompson, Z. S. Aspin, N. Shamsaei, A. Elwany, and L. Bian, "Additive manufacturing of heat exchangers: A case study on a multi-layered Ti–6Al–4V oscillating heat pipe," *Addit. Manuf.*, vol. 8, pp. 163–174, Oct. 2015.
[145] "Heat Sinks are an Ideal DMLS Application | i3D MFG." [Online]. Available: https://www.i3dmfg.com/heat-sinks-ideal-dmls-application/. [Accessed: 06-Mar-2019].
[146] Y. Cormier, P. Dupuis, A. Farjam, A. Corbeil, and B. Jodoin, "Additive manufacturing of pyramidal pin fins: Height and fin density effects under forced convection," *Int. J. Heat Mass Transf.*, vol. 75, pp. 235–244, Aug. 2014.
[147] J. Assaad, A. Corbeil, P. F. Richer, and B. Jodoin, "Novel Stacked Wire Mesh Compact Heat Exchangers Produced Using Cold Spray," *J. Therm. Spray Technol.*, vol. 20, no. 6, pp. 1192–1200, Dec. 2011.
[148] C. Hutter, D. Büchi, V. Zuber, and P. Rudolf von Rohr, "Heat transfer in metal foams and designed porous media," *Chem. Eng. Sci.*, vol. 66, no. 17, pp. 3806–3814, Sep. 2011.
[149] D. A. Ramirez *et al.*, "Open-cellular copper structures fabricated by additive manufacturing using electron beam melting," *Mater. Sci. Eng. A*, vol. 528, no. 16–17, pp. 5379–5386, Jun. 2011.
[150] R. Neugebauer, B. Müller, M. Gebauer, and T. Töppel, "Additive manufacturing boosts efficiency of heat transfer components," *Assem. Autom.*, vol. 31, no. 4, pp. 344–347, Sep. 2011.
[151] M. Wong, I. Owen, C. J. Sutcliffe, and A. Puri, "Convective heat transfer and pressure losses across

novel heat sinks fabricated by Selective Laser Melting," *Int. J. Heat Mass Transf.*, vol. 52, no. 1–2, pp. 281–288, Jan. 2009.

[152] V. Kumar, G. Manogharan, and D. R. Cormier, "DESIGN OF PERIODIC CELLULAR STRUCTURES FOR HEAT EXCHANGER APPLICATIONS."

[153] S. Tsopanos, C. J. Sutcliffe, and I. Owen, "THE MANUFACTURE OF MICRO CROSS-FLOW HEAT EXCHANGERS BY SELECTIVE LASER MELTING."

[154] G. M. Harpole and J. E. Eninger, "Micro-channel heat exchanger optimization," in *1991 Proceedings, Seventh IEEE Semiconductor Thermal Measurement and Management Symposium*, pp. 59–63.

[155] W. Escher, T. Brunschwiler, B. Michel, and D. Poulikakos, "Experimental Investigation of an Ultrathin Manifold Microchannel Heat Sink for Liquid-Cooled Chips," *J. Heat Transfer*, vol. 132, no. 8, p. 081402, 2010.

[156] E. Cetegen, "FORCE FED MICROCHANNEL HIGH HEAT FLUX COOLING UTILIZING MICROGROOVED SURFACES," 2010.

[157] R. Mandel, S. Dessiatoun, and M. Ohadi, "Embedded two-phase cooling of high flux electronics using a directly bonded FEEDS manifold," *Proc. 15th Intersoc. Conf. Therm. Thermomechanical Phenom. Electron. Syst. ITherm 2016*, pp. 77–84, 2016.

[158] D. G. Bae *et al.*, "Embedded two-phase cooling of high heat flux electronics on silicon carbide (SiC) using thin-film evaporation and an enhanced delivery system (FEEDS) manifold-microchannel cooler," in *2017 16th IEEE Intersociety Conference on Thermal and Thermomechanical Phenomena in Electronic Systems (ITherm)*, 2017, pp. 466–472.

[159] F. Battaglia, F. Singer, S. V. Dessiatoun, and M. M. Ohadi, "Comparison of near source two-phase flow cooling of power electronics in thermosiphon and forced convection modes," in *2017 16th IEEE Intersociety Conference on Thermal and Thermomechanical Phenomena in Electronic Systems (ITherm)*, 2017, pp. 752–758.

[160] E. Kermani, S. Dessiatoun, A. Shooshtari, and M. M. Ohadi, "Experimental investigation of heat transfer performance of a manifold microchannel heat sink for cooling of concentrated solar cells," in *2009 59th Electronic Components and Technology Conference*, 2009, pp. 453–459.

[161] K. Yang and C. Zuo, "A novel multi-layer manifold microchannel cooling system for concentrating photovoltaic cells," *Energy Convers. Manag.*, vol. 89, pp. 214–221, Jan. 2015.

[162] V. Jha, S. Dessiatoun, A. Shooshtari, E. S. Al-Hajri, and M. M. Ohadi, "Experimental Characterization of a Nickel Alloy-Based Manifold-Microgroove Evaporator," *Heat Transf. Eng.*, vol. 36, no. 1, pp. 33–42, 2015.

[163] M. A. Arie, A. H. Shooshtari, S. V. Dessiatoun, E. Al-Hajri, and M. M. Ohadi, "Numerical modeling and thermal optimization of a single-phase flow manifold-microchannel plate heat exchanger," *Int. J. Heat Mass Transf.*, vol. 81, pp. 478–489, Feb. 2015.

[164] R. Mandel, A. Shooshtari, and M. Ohadi, "A '2.5-D' modeling approach for single-phase flow and heat transfer in manifold microchannels," *Int. J. Heat Mass Transf.*, vol. 126, pp. 317–330, Nov. 2018.

[165] R. Mandel, M. Arie, A. Shooshtari, and M. Ohadi, "A Heat Spreading Model for Double-Sided, Cross-Flow, Manifold-Microchannel Heat Exchangers," in *2018 17th IEEE Intersociety Conference on Thermal and Thermomechanical Phenomena in Electronic Systems (ITherm)*, 2018, pp. 147–155.

[166] V. Aute, K. Saleh, O. Abdelaziz, S. Azarm, and R. Radermacher, "Cross-validation based single response adaptive design of experiments for Kriging metamodeling of deterministic computer simulations," *Struct. Multidiscip. Optim.*, vol. 48, no. 3, pp. 581–605, Sep. 2013.

[167] S. N. Lophaven, H. B. Nielsen, and J. Søndergaard, "DACE A MATLAB Kriging Toolbox."

[168] R. Kukowski, "MDT: Micro Deformation Technology," in *Materials*, 2003, vol. 2003, pp. 305–308.

[169] S. K. Mylavarapu, X. Sun, R. N. Christensen, R. R. Unocic, R. E. Glosup, and M. W. Patterson, "Fabrication and design aspects of high-temperature compact diffusion bonded heat exchangers," *Nucl. Eng. Des.*, vol. 249, pp. 49–56, Aug. 2012.

[170] "Laser Micromachining - Potomac Photonics Services," *https://www.potomac-laser.com/*.
[171] X. Zhang, "DESIGN AND PERFORMANCE CHARACTERIZATION OF AN ADDITIVELY-MANUFACTURED HEAT EXCHANGER FOR HIGH TEMPERATURE APPLICATIONS," University of Maryland, 2018.
[172] "How to Print Overhangs, Bridges and Beyond the 45° Rule + No Supports." [Online]. Available: https://rigid.ink/blogs/news/how-to-print-overhangs-bridges-and-exceeding-the-45-rule. [Accessed: 25-Mar-2019].
[173] "ProX DMP 200 - Metal 3D Printer | 3D Systems." [Online]. Available: https://www.3dsystems.com/3d-printers/prox-dmp-200?utm_medium=search&utm_source=google&utm_campaign=70134000001YZgy&utm_term=DYNAMIC+SEARCH+ADS&utm_content=General&gclid=EAIaIQobChMI86OMjt7r5wIVi5yzCh0FXQrZEAAYASAAEgLo5vD_BwE&gclsrc=aw.ds. [Accessed: 24-Feb-2020].
[174] "ProX DMP 300 - Metal 3D Printer | 3D Systems." [Online]. Available: https://au.3dsystems.com/3d-printers/prox-dmp-300?utm_medium=search&utm_source=google&utm_campaign=70134000001YZgy&utm_term=DYNAMIC+SEARCH+ADS&utm_content=General&gclid=EAIaIQobChMIya_xrN7r5wIVRj0MCh0fJwRcEAAYASAAEgKgKPD_BwE&gclsrc=aw.ds. [Accessed: 24-Feb-2020].
[175] "EOS M 290 - industrial 3D printed parts from metal materials." [Online]. Available: https://www.eos.info/eos-m290. [Accessed: 24-Feb-2020].
[176] "Layer Thickness : Precision of 3D Printing." [Online]. Available: https://www.sculpteo.com/en/glossary/layer-thickness-definition/. [Accessed: 27-Mar-2019].
[177] T. Craeghs, S. Clijsters, E. Yasa, and J.-P. Kruth, "Online Quality Control of Selective Laser Melting," *SOLID Free. Fabr. Proc.*, pp. 212–226, 2011.
[178] B. N. Taylor and C. E. Kuyatt, "Guidelines for Evaluating and Expressing the Uncertainty of NIST Measurement Results," 1994.
[179] G. Nellis and S. A. Klein, *Heat transfer*. Cambridge University Press, 2009.
[180] S. Liu, Y. Huang, and J. Wang, "Theoretical and numerical investigation on the fin effectiveness and the fin efficiency of printed circuit heat exchanger with straight channels," *Int. J. Therm. Sci.*, vol. 132, pp. 558–566, Oct. 2018.
[181] I. H. Kim and H. C. NO, "Thermal-hydraulic physical models for a Printed Circuit Heat Exchanger covering He, He-CO2 mixture, and water fluids using experimental data and CFD," *Exp. Therm. Fluid Sci.*, vol. 48, pp. 213–221, 2013.
[182] S. U. Yuruker, R. K. Mandel, A. Shooshtari, and M. M. Ohadi, "A metamodeling approach for optimization of manifold microchannel systems for high heat flux cooling applications," in *InterSociety Conference on Thermal and Thermomechanical Phenomena in Electronic Systems, ITHERM*, 2019, vol. 2019-May, pp. 982–990.